Universidade do Minho
Escola de Engenharia

Basel Ahmed Mohamed Saad Ali Fouda

Strengthening of Steel profiles with Web Openings using FRP

FRP++
Advanced structural analysis and design using composite materials

Funded by the European Union

September 2026

Strengthening of Steel profiles with Web Openings using FRP
Basel Ahmed Mohamed Saad Ali Fouda
FRP++ Advanced structural analysis and design using composite materials
UMinho | 2026

The European Master in Advanced Structural Analysis and Design using Composite Materials is a join initiative of:

Universidade do Minho · Universitat de Girona · Università degli Studi di Napoli Federico II · INSA Institut National des Sciences Appliquées Toulouse · Université de Toulouse

Universidade do Minho
Escola de Engenharia

Basel Ahmed Mohamed Saad Ali Fouda

Strengthening of Steel Profiles with Web Openings using FRP

FRP++
Advanced structural analysis and design using composite materials

Master Dissertation
European Master Advanced Structural Analysis and Design using Composite Materials

Work developed under the supervision of
Professor Isabel Valente
Doctor João Pereira

Funded by the European Union

September 2026

DIREITOS DE AUTOR E CONDIÇÕES DE UTILIZAÇÃO DO TRABALHO POR TERCEIROS

Este é um trabalho académico que pode ser utilizado por terceiros desde que respeitadas as regras e boas práticas internacionalmente aceites, no que concerne aos direitos de autor e direitos conexos.

Assim, o presente trabalho pode ser utilizado nos termos previstos na licença abaixo indicada.

Caso o utilizador necessite de permissão para poder fazer um uso do trabalho em condições não previstas no licenciamento indicado, deverá contactar o autor, através do RepositóriUM da Universidade do Minho.

Licença concedida aos utilizadores deste trabalho



Atribuição CC BY

https://creativecommons.org/licenses/by/4.0/

ACKNOWLEDGEMENTS

Praise be to Allah, the Most Gracious, the Most Merciful

I would like to express my sincere gratitude to my family for their unwavering support, and to my supervisors, Prof. Isabel Valente and Dr. João Pereira, for their invaluable guidance, encouragement, patience, and constructive feedback throughout the development of this thesis. My thanks also extend to all the professors who taught me during the program, as well as to those in Egypt, and to everyone who contributed to this work in any capacity.

I would like to gratefully acknowledge the financial support provided by the European Union for participation in the Erasmus Mundus FRP++ European Master Course in Advanced Structural Analysis and Design using Composite Materials (Project no. 101048961). This work was funded by NORTE2030 through the R&D project "EcoBEAM - Desenvolvimento de soluções inovadoras de vigas mistas, com foco na sustentabilidade" with reference NORTE2030-FEDER-01432600. This work was also supported by FCT/MCTES under the R&D Unit Institute for Sustainability and Innovation in Structural Engineering (ISISE), under the references UID/4029/2025 (DOI: 10.54499/UID/04029/2025), UID/PRR/04029/2025 (DOI: 10.54499/UID/PRR/04029/2025) and UID/PRR2/04029/2025 (DOI: 10.54499/UID/PRR2/04029/2025), and under the Associate Laboratory Advanced Production and Intelligent Systems ARISE under reference LA/P/0112/2020 (DOI: 10.54499/LA/P/0112/2020).

STATEMENT OF INTEGRITY

I hereby declare having conducted this academic work with integrity. I confirm that I have not used plagiarism or any form of undue use of information or falsification of results along the process leading to its elaboration.

I further declare that I have fully acknowledged the Code of Ethics and Conduct of the University of Minho.

DECLARATION ON THE USE OF ARTIFICIAL INTELLIGENCE (AI) TOOLS

I hereby declare having acted this academic work with integrity and confirm that I have not resorted to any form of undue use of AI tools, nor to the falsification or omission of information, sources, data, results or processes in any of the stages leading to its elaboration.

I further declare that any use of AI tools was done in a transparent and responsible manner, being duly noted in the work, and that I critically verified the accuracy of the content produced with their support, assuming full responsibility for what I submit.

I further declare that I have fully acknowledged the Code of Ethics and Conduct of the University of Minho, as well as the applicable standards of academic integrity and data protection.

Reforço de Perfis de Aço com Aberturas na Alma Utilizando FRP

RESUMO

A introdução de grandes aberturas na alma de vigas de aço é frequentemente necessária para permitir a passagem de instalações técnicas, podendo, contudo, reduzir a capacidade resistente e promover mecanismos de rotura locais, nomeadamente o mecanismo de Vierendeel. As soluções convencionais com rigidificadores de aço soldados são eficazes, mas apresentam limitações relacionadas com o aumento de peso, corrosão, necessidade de soldadura e condicionantes de instalação. Esta dissertação investiga a utilização de polímero reforçado com fibras de carbono (CFRP), coladas externamente, como alternativa para o reforço de vigas de aço lateralmente restringidas com grandes aberturas na alma.

Foi desenvolvido em Abaqus um modelo não linear de elementos finitos, avaliado por comparação com resultados experimentais disponíveis na literatura. O estudo paramétrico considerou aberturas retangulares e circulares de diferentes dimensões, localizadas junto ao apoio ou a meio vão, bem como diferentes configurações de CFRP aplicadas na alma, nos banzos ou em ambos. Foram comparadas condições de ligação perfeita e modelos de interface coesiva, incluindo adesivos com comportamento linear e não linear. Rigidificadores convencionais de aço foram também analisados como referência, tendo sido ainda desenvolvida uma abordagem analítica para estimar a resistência das vigas reforçadas.

Os resultados mostram que a eficácia do CFRP depende do mecanismo estrutural dominante. Em regiões de esforço transverso elevado, o reforço da alma é mais eficaz, enquanto a meio vão o reforço dos banzos apresenta melhor desempenho. As aberturas circulares mostraram-se menos penalizadoras do que as retangulares para dimensões comparáveis. O descolamento reduziu a eficácia do CFRP relativamente à ligação perfeita, enquanto os adesivos não lineares permitiram uma utilização mais eficiente do reforço. Para as configurações analisadas, o CFRP demonstrou potencial como alternativa leve aos rigidificadores de aço, e a abordagem analítica apresentou uma concordância encorajadora com os resultados numéricos.

PALAVRAS-CHAVE: Reforço com CFRP; Vigas de aço; Aberturas na alma; Adesivo; Análise por elementos finitos.

Strengthening of Steel Profiles with Web Openings Using FRP

ABSTRACT

Large web openings are frequently introduced in steel beams to accommodate building services, but they may significantly reduce load-carrying capacity and promote local failure mechanisms, particularly Vierendeel bending. Conventional welded steel stiffeners are effective but present disadvantages related to additional weight, corrosion, welding requirements, and installation constraints. This dissertation investigates externally bonded carbon fibre-reinforced polymer (CFRP) plates as an alternative strengthening solution for laterally restrained steel beams with large web openings.

A nonlinear finite element modelling framework was developed in Abaqus and assessed against experimental results from the literature. A parametric study considered rectangular and circular openings of different depths, located near the support or at mid-span, together with different CFRP configurations applied to the web, flanges, or both. Perfect bonding and cohesive interface modelling were compared, including linear and nonlinear adhesive behaviour. Conventional steel stiffeners were also analysed as a reference. In parallel, an analytical approach was developed to estimate the resistance of CFRP-strengthened beams and compared with the numerical results.

The results show that CFRP effectiveness depends strongly on the governing structural mechanism. For openings in high-shear regions, CFRP bonded to the web is most effective and may shift failure from Vierendeel action to global flexure, whereas flange strengthening is generally more effective at mid-span. Circular openings were less detrimental than rectangular ones for comparable dimensions. Debonding reduced the effectiveness of CFRP relative to the perfect-bond assumption, while nonlinear adhesives allowed greater utilisation of the strengthening system than linear adhesives. Within the configurations investigated, CFRP showed potential as a lightweight alternative to conventional steel stiffeners. The analytical approach also showed encouraging agreement with the numerical results, although its applicability remains dependent on the adopted debonding formulation.

KEYWORDS: CFRP strengthening; Steel beams; Web openings; Adhesive debonding; Finite element analysis.

TABLE OF CONTENTS

Acknowledgements iii
Resumo v
Abstract vi
Table of Contents viii
List of Figures xi
List of Tables xviii
List of Abbreviations and Symbols xix
1. Introduction 1
1.1. Background and motivation 1
1.2. Problem statement 3
1.3. Aims and objectives 4
1.4. Scope and limitations 5
1.5. Structure of the thesis 6
1.6. Contributions to knowledge 7
2. Literature review 9
2.1. Structural behaviour of steel members with web openings 9
2.1.1. Types of steel members with web openings 9
2.1.2. Failure modes 10
2.2. Conventional strengthening and retrofit techniques 12
2.2.1. Steel plate and stiffener-based solutions 12
2.2.2. Advantages and limitations of steel stiffeners 13
2.3. FRP strengthening of steel members: fundamentals 14
2.3.1. Mechanical properties and advantages and disadvantages of FRP 14
2.3.2. Bond between FRP and steel 14
2.3.3. Common strengthening forms 15
2.3.4. Method of installation 16
2.3.5. Typical failure modes of FRP-strengthened steel members 16
2.3.6. Debonding and anchorage issues 17
2.4. FRP strengthening of steel beams with discrete web openings 20
2.5. Strengthened steel beams with multiple or regularly spaced openings 24

2.6. Other steel members with FRP strengthening 28
2.6.1. Plate girders (fabricated girders) 28
2.6.2. Steel plate shear walls (SPSW) 33
2.7. Summary 36
3. Analytical Investigation on Perforated Beams 39
3.1. Introduction 39
3.2. Material properties 39
3.3. Geometry and cross-sectional properties 40
3.4. Classification of the cross section 41
3.5. Shear stud connectors 43
3.6. Degree of shear connection 45
3.7. Load combinations 47
3.8. Ultimate limit states verification 47
3.8.1. Global bending resistance of perforated beams at openings 50
3.8.2. Local bending resistance of perforated beams at openings (Vierendeel bending resistance) 52
3.8.3. Elastic bending resistance of Tees 55
3.8.4. Shear resistance of perforated steel section 56
3.8.5. Design bending resistance of beams with stiffened openings 59
3.8.6. Elastic bending resistance of Tees 59
3.9. Serviceability limit states 60
3.10. Estimating the strength of the CFRP plates 62
3.10.1. Axial tension 62
3.10.2. Axial compression 63
3.11. Estimating the strength of the CFRP strengthened beam 63
3.11.1. Debonding load 63
3.11.2. For openings positioned at mid span 64
3.11.3. For openings positioned near the support 66
3.11.4. Vierendeel bending failure 66
3.11.5. Flexural failure 68
4. Numerical Modelling and Validation 69
4.1. Introduction 69
4.2. Finite element modelling and numerical validation 69
4.2.1. Benchmark 1 – Local buckling 70

4.2.2. Benchmark 2 – Laterally restrained beams 72
4.2.3. Benchmark 3-Cellular beam 75
4.2.4. Summary of Validation 78
4.3. Numerical model adopted for the parametric study 78
4.3.1. Geometry and steel material 78
4.3.2. CFRP material and strengthening configurations 79
4.3.3. Steel-CFRP interface 80
4.3.4. Loading and boundary conditions 83
4.3.5. Loading and solution procedure 84
4.3.6. Element type and mesh sensitivity 84
5. Parametric study 87
5.1. Introduction 87
5.2. Influence of opening geometry and location 89
5.2.1. Quarter-span openings 89
5.2.2. Mid-span openings 93
5.3. Influence of strengthening configuration – perfect bond 97
5.3.1. Quarter-span opening 97
5.3.2. Mid-span opening 106
5.4. Influence of interface debonding 110
5.4.1. Quarter-span opening 110
5.4.2. Mid-span opening 117
5.5. Influence of adhesive behaviour 126
5.5.1. CFRP web strengthening 126
5.5.2. CFRP flange strengthening 129
5.6. Assessment of the analytical approach 132
5.7. Summary 133
6. Conclusions and Future Work 139
6.1. Summary of research 139
6.2. Key conclusions 140
6.3. Limitations and future work 142
References 145

LIST OF FIGURES

Figure 1-1: Typical stress-strain curve for FRP and mild steel [9] 2
Figure 2-1: Openings in different structural members: a) Hot-rolled sections; b) Fabricated plate girders; c) Door-type opening in SPSW; d) Window-type opening in SPSW [13,14] 9
Figure 2-2: Conventional failure modes: a) Plastic hinge formation; b) Lateral torsional buckling [15,16,17]. 10
Figure 2-3: Failure modes due to discrete openings: a) Flexural mechanism with L.T.B of the middle segment; b) schematic for Vierendeel mechanism; c) Real Vierendeel failure [6,7,19] 11
Figure 2-4: Failure modes with regularly spaced openings: a) Web-post buckling under shear; b) Weld rupture; c) Web-post buckling under compression; d) Web crippling [21,22,23,24] 12
Figure 2-5: Vierendeel mechanism and longitudinal steel stiffener a) Effect of adding stiffeners; b) Buckling and tearing along the two diagonals; c) Elongated and shortened diagonals [25] 13
Figure 2-6: Various conventional strengthening techniques: a) Double transverse stiffeners; b) Ring stiffener; c) Transverse stiffener [26,27,28] 13
Figure 2-7: Different forms of FRP: a) Wet lay-ups; b) Prepreg; c) Profiles [34,35]..... 15
Figure 2-8: Schematic for failure modes in CFRP-bonded steel systems [9] 17
Figure 2-9: Bilinear traction separation law for mixed mode loading; a) Interaction between different modes; b) Mode II ; c) Mixed mode; d) Mode I [36] 18
Figure 2-10: Cohesive zone modelling: a) Cohesive zone element; b) Cohesive surface [37] 19
Figure 2-11: Measures to prevent debonding: a) U-Jacket; b) Anchorage system [9,38] 20
Figure 2-12: CFRP strengthening configurations [23]..... 22
Figure 2-13: GFRP strengthening configurations [40] 23
Figure 2-14: Different opening configurations [16]..... 24
Figure 2-15: Web post: a) Before strengthening; b) After strengthening [27] 26
Figure 2-16: CFRP and mild steel stiffeners [28] 26
Figure 2-17: Transverse stiffeners [42]..... 27
Figure 2-18: CFRP wrapped all around the beam [30,43]..... 28
Figure 2-19: Strengthening method; a) Out of plane; b) In plane [45] 30
Figure 2-20: Strengthening scheme [46]..... 30
Figure 2-21: Strengthening scheme Type 1 (on the left) and Type 2 (on the right) [47]..... 31

Figure 2-22: Opening types: a) Window opening; b) Door opening [13] 34
Figure 2-23: Unstrengthened and strengthened schemes for SPSW: a) Steel plate shear wall (SPSW); b) SPSW with bonded laminate; c) SPSW with stiffened laminate [50] 35
Figure 2-24: Different CFRP configurations: a) Horizontal and vertical; b) Oriented along the diagonals; c) Combined horizontal and vertical and inclined [51] 36
Figure 3-1: Different Geometries a) Circular opening; b) Rectangular opening; c) Elongated opening; d) Closely spaced circular opening [11] 41
Figure 3-2: Max Width and thickness for compression parts: a) Internal parts; b) Outstand flange [52] 42
Figure 3-3: Stress distribution due to the shear lag effect and the concept of the effective stress [29] 42
Figure 3-4: Deflected shape of both; a) Non-composite beam; b) Composite beam; c) Different strain distribution [29] 44
Figure 3-5: Various failure modes [12] 48
Figure 3-6: Equilibrium of the beam at openings under pure bending [12] 50
Figure 3-7: Equilibrium of the beam at openings under pure bending [12] 52
Figure 3-8: Shear forces at an opening [12] 57
Figure 3-9: Dimensions of the Tee sections at the opening location; a) CFRP attached to the flange; b) CFRP attached to the web 64
Figure 3-10: Longitudinal section of the beam with the opening 67
Figure 3-11: Middle cross section with the plastic stress distribution 68
Figure 4-1: Geometry of the beam with the locations for different strain gages [56] 70
Figure 4-2: Material model for steel [56] 70
Figure 4-3: Reference point and coupling constraint for support application 71
Figure 4-4: Stress distribution of the beam 71
Figure 4-5: Force-displacement response for model 1 71
Figure 4-6: Lateral restraint and boundary condition; a) plan view for lateral restraint [39]; b) Reference point with coupling constraint for the support 72
Figure 4-7: Loading configurations: a) Schematic for loading [39]; b) Tested beam [39] and loading on the model 73
Figure 4-8: First Buckling Mode used as Imperfection 74
Figure 4-9: Force-displacement response for model 2 74
Figure 4-10: Failure mode; a) Experiment [39]; b) Numerical model 75
Figure 4-11: Loading, boundary conditions and lateral supports 76

Figure 4-12: Buckling mode 77
Figure 4-13: Force-displacement response for model 3 77
Figure 4-14: Deformed beam; a) Model vertical displacement; b) Deformed shape from experiment [21] 77
Figure 4-15: Beam model; a) 3D view; b) Cross section view 79
Figure 4-16: Geometric Parameters of the opening 79
Figure 4-17: Different CFRP configurations: a) To flanges; b) To web; c) To flanges and web 80
Figure 4-18: Linear damage evolution model [56] 82
Figure 4-19: Reference point coupled to the support area 83
Figure 4-20: Reference point coupled to the top flange for load application 84
Figure 4-21: Beam divisions in sensitivity analysis a) Longitudinal Section; b) Cross section 85
Figure 4-22: Force-displacement response for the models used for sensitivity analysis 86
Figure 5-1: Force-displacement response for various rectangular opening sizes at quarter span 89
Figure 5-2: Stress distribution and displacement for beam with 0.5h rectangular opening: a) Solid beam-stress distribution; b) Stress distribution; c) Solid beam-displacement; d) Displacement 90
Figure 5-3: Stress distribution and displacement for beam with 0.65h rectangular opening: a) Stress distribution; b) Stress distribution around the opening; c) Displacement 91
Figure 5-4: Explanation of plastic hinge formation for 075h. opening a) Opening collapse from model; b) Forces and moments around the opening [12] 91
Figure 5-5: Force-displacement response for quarter span circular opening 92
Figure 5-6: Stress distribution and displacement for beam with 0.65h circular opening; a) Stress distribution; b) Displacement 92
Figure 5-7: Stress distribution and displacement for beam with 0.8h circular opening: a) Stress distribution; b) Stress distribution around the opening; c) Displacement 93
Figure 5-8: Force-displacement response for various rectangular opening sizes at mid span 93
Figure 5-9: Stress distribution and displacement for beam with 0.65h rectangular: a) Stress distribution; b) Stress distribution around the opening; c) Displacement 94
Figure 5-10: Stress distribution and displacement for beam with 0.75h rectangular opening: a) Stress distribution; b) Stress distribution around the opening; c) Displacement 95
Figure 5-11: Trend in strength reduction with opening size 95

Figure 5-12: Force-displacement response for various circular opening sizes at mid span.... 96
Figure 5-13: Stress distribution and displacement for beam with 0.5h circular opening: a) Beam stress distribution; b) Beam displacement.... 96
Figure 5-14: Trend in strength reduction with opening size.... 97
Figure 5-15: Force-displacement response for rectangular opening quarter span with strengthening schemes for 0.65h.... 98
Figure 5-16: Stress distribution and displacements; a) Beam stress distribution with CFRP to the flange; b) Displacement.... 98
Figure 5-17: Stress distribution and displacement for beam with 0.65h rectangular opening ; a) Beam with steel stiffener stress distribution; b) Stresses around the opening; c) Displacement 99
Figure 5-18: Force-displacement response for rectangular opening quarter span with strengthening schemes for 0.75h.... 99
Figure 5-19: Stress distribution and displacement for beam with 0.75h rectangular opening; a) Beam stress distribution with CFRP to the flange; b) Displacement.... 100
Figure 5-20: Stress distribution and Displacement for beam with 0.75h rectangular opening; a) Beam stress distribution with steel stiffener with 150 mm anchorage length; b) Displacement 100
Figure 5-21: Force-displacement response for rectangular opening quarter span with different anchorage length for steel stiffeners.... 101
Figure 5-22: Stress distribution and displacement; a) Beam stress distribution with steel stiffener of 250 mm anchorage length; b) Displacement.... 101
Figure 5-23: Force-displacement response for rectangular opening quarter span with web strengthening schemes.... 102
Figure 5-24: Stress distribution and displacement: a) Beam with 0.65h opening-stress distribution; b) Beam with 0.75h opening-stress distribution; c) CFRP stress distribution for 0.65h opening; d) CFRP stress distribution for 0.75h opening; e) Displacement for beam with 0.65h opening; f) Displacement for beam with 0.75h opening.... 102
Figure 5-25: Force-displacement response for rectangular opening quarter span with flanges and web strengthening schemes.... 103
Figure 5-26: Stress distribution and displacement: a) Beam with 0.65h opening-stress distribution; b) Beam with 0.75h opening-stress distribution; c) Displacement for beam with 0.65h opening; d) Displacement for beam with 0.75h opening.... 103

Figure 5-27: Force-displacement response for circular opening quarter span strengthening schemes for 0.8h 104
Figure 5-28: Stress distribution for beam with 0.8h circular opening with various strengthening schemes; a) Beam; b) CFRP to the flange; c) Beam; d) CFRP to the web; e) Beam; f) To flanges and web; g) Beam; h) Steel stiffener 105
Figure 5-29: Force-displacement response for rectangular opening with different strengthening scheme for 0.65h 106
Figure 5-30: Stress distribution and displacement for 0.65h rectangular opening with CFRP to web; a) Beam stress distribution; b) Stresses around the opening; c) Displacement 106
Figure 5-31: Force-displacement response for rectangular opening with different strengthening scheme for 0.75h 107
Figure 5-32: Stress distribution and displacement for beam with 0.75h rectangular opening with CFRP to web; a) Beam stress distribution; b) Stresses around the opening; c) Displacement 107
Figure 5-33: Force-displacement response for circular opening with different strengthening scheme for a) 0.65h; b) 0.8h 108
Figure 5-34: Stress distribution and displacement; a) Beam stress distribution; b) CFRP stress distribution; c) Displacement (0.65h) 109
Figure 5-35: Stress distribution and displacement; a) Beam stress distribution; b) CFRP stress distribution; c) Displacement (0.8h) 109
Figure 5-36: Force-displacement response for rectangular opening with different web bonding conditions for 0.65h opening 111
Figure 5-37: Stress distribution and displacement; a) Plastic hinges formed at the LMS; b) Displacement at damage initiation; c) Damage initiation top stem; d) Damage initiation bottom stem 112
Figure 5-38: Stress distribution and displacement; a) CFRP stress distribution; b) Displacement; c) Damage evolution top stem; d) Damage evolution bottom stem 113
Figure 5-39: Force-displacement response for different bonding conditions for CFRP flange strengthening 113
Figure 5-40: Stress distribution and displacement for beam with 0.65h rectangular opening; a) Stress distribution around the opening; b) Displacement at damage initiation; c) Damage initiation top flange; d) Damage initiation bottom flange 114
Figure 5-41: CFRP stress distribution 114

Figure 5-42: Displacement and damage evolution for beam with 0.65h rectangular opening; a) Displacement at debonding; b) Damage top flange; c) Damage bottom flange 115
Figure 5-43: Force-displacement response for circular opening with different bonding conditions for 0.8h opening..... 116
Figure 5-44: Stress distribution and displacement for beam with 0.8h circular opening; a) Stress distribution around the opening; b) Displacement at damage initiation; c) Damage initiation top stem; d) Damage initiation bottom stem 116
Figure 5-45: Displacement and damage evolution for beam with 0.8h circular opening; a) Displacement b) Damage top stem; c) Damage bottom stem 117
Figure 5-46: Stress distribution for beam with 0.8h circular opening; a) Steel beam; b) CFRP plates..... 117
Figure 5-47: Force-displacement response for rectangular opening with different bonding conditions for 0.65h opening..... 118
Figure 5-48: Stress distribution and displacement for beam with 0.65h rectangular opening; a) Beam stress distribution; b) CFRP stress distribution; c) Displacement at damage initiation; d) Damage initiation top stem; e) Damage initiation bottom stem..... 118
Figure 5-49: Stress distribution and displacement; a) Beam stress distribution; b) CFRP stress distribution; c) Displacement at debonding; d) Damage evolution to top stem; e) Damage evolution to bottom stem..... 119
Figure 5-50: Force-displacement response for different bonding conditions for 0.65h rectangular openings 120
Figure 5-51: Displacement and damage initiation for beam with 0.65h rectangular opening; a) Displacement at damage initiation; b) Damage initiation top flange; c) Damage initiation bottom flange..... 120
Figure 5-52: Stress distribution and displacement for beam with 0.65h rectangular opening; a) Beam stress distribution; b) CFRP stress distribution; c) Displacement at debonding; d) Damage evolution top flange; e) Damage evolution bottom flange..... 121
Figure 5-53: Force-displacement response for 0.8h circular opening with different bonding condition..... 122
Figure 5-54: Stress distribution and displacement for beam with 0.8h circular opening; a) Beam stress distribution; b) CFRP stress distribution; c) Displacement at damage initiation; d) Damage initiation top stem; e) Damage initiation bottom stem..... 122
Figure 5-55: Displacement and damage evolution for beam with 0.8h circular opening; a) Beam displacement; b)Damage evolution top stem; c) Damage evolution bottom stem 123

Figure 5-56: Stress distribution; a) Steel Beam; b) CFRP plates 123
Figure 5-57: Force-displacement response for 0.8h circular opening with different bonding conditions 124
Figure 5-58: Stress distribution and displacement for beam with 0.8h circular opening; a) Beam stress distribution; b) Displacement; c) Damage top flange; d) Damage bottom flange 124
Figure 5-59: Stress distribution and displacement for beam with 0.8h circular opening; a) Beam stress distribution; b) CFRP stress distribution; c) Displacement at debonding; d) Damage top flange; e) Damage bottom flange 125
Figure 5-60: Constitutive model for adhesive; a) Linear; b) Nonlinear [9] 126
Figure 5-61: Force-displacement response for 0.65h rectangular opening with linear and nonlinear adhesive 127
Figure 5-62: Stress distribution and displacement for beam with linear adhesive; a) Beam stress distribution; b) CFRP stress distribution; c) Displacement at damage initiation; d) Damage top stem; e) Damage bottom stem 128
Figure 5-63: Stress distribution and displacement for beam with linear adhesive; a) Beam stress distribution; b) CFRP stress distribution; c) Displacement at debonding; d) Damage top stem; e) Damage bottom stem 128
Figure 5-64: Stress distribution a) around opening corners; b) CFRP plate 129
Figure 5-65: Stress distribution vs displacement for 0.65h rectangular opening with different adhesives 129
Figure 5-66: Stress distribution and displacement; a) Beam stress distribution; b) CFRP stress distribution; c) Displacement at damage initiation; d) Damage initiation top flange; e) Damage initiation bottom flange 130
Figure 5-67: Displacement and damage initiation; a) Displacement at damage initiation; b) Top flange damage initiation; c) Bottom flange damage initiation 131
Figure 5-68: Stress distribution; a) Around the corners of the opening; b) CFRP plates 131

LIST OF TABLES

Table 3-1: Yield and Ultimate strength of various steel grades [52] 39
Table 3-2: Properties of CFRP and adhesive [23,53] 40
Table 3-3: Compressive strength and young's modulus of different concrete classes [54] 40
Table 3-4: Limitations on the dimensions of different unstiffened openings [11] 41
Table 3-5: Upper limits Kt, max for the reduction factor Kt [12] 45
Table 3-6: Equivalent rectangular opening dimensions of different opening shapes for verification of Vierendeel bending [11] 55
Table 4-1: Material Properties for steel adopted from [39] 72
Table 4-2: Geometric parameters for the cellular beam adopted from [21] 76
Table 4-3: Comparison of the capacity for different benchmarks 78
Table 4-4: Engineering properties of the CFRP [23] 79
Table 4-5: Stresses at failure [23] 80
Table 4-6: Properties of the adhesives used [53] 83
Table 4-7: Different schemes used for mesh sensitivity analysis 85
Table 5-1: Parametric study matrix 88
Table 5-2: Camparison between the analytical predictions and the corresponding numerical model 132
Table 5-3: Load-carrying capacity of unstrengthened beams with different opening shapes, sizes and locations 134
Table 5-4: Comparison of load-carrying capacity for perfect-bond and cohesive-interface models 135
Table 5-5: Influence of adhesive behavior on the load-carrying capacity of the CFRP-strengthened beam 136

LIST OF ABBREVIATIONS AND SYMBOLS

Abbreviations

CEN	European Committee for Standardization
LTB	Lateral Torsional Buckling
SPSW	Steel Plate Shear Wall
FRP	Fibre Reinforced Polymer
CFRP	Carbon Fibre Reinforced Polymer
GFRP	Glass Fibre Reinforced Polymer
ULS	Ultimate Limit States
SLS	Serviceability Limit States
FE	Finite Element
LMS	Low Moment Side
HMS	High Moment Side

Symbols

a_{eff}	Effective length of an opening for buckling and deflection calculations
a_{eq}	Equivalent length of an opening for Vierendeel bending
a_o	Overall length of an opening
A_{bT}	Cross-sectional area of bottom Tee
A_{s}	Cross-sectional area of stiffener
A_{tT}	Cross-sectional area of top Tee
$A_{\mathrm{v,bT}}$	Shear area of the bottom Tee
$A_{\mathrm{v,tT}}$	Shear area of the top Tee
b_{o}	Width of the horizontal part of a hexagonal or sinusoidal opening
b_{s}	Length of sinusoidal part of opening
b_{eff}	Effective width of web next to an opening for web buckling
d_{t}	Depth of web outstand of Tee section. For rolled profiles, the outstand d_{t} is measured from the root radius. For welded sections, d_{t} is measured from the weld toe.
E	Modulus of elasticity of steel
f_{y}	yield strength of the steel section
f_{ys}	yield strength of the stiffeners
$f_{\mathrm{y,bT}}$	yield strength of the bottom Tee
$f_{\mathrm{y,tT}}$	yield strength of the top Tee

$f_{\mathrm{y,red}}$	Reduced yield strength considering shear effect
H	Depth of steel section
h_{b}	Depth of bottom Tee
h_{eff}	Effective depth of steel section between the centroids of the Tees
h_{o}	Depth of opening (or diameter of circular opening)
h_{t}	Depth of top Tee
h_{eq}	Equivalent rectangular opening height
h_{w}	Depth of web of solid web section
I_{a}	Second moment of area of the solid web section
I_{bT}	Second moment of area of bottom Tee with or without longitudinal stiffeners
$I_{\mathrm{eff,a,o}}$	Effective second moment of area of the section at an opening used for global analysis
I_{tT}	Second moment of area of top Tee with or without longitudinal stiffeners
K_{o}	Factor on the shear deflection in *Vierendeel* bending due to the effect of longitudinal stiffeners
L	Span length of beam
$M_{\mathrm{add,Ed}}$	Design value of the bending moment due to the uniform loads applied to the compressed Tee at an opening, assuming that both chord ends are fixed and considering the chord length a_{eff}
$M_{\mathrm{bT,Rd}}$	Design value of bending resistance of bottom Tee
M_{Ed}	Design value of the global bending moment at the centreline of the opening
$M_{\mathrm{i,Ed}}$	Applied bending moment in the Tee cross-section of index *i*
$M_{\mathrm{N,bT,Rd}}$	Design value of reduced bending resistance of bottom Tee due to axial force
$M_{\mathrm{NV,T,Rd}}$	Design value of reduced bending resistance of Tee due to axial force and shear
$M_{\mathrm{NV,bT,Rd}}$	Design value of reduced bending resistance of bottom Tee due to axial force and shear
$M_{\mathrm{NV,tT,Rd}}$	Design value of reduced bending resistance of top Tee due to axial force and shear
$M_{\mathrm{pl,Rd}}$	Design value of plastic bending resistance of Tee
$M_{\mathrm{v,pl,Rd,i}}$	Design of plastic bending resistance of the Tee cross-sections of index *i*, reduced due to the presence of shear force
$M_{\mathrm{o,Rd}}$	Design value of bending resistance of beam at the opening position
$M_{\mathrm{o,pl,Rd}}$	Design value of plastic bending resistance of beam at the opening position
$M_{\mathrm{o,el,Rd}}$	Design value of elastic bending resistance of beam at the opening position
$M_{\mathrm{tT,Rd}}$	Design value of bending resistance of top Tee
$M_{\mathrm{T,el,Rd}}$	Design value of elastic bending resistance of the Tee
$M_{\mathrm{T,pl,Rd}}$	Design value of plastic bending resistance of the Tee
$M_{\mathrm{T,Rd}}$	Design value of bending resistance of the compressed Tee section in the plane of the web

N_{Ed}	Design value of the axial force
$N_{i,Ed}$	Applied axial force in the Tee cross-section of index *i*
$N_{b,Ed}$	Design value of the axial force in a cross-section the bottom Tee
$N_{T,Ed}$	Design value of the axial force applied to the compressed Tee due to global bending and additional axial forces.
$N_{bT,Rd}$	Design value of axial resistance of bottom Tee
$N_{bT,Rd}$	Design value of buckling resistance of the compressed Tee for buckling in the plane of the web and is determined for a buckling length of 0.5 a_{eff}
$N_{o,pl,Rd}$	Design value of the plastic axial resistance of a steel section with opening
$N_{pl,Rd}$	Design value of axial resistance
$N_{t,Ed}$	Design value of the axial force in a cross-section of the top Tee
$N_{T,el,Rd}$	Compression elastic resistance of the Tee
$N_{T,pl,Rd}$	Compression plastic resistance of the Tee
$N_{tT,Rd}$	Design value of axial resistance of top Tee
r	Root radius of rolled section
r_o	Radius at the corners of rectangular openings
s	Centre to centre spacing of adjacent openings
t_f	Thickness of flange (subscripts b and t refer to bottom and top flanges)
t_w	Thickness of web (subscripts b and t refer to bottom and top webs)
$t_{w,min}$	Minimum value of the web thickness for beams with webs of different thicknesses
$t_{w,tT}$	Thickness of the web of the top Tee
$t_{w,bT}$	Thickness of the web of the bottom Tee
$V_{b,Ed}$	Design value of the shear force in a cross-section of the bottom Tee
$V_{b,Rd}$	Design value of the shear resistance of the bottom Tee limited by pure shear or *Vierendeel* bending
V_{Ed}	Design value of the shear force acting on the beam at the centreline of opening
$V_{m,Ed}$	Design value of the shear force acting on a Tee due to the global bending at mid length of an opening
$V_{pl,Rd,b}$	Design value of plastic shear resistance of the bottom Tee
$V_{pl,Rd,t}$	Design value of plastic shear resistance of the top Tee
$V_{o,pl,Rd}$	Design value of plastic shear resistance at the opening
$V_{pl,Rd}$	Design value of plastic shear resistance of the solid web beam
$V_{t,Ed}$	Design value of the shear force in a cross-section of the top Tee
$V_{t,Rd}$	Design value of the shear resistance of the top Tee limited by pure shear or *Vierendeel* bending
$V_{w,Ed}$	Design value of the buckling resistance of the web

w_{add}	Additional deflection at mid-span due to the web openings
w_{b}	Mid-span deflection of solid web beam
X_{o}	Distance of centre of opening from nearer support
Z_{b},Z_{t}	Distance of the centroid of the T-section from outer edge of flange (subscripts b and t refer to bottom and top flange)
ε	Material parameter depending on f_y
$\Upsilon_{\mathrm{M_o}}, \Upsilon_{\mathrm{M_1}}$	Partial factors for steel
W	Value of the uniformly distributed load applied to the beam in kN/m
X	Length of the beam from the support to the nearest edge of the opening
R	Reaction at nearer support
Z_{el}	Distance from the elastic neutral axis of the steel section with the CFRP plate measured from the outer flange
Z_{pl}	Plastic neutral axis distance of the steel section with the CFRP plate measured from the outer flange
P_{u}	Load at which debonding is expected to occur
h_{eff}	Distance between the centroids of the top Tee and bottom Tee sections
$Z_{\mathrm{el,st}}$	distance from the centroid of the Tee section
A_{T}	Area of the Tee section
A_{P}	Area of the CFRP plate
E_{st}	Modulus of elasticity of the steel
h'	Distance from the centroid of the CFRP plate to the outer face of the top flange
b_{p}	CFRP plate width
t_{p}	Thickness of the CFRP plate
E_{p}	Elastic modulus of the CFRP plate
G_{f}	Interfacial fracture energy
$N_{\mathrm{c,Rd}}$	Design value of the compression resistance of the cross section in the longitudinal (x) direction
$f_{\mathrm{x,c,k}}$	Characteristic value of the compressive strength in the longitudinal (x) direction of the material
$N_{\mathrm{t,Rd}}$	Design value of the tensile resistance of the cross section in the longitudinal (x) direction
$f_{\mathrm{x,t,k}}$	Characteristic value of the tensile strength in the longitudinal (x) direction of the material
γ_{m}	Partial factor for the material accounting for the unfavourable deviations of the representative material from its characteristic values

γ_{Rd}	Partial factor accounting for the uncertainty in the resistance model, and for geometrical deviations, if they are not modelled explicitly
η_{c}	A factor accounting for the changes of material properties due to material temperatures in service conditions relative to the material properties at $20°C$, excluding the effects of long-term exposure.
A	Gross area of the cross section

THIS PAGE WAS INTENTIONALLY LEFT BLANK

1. INTRODUCTION

1.1. Background and motivation

In contemporary building design, the integration of HVAC ductwork, electrical conduits [1], and water supply pipes [2] within the floor-ceiling zone [3] constitutes a critical strategy for optimising spatial efficiency and reducing overall construction depth, thereby achieving a simplified and coordinated layout that satisfies functional demands while maintaining a shallow, economical structural zone [2]. Consequently, structural floor beams are frequently detailed with large web openings, most commonly of rectangular or circular geometry, to permit the passage of utilities [4]. This approach proves particularly advantageous in multi-storey buildings, where stringent headroom requirements and economic constraints preclude increasing floor-to-floor heights [5] or rerouting services beneath the structural frame, both of which incur significant additional costs and spatial inefficiencies [6].

The incorporation of web openings in steel beams, while functionally necessary, fundamentally alters the internal stress distribution and exerts a severe penalty on both the structural load-carrying capacity and stiffness of the member, with the magnitude of this reduction contingent upon the geometry, size, and position of the opening. Although the associated loss in moment capacity is generally minimal, owing to the web's inherently marginal contribution to overall flexural resistance, the corresponding reduction in shear capacity is substantial [6]. The most critical structural consideration, however, is the Vierendeel mechanism, which predominates in beams containing a single large web opening, where global shear forces are transferred across the opening length and must be resisted by the local moment capacities of the Tee sections above and below the perforation [5]. Within this mechanism, the initial formation of a plastic hinge at the top Tee section on the low-moment side of the opening does not precipitate immediate failure; rather, the beam retains residual load-carrying capacity until four plastic hinges develop at critical locations of the perforated section, ultimately leading to collapse[2].

Welded steel stiffeners have traditionally served as the primary means of strengthening steel beams with web openings, significantly enhancing both ultimate load-carrying capacity and deformation capacity [7],[8]. Nevertheless, this conventional approach entails inherent practical difficulties, including the need for heavy lifting equipment to position steel plates, the complexity of accommodating irregular geometries, and the necessity of on-site welding.

Furthermore, the addition of steel plates increases structural self-weight while exacerbating susceptibility to corrosion, fatigue damage, and residual stress development, all of which compromise long-term durability and serviceability [1]. As a viable alternative, carbon fibre-reinforced polymer (CFRP) has emerged as an effective strengthening solution, offering a superior strength-to-weight ratio, exceptional corrosion resistance, high elastic modulus, and a density approximately one-fifth that of steel, thereby facilitating ease of handling and installation (see Figure 1-1).

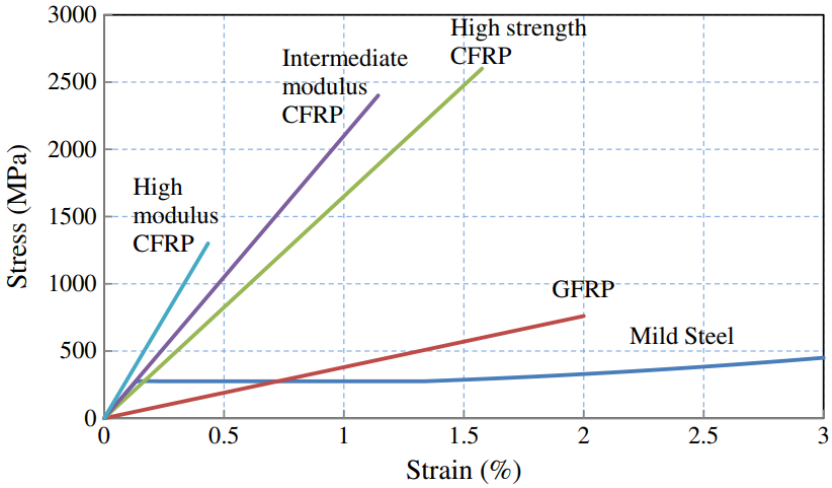


Figure 1-1: Typical stress-strain curve for FRP and mild steel [9]

CFRP is particularly favoured owing to its high strength and stiffness [7], which enable effective restoration of lost load-carrying capacity and mitigation of stress concentrations around the perforation [4]. Although CFRP plates and laminates have been extensively investigated for flexural strengthening applications, particularly when bonded to the bottom flange of steel beams, the broader application of CFRP to steel beams with web openings remains an evolving area within the existing literature. Accordingly, this study investigates the retrofitting of steel floor beams with web openings under static loading using CFRP composites to recover the strength and stiffness compromised by the opening. The investigation specifically addresses strengthening configuration and the influence of adhesive type, with the objective of assessing whether CFRP strengthening can restore, or potentially enhance, the structural performance of perforated steel beams relative to unstrengthened and conventionally steel-stiffened configurations.

1.2. Problem statement

The central challenge addressed in this thesis is as follows: to what extent can CFRP composites, bonded to the steel surface using a structural adhesive, serve as a viable substitute for conventional steel stiffeners in strengthening steel beams with web openings, and what key parameters govern the effectiveness of this substitution? This overarching question encompasses several interrelated sub-problems that require systematic resolution.

First, the structural behaviour of steel beams with web openings is highly dependent on the location of the aperture, whether situated in a high-shear region, where more severe Vierendeel bending occurs, or at midspan, where flexural demands predominate, as well as on the geometry of the opening, typically circular or rectangular, which is frequently dictated by architectural and service coordination requirements rather than structural optimisation. Increasing the opening size generally leads to greater reductions in load-carrying capacity. Consequently, the efficacy of any strengthening solution must be rigorously evaluated across a range of these geometric parameters to establish its applicability under varying structural and service conditions.

Second, when CFRP is bonded to a steel surface using a structural adhesive, the integrity of the bond, which governs the composite action between the two materials, is critical to the effective transfer of forces across the interface. Unlike a welded steel stiffener, for which force transfer does not depend on an adhesive interface, the effectiveness of CFRP strengthening depends strongly on the behaviour of the bonded steel–CFRP interface. Furthermore, the selection of adhesive type warrants particular attention, specifically the distinction between linear and nonlinear adhesive behaviour, as this choice significantly influences the stress distribution and failure progression at the bonded interface. The extent to which debonding limits the structural contribution of the CFRP, and the degree to which the assumption of a perfectly bonded interface overestimates actual capacity, must therefore be rigorously quantified if CFRP strengthening is to be reliably implemented in engineering practice.

Third, the analytical formulations currently available for the design of steel beams with web openings, principally those outlined in SCI P355 [10], were developed specifically for steel-stiffened configurations and do not account for the use of FRP strengthening. The applicability and accuracy of extending these guidelines through the incorporation of debonding load equations adapted from the concrete-to-CFRP literature must therefore be critically assessed

against numerical predictions. Such an evaluation is essential to assess the potential and limitations of a simplified analytical approach for predicting the resistance of the CFRP-strengthened configurations considered.

1.3. Aims and objectives

The aim of this thesis is to provide a systematic and evidence-based assessment of the viability of CFRP composites as an alternative to conventional steel stiffeners in steel beams with web openings, through a comprehensive numerical investigation. In addition, the study seeks to elucidate the potential of nonlinear adhesives in enhancing the structural performance of the bonded interface and to develop and evaluate an analytical formulation for assessing the load-carrying capacity of CFRP-strengthened perforated steel beams.

The specific objectives of the study are as follows:

1. To develop and validate a finite element modelling framework for the nonlinear response of steel beams with web openings, and to extend this framework to CFRP-strengthened configurations incorporating cohesive-interface modelling of adhesive debonding.
2. To conduct a comprehensive parametric numerical study investigating the influence of opening location, opening shape, opening depth, CFRP configuration, bond model, and adhesive type on the load-carrying capacity and failure behaviour of the strengthened beam, and to compare these outcomes with those of conventionally strengthened steel counterparts, for selected representative configurations.
3. To quantify the difference in load-carrying capacity between perfectly bonded (upper bound) and realistically debonding CFRP configurations, thereby establishing the degree to which debonding limits the effectiveness of CFRP strengthening relative to the upper bound.
4. To develop an analytical tool based on the SCI P355 design guidance [10], extending its applicability beyond unstrengthened and steel-stiffened beams to encompass CFRP-strengthened configurations, identifying the conditions under which the analytical tool provides sufficient reliability for capacity prediction and to evaluate its accuracy and limitations through comparison with the numerical results.

1.4. Scope and limitations

The study focuses on a specific steel I-section beam geometry, selected as representative of long-span beams in which flexural behaviour predominates. The investigated steel beam is assumed to be continuously laterally restrained along the top flange, representing the restraint provided by the floor/roof deck; lateral–torsional buckling is therefore excluded as a governing global failure mode. The generality of the findings to other cross-sectional geometries and span configurations should therefore be confirmed through further investigation. The opening configurations examined include rectangular openings at 50%, 65%, and 75% of the beam depth, and circular openings at 50%, 65%, 75%, and 80% of the beam depth, with the maximum size in both geometries corresponding to the upper limit permitted by Eurocode 3 [11]. Additionally, two opening locations are considered: at one-quarter of the beam span (L/4), representing a near-support opening selected in accordance with the findings of [3], and at midspan. The CFRP strengthening configurations comprise three distinct schemes: web attachment only, flange attachment only, and combined web and flange attachment. The CFRP is modelled as a linear elastic orthotropic material, with damage incorporated for the perfectly bonded case, while debonding is excluded, thereby establishing an idealized upper bound for strengthening effectiveness.

The adhesive considered in this study is nonlinear and is modelled as a cohesive surface governed by a trilinear traction-separation law. For comparative purposes, additional models employ a linear adhesive characterized by a bilinear traction-separation relationship. In both cases, the adhesive properties are derived from available material data for a structural epoxy adhesive. Temperature effects, sustained loading, fatigue and environmental degradation of the bonded interface are outside the scope of this study, and all analyses are conducted under monotonic static loading. The analytical tool developed herein is based on Eurocode 3 [11], Eurocode 4 [12], and SCI P355 [10], extended through the incorporation of a debonding load equation adapted from the concrete-to-CFRP strengthening literature. Its applicability to beam geometries or opening configurations beyond those investigated in this study has not been verified.

1.5. Structure of the thesis

The thesis is organized into six chapters, structured as follows:

Chapter 1: Introduction presents the background and motivation underpinning the study, followed by the formulation of the problem statement. It further delineates the scope and limitations of the investigation and concludes by outlining the contributions of this thesis to the existing body of knowledge.

Chapter 2: Literature Review presents the structural behaviour and failure mechanisms of steel members with web openings, with particular emphasis on beams with discrete openings. Conventional steel strengthening techniques are discussed, followed by the use of fibre-reinforced polymers (FRPs) for strengthening steel structures. Particular attention is given to CFRP strengthening configurations, steel–FRP bond behaviour, adhesive debonding, and the main research gaps addressed in this thesis.

Chapter 3: Analytical Investigation on Perforated Beams presents the analytical framework adopted to assess the resistance and serviceability of steel beams with web openings. Existing design approaches for unstrengthened and steel-stiffened openings are described and subsequently extended to CFRP-strengthened configurations, including consideration of the debonding resistance of the bonded CFRP. The resulting analytical predictions are later compared with the numerical results.

Chapter 4: Numerical Modelling and Validation describes the finite element modelling strategy adopted in the study. The numerical modelling approach is first assessed against experimental results available in the literature, considering different beam configurations and failure mechanisms. The numerical model subsequently used in the parametric investigation is then presented, including the material models, boundary conditions, CFRP and adhesive modelling, and mesh sensitivity analysis.

Chapter 5: Parametric Study presents the main numerical investigation of the thesis. The influence of opening location, shape and depth on the structural response is first examined, followed by an assessment of different CFRP strengthening configurations. Both perfect bonding and adhesive debonding are considered, together with the influence of linear and nonlinear adhesive behaviour. The performance of CFRP strengthening is also compared with

conventional steel stiffeners, and the analytical predictions developed in Chapter 3 are assessed against the numerical results.

Chapter 6: Conclusions and Future Work summarizes the principal findings of the investigation in relation to the objectives established in Chapter 1. The main conclusions regarding opening geometry, strengthening configuration, adhesive behaviour, and analytical prediction are presented, followed by the limitations of the study and recommendations for future research.

1.6. Contributions to knowledge

This thesis makes the following original contributions to the existing body of knowledge:

A systematic quantification of the influence of opening location, shape, depth, and CFRP configuration on the structural performance of CFRP-strengthened steel beams with web openings, conducted using a finite element framework validated for the structural response of steel beams and extended to incorporate cohesive-interface modelling of steel–CFRP debonding.

A direct, parametric comparison of CFRP strengthening, accounting for cohesive-interface modelling of adhesive debonding, against conventional steel stiffening across a range of geometric configurations.

A quantitative assessment is provided of the reduction in load-carrying capacity attributable to adhesive debonding, measured relative to the perfectly bonded upper bound, thereby establishing the magnitude of error introduced by the perfect-bond assumption across the configurations examined in this study. An assessment of the potential benefits of the investigated nonlinear adhesive relative to the linear adhesive, with particular emphasis on debonding and load-carrying capacity.

A critical evaluation of the applicability of the SCI P355 [10] analytical framework, extended to include CFRP strengthening via an adapted debonding equation, for the design of CFRP-strengthened steel beams with web openings, including preliminary evaluation of its applicability and limitations for the configurations investigated.

THIS PAGE WAS INTENTIONALLY LEFT BLANK

2. LITERATURE REVIEW

2.1. Structural behaviour of steel members with web openings

2.1.1. Types of steel members with web openings

Steel is widely employed as a structural material, enabling the fabrication of various load-bearing members, including beams, columns, and shear walls. In many practical applications, openings must be introduced into these members to accommodate building services integration, which is typically achieved by introducing openings directly into the web as shown in Figure 2-1. This practice is commonly observed in steel beams, where either a single web opening or multiple regularly spaced openings may be provided. When the openings are hexagonal, the resulting configuration is known as a castellated beam; when they are circular, the beam is referred to as cellular. Furthermore, this concept extends beyond hot-rolled sections to fabricated plate girders. Similarly, steel plate shear walls (SPSW) may also incorporate web openings for analogous purposes, as well as to accommodate windows and doors (see Figure 2-1)[13].

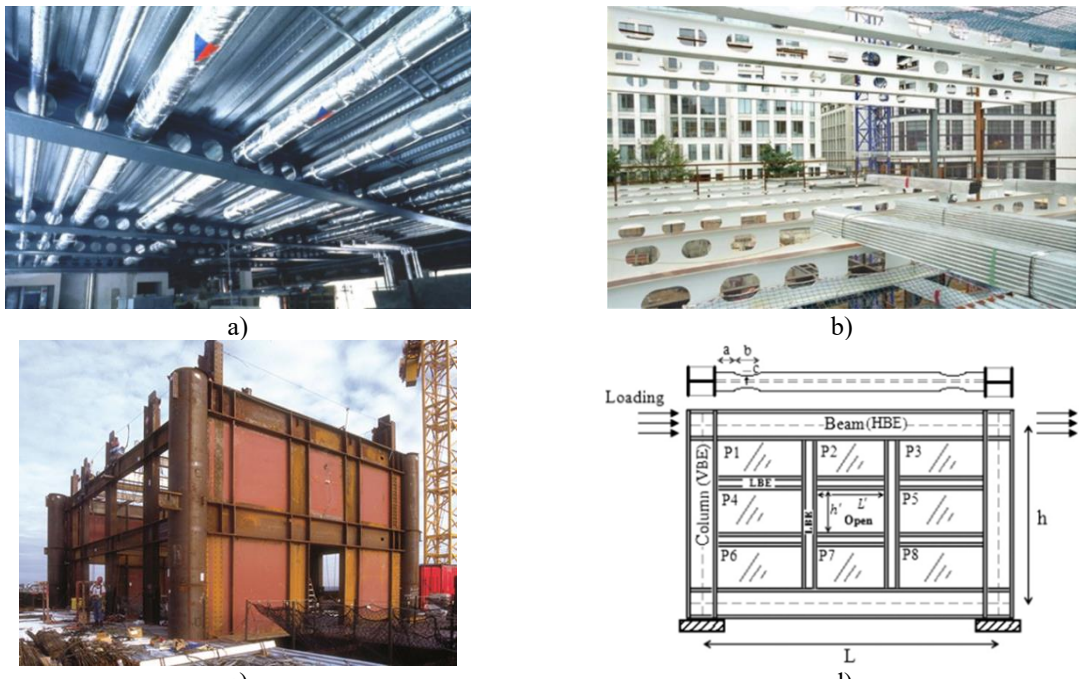
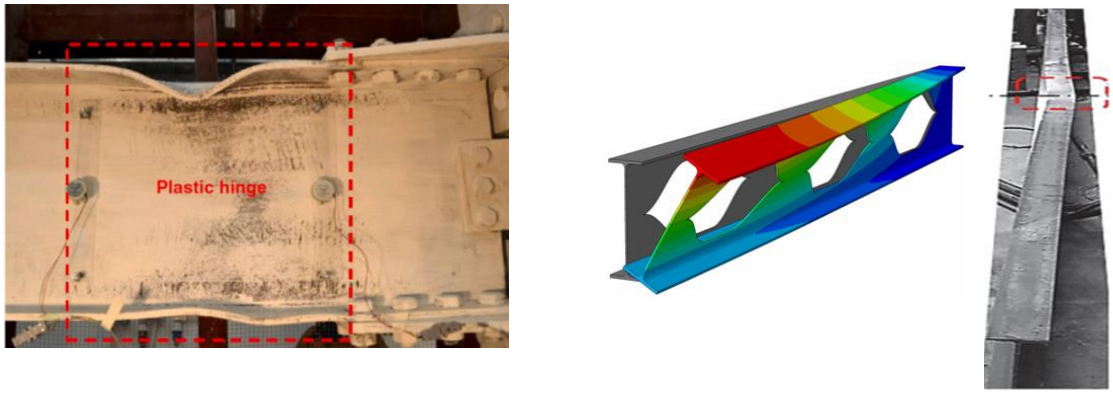


Figure 2-1: Openings in different structural members: a) Hot-rolled sections; b) Fabricated plate girders; c) Door-type opening in SPSW; d) Window-type opening in SPSW [13,14]

2.1.2. Failure modes

2.1.2.1. Conventional failure modes

For beams without web openings, the principal global failure mechanisms relevant to the present study include flexural yielding/plastic-hinge formation and lateral–torsional buckling, which is a global stability-related phenomenon as depicted in Figure 2-2.



a) b)

Figure 2-2: Conventional failure modes: a) Plastic hinge formation; b) Lateral torsional buckling [15,16,17].

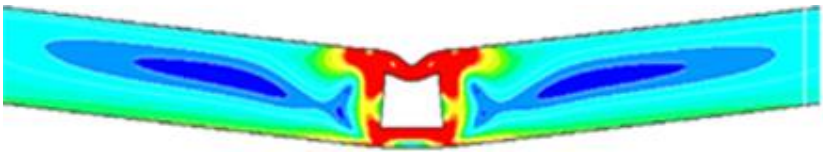
2.1.2.2. Failure modes associated with web openings

The introduction of web openings gives rise to additional failure modes [18] that depend critically on two factors: the location of the openings along the span, and whether the openings are discrete or regularly spaced.

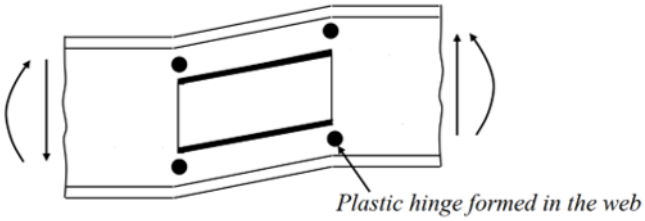
2.1.2.2.1. Influence of discrete openings

When discrete openings are in a moment-dominated region, failure typically occurs through a flexural mechanism, albeit with a reduced cross-section due to the presence of the opening. This mode is valid provided that the top Tee does not buckle under the high compressive stresses acting on this reduced section [7]. Furthermore, this flexural failure may be accompanied by lateral–torsional buckling of the top Tee if the spacing between lateral restraints is insufficient to prevent such instability, as in Figure 2-3a.

Conversely, when an opening is situated in a shear-dominated region, such as near the supports, a Vierendeel mechanism develops [2]. This mechanism is characterized by the formation of plastic hinges at the four corners of the opening, arising directly from the transfer of shear forces across the perforation, as illustrated in Figure 2-3b,c.



a)





b) c)

Figure 2-3: Failure modes due to discrete openings: a) Flexural mechanism with L.T.B of the middle segment; b) schematic for Vierendeel mechanism; c) Real Vierendeel failure [6,7,19]

2.1.2.2.2. Influence of regularly spaced openings

In cases where multiple or regularly spaced openings are present, the segment of web material between adjacent openings is named “web post”. When openings are closely spaced, this web post becomes susceptible to buckling. The nature of this buckling depends on the region in which the openings reside:

1. In shear-dominated areas, the web post buckles primarily due to shear forces. This involves the formation of diagonal tension and compression fields. Owing to the presence of welds and the resulting tension field, the mid-height of the web post is constrained from outward movement, leading to double curvature rather than single curvature. Since one portion of the web tends to buckle while the adjacent portion is restrained, and given the existence of free edges, lateral–torsional buckling also occurs as in Figure 2-4a. If the web is sufficiently thick or the web post width is large enough buckling is precluded, two plastic hinges form instead [20],[21].
2. In moment-dominated areas, buckling arises from the compressive stresses transmitted through the top Tee as part of the flexural mechanism, resembling web crippling. Additionally, in the vicinity of concentrated loads, the web post may buckle under compression loads in an analogous manner (see Figure 2-4 b,c).

Finally, weld rupture [18],[22] represents another potential failure mode. When the shear stresses induced in the weld exceed its capacity, rupture occurs along the weld line as can be seen in Figure 2-4d.

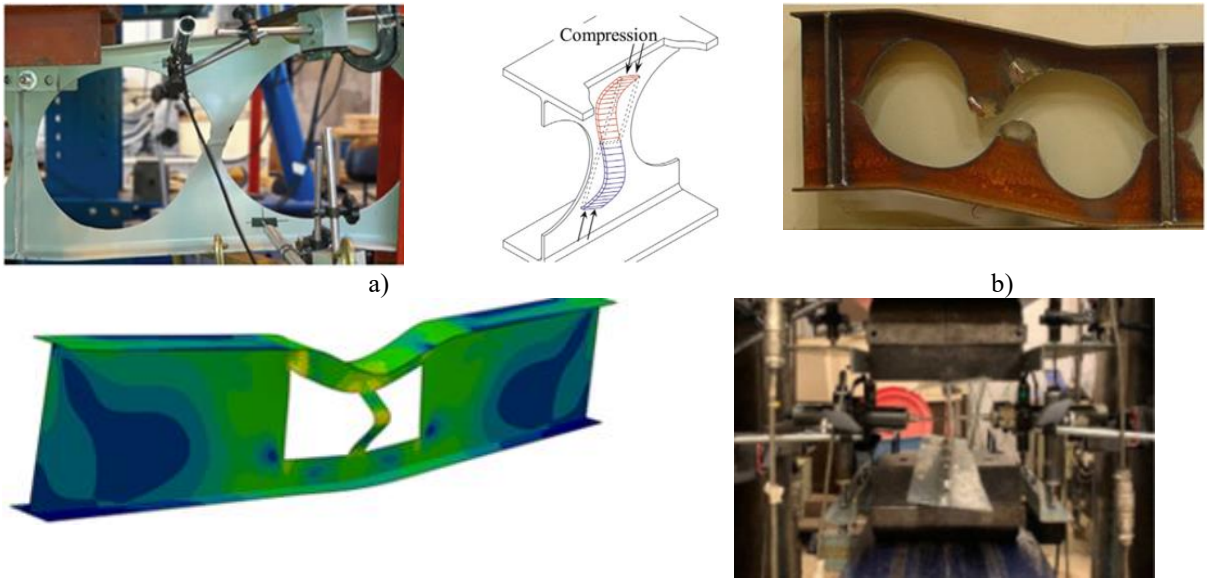


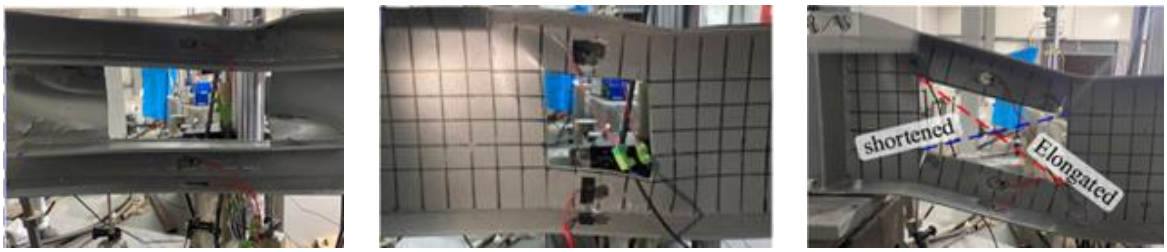
Figure 2-4: Failure modes with regularly spaced openings: a) Web-post buckling under shear; b) Weld rupture; c) Web-post buckling under compression; d) Web crippling [21,22,23,24]

2.2. Conventional strengthening and retrofit techniques

2.2.1. Steel plate and stiffener-based solutions

The conventional method for strengthening steel beams with discrete web openings involves welding longitudinal steel stiffeners at the top and bottom of the opening [25], extending beyond the opening to provide an adequate anchorage length as illustrated in Figure 2-5a. The primary purpose of the longitudinal stiffeners is to increase the local bending resistance and stiffness of the upper and lower Tees, thereby increasing the resistance to Vierendeel failure, effectively converting them into I-sections. This increases both stiffness and strength at the four corners of the opening. Consequently, buckling along the elongated diagonal and tearing along the shortened diagonal are prevented as in Figure 2-5.

For regularly spaced openings, various techniques are proposed for strengthening, either through the provision of stiffeners around the openings that could be ring stiffeners, double plate stiffeners across the width of the web post or a transverse stiffener in each web post, as shown in Figure 2-6.



a) b) c)

Figure 2-5: Vierendeel mechanism and longitudinal steel stiffener a) Effect of adding stiffeners; b) Buckling and tearing along the two diagonals; c) Elongated and shortened diagonals [25]



a)



b) c)

Figure 2-6: Various conventional strengthening techniques: a) Double transverse stiffeners; b) Ring stiffener; c) Transverse stiffener [26,27,28]

2.2.2. Advantages and limitations of steel stiffeners

Steel stiffeners offer high flexural stiffness and are relatively straightforward to apply. Importantly, they do not suffer from detachment or debonding phenomena, which often result in brittle failure modes. In contrast, steel provides enhanced strength, stiffness, and ductility. Furthermore, when steel plates are used, the same base material is employed for both the plate and the welding, ensuring material compatibility. Additionally, welding can transmit tensile stresses alongside shear stresses [29].

However, several drawbacks must be acknowledged. First, welding introduces fatigue sensitivity and residual stresses into the structure. Furthermore, high-strength steel experiences significant local strength reduction in the heat-affected zones (HAZ). Second, the installation process may disturb building operation. Third, steel is susceptible to corrosion over time. Fourth, the material offers limited shape flexibility. On top of these issues, steel is a heavy material, which increases the overall self-weight of the structure and consequently elevates the

demand on both the supporting elements and the foundations. Moreover, the high flexural stiffness provided by steel plates can lead to high peel stresses in case of bonded steel joints [1,9,30].

2.3. FRP strengthening of steel members: fundamentals

2.3.1. Mechanical properties and advantages and disadvantages of FRP

Fibre-reinforced polymers (FRPs) possess a high strength-to-weight ratio, a high stiffness-to-weight ratio, enables their use without adding significant mass to the structure as well as their excellent fatigue and corrosion resistance. Also, the speed and ease of their installation reduce disturbance to building services and allows for easier traffic flow in the context of transportation infrastructure. FRPs are highly adaptable to curved surfaces and can be tailored in terms of their directional properties to match specific design requirements, particularly when applied using the wet lay-up technique. For instance, fibres may be oriented in the longitudinal direction when strengthening the top flange of a steel beam. Conversely, fibres may be arranged in the transverse direction for confining concrete or concrete-filled steel tubes, thereby preventing local buckling and enhancing ductility. Additionally, bonded FRP strengthening may improve fatigue performance while avoiding the fatigue-sensitive details and residual stresses associated with welding. In applications such as oil tanks, welding can endanger structural integrity, whereas FRP bonding offers a safer alternative [9]. For all these reasons, the application of FRPs to steel structures has received considerable attention in recent years [9,31].

2.3.2. Bond between FRP and steel

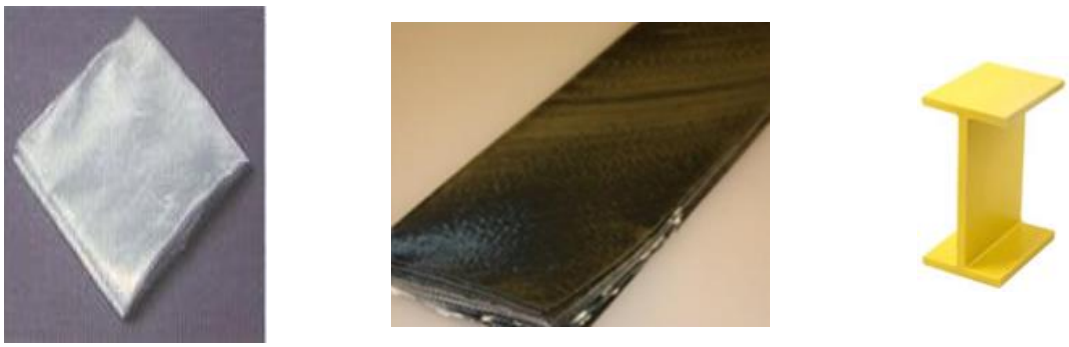
Attaching FRP plates or laminates to steel elements can be accomplished in two commonly considered approaches. The first method involves the use of bolted connections. However, this approach is generally avoided for two main reasons. First, drilling holes through the FRP damages the continuous fibres, thereby disrupting the continuity of the load path and reducing the effective cross-sectional area available to resist applied loads. Second, the presence of bolt holes introduces significant stress concentrations, which can become initiation sites for premature failure, particularly under fatigue loading [32].

The second, and generally preferred, method is to bond the FRP directly to the steel surface using structural adhesives. Adhesive bonding offers several distinct advantages over bolting. It preserves the integrity of the fibres, ensures a more uniform transfer of stresses across the entire interface, and eliminates the need for drilling, which would otherwise compromise the composite material. Furthermore, bonded joints distribute loads over a larger area, reducing localized stress peaks and enhancing the overall fatigue performance of the strengthened system. For these reasons, adhesive bonding has become the predominant technique for attaching FRP reinforcements to steel structures [33].

2.3.3. Common strengthening forms

The use of the wet lay-up method is common due to the ease of application. It can be used on site where the first layer of epoxy is applied to the surface, then the dry fibres are placed and impregnated with resins with a roller or a brush. This method offers flexibility for irregular shapes as the materials can be wrapped around the structural members. Also, the properties can be tailored by changing the orientations of the fibres. In this way, strengthening can be used in all types of structural members beams, slabs, and columns but the drawback is that the quality depends on the workmanship [9].

To get higher quality and strength, FRP laminates are used. The laminates are prepreg layup cured in the oven or autoclave. This method offers thin sheets with high quality, consistent thickness and a controlled ratio of fibres. The FRP laminates are attached to the steel surface by adhesive bonding. The last form is the FRP plates or profiles, which are produced by pultrusion. FRP profiles are thick and less adaptable to irregular shapes (see Figure 2-7).



a) b) c)

Figure 2-7: Different forms of FRP: a) Wet lay-ups; b) Prepreg; c) Profiles [34,35]

2.3.4. Method of installation

The bonding procedure begins with thorough surface preparation of the steel substrate. First, the surface is cleaned using a solvent such as acetone to remove contaminants, including oil, grease, and moisture, thereby enhancing the surface condition. Subsequently, the surface characteristics are modified through mechanical abrasion to improve the surface roughness and mechanical interlocking. This is typically accomplished via grit blasting or the use of a wire brush. Following abrasion, the surface is cleaned and coated with a degreasing and corrosion-inhibiting agent.

After the surface treatment has been completed, the adhesive is applied. A two-component epoxy adhesive is mixed according to the manufacturer's specified proportions. The mixture is then applied to the prepared steel surface using brushes and evenly spread with steel rollers to achieve a uniform thickness.

Next, the surface of the carbon fibre-reinforced polymer (CFRP) laminate is cleaned. The CFRP is then placed onto the prepared steel surface and pressed firmly to ensure full contact, allowing excess adhesive to squeeze out and thereby eliminating any voids. Finally, rollers or temporary plates are used to press the assembly, remove trapped air pockets, and allow the adhesive to cure under controlled conditions [9].

2.3.5. Typical failure modes of FRP-strengthened steel members

Failure modes [9] in FRP-bonded steel systems are attributed to the failure of any constituent within the system. In the steel member, failure may manifest as steel yielding. Within the FRP component, failure can occur as FRP rupture or delamination, the latter representing interlaminar failure within the FRP material. The adhesive layer itself may also fail through cohesive failure within the adhesive. Additionally, failure can occur at the interfaces, including CFRP–adhesive interfacial failure or steel–adhesive interfacial failure (see Figure 2-8).

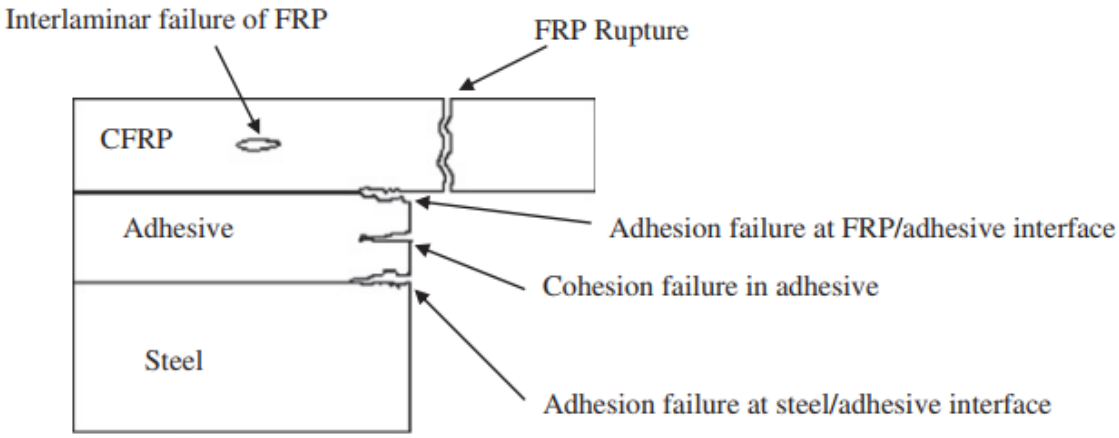


Figure 2-8: Schematic for failure modes in CFRP-bonded steel systems [9]

2.3.6. Debonding and anchorage issues

As previously stated, adhesive bonding is generally preferred over bolting for attaching FRP reinforcements to steel structures. Bonding reduces stress concentrations, provides a larger area for stress transfer, and is comparatively easier to apply. However, the effectiveness of bonded systems is limited by a critical phenomenon: debonding, which refers to the loss of adhesion between the connected elements therefore losing the composite action achieved through the attachment of the FRP to the steel.

Debonding occurs most prominently in flexural strengthening applications. This is primarily due to the development of high peel stresses, which arise from the difference in flexural stiffness between the steel member and the FRP laminate. Compounding this effect are the shear stresses that must be transferred across the bonded interface. The interaction between these two stress components, Mode I (opening) for peel stresses and Mode II (shearing) for shear stresses, ultimately leads to debonding failure.

Debonding in FRP-strengthened steel structures occurs through two primary mechanisms: end debonding, which initiates at the CFRP termination where material discontinuity exists, and intermediate debonding, which develops away from the plate ends due to defects, cracks, or yielding of highly stressed steel sections. In the latter case, the FRP experiences high stresses at the critical location, which diminish progressively toward the plate ends. The modelling of end debonding is governed by both interfacial normal and shear stresses, with bond strength being dependent on fracture energy rather than solely on adhesive strength. Accurate prediction of debonding failures in CFRP-strengthened steel beams therefore requires the interface model

to capture two essential characteristics: first, the nonlinear and damage behaviour of the interface under mode I and mode II loading, and second, the interaction between these modes during damage propagation along the interface. To address the first requirement, a bond–slip model is employed for mode II loading, while a bond separation model is used for mode I loading. The second requirement necessitates the incorporation of a mixed-mode cohesive law. Cohesive zone models are widely used to simulate fracture in ductile and brittle solids, delamination in composites, and the behaviour of adhesively bonded joints. A coupled cohesive model integrates three components: the bond–slip model for mode II loading, the bond separation model for mode I loading, and a mixed-mode cohesive law. The bilinear bond–slip model provides accurate predictions of the bond behaviour of CFRP-to-steel joints subjected to mode II loading. The bond separation model characterizes mode I fracture energy using double cantilever beam tests; in the absence of such data for linear adhesives, a close approximation can be derived from the tensile stress–strain response of the adhesive. The mixed-mode cohesive law accounts for the interaction between mode I and mode II, incorporating three bond stress components: the normal component and two shear components acting along the interface. These stresses constitute the tractions, while their corresponding displacement components are referred to as separations (see Figure 2-9) [36].

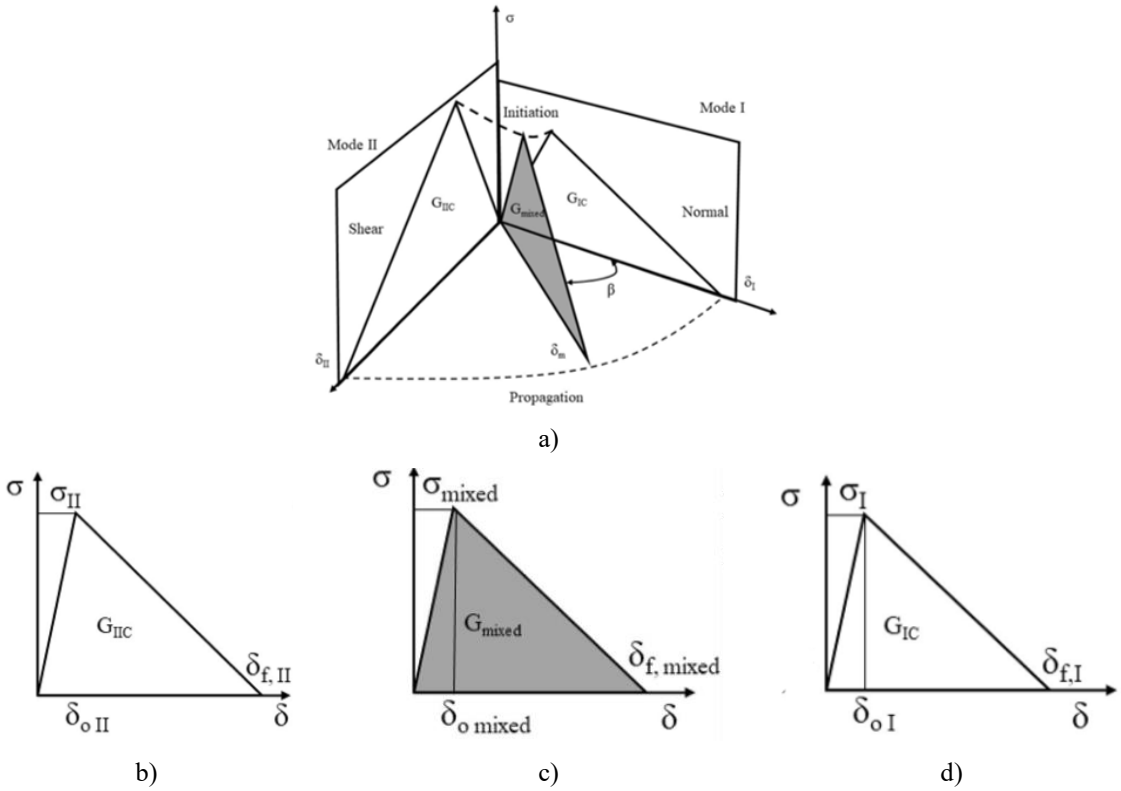


Figure 2-9: Bilinear traction separation law for mixed mode loading; a) Interaction between different modes; b) Mode II ; c) Mixed mode; d) Mode I [36]

Two approaches exist for modelling the adhesive layer. The first employs cohesive zone elements, which may be implemented either with coincident nodes, whereby the nodes of the adherends align with those of the explicitly modelled adhesive layer, or with non-coincident nodes, which afford greater meshing flexibility. Although the coincident-node approach simplifies pre-processing, both variants necessitate the use of constraint equations to tie the adhesive to the adherends on both sides, thereby increasing computational processing time. The second approach models the adhesive implicitly as a cohesive interface, eliminating the requirement for tying constraints and permitting non-coincident meshing while also enabling the inclusion of frictional interaction between the contacting surfaces (see Figure 2-10) [37]. This formulation offers simplicity and enhanced computational efficiency without sacrificing the capacity to accurately represent interfacial behavior. Accordingly, the surface-based cohesive formulation is adopted in the numerical model described in Chapter 4.

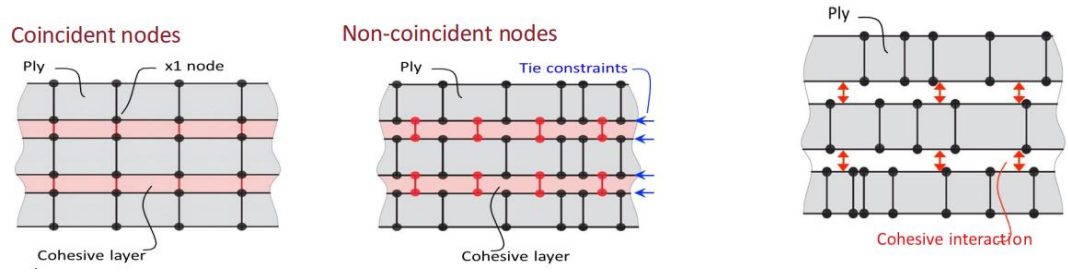
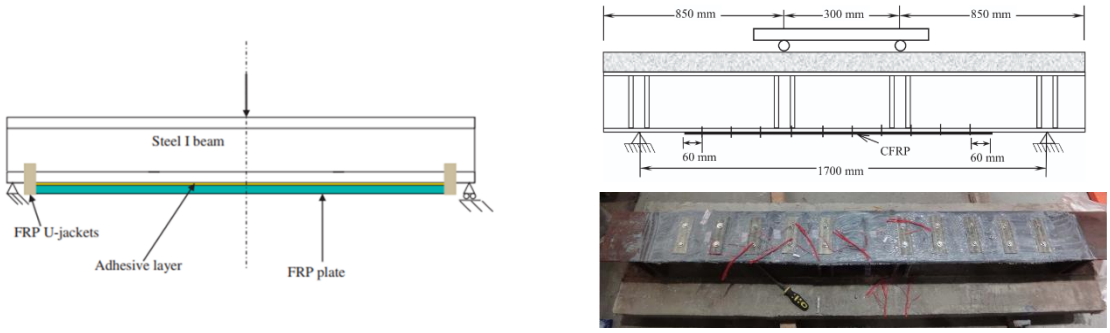


Figure 2-10: Cohesive zone modelling: a) Cohesive zone element; b) Cohesive surface [37]

Yu et al. [38] conducted an experimental campaign comprising 18 single-lap pull-out specimens to systematically investigate the effects of adhesive mechanical properties, adhesive thickness, and CFRP axial rigidity on the behaviour of bonded joints. The findings directly relevant to this thesis are multifaceted. First, the study demonstrated that adhesive stiffness and ductility exert a strong influence on force transfer across the bonded interface, with adhesive type governing both the failure mode and the ultimate joint capacity. Second, the concept of effective bond length, previously established for FRP-to-concrete joints, was confirmed to apply equally to FRP-to-steel bonded joints, whereby increasing bond length enhances bond strength only up to a limiting value, beyond which further increases contribute solely to ductility in the failure process. Third, adhesive thickness was found to affect both bond behaviour and failure mode; although increased thickness enhanced bond strength, it simultaneously elevated bending stresses in the CFRP plate, thereby increasing the propensity for interlaminar failure. Fourth, the investigated linear and nonlinear adhesives exhibited fundamentally different bond–slip responses, with linear adhesives following a bilinear traction–separation law analogous to that

observed in FRP-to-concrete joints, whereas nonlinear adhesives displayed a trapezoidal bond–slip relationship characterized by greater deformation capacity. Finally, fracture energy was identified as a particularly important parameter governing damage evolution, with the bond strength of nonlinear adhesives exceeding that of linear adhesives, resulting in higher ultimate loads and more extensive strain distribution in the CFRP plate over the bonded area.

To mitigate debonding and thereby increase the load-carrying capacity of the system, several methods have been proposed. These include the use of U-wraps at the laminate ends as well as the implementation of mechanical anchorages which are necessary for prestressing applications (see Figure 2-11). Such techniques help to delay or prevent the initiation and propagation of debonding, allowing the bonded reinforcement to achieve a greater proportion of its theoretical capacity [9,38].



a) b)

Figure 2-11: Measures to prevent debonding: a) U-Jacket; b) Anchorage system [9,38]

2.4. FRP strengthening of steel beams with discrete web openings

A growing body of research has investigated the application of fibre-reinforced polymers (FRPs) for strengthening steel beams containing web openings, as well as those affected by corrosion-induced damage. Silwal *et al*. [1] examined two distinct scenarios: corrosion damage of the bottom flange and the presence of web openings. In the corrosion study, damage levels of 2.5%, 5%, 10%, 15%, and 20% were introduced over 80% of the beam length. The optimal number of carbon FRP (CFRP) layers required to restore both yield and ultimate strength was determined, with a cross-wrap extending to mid-height of the web employed to prevent debonding. Notably, the number of layers required to restore yield strength differed from that of ultimate strength, where fewer layers led to reduced ductility caused by premature rupture. An optimal layer configuration was therefore adopted, resulting in yield and ultimate strengths exceeding those of the undamaged beam, along with increased stiffness and reduced deflection.

A linear relationship between strength and damage level was subsequently established. In the second part, beams with circular web openings in the moment-dominated region were examined. Maintaining a constant total opening area while increasing the number of small openings (opening ratio below 0.5) did not affect yield strength, although ultimate strength decreased by approximately 5%. Among six strengthening schemes for a single circular opening (80% opening ratio), the most effective solution comprised CFRP sheets applied to the bottom of the top flange, the top of the bottom flange, and the web portions of both Tees, yielding higher stiffness and load capacity than the solid beam.

Extending this line of inquiry, another study [19] focused on beams with web openings in the shear-dominated region, tested under four-point bending. Three opening configurations with equal total area were considered: three circular openings, two circular openings, and two rectangular openings. Using ANSYS for numerical analysis, three strengthening schemes were evaluated: CFRP laminates placed between openings, on the bottom flange, and on both the web and bottom flange. The latter proved most effective in enhancing load capacity and stiffness. By increasing CFRP thickness from 1.2 mm to 1.4 mm no discernible effect was observed. Failure in the most effective scheme occurred due to debonding, a mode also observed when CFRP was applied only to the web. In contrast, the scheme with CFRP only on the bottom flange failed via Vierendeel mechanism, with these behaviours persisting after the thickness increase.

Extending the investigation to different loading and opening conditions, Al Taee *et al* [23] performed a numerical analysis employing ABAQUS to examine uniformly loaded steel beams featuring web openings at various positions along the span, employing CFRP plates and profiles. Six strengthening schemes were proposed, including three variations of Scheme B based on the CFRP length: one with twice the opening length (Scheme D), another with three times the opening length (Scheme C), and a third with four times the opening length (Scheme B), as illustrated in Figure 2-12. For openings in the shear zone, unstrengthened beams experienced Vierendeel bending. Strengthening proved efficient in recovering elastic strength and stiffness, with failure due to debonding of flange plates coinciding with top flange yielding. Three configurations yielded good results: Scheme B and C, with CFRP lengths of four and three times the opening length respectively, incorporating plates on both flanges combined with plates on the stems of the top and bottom Tee sections, and Scheme F, which comprised plates attached to the top and bottom flanges together with angles connected to the web. For openings positioned at mid-span, where the bending moment is highest, two of the three effective

configurations, scheme B with a CFRP length of four times the opening length and Scheme F, not only fully recovered the strength of the solid beam but also achieved enhancements of up to 20%. Configuration B with four times the opening length was deemed superior due to its ductile failure, contrasting with the brittle failure of Scheme F. For two rectangular openings at mid-span with a web post, the best configuration supplemented with angles on the web post performed well but could not prevent web post buckling when debonding of the angles occurred, resulting in non-ductile failure. Nevertheless, strength and stiffness were recovered compared to the solid-web beam.

Al Taee *et al* [39] continued this work experimentally, testing four beams under six-point bending to simulate uniform loading, with lateral supports at three points. For configuration 1 (web opening at mid-span), a plastic hinge formed at the end of the CFRP on the top flange, similar to a reduced beam section, followed by lateral-torsional buckling (LTB). The same phenomenon was observed for configuration 3 (two web openings at mid-span), though web post buckling was not observed, contrary to numerical predictions. For configuration 2 (web opening in the shear-dominated area), a plastic hinge occurred at mid-span with LTB of the middle portion, contrasting with the unstrengthened beam that failed via Vierendeel mechanism. This shift in failure mode demonstrated the effectiveness of CFRP, with no debonding observed. In all strengthened cases, stiffness and strength surpassed those of the solid-web beam.

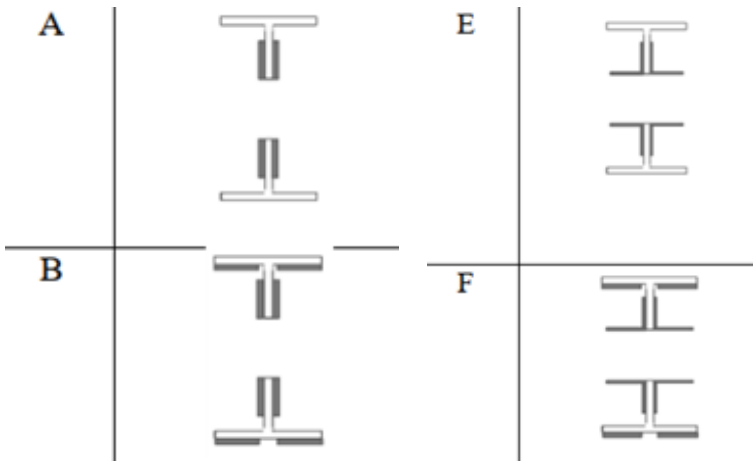


Figure 2-12: CFRP strengthening configurations [23]

With the aim of employing GFRP materials, Guedaoura *et al* [40] examined the use of GFRP profiles for strengthening beams containing web openings, proposing four distinct configurations with varying thicknesses as represented in Figure 2-13. Applying 6 mm thick

GFRP to both a mid-span opening and a shear-zone opening restored strength and stiffness to levels comparable to those achieved with 3 mm thick CFRP proposed by Al Taee [[39]]. For the shear-zone opening, three configurations failed in the mid-span region outside the strengthened area, while the remaining configuration failed within the shear zone via Vierendeel mechanism. For mid-span openings, two failure modes were observed: plastic hinge formation transitioning into LTB, and failure at the GFRP termination point on the top flange. End debonding was nevertheless noted for both opening types, though only after original strength had been recovered.

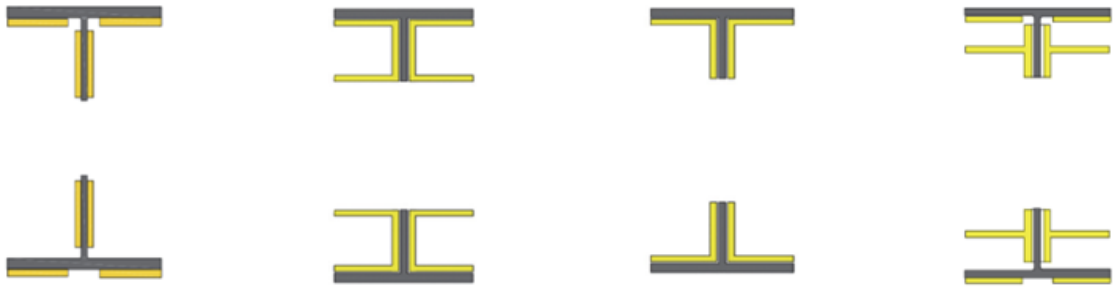


Figure 2-13: GFRP strengthening configurations [40]

Benzane *et al* [16] turned their attention to simply supported beams subjected to three-point bending, focusing specifically on trapezoidal and inverted trapezoidal openings located at mid-span. The top base dimension varied from $0.5H$ to H, affecting top Tee length and thus Vierendeel bending occurred at the corners (see Figure 2-14). Trapezoidal openings with a top base equal to H led to top Tee buckling, unlike other trapezoidal cases. For inverted trapezoidal openings, top Tee buckling governed all configurations. A strengthening scheme using GFRP plates on the top and bottom flanges and Tee sections of three thicknesses (3, 6, and 10 mm) for the webs on each side of the opening was implemented, with reinforcement extending four times the opening length. By selecting the appropriate thickness, the failure mode shifted from top Tee buckling to flexural mechanism, and strength was restored for all configurations, although end debonding was observed.

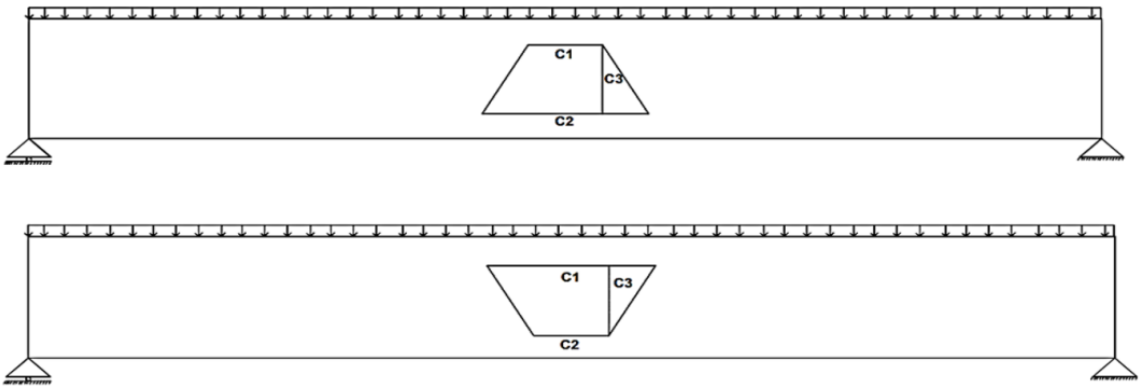


Figure 2-14: Different opening configurations [16]

Collectively, these studies underscore the potential of FRP-based strengthening systems for steel beams with web openings, while also highlighting the importance of failure mode control, debonding prevention, and configuration optimisation.

2.5. Strengthened steel beams with multiple or regularly spaced openings

The studies reviewed thus far have predominantly addressed single or few openings in steel beams. A distinct but related class of structural members emerges when regularly spaced openings are introduced along the beam length, giving rise to castellated/cellular beams. These beams are produced through a specific manufacturing technique: the parent beam is cut along its centreline, the two halves are offset, and then rejoined, resulting in a depth increase of approximately 50% [28]. This depth gain enhances the section modulus and bending stiffness, allowing a higher bending resistance for a given quantity of steel, while exhibiting reduced deflection. However, this structural efficiency introduces the new failure modes discussed before. To prevent such failures, stiffeners of various configurations are typically employed.

Al-Thabhawee and Mohammed [27] experimentally investigated the efficacy of circular and octagonal ring stiffeners in beams with octagonal web openings. The study comprised five beam configurations: a solid-web parent beam; a castellated beam with hexagonal web openings; a castellated beam with octagonal web openings formed using beam expansion plates; beams with octagonal web openings and circular ring stiffeners; and beams with octagonal web openings and octagonal stiffeners. The addition of expansion plates increased the beam depth to twice that of the parent beam, compared to a 1.4-fold increase observed in the castellated beam. This greater depth rendered the web slender, such that failure was governed by web post buckling as shown in Figure 2-15. In contrast, the castellated beam with hexagonal openings failed through the Vierendeel mechanism and exhibited a loss of ductility.

Al-Thabhawee reported that beams with circular ring stiffeners achieved the highest increases in both strength and stiffness, while maintaining ductility equal to that of the parent beam. Conversely, octagonal stiffeners resulted in reduced ductility. The study concluded that circular ring stiffeners delivered the best overall performance, with a 37% increase in weight (attributable to the expansion plates and circular ring stiffeners) relative to the parent beam.

Whereas Al-Thabhawee concentrated on stiffener geometry and its effect on strength and ductility, Morkhade *et al* [41] adopted a parametric approach using ABAQUS to examine the influence of base geometric variables on cellular beam behaviour under three-point bending and the effect of strengthening the beam by adding steel cover plates. Three parameters were systematically varied: beam depth (ranging from 1.4h to 1.6h), opening diameter (h, 1.1h, 1.2h, and 1.3h), and centre-to-centre spacing between openings (1.1D, 1.2D, and 1.3D). Cover plates of 10 mm thickness were attached to the flanges. The findings revealed that, for a given opening diameter, increasing the centre-to-centre spacing enhanced both strength and stiffness, whereas larger opening diameters reduced strength and the addition of the strengthening increased the strength of the beam. Failure modes observed included local buckling of the stiffener at the loading point, Vierendeel mechanism, and web post buckling.

Shifting focus from geometric parameters to strengthening materials, Kumbhar and Jamadar [[28] investigated the behaviour of castellated beams reinforced with transverse steel stiffeners made of mild steel (MS) as well as CFRP doubler plates attached to the web posts as illustrated in Figure 2-16. The investigation involved MS stiffeners of three different thicknesses and CFRP plates of three distinct stiffness levels. The findings revealed that varying the thickness of either the MS stiffeners or the CFRP stiffeners did not result in a substantial increase in strength. This is a notable shift from Morkhade's observations on steel strengthening, where the cover plates had produced strength enhancements up to 40 %. Mild steel stiffeners provided a higher load-carrying capacity accompanied by greater deflection, whereas CFRP stiffeners exhibited the opposite trend: lower load capacity with reduced deflection. It is worth noting that, for both strengthening materials, the load-carrying capacity increased compared to beams without any stiffeners.



a) b)

Figure 2-15: Web post: a) Before strengthening; b) After strengthening [27]



Figure 2-16: CFRP and mild steel stiffeners [28]

Kumbhar *et al* [42] investigated beams with web openings stiffened with transversely oriented CFRP plates, as illustrated in Figure 2-17. The experimental campaign included two beams: a control beam without strengthening and a second beam with transverse stiffeners of 1.4 mm thickness. Subsequently, Pawar extended the study numerically to examine the effect of varying the stiffener thickness. The results indicated that increasing stiffener thickness led to an increase in load-carrying capacity, which is partially consistent with Kumbhar's findings, while also revealing that the stiffener dimensions selected in Kumbhar study were suboptimal, which limited the extent of enhancement achieved.

Building on the discrete CFRP stiffeners employed by Kumbhar [28] and the localized configurations examined by Pawar [42], Thomas and Baskar [30] experimentally investigated the behaviour of castellated beams strengthened with fully wrapped CFRP extending along the entire length and even closing the web openings as shown in Figure 2-18. The first part of the research aimed to establish the most effective surface preparation method by testing six specimens to evaluate bond strength and tensile strength. From this, it was concluded that copper-slag blasting yielded the highest bond strength; consequently, this surface preparation method was adopted for the second part of the study. The second part of the research involved two section types, compact and semi-compact, with varying beam lengths designed to produce shear-dominated, moment-dominated, or combined shear-and-moment-dominated behaviour.

Depending on the span length, failure in unstrengthened beams occurred either via the Vierendeel mechanism or web post buckling in shear-dominated cases, echoing the failure modes identified by Al-Thabhawee [27] and Morkhade [17], or via plastic hinge formation in moment-dominated cases. Thomas and Baskar [30] reported that the addition of CFRP increased both stiffness and strength. For strengthened beams governed by shear, the increase in stiffness was more pronounced than that observed in moment-dominated and combined shear–moment cases, owing to their shorter span. This stiffness increase led to CFRP rupture followed by web post instability. In contrast, semi-compact sections exhibited delamination, then CFRP rupture, and finally web post buckling. This failure sequence was also observed in the combined shear-and-moment-dominated cases. Conversely, strengthened moment-dominated compact sections failed through a flexural mechanism, whereas semi-compact moment-dominated sections experienced the same flexural mechanism accompanied by local web post buckling. Notably, for semi-compact moment-dominated and combined beams, the CFRP-strengthened specimens exhibited more ductile behaviour than their unstrengthened counterparts

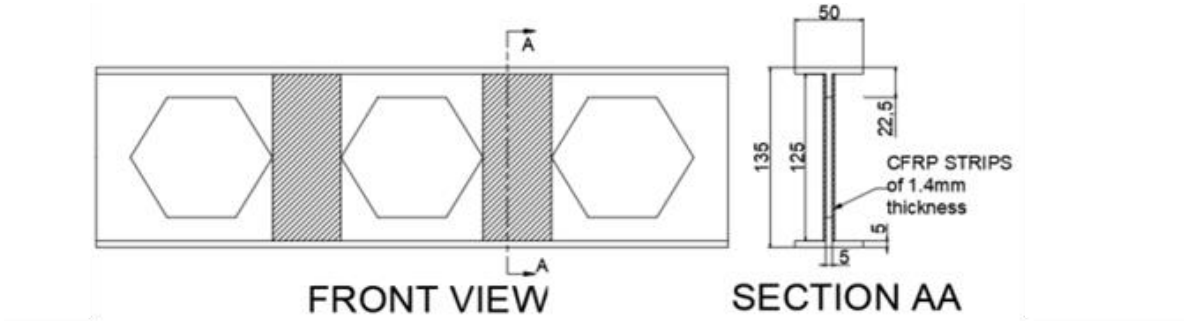


Figure 2-17: Transverse stiffeners [42]

Based on these experimental results, Thomas and Baskar [43] conducted a numerical investigation to identify the most effective strengthening scheme among three proposed techniques. This numerical study focused on beams with low shear, defined according to Thomas's criterion as a moment-to-shear ratio (M/V) of 1.5. The parametric analysis examined three different ratios of opening depth h_o to web depth d_w, as well as three different ratios of weld length l_w to h_o. The findings revealed that as the ratio h_o / d_w increases, strength decreases. This reduction is attributed to the enlargement of the unstiffened portion of the web between adjacent openings, which renders the web post more susceptible to buckling. Furthermore, an increase in weld length was also found to reduce beam strength. Among the three strengthening configurations, the third scheme, involving wrapping of the beam web as well as both the top

and bottom flanges on both sides, yielded the highest strength and stiffness. For all strengthened configurations, web post buckling was no longer the governing failure mode; instead, failure was dominated by CFRP debonding.



Figure 2-18: CFRP wrapped all around the beam [30,43]

In contrast to the monotonic loading regimes employed so far, Tanady and Suryoatmono [44] numerically investigated the behaviour of castellated beams under cyclic loading, specifically within the context of moment-resisting frames. The study compared castellated beams to their solid-web parent beams. The results revealed that the parent beam exhibited greater energy absorption, strength, and ductility than the castellated beam. Additionally, the stiffness degradation of the castellated beam was higher than that of the parent beam. It is noteworthy that, due to its greater depth and consequently higher moment of inertia, the castellated beam initially displayed higher stiffness than the parent beam. However, under cyclic loading, this initial advantage proved insufficient to overcome the detrimental effects of local stress concentration at the last opening corners near the column, where failure ultimately occurred. In contrast, the parent beam failed through bending, allowing for greater exploitation of the section compared to the castellated beam.

2.6. Other steel members with FRP strengthening

2.6.1. Plate girders (fabricated girders)

A distinct class of structural members that warrants attention is fabricated plate girders. In these girders, the presence of web openings introduces different failure modes. Unlike rolled steel beams, plate girders are typically proportioned so that their shear capacity derives from the sum of the critical buckling shear load and the post-buckling load capacity, which is responsible for most of the load-carrying capacity. Consequently, the tension field developed between

transverse stiffeners is disrupted by the presence of the openings leading to a high reduction in shear resistance.

Within this framework, Okeil *et al* [45] proposed novel techniques for inhibiting buckling in end panels of plate girders using glass fibre-reinforced polymer (GFRP) profiles, recognizing that GFRP offers a significantly lower modulus of elasticity compared to the more costly CFRP. To validate this concept, a pilot experimental campaign was conducted to assess whether GFRP profiles could effectively suppress instability. The investigation initially involved testing GFRP-strengthened steel bars under tension to evaluate enhancements in both strength and stiffness resulting from in-plane strengthening configurations Figure 2-19a. The findings revealed a 13% increase in stiffness, indicating potential utility for flexible structures where deflection control is a primary concern. In a subsequent application, a fabricated girder designed to fail by shear buckling of the end panel was strengthened by placing GFRP profiles at the mid-panel location on both sides of the web (see Figure 2-19b). The results demonstrated an increase in the stiffness by 17% and a 56% increase in load-carrying capacity, accompanied by some ductility, albeit less than that of the unstiffened beam, owing to debonding of the GFRP followed by web buckling. This outcome confirmed that the GFRP profiles were effective in delaying the onset of buckling. An analytical assessment was also attempted using AASHTO provisions for plate girder design, with the GFRP assumed to behave analogously to steel; however, this approach substantially overestimated the capacity because debonding was not accounted for. Consequently, the study underscored the necessity for more extensive investigation to incorporate debonding effects into analytical predictions.

Kadim *et al* [46] studied plate girders with web openings strengthened using CFRP. The research included five specimens, three of which served as control beams: the first had a solid web, while the other two featured square and circular web openings, respectively, located in the end panel. The remaining two specimens were strengthened with CFRP. For the square opening, CFRP strips were placed parallel to the flanges on one side of the web and perpendicular to the flanges on the other side. For the circular opening, the strips were oriented along the tension field on one side and along the compression field on the other side as presented in Figure 2-20. The results indicate that introducing a web opening with a depth equal to 40% of the web depth leads to a reduction in load-carrying capacity compared to the solid-web control girder of 50% for the beam with square openings and 30% for the beam with circular openings. This difference in strength reduction was attributed to stress concentration at the opening corners. The strengthening scheme was able to restore and even exceed the strength of

the solid-web girder for the circular opening, but it failed to recover the strength for the square opening. Failure in the strengthened specimens occurred due to tearing and debonding of the CFRP strips. Most importantly, neither strengthening scheme was able to restore stiffness to that of the solid-web girder, underscoring the persistent challenge of stiffness recovery in plate girders with web openings.

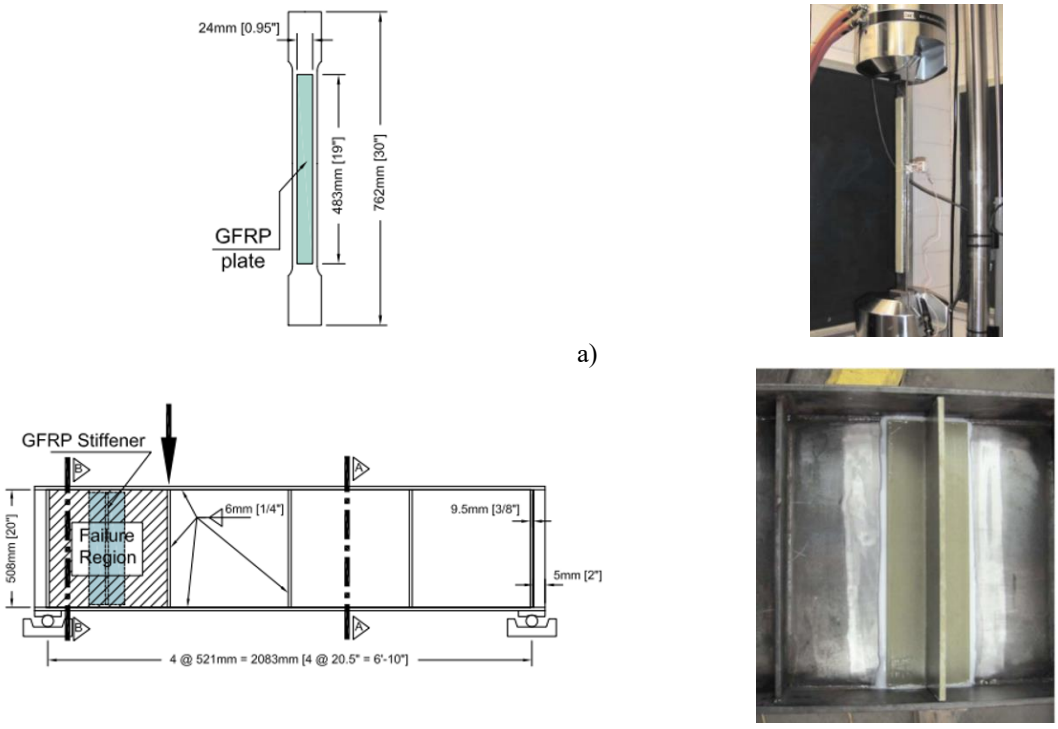


Figure 2-19: Strengthening method; a) Out of plane; b) In plane [45]

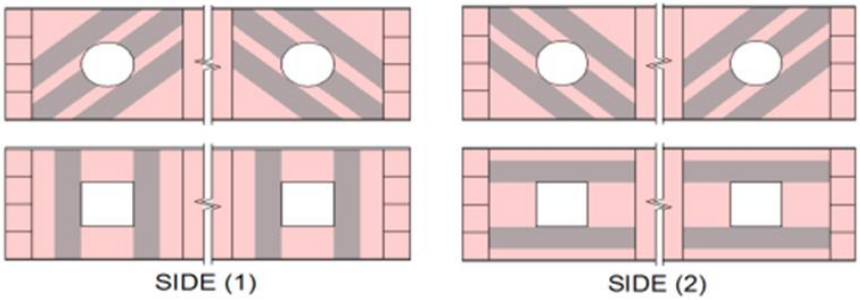


Figure 2-20: Strengthening scheme [46]

Extending the investigation to different opening geometries in the end panel, Hamood *et al* [47] examined plate girders with square and diamond-shaped openings. The depth of each opening was again 40% of the web depth, and the beams were tested under three-point bending. For the control beam without openings, the failure mode was observed to be buckling of the web panel. In contrast, the beams with web openings exhibited reductions in both stiffness and strength: 38% strength reduction for square openings and 44.5% for diamond openings. The failure mode

observed was buckling along the diagonal compression combined with tearing failure at the corners of the openings along the diagonal tension field, a failure mechanism consistent with the disruption of the tension field discussed earlier. Two strengthening configurations were then proposed around the openings. The first involved CFRP laminates placed parallel and perpendicular to the flanges, while the second employed laminates oriented diagonally and perpendicular to it as shown in Figure 2-21. Both configurations resulted in higher strength compared to the beams with unstrengthened openings; however, neither was able to fully restore the strength of the solid-webbed plate girder. The strengthening scheme with laminates oriented parallel and perpendicular to the flanges proved to be the most effective, particularly for diamond-shaped openings.

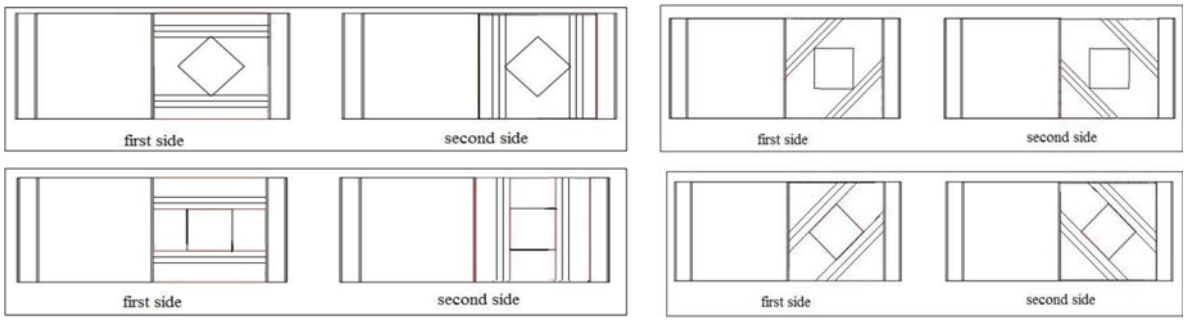


Figure 2-21: Strengthening scheme Type 1 (on the left) and Type 2 (on the right) [47]

Complementing these findings, Youssef's [48] conducted an experimental campaign where she compared various CFRP strengthening schemes. Two fibre orientations were investigated: a 0°/90° configuration and a ±45° configuration. Both were compared against a reference scheme in which steel plates were placed over the openings. The research revealed that beams without CFRP strengthening, both with and without web openings, exhibited more ductile behaviour than all the FRP-strengthened schemes, including plain webs with diagonally (±45°) placed CFRP strips. For the CFRP-strengthened plate girders, failure occurred in all cases due to debonding at high loads, after which instability ensued and was followed by complete failure. The schemes employing ±45° orientation and combined 0°/90° orientation were able to recover both strength and stiffness. Notably, the 0° and 90° scheme showed the highest increase in stiffness and strength compared to the unstrengthened beam with web openings. This improvement was attributed to the overlapping between the two strips, which created a degree of anchorage that delayed debonding.

In a subsequent investigation, Hamood *et al* [49] examined the behaviour of the web panels using different CFRP orientations, focusing specifically on the effect of applying laminates on

one side versus both sides of the web. The experimental program involved placing CFRP laminates either on one side or on both sides of the web, with orientations aligned either along the tension field direction or along the compression field direction. Hamood reported that placing the laminate along the tension field or along the compression field yielded comparable stiffness and strength, with any differences between the two configurations appearing only in the post-buckling range following debonding of the layer. Overall, their performance was similar. In contrast, when laminates were applied on both sides of the web, with one side oriented along the tension field direction and the other along the compression field direction, both stiffness and strength were higher, although the same debonding issue persisted. It is noteworthy that, in all strengthening cases, the stiffness exceeded that of the unstrengthened beam, offering a more optimistic outcome than Kadim's [[46]] finding that stiffness recovery to solid-web levels remained unattainable. Collectively, these studies on plate girders reveal that while CFRP strengthening can recover or even exceed the strength of solid-webbed girders in certain configurations (notably circular openings and diamond-shaped openings with optimized laminate orientation), stiffness recovery and debonding prevention remain persistent challenges requiring further investigation.

The studies for FRP strengthening of plate girders with web openings reveal that:

- FRP orientation is critical. Youssef [48] showed that 0°/90° and ±45° configurations were most effective, with the 0°/90° scheme providing the best results due to enhanced anchorage. Hamood et al [47] similarly found that laminates parallel and perpendicular to the flanges outperformed diagonal orientations.
- Strengthening can delay web instability. Okeil et al [45] demonstrated a 56% increase in load capacity and 17% stiffness improvement using GFRP profiles, effectively suppressing buckling onset until debonding occurred.
- Stiffness recovery is more difficult than strength recovery. Kadim et al [46] found that while strength could be restored or exceeded for circular openings, stiffness recovery to solid-web levels remained unattainable. Hamood et al [49] achieved some improvement with double-sided laminates, but full recovery proved elusive.
- Recovery is configuration dependent. Full strength recovery was achieved for circular openings [46], partial recovery for diamond-shaped openings [47], but square openings resisted recovery due to corner stress concentrations.

- Debonding governs once steel failure mechanisms are suppressed. This was observed across all studies and led to substantial overestimation in analytical models that did not account for it [45].

2.6.2. Steel plate shear walls (SPSW)

On a closely related note, a high degree of similarity exists between plate girders and steel plate shear walls, the latter having proven to be an efficient dual system for lateral load resistance. Both constitute shear-dominated members and therefore may require shear strengthening. However, a shift in perspective is now required: from the monotonic loading regimes applied to plate girders to the cyclic loading conditions characteristic of seismic applications.
Hosseinzadeh and Tehranizadeh [13] conducted a numerical investigation into the behaviour of SPSWs featuring large rectangular openings, with a particular focus on how such openings influence the infill plate's shear force distribution. Compared to a solid wall without openings, the presence of a window-like opening or a door-like opening resulted in higher stiffness and an earlier attainment of the maximum shear force, due to the existence of the local boundary elements, at a drift ratio of 1%, whereas the solid wall reached its peak shear force at 1.5% drift, accompanied by lower stiffness. The study further examined the effect of infill plate thickness at the opening level. Increasing the plate thickness beyond the required value led to a proportional increase in the force carried by the infill plate and a corresponding decrease in the force resisted by the surrounding frame. Although this relationship was linear, doubling the plate thickness did not produce a commensurate increase in the plate's force contribution. Overall, the global behaviour of the SPSW improved only marginally with increased thickness.

In contrast, the geometry of the opening, whether window-type or door-type (see Figure 2-22) and its specific location (right, left, or centre) had virtually no impact on the system's load-bearing capacity. The authors also observed that enlarging the local boundary elements beyond the minimum required dimensions enhanced the ultimate strength of the system, an effect attributed to the increased strength of the surrounding frame. Interestingly, contrary to what might be expected, the introduction of web openings was found to increase both the strength and stiffness of the system. Based on their findings, Hosseinzadeh and Tehranizadeh proposed upper and lower bounds for the system's base shear–displacement response curves. The behaviour of a wall with openings lies between that of a solid SPSW (lower limit) and an SPSW with openings on all stories (upper limit). As the aspect ratio (length to height) of the wall

increases, so does the system's stiffness. However, the presence of openings consistently reduces ductility, with the most significant loss observed at the lowest aspect ratios. In such cases, the wider plate is having the buckling more pronounced, thereby limiting its post-buckling behaviour.

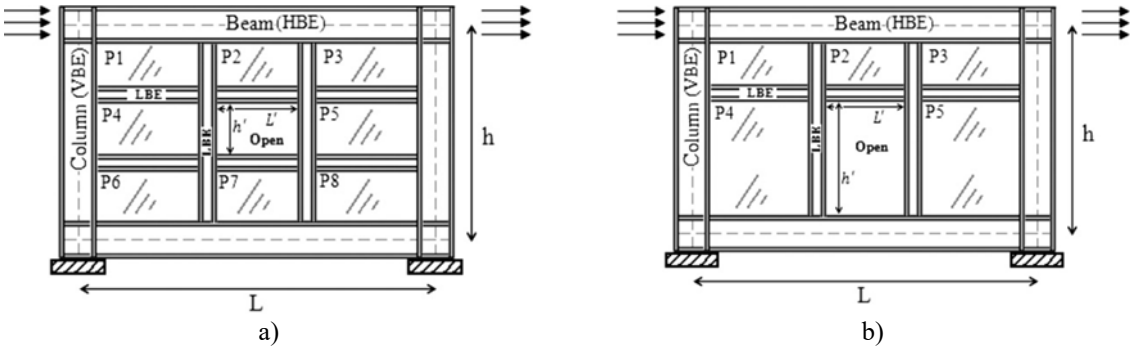
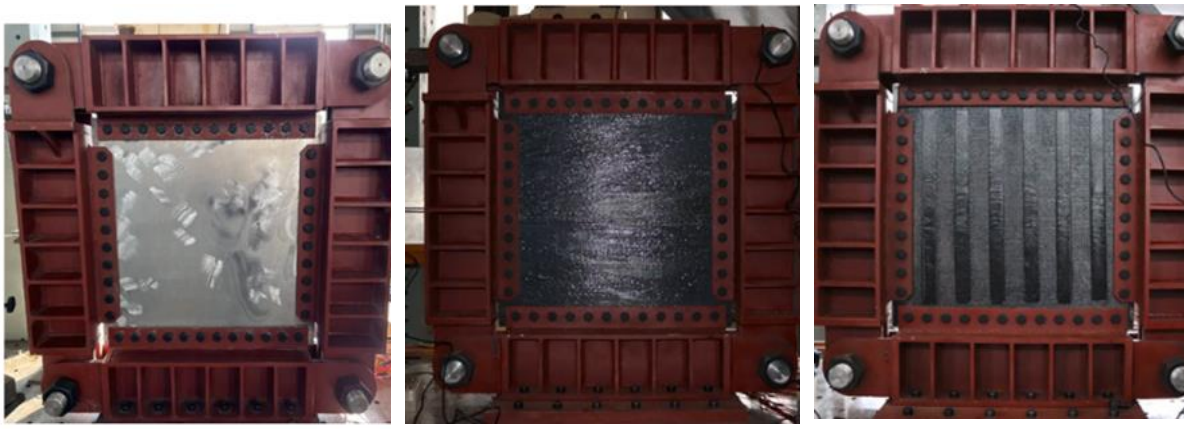


Figure 2-22: Opening types: a) Window opening; b) Door opening [13]

Du *et al* [50] investigated the shear performance of FRP-stiffened steel plate shear walls through an experimental program comprising three configurations: a steel plate without any stiffening, a steel plate with an FRP laminate attached, and a steel plate with a stiffened FRP laminate attached as seen in Figure 2-23. The results indicate that the addition of the stiffened FRP laminate provides the greatest enhancement in shear performance. Specifically, the shear stiffness increased to three times that of the FRP laminate alone, resulting in reduced out-of-plane deformation. Furthermore, both the yielding and ultimate load-carrying capacity increased, although the improvement in stiffness was more pronounced than that in strength, with the stiffened FRP laminate exhibiting the highest overall strength. Most importantly, failure of the steel plate with the stiffened FRP laminate occurred due to fracture of the CFRP. A numerical analysis followed the experimental campaign to investigate additional factors. One parameter examined was the effect of varying the thickness of the stiffeners. The findings revealed that increasing the stiffener thickness enhanced stiffness up to a certain point, beyond which further increases yielded diminishing returns. The conclusion was that adding stiffeners of low thickness increases stiffness, and to mitigate debonding, a moderate stiffener thickness is recommended. This is attributed to the fact that, at moderate plate thicknesses, the opening mode induced by buckling-related bending, combined with slip arising from in-plane shear, is diminished, thereby reducing the likelihood of debonding. Another factor considered was the placement of the stiffened FRP laminate on both sides of the steel plate shear wall. It was found that the effect on stiffness was greatest when using laminates with lower stiffener heights on both sides, and this benefit decayed as the stiffener height on one side increased. Additionally,

a slight increase in yield and ultimate load-carrying capacity was observed, though the increase diminished as the stiffener thickness grew larger.

A theoretical verification was also undertaken. The results revealed a deviation as high as 30% for the buckling load, attributed to the omission of initial imperfections in the analytical calculations. Consequently, it was proposed to reduce the analytical results by 30% to account for such effects. The conclusion was that placing the stiffened FRP laminate on single side is equivalent to placing it symmetrically on both sides with half the thickness of the single-sided configuration. Notably, the buckling mode changed with the addition of the stiffeners to the laminate: instead of a single wave along the diagonal compression, a Z-shaped three-fold buckling mode emerged as a direct effect of the stiffeners. Finally, it was recommended that if increased stiffness is desired, increasing the number of stiffeners is the preferred approach.

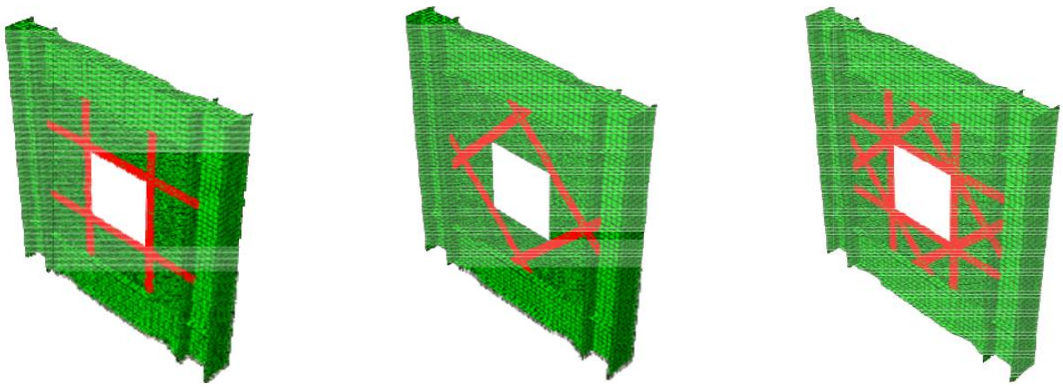


a) b) c)

Figure 2-23: Unstrengthened and strengthened schemes for SPSW: a) Steel plate shear wall (SPSW); b) SPSW with bonded laminate; c) SPSW with stiffened laminate [50]

Complementing the work of Du *et al* [50], Tabrizi and Rahai [51] considered various FRP materials: high-strength CFRP, high-modulus CFRP, standard CFRP, and GFRP, along with different strip geometries. Additionally, the influence of opening size was analysed, revealing a linear decay in stiffness, ultimate strength, yield stress, and energy dissipation as the opening size increased. Tabrizi proposed three distinct strengthening schemes (see Figure 2-24). In the first scheme, involving horizontal and vertical strips, the narrowest strips yielded the highest stiffness, whereas wider strips resulted in superior yield strength, ultimate strength, and energy dissipation. This improvement was attributed to the wider strips' ability to redistribute stress concentrations at the corners, thereby facilitating yielding and the development of tension field action across most of the plate. Regarding the material effect, both high-modulus and high-strength CFRP demonstrated the best performance. In the second scheme, strips oriented at 45 degrees enhanced stiffness and strength; however, once the strips failed in tension, their

effectiveness diminished. The third scheme, which combined both orientations (horizontal/vertical and diagonal strips), exhibited the best overall behaviour. Nevertheless, this improvement came at the cost of doubling the amount of FRP used, while only a marginal increase in stiffness was achieved, a factor of particular importance for the stability of hysteretic loops.



a) b) c)

Figure 2-24: Different CFRP configurations: a) Horizontal and vertical; b) Oriented along the diagonals; c) Combined horizontal and vertical and inclined [51]

2.7. Summary

The utilization of fibre-reinforced polymers (FRPs) for the strengthening of hot-rolled steel beams, fabricated girders, and steel plate shear walls containing web openings has demonstrated significant potential for recovering part or all of the strength and stiffness lost due to web openings, depending on the strengthening configuration and governing failure mode. From a materials perspective, a change in reinforcement type, from carbon FRP (CFRP) to glass FRP (GFRP), has been found to alter the optimal strengthening configurations, underscoring the material-dependent nature of the strengthening response. However, because FRPs are typically adhesively bonded to steel, a critical challenge arises, namely end debonding of the strengthening configuration, which significantly limits the efficiency of both systems. Debonding not only shifts the failure mode from ductile to brittle but also prevents the full utilization of the FRP material's tensile strength. To delay this phenomenon, literature has focused on the use of linear epoxy adhesives, valued for their high stiffness and tensile strength. Nevertheless, little research has addressed the potential of nonlinear epoxies. These adhesives, despite exhibiting lower stiffness and tensile strength than their linear counterparts, offer adequate strength and accommodate large strains, thereby providing greater ductility and larger load-carrying capacity. These observations motivate the investigation of adhesive constitutive behaviour undertaken in the present study. Beyond adhesive selection, the introduction of

anchorage systems has also been proposed for the prevention of debonding. Although effective in certain cases, debonding has subsequently been observed to occur at mid-span (intermediate debonding) due to defects or yielding of the steel member, followed by FRP rupture, which results in a sudden drop in load capacity. Resolving this issue would substantially advance the application of FRPs across various steel structure contexts, moving beyond the familiar domain of strengthening deteriorated bottom flanges in bridge decks.

Shifting focus from material considerations to structural behaviour, existing studies have investigated the effects of varying the opening depth, the geometry of the web opening, and the location of the opening on structural performance. However, little attention has been devoted to incorporating all of these parameters simultaneously. It is precisely these gaps that the present work aims to address, through a comprehensive parametric study on strengthened steel beams with discrete web openings. An additional complication is that no single strengthening scheme has been universally agreed upon as the most effective, unlike the established case of longitudinal steel stiffeners for the conventional strengthening of steel beams with discrete web openings. This is where the present work seeks to make its primary contribution: by assessing a mechanics-based strengthening scheme that offers a viable technological solution.

THIS PAGE WAS INTENTIONALLY LEFT BLANK

3. ANALYTICAL INVESTIGATION ON PERFORATED BEAMS

3.1. Introduction

This chapter presents an analytical framework for evaluating the strength and serviceability of composite steel-concrete beams incorporating large web openings, in accordance with EN 1993-1-13 [11], EN 1994-1-1 [12], and SCI P355 [10]. The procedure begins by establishing whether the beam in its current configuration needs strengthening. Then, it identifies where strengthening is needed and determines the appropriate dimensions for conventional steel strengthening techniques. Building upon this foundation, an analytical approach is subsequently proposed for evaluating the structural performance of such beams when they are reinforced using bonded Fibre-Reinforced Polymer (FRP) composites, offering an alternative strengthening solution that addresses the limitations of traditional methods.

3.2. Material properties

EN 1993-1-1 [52] specifies the nominal mechanical properties of structural steel grades, defining both the yield strength and ultimate tensile strength for commonly used grades, as summarised in **Table 3-*1***.

Table 3-1: Yield and Ultimate strength of various steel grades [52]

Steel Grade	Nominal Thickness of Element, t (mm)			
	$t \leq 16$ mm		16 mm $< t \leq 40$ mm	
	f_y (N/mm^2)	f_u (N/mm^2)	f_y (N/mm^2)	f_u (N/mm^2)
S235	235	360	225	360
S275	275	430	265	410
S355	355	510	345	470

The mechanical properties of the CFRP plates utilized in this chapter include the elastic modulus in the longitudinal direction, as well as the tensile and compressive strengths are presented in **Table 3-*2*** and were adopted from [39]. Similarly, the mechanical properties of the adhesives, including stiffness, shear strength, and fracture energy, were sourced from [53].

Correspondingly, EN 1992-1-1 [54] provides the characteristic compressive strength and modulus of elasticity for concrete across a range of concrete classes, as presented in **Table 3-*3*.**

Table 3-2: Properties of CFRP and adhesive [23,53]

Properties of the CFRP plate		
Ex (GPa)	Tensile strength (MPa)	Compressive strength (MPa)
200	2950	1800
Properties of the nonlinear adhesive		
E (Gpa)	Shear strength (MPa)	Fracture energy (N/mm)
1.75	14.73	12.78

Table 3-3: Compressive strength and young's modulus of different concrete classes [54]

Properties of Concrete	Strength class of concrete				
	C20/25	C25/30	C30/37	C35/45	C40/50
f_{1ck} (MPa)	20	25	30	35	40
$f_{1ck,\ cube}$ (MPa)	25	30	37	45	50
E_{1cm} (GPa)	30	31	33	34	35

3.3. Geometry and cross-sectional properties

Figure 3-1 illustrates the opening geometries considered in this study, together with the geometric parameters required for the design and assessment of composite beams with large web openings.

EN 1993-1-13 [11] establishes the geometrical limitations governing the dimensions of web openings as shown in **Table 3-*4***, while also noting that openings exceeding these prescribed limits may still be adopted, provided they are justified by appropriate analytical calculations.

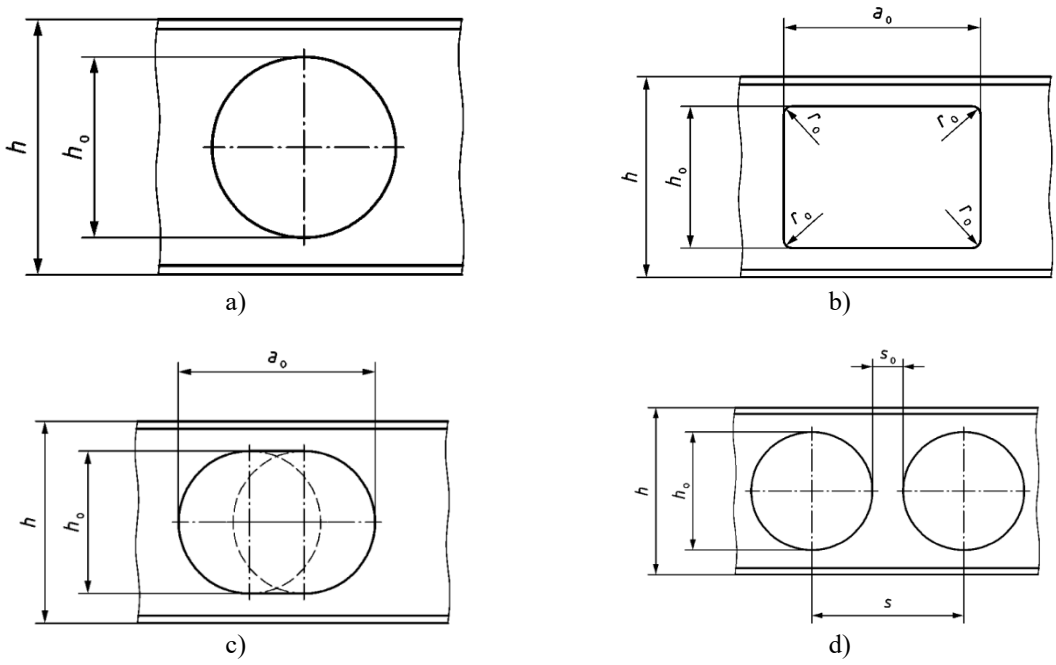


Figure 3-1: Different Geometries a) Circular opening; b) Rectangular opening; c) Elongated opening; d) Closely spaced circular opening [11]

Table 3-4: Limitations on the dimensions of different unstiffened openings [11]

Shape of opening	Maximum opening height, h_o	Maximum opening length, a_o	Minimum edge to edge spacing, s_o	Minimum depth of Tee	
				Tee in compression	Tee in tension
Circular	0.8h	-	$0.1h_o$	Max ($t_f + r$ +10 mm: t_f + 30 mm)	Max ($t_f + r$ +10 mm: t_f + 30 mm)
Hexagonal	$0.75h$	$1.5h_o$	$0.25h_o$		
Rectangular	$0.75h$	$2.5h_o$	Max ($0.5a_o$: h_o)	Max ($\frac{a_o}{12}$:$0.1h$)	$0.1h$
Elongated	$0.8h$	$3h_o$	Max ($0.25h_{eff}$: $0.5h_o$)	$\frac{a_{eff}}{12}$	Max ($t_f + r$ +10 mm: t_f + 30 mm)
Sinusoidal	$0.8h$	$5h_o$	$0.25h_o$		

3.4. Classification of the cross section

First to determine whether the cross-section is capable of attaining its full plastic moment capacity, or whether it will be governed by local instability leading to a reduced elastic moment capacity, a cross-section classification is performed in accordance with EN 1993-1-1 [52]. The standard prescribes the limiting width-to-thickness ratios for compressed elements, distinguishing between interior elements and outstand flanges as in Figure 3-2 on the basis of their position within the cross-section, as well as the applied stress distribution, whether the element is subjected to uniform compression or to a stress gradient induced by bending. The

classification is done for both the solid-webbed portion of the beam and the perforated region, the latter encompassing the top and bottom Tee sections formed at the opening locations.



a) b)

Figure 3-2: Max Width and thickness for compression parts: a) Internal parts; b) Outstand flange [52]

Following the cross-section classification, the effective width of the concrete slab acting compositely with the steel beam is determined following the stress distribution assumed in Figure 3-3, accounting for the shear lag effect arising in the concrete flange as a result of the attachment between the slab and the steel section. This effective width is not constant along the length of the beam but varies depending on the location under consideration, as prescribed by EN 1994-1-1 [12].

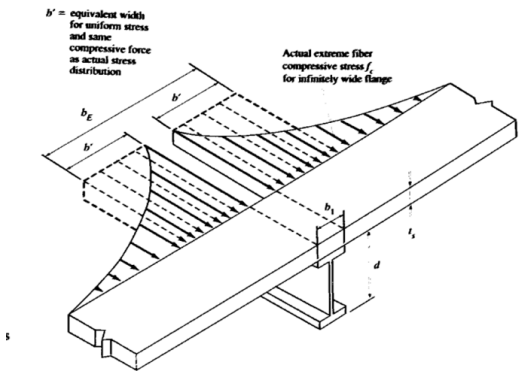


Figure 3-3: Stress distribution due to the shear lag effect and the concept of the effective stress [29]

The effective slab width, at mid span, is identified by Eq 3-1,

$$b_{\text{eff}} = b_{\text{o}} + \Sigma b_{\text{ei}} \qquad \textit{Eq 3-1}$$

where:

b_{ei} is the effective slab width on either side of the web. It is taken equal to $L_e/8$ no more than the geometric width.

L_e is the effective span which for simply supported beam is its span L.

b_{o} Is the distance between centres of outstand shear connectors in a group.

The effective slab width at end support, is obtained by Eq 3-2.

$$b_{\text{eff}} = b_{\text{o}} + \Sigma\beta_{\text{i}} b_{\text{ei}} \qquad \textit{Eq 3-2}$$

with the value of β defined by Eq 3-3

$$\beta = 0.55 + 0.025 L_e / b_{ei} \leq 1 \qquad \textit{Eq 3-3}$$

For simply supported beams, the effective slab width at the end of the span is given by Eq 3-4:

$$b_{\text{eff}} = b_0 + 0.187L \qquad \textit{Eq 3-4}$$

In general, the effective slab width at the support is smaller than that at mid-span.

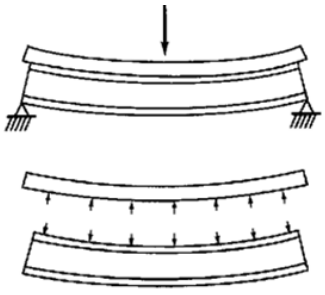
Effective width of slab acting with the beam at an opening is given by Eq 3-5 and Eq 3-6 according to the opening distance from support x.

$$b_{\text{eff,o}} = \frac{3L_{\text{e}}}{16} + \frac{x}{4} \; for \; x \leq L_{\text{e}}/4 \qquad \textit{Eq 3-5}$$

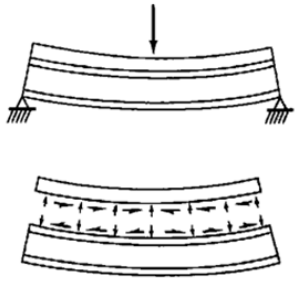
$$b_{\text{eff,o}} = L_{\text{e}}/4 \; for \; x > L_{\text{e}}/4 \qquad \textit{Eq 3-6}$$

3.5. Shear stud connectors

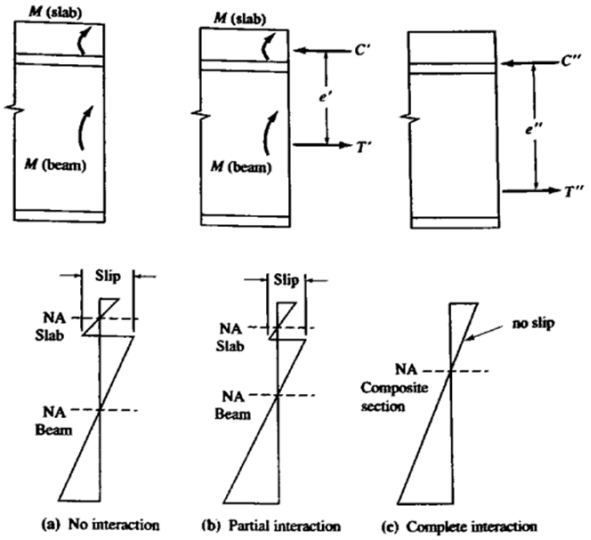
The composite interaction between the concrete slab and the steel beam is achieved through the provision of shear studs, which serve as mechanical connectors at the steel-concrete interface. These connectors are responsible for transferring the interfacial shear forces that develop between the two components, thereby preventing or limiting relative slip and, in essence, enabling composite action to be achieved (see Figure 3-4a,b). Depending on the number and spacing of shear connectors provided, the beam may be classified as non-composite, partially composite, or fully composite, each condition giving rise to a distinct strain distribution across the cross-section, as illustrated in Figure 3-4c.



a)



b)



c)

Figure 3-4: Deflected shape of both; a) Non-composite beam; b) Composite beam; c) Different strain distribution [29]

In accordance with EN 1994-1-1 [12], the design shear resistance of a shear stud connector is taken as the lesser of the following two failure modes: shear failure of the stud shank, and bearing failure of the surrounding concrete, as expressed in Eq 3-7 and Eq 3-8:

Shearing of the shank $$P_{\mathrm{Rd}} = \frac{0.8 f_{\mathrm{u}} \pi d^2/4}{\Upsilon_{\mathrm{v}}} \qquad \textit{Eq 3-7}$$

Bearing on the concrete $$P_{\mathrm{Rd}} = \frac{0.29 \alpha d^2 \sqrt{f_{\mathrm{ck}} E_{\mathrm{cm}}}}{\Upsilon_{\mathrm{v}}} \qquad \textit{Eq 3-8}$$

with the parameter a calculated as per Eq 3-9 and Eq 3-10 according to the ratio of h_{sc}/d:

$$a = 0.2\left(\frac{h_{\mathrm{sc}}}{d} + 1\right) \quad for\ 3 \le h_{\mathrm{sc}}/d \le 4 \qquad \textit{Eq 3-9}$$

$$a = 1 \quad for\ h_{\mathrm{sc}} > 4 \qquad \textit{Eq 3-10}$$

where:

d	is the diameter of the shank of the stud (16 mm ≤ d ≤ 25 mm)
h_{sc}	is the nominal height of the stud
f_{u}	is the specified ultimate tensile strength of the stud material
f_{ck}	is the characteristic cylinder compressive strength of the concrete (with density not less than 1750 kg/m^3)
E_{cm}	is the secant modulus of elasticity of the concrete as in Table 3-3.

Given that profiled steel sheeting is employed in lieu of a conventional solid concrete slab, and the ribs are usually oriented perpendicularly to the steel profile, reduction factor, k_t, is applied

to the design shear resistance of the stud connector to account for the geometry of the profiled deck and the number of shear connector. This strength reduction factor is defined by Eq 3-11.

$$K_{\mathrm{t}} = \frac{0.7}{\sqrt{n_{\mathrm{r}}}} \frac{b_{\mathrm{o}}}{h_{\mathrm{p}}} \left(\frac{h_{\mathrm{sc}}}{h_{\mathrm{p}}} - 1\right) \not> K_{\mathrm{t,max}} \qquad \textit{Eq 3-11}$$

where:

b_{o} is the average rib width (or minimum width for re-entrant profiles)

h_{sc} is the nominal height of the stud

h_{p} is the profile height (to the shoulder of the profile)

n_{r} is the number of studs per rib (n_{r} =1 or 2)

K_{t} is the upper limit on k_{t} (see **Table 3-*5***)

Table 3-5: Upper limits Kt, max for the reduction factor Kt [12]

Number of stud connectors per Rib	Thickness *t* of the sheet (mm)	Studs with $d \leq 20$ mm and welded through profiled sheeting	Profiled sheeting with holes and studs with d = 19 mm OR 22 mm
$n_{\mathrm{r}} = 1$	≤ 1	0.85	0.75
	> 1	1	0.75
$n_{\mathrm{r}} = 2$	≤ 1	0.70	0.60
	> 1	0.80	0.60

3.6. Degree of shear connection

The degree of shear connection governs the extent of slip permitted at the steel–concrete interface and controls the percentage of the plastic moment resistance of the composite section that can be developed and calculated as per Eq 3-12. It is defined at the point of maximum moment and is dependent upon the accumulation of longitudinal shear.

$$\eta = \frac{n}{n_f} \qquad \textit{Eq 3-12}$$

where:

n is the number of shear connectors between the point of zero and max moment

n_f is the number of shear connectors required for the full shear connection

When the tensile resistance of the steel beam exceeds the compressive resistance of the concrete slab ($N_{a,Rd} > N_{c,Rd}$), the degree of shear connection is calculated as a function of the lesser of the maximum longitudinal forces that can be sustained by either the concrete slab or the steel section in isolation in accordance with EN 1994 -1-1 [12], given by Eq 3-13.

$$\eta = \frac{N_{\mathrm{c,max}}}{N_{\mathrm{c,s\ Rd}}} \qquad \textit{Eq 3-13}$$

where:

$N_{\mathrm{c,max}}$ is the total shear force transferred by the shear connectors between the points of zero and maximum bending moment ($= nP_{\mathrm{Rd}}$).

$N_{\mathrm{c,s,Rd}}$ is the concrete compressive strength over the effective width of the slab and calculated as $N_{\mathrm{c,s,Rd}} = 0.85 f_{\mathrm{cd}} b_{\mathrm{eff}} h_{\mathrm{c}}$

b_{eff} is the effective width at the position of the maximum bending moment;

h_{c} is the depth of the concrete above the profile.

P_{Rd} denotes the design resistance of the shear connectors used with profiled sheeting multiplied by k_t as given Eq 3-11

when the tensile resistance of the steel beam is less than the compressive resistance of the concrete slab ($N_{\mathrm{a,Rd}} < N_{\mathrm{c,s,Rd}}$). In this case, the maximum force that the concrete slab can develop is equal to $N_{\mathrm{a,Rd}}$ and the degree of shear connection is expressed as in Eq 3-14.

$$\eta = \frac{N_{\mathrm{c,max}}}{N_{\mathrm{a,Rd}}} \qquad \textit{Eq 3-14}$$

The minimum degree of shear connection for symmetrical steel sections, applicable to solid-web composite beams and beams with widely spaced circular openings or other opening shapes depends on the effective length and is calculated in accordance with Eq 3-15 and Eq 3-16.

$L_{\mathrm{e}} \leq 25$: $\eta \geq 1 - (\frac{355}{f_y})(0.75 - 0.03L_e)$ $\eta \geq 0.4$ *Eq 3-15*

$L_{\mathrm{e}} > 25$: $\eta \geq 1$ *Eq 3-16*

where:

L_{e} is the distance between points of contraflexure, which, for simply supported beams, corresponds to the beam span in meters.

3.7. Load combinations

Two phases are considered in this study. The first corresponds to the composite phase, in which the steel beam and the hardened concrete slab act together to resist the applied loads. The second corresponds to the construction phase, during which the concrete slab has not yet gained sufficient strength and is therefore considered wet and ineffective in contributing to the structural resistance. In this phase, the steel beam alone is assumed to carry all applied loads, and the system is treated as non-composite.

The general load combination format adopted is formulated in accordance with EN 1990 [55], which combines permanent and variable actions at the ultimate limit state (ULS) and is expressed in Eq 3-17.

$$E_{\mathrm{d}} = \Sigma\, \Upsilon_{\mathrm{G,j}}\, G_{\mathrm{k,i}} + \Upsilon_{\mathrm{Q,1}} Q_{\mathrm{k,1}} + \Sigma\, \Upsilon_{\mathrm{Q,1}} \Psi_{\mathrm{0,i}} Q_{\mathrm{k,i}} \qquad \textit{Eq 3-17}$$

where:

$G_{\mathrm{k,i}}$ is the characteristic value of the jth permanent action

$Q_{\mathrm{k,1}}$ is the characteristic value of the leading variable action

$Q_{\mathrm{k,i}}$ is the characteristic value of the ith variable action

$\Upsilon_{\mathrm{G,j}}$ is the partial factor for the jth permanent action

$\Upsilon_{\mathrm{Q,1}}$ is the partial factor for leading variable action

$\Upsilon_{\mathrm{Q,i}}$ is the partial factor for the ith variable action

$\Psi_{\mathrm{0,i}}$ is the combination factor for other actions

3.8. Ultimate limit states verification

The ultimate limit states considered for the resistance of the steel beam include:

- Bending moment of the perforated section
- Vierendeel bending resistance
- Shear capacity of the perforated section

The forces and moments acting at failure are shown in Figure 3-5**.**

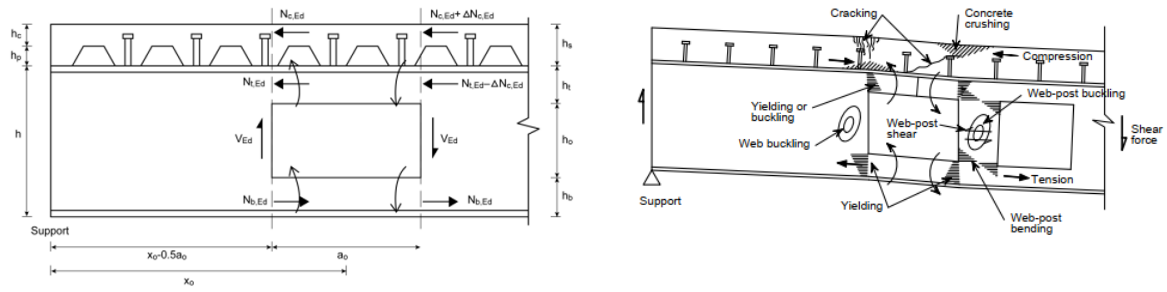


Figure 3-5: Various failure modes [12]

Under the action of a sagging bending moment, a tensile force develops in the bottom Tee and remains constant across the width of the opening. This force is balanced by a compressive force in the concrete slab, and, depending on the relative proportions of the slab and the Tee sections, an additional compressive force may develop in the top Tee. In general, the top Tee is not assumed to develop any tensile forces, as their development would necessitate the attainment of substantial plastic strains. In the absence of composite action, the top Tee carries the compressive force required to balance the tensile force developed in the bottom Tee. The compressive force in the slab is developed through the shear connectors welded to the top flange, which are uniformly distributed along the beam for the case of uniform loading. It is worth noting that the force transferred from the beam to the slab is limited by the number of shear connectors provided. If the connectors are insufficient to transfer the full force, the condition is referred to as partial shear connection. The variation of the bending moment across the opening is accommodated through Vierendeel action, which involves local bending of the Tee sections at the four corners of the opening. In the top Tee, this Vierendeel bending is resisted by local composite action with the concrete slab.

The global bending resistance is verified at the centre of the opening assuming zero Vierendeel moment at that point. However, this assumption does not strictly hold, as the point of zero moment shifts towards the low-moment side of the opening when the Vierendeel resistance provided by local composite action of the slab is relatively high and plastic redistribution takes place after the development of the plastic hinges at the corners of the high moment side of the opening. Nevertheless, this simplification yields conservative estimates of the resistance.

Under ultimate limit state conditions, failure at an opening may occur either through the formation of plastic hinges at the corners in regions of high shear and low bending moment, or through tensile yielding of the bottom Tee in regions of low shear and high bending moment. The top and bottom Tees are simultaneously subjected to axial force, shear, and bending, and

this combined loading influences the development of plasticity and permits redistribution of the Vierendeel moment around the opening. Given this complexity, simplifying assumptions are introduced to facilitate the evaluation of the internal forces at the opening and to narrow down the scope of the study.

1. The Profiled metal deck is perpendicular to the steel beam and has a concrete slab on top of it
2. Openings are centred with the beam centroid
3. The study complies with the geometric limits of the beam with web openings
4. Applicable to rolled sections
5. All sections are symmetric with constant web thickness
6. Simply supported beams are subjected to positive bending moments
7. The loading schemes include uniform and concentrated loads.
8. For a uniformly loaded beam, the shear force is calculated at the higher shear side
9. For a point loaded beam, the shear force is constant over the opening length
10. The axial forces in the Tees and in the concrete are based on plastic analysis at all load levels, meaning rectangular stress block is considered.
11. The compression force in the slab is based on the number of shear connectors form the support to the centreline of the opening
12. At the opening, vertical shear is resisted by the two Tee sections and by the concrete slab due to the local composite action at the opening
13. The shear resistance of the concrete slab is based on the punching shear resistance.
14. The distribution of shear between the top and bottom Tees is governed by their respective resistances to Vierendeel bending. Local composite action enhances the Vierendeel bending resistance of the top Tee; consequently, for large openings, the shear resisted by the bottom Tee can be considered negligible.
15. The compressive force in the concrete and the tensile force in the bottom Tee is established from the design moment acting at the centreline of the opening.
16. The increase in the bending resistance across the opening is due to local composite action of the top Tee acting with the slab, which depends on the number of shear connectors placed over the opening.
17. The plastic or elastic bending resistances of the Tee sections depend on the cross-section classification. They are reduced to account for coexisting shear and axial forces.

3.8.1. Global bending resistance of perforated beams at openings

The bending resistance of the composite beam is assessed at the centreline of the opening. The plastic bending capacity of the perforated cross-section depends on the classification of the top Tee and on whether partial or full shear connection is adopted. For Class 1 and Class 2 sections, the plastic bending resistance can be fully developed, whereas Class 3 and Class 4 sections are limited to their elastic bending resistance.

In an unperforated composite beam, the plastic neutral axis is typically located within or above the top flange of the steel section. However, in a perforated section, the plastic neutral axis shifts into the web. As a result, the perforated composite section tends to be classified as Class 2 or better and is therefore capable of developing its plastic moment capacity.

Two cases are identified depending on the location of the Plastic Neutral Axis (PNA) relative to the cross-section, specifically whether it falls within the concrete slab or within the steel section (top Tee).

Case 1 (Figure 3-6): $N_{\mathrm{c,Rd}} > N_{\mathrm{bT,Rd}}$ (PNA in slab)

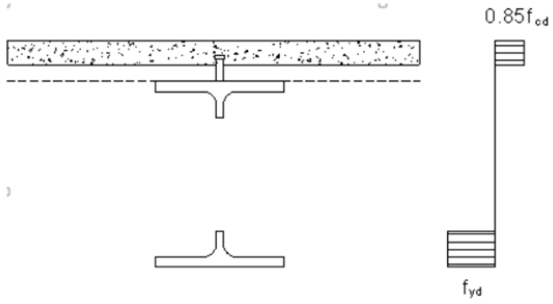


Figure 3-6: Equilibrium of the beam at openings under pure bending [12]

In the case where the PNA is located within the concrete slab, the compressive resistance of the full depth of the slab is greater than the tensile resistance of the bottom Tee. It is assumed that the top Tee section carries no tensile force, and that the entire tensile resistance is mobilized solely by the bottom Tee section. Under this assumption, the tensile resistance of the bottom Tee section is expressed by Eq 3-18.

$$N_{\mathrm{bT,Rd}} = \frac{A_{\mathrm{a,bT}} f_{\mathrm{y}}}{\Upsilon_{\mathrm{M_0}}} \qquad \textit{Eq 3-18}$$

where:

$A_{\mathrm{a,bT}}$ is the cross-sectional area of the bottom Tee.

f_y is the design value of the yield strength.

The compressive force sustained by the concrete slab is taken as the lesser of the compressive capacity of the concrete slab and the total longitudinal shear force transferable by the shear connectors between the end of the beam and the centreline of the opening, as expressed by Eq 3-19, with the latter being dependent on the degree of shear connection provided.

$$N_{\mathrm{c,Rd}} = \min\{0.85 f_{\mathrm{cd}} b_{\mathrm{eff}} h_{\mathrm{c}}; n_{\mathrm{sc}} P_{\mathrm{Rd}}\} \qquad \textit{Eq 3-19}$$

where:

f_{cd} is the design strength of the concrete and is calculated as $f_{\mathrm{ck}} \ / \Upsilon_{\mathrm{c}}$

b_{eff} is the effective slab width at the opening

h_{c} is the depth of the concrete topping ($h_{\mathrm{c}} = h_{\mathrm{s}} - h_{\mathrm{d}}$)

h_{s} is the slab depth

h_{d} is the overall depth of the decking profile

n_{sc} is the number of shear connectors placed over the distance from the nearer support to the centreline of the opening

The plastic bending resistance of the cross-section at the opening location is determined by taking moments about any of the internal force resultants, as defined by Eq 3-20.

$$M_{\mathrm{o,Rd}} = N_{\mathrm{bT,Rd}}(h_{\mathrm{eff}} + Z_{\mathrm{t}} + h_{\mathrm{s}} - 0.5 Z_{\mathrm{c}}) \qquad \textit{Eq 3-20}$$

where:

h_{eff} is the effective depth of the beam between the centroids of the Tees

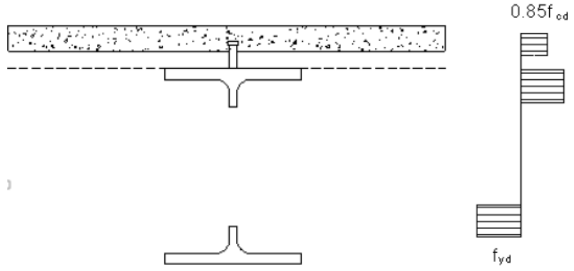
Z_{t} is the depth of the centroid of the top Tee from the outer edge of the flange

Z_{c} is the depth of concrete in compression, given by $\frac{N_{\mathrm{c,Rd}}}{0.85 f_{\mathrm{cd}}\, b_{\mathrm{eff,o}}} \leq h_c$

In order to assess the tensile force demand acting on the bottom Tee section, the global bending moment at the opening location is resolved into an equivalent force couple, giving the tensile resultant forces as defined by Eq 3-21.

$$N_{\mathrm{b,Ed}} = \frac{M_{\mathrm{Ed}}}{(h + h_{\mathrm{s}} - Z_{\mathrm{b}} - 0.5 Z_{\mathrm{c}})} \qquad \textit{Eq 3-21}$$

Case 2 (Figure 3-7): $N_{\mathrm{c,Rd}} < N_{\mathrm{bT,Rd}}$



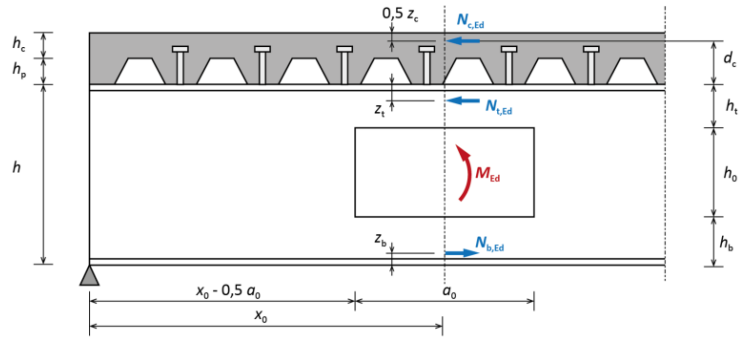


Figure 3-7: Equilibrium of the beam at openings under pure bending [12]

Here in Figure 3-7, the compression resistance of the slab is less than the tension resistance of the bottom Tee, so equilibrium is achieved by developing compression in the top Tee. The top Tee is assumed to be stressed uniformly. The compression force in the top Tee $N_{\mathrm{t,Ed}}$ is equal to the difference between the tension resistance of the bottom Tee and the compression resistance of the concrete slab as given by Eq 3-22 and Eq 3-23.

$$N_{\mathrm{t,Ed}} = N_{\mathrm{b,Ed}} - N_{\mathrm{c,Ed}} \qquad \textit{Eq 3-22}$$

$$N_{\mathrm{tT,Rd}} = \frac{A_{\mathrm{a,tT}}\, f_{\mathrm{y}}}{\Upsilon_{\mathrm{M_o}}} \qquad \textit{Eq 3-23}$$

If $N_{\mathrm{bT,Ed}} > N_{\mathrm{c,Rd}}$

The tensile force demand on the bottom Tee section is determined by subtracting the contribution of the composite action moment from the total global bending moment demand at the opening location, thereby isolating the net tensile force resultant to be resisted by the bottom Tee section alone as in Eq 3-24.

$$N_{\mathrm{b,Ed}} = \frac{M_{\mathrm{Ed}} - N_{\mathrm{c,Ed}}(h_{\mathrm{s}} + Z_{\mathrm{t}} - 0.5Z_{\mathrm{c}})}{h - Z_{\mathrm{b}} - Z_{\mathrm{t}}} \qquad \textit{Eq 3-24}$$

Similarly, the plastic moment resistance at the opening location is determined by taking moments about the compressive force resultant acting within the top Tee section as in Eq 3-25.

$$M_{\mathrm{o,Rd}} = N_{\mathrm{bT,Rd}} h_{\mathrm{eff}} + N_{\mathrm{c,Rd}}(Z_{\mathrm{t}} + h_{\mathrm{s}} - 0.5h_{\mathrm{c}}) \qquad \textit{Eq 3-25}$$

3.8.2. Local bending resistance of perforated beams at openings (Vierendeel bending resistance)

As a preliminary step, the compressed elements of the Tee cross-section, namely the flange and the web, must be classified in accordance with EN 1993-1-1 [52]. The classification is performed by comparing the relevant width-to-thickness ratios of the compressed elements

against the limiting values prescribed by the code. In the event that the web is found to be Class 3, an effective reduced depth of the web satisfying the Class 2 limiting slenderness may be adopted, thereby allowing the entire cross-section to be treated as Class 2. This is particularly significant as a Class 2 classification permits the cross-section to attain its full plastic moment capacity, as opposed to the elastic moment capacity associated with a Class 3 cross-section.

$$a_{\text{eff}} > 32t_{\text{w}}\varepsilon \qquad \text{Web is class 3}$$

$$d_{\text{t}} \leq \frac{10t_{\text{w}}\varepsilon}{\sqrt{1-(\frac{32t_{\text{w}}\varepsilon}{a_{\text{eff}}})^2}} \qquad \text{Web depth to be classified as class 2}$$

By extension, an analogous approach is applicable to cross-sections with Class 4 webs, whereby an effective reduced depth corresponding to the Class 3 limiting slenderness is adopted, and the bending resistance is subsequently calculated on the basis of elastic section properties.

$$a_{\text{eff}} > 36t_{\text{w}}\varepsilon \qquad \text{web is class 4}$$

$$d_{\text{t}} \leq \frac{14t_{\text{w}}\varepsilon}{\sqrt{1-(\frac{36t_{\text{w}}\varepsilon}{a_{\text{eff}}})^2}} \qquad \text{web depth to be classified as class 3}$$

where:

a_{eff} is the effective opening length.

d_{t} is the depth of the top Tee

In the calculation of the plastic bending resistance, the influence of the applied shear force must be considered as given by Eq 3-26, as its presence accelerates the onset of yielding within the cross-section. In accordance with EN 1993-1-1 [52], the effect of shear is taken into account when the design shear force exceeds half of the plastic shear resistance of the cross-section, that is, when $V_{\text{Ed}} > 0.5V_{\text{o,pl,Rd}}$. Under this condition, the interaction between shear and bending is accounted for by reducing the yield strength of the shear area, thereby obtaining a reduced plastic moment resistance that reflects the combined effect of both actions.

$$f_{\text{y,red}} = f_{\text{y}}[1-\rho] \qquad \textit{Eq 3-26}$$

where:

$f_{\text{y,red}}$ is the reduced yield strength due to the existence of the shear.

ρ is the utilization ratio of the cross section in shear and given by Eq 3-27

$$\rho = (2V_{\text{Ed}}/V_{\text{o,pl,Rd}} - 1)^2 \qquad \textit{Eq 3-27}$$

To calculate the plastic bending resistance in the absence of axial force Eq 3-28 is used:

$$M_{\text{T,pl,Rd}} = \frac{A_{\text{w,T}}\, f_{\text{y,red}}}{\Upsilon_{\text{M}_0}}\left(0.5h_{\text{w,T}} + t_{\text{f}} - Z_{\text{pl}}\right) + \frac{A_{\text{f}}\, f_{\text{y,red}}}{\Upsilon_{\text{M}_0}}\left(0.5h_{\text{f}} - Z_{\text{pl}} + \frac{Z_{\text{pl}}^2}{t_{\text{f}}}\right) \qquad \textit{Eq 3-28}$$

where:

Z_{pl} is the distance between PNA and the extreme fibre of the steel flange

$$= (A_{\mathrm{f}} + A_{\mathrm{w,T}})/(2b_{\mathrm{f}})$$

$A_{\mathrm{w,T}}$ is the cross-sectional area of web of the Tee ($= h_{\mathrm{w,T}}\, t_{\mathrm{w}}$)

$h_{\mathrm{w,T}}$ is the depth of web of the Tee

t_{f} is the flange thickness

In addition to the shear force, the axial force induced by the global bending moment also contributes to accelerating the spread of plasticity across the cross-section. The influence of the axial force on the plastic bending resistance is accounted for by applying a reduction factor expressed in quadratic form as a function of the ratio between the acting normal force and the corresponding plastic normal force resistance of the cross-section, in accordance with EN 1993-1-13 [11] as given by Eq 3-29.

$$M_{NV,\mathrm{T,Rd}} = M_{T,Pl,\mathrm{Rd}}\left(1 - \left(\frac{N_{\mathrm{m,Ed}}}{N_{\mathrm{T,pl,Rd}}}\right)^2\right) \qquad \textit{Eq 3-29}$$

where:

$M_{\mathrm{NV,T,Rd}}$ is the bending resistance of the Tee section reduced to take into account the interaction with axial force and shear force.

$M_{\mathrm{T,pl,Rd}}$ is the plastic bending resistance of the Tee section including the reduced yield strength

$N_{\mathrm{T,pl,Rd}}$ is the compression plastic resistance of the Tee including the reduced yield strength

$N_{\mathrm{m,Ed}}$ is the design value of the axial force on the Tee due to the global bending action at the centreline of the opening, either the compression force in the top Tee, $N_{\mathrm{tT,Ed}}$ or the tension force in the bottom Tee $N_{\mathrm{bT,Ed}}$

Having determined the plastic moment capacity of both the top and bottom Tee sections, the Vierendeel moment demand at the opening location is subsequently evaluated.

The Vierendeel resistance due to local composite action is given by Eq 3-30.

$$M_{\mathrm{Vc,Rd}} = \Delta N_{\mathrm{c,Rd}}(d_{\mathrm{c}} + Z_{\mathrm{t}}) \qquad \textit{Eq 3-30}$$

Where $\Delta N_{\mathrm{c,Rd}}$ is the compression force developed by the shear connectors placed over the opening = $n_{\mathrm{SC,o}} P_{\mathrm{Rd}}$.

As the opening length increases, the beam becomes increasingly flexible, resulting in a reduction of the available Vierendeel moment resistance given by Eq 3-31.

$$K_{\mathrm{a}} = \left(1 - \frac{a_{\mathrm{eff}}}{25h_{\mathrm{t}}}\right) \qquad \textit{Eq 3-31}$$

With $K_{\mathrm{a}} = 1$ when $a_{\mathrm{eff}} \leq 5h_{\mathrm{t}}$.

The Vierendeel bending capacity of the Tee sections is verified against the Vierendeel bending moment demand induced by the applied loading as given by Eq 3- 32.

$$2M_{\mathrm{NV,bT,Rd}} + 2M_{\mathrm{NV,tT,Rd}} + K_{\mathrm{a}}M_{\mathrm{Vc,Rd}} \geq V_{\mathrm{Ed}}a_{\mathrm{eq}} \qquad \textit{Eq 3- 32}$$

where:

$M_{\mathrm{NV,b,Rd}}$ is the bending resistance of the bottom Tee, reduced for coexisting axial tension and shear.

$M_{\mathrm{NV,t,Rd}}$ is the bending resistance of the top Tee, reduced for coexisting axial compression and shear.

$M_{\mathrm{Vc,Rd}}$ is the local composite Vierendeel bending resistance.

V_{Ed} is the design value of the vertical shear force taken as the value at the lower moment side of the opening.

a_{eq} is the effective length of the opening for Vierendeel bending as shown in **Table 3-*6***.

Table 3-6: Equivalent rectangular opening dimensions of different opening shapes for verification of Vierendeel bending [11]

Shape of opening	Equivalent opening length, a_{eq}	Equivalent opening height, h_{eq}
Rectangular	a_{o}	h_{o}
Circular	$0.45h_{\mathrm{o}}$	$0.9h_{\mathrm{o}}$
Elongated	a_{o}-$0.55h_{\mathrm{o}}$	$0.9h_{\mathrm{o}}$
Hexagonal	b_{o}+$0.25h_{\mathrm{o}}$	h_{o}
Sinusoidal	For $h_{\mathrm{o}} \leq 2b_{\mathrm{s}}$: $a_{\mathrm{eq}}=b_{\mathrm{o}}+2b_{\mathrm{s}}-0.5h_{\mathrm{o}}$	h_{o}
	For $h_{\mathrm{o}}>2b_{\mathrm{s}}$: $a_{\mathrm{eq}}=b_{\mathrm{o}}+b_{\mathrm{s}}$	h_{o}

3.8.3. Elastic bending resistance of Tees

The elastic bending resistance of the top or bottom Tee sections in the absence of axial force and given by Eq 3-33.

$$M_{\mathrm{T,el,Rd}} = \frac{A_{\mathrm{w,T}}\, f_{\mathrm{y,red}}(0.5h_{\mathrm{w,T}} + t_{\mathrm{f}} - Z_{\mathrm{el}})^2 + A_{\mathrm{f}}\, f_{\mathrm{y,red}}\, (Z_{\mathrm{el}} - 0.5t_{\mathrm{f}})^2}{h_{\mathrm{w,T}} + t_{\mathrm{f}} - Z_{\mathrm{el}}} \qquad \textit{Eq 3-33}$$

Where Z_{el} is the distance from the centroid of the Tee to the extreme fibre of the flange given by Eq 3-34.

$$Z_{\mathrm{el}} = \frac{A_{\mathrm{w,T}}\left(0.5h_{\mathrm{w,T}} + t_{\mathrm{f}}\right) + 0.5t_{\mathrm{f}}\, A_{\mathrm{f}}}{(A_{\mathrm{f}} + A_{\mathrm{w,T}})} \qquad \textit{Eq 3-34}$$

For class 3 and 4 sections, the elastic bending resistance in the presence of an axial force is reduced linearly in proportion to the ratio of the applied normal force to the axial resistance of the cross-section as given by Eq 3-35.

$$M_{\mathrm{NV,T,Rd}} = M_{\mathrm{T,el,Rd}}\left(1 - \left(\frac{N_{m,\mathrm{Ed}}}{N_{\mathrm{T,el,Rd}}}\right)\right) \qquad \textit{Eq 3-35}$$

where:

$M_{\mathrm{NV,T,Rd}}$ is the bending resistance of the Tee section reduced to take into account the interaction with axial force and shear force

$M_{\mathrm{T,el,Rd}}$ is the elastic bending resistance of the Tee section including the reduced yield

$N_{\mathrm{T,el,Rd}}$ is the compression elastic resistance of the Tee including the reduced yield strength

$N_{\mathrm{m,Ed}}$ is the design value of the axial compression or tension force in the Tee due to the global bending action

3.8.4. Shear resistance of perforated steel section

The shear resistance at the opening location is coming from the contribution of the concrete slab in addition to both the top and bottom Tee sections as in Figure 3-8.

$$V_{\mathrm{Rd}} = V_{\mathrm{c,Rd}} + V_{\mathrm{a,Rd}} \qquad \textit{Eq 3-36}$$

$$V_{\mathrm{a,Rd}} = V_{\mathrm{t,Rd}} + V_{\mathrm{b,Rd}} \qquad \textit{Eq 3-37}$$

where:

V_{Rd} is the shear resistance of the perforated composite section given by Eq 3-36

$V_{\mathrm{a,Rd}}$ is the shear force carried by the perforated steel section and given by Eq 3-37

$V_{\mathrm{c,Rd}}$ is the design resistance of reinforced concrete slab

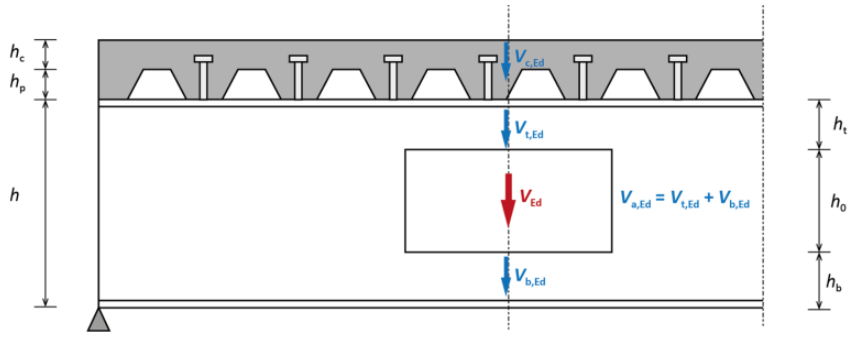


Figure 3-8: Shear forces at an opening [12]

Both the top and bottom Tee sections are capable of attaining their full plastic shear resistance, provided that their web slenderness satisfies the prescribed limiting ratios, with the plastic shear resistance of the solid section expressed by Eq 3-38.

$$V_{\mathrm{pl,Rd}} = \frac{A_{\mathrm{v}}\, f_{\mathrm{y}}/\sqrt{3}}{\Upsilon_{\mathrm{M_0}}} \qquad \textit{Eq 3-38}$$

where:

$V_{\mathrm{pl,Rd}}$ is the plastic shear resistance of the top Tee $V_{\mathrm{t,Rd}}$ and bottom Tee $V_{\mathrm{b,Rd}}$ respecively.

A_{v} is the shear area and calculated as in Eq 3-39.

$$A_{\mathrm{v}} = (A - b_{\mathrm{f}}t_{\mathrm{f}} + (2r + t_{\mathrm{w}}) \times 0.5t_{\mathrm{f}} \qquad \textit{Eq 3-39}$$

where:

A is the cross-sectional area of the steel section

b_{f} is the overall width of the Tee

t_{w} is the web thickness of the Tee

t_{f} is the flange thickness of the Tee

r is the root radius of the Tee

while the plastic shear resistance of the perforated section is given by Eq 3-40.

$$V_{\mathrm{pl,Rd}} = \frac{(A_{t,\mathrm{bT}} + A_{v,\mathrm{bT}})f_{\mathrm{y}}/\sqrt{3}}{\Upsilon_{\mathrm{M_0}}} \qquad \textit{Eq 3-40}$$

Where $A_{\mathrm{t,bT}}$ and $A_{\mathrm{v,bT}}$ are the shear areas of the top and bottom Tees.

The shear resistance is verified by ensuring that the plastic shear resistance $V_{\mathrm{pl,Rd}}$ is greater than or equal to the design shear force demand $V_{\mathrm{a,Ed}}$ expressed as in Eq 3-41.

$$V_{\mathrm{a,Ed}} \leq V_{\mathrm{Pl,Rd}} \qquad \textit{Eq 3-41}$$

The design shear resistance of the concrete slab is given by Eq 3-42 assuming the effective slab width is equal to the beam flange width plus twice the effective depth of the concrete slab.

$$V_{c,Rd} = C_{Rd,c}K(100\rho_1 f_{ck})^{1/3} + K_1\sigma_{cp})b_w d \nless (v_{min} + K_1\sigma_{cp})b_w d \quad \textit{Eq 3-42}$$

where:

$$C_{Rd,c} = \frac{0.18}{\Upsilon_c}$$

$$K = 1 + \sqrt{\frac{200}{d}} < 2.0 \text{ with } d \text{ in mm}$$

$$\rho_1 = \frac{A_{sl}}{b_w d} < 0.02$$

And A_{sl} is the area of tensile reinforcement for crack control mesh.

The normal stress (σ_{cp}) will be coming from the component of the bending moment as in Eq 3-43 and can be neglected for openings near the support.

$$\sigma_{cp} = \frac{N_{c,Ed}}{A_c} < 0.2 f_{cd} \quad \textit{Eq 3-43}$$

Where A_c is the area of the concrete and given by Eq 3-44.

$$A_c = b_{eff}\, h_c \quad \textit{Eq 3-44}$$

Where b_{eff} is the effective width of the concrete flange for shear and given by Eq 3-45.

$$b_{eff} = b_f + h_{s,eff} \quad \textit{Eq 3-45}$$

with $v_{min} = 0.035k^{3/2}f_{ck}^{1/2}$

The shear force acting on the concrete slab due to the applied loading is expressed by Eq 3-46

$$V_{c,Ed} = \frac{n_{sc,o}\, P_{Rd}\, (h_s - 0.5Z_c)}{a_o} \quad \textit{Eq 3-46}$$

where:

$n_{sc,o}$ is the number of shear connectors placed over the opening

P_{Rd} is the design resistance of shear connectors used with profiled sheeting

h_s is the overall depth of the slab.

a_o is the overall length of an opening

The shear force carried by the perforated steel section is given by Eq 3-47:

$$V_{a,Ed} = V_{Ed} - V_{c,Ed} \quad \textit{Eq 3-47}$$

The shear force carried by each Tee is determined by assuming that the total shear force is distributed between the top and bottom Tees in proportion to their respective plastic shear resistances. Given that both Tee sections share the same yield stress, the distribution simplifies to a ratio based on their respective cross-sectional areas as given by Eq 3-48 and Eq 3-49.

$$V_{\mathrm{t,Ed}} = V_{\mathrm{a,Ed}} \frac{A_{\mathrm{v,tT}}}{A_{\mathrm{v,tT}} + A_{\mathrm{v,bT}}} \qquad \textit{Eq 3-48}$$

$$V_{\mathrm{b,Ed}} = V_{\mathrm{a,Ed}} - V_{\mathrm{t,Ed}} \qquad \textit{Eq 3-49}$$

3.8.5. Design bending resistance of beams with stiffened openings

For the plastic Vierendeel bending resistance of stiffened opening, it follows the same form as that of the unstiffened case in Eq 3-28, with the addition of a supplementary term accounting for the contribution of the stiffener as in Eq 3-50.

$$M_{\mathrm{T,pl,Rd}} = \frac{A_{\mathrm{w,T}}\, f_{\mathrm{y,red}}}{\gamma_{\mathrm{M_o}}}\left(\frac{h_{\mathrm{wt}}}{2} + t_{\mathrm{f}} - Z_{\mathrm{pl}}\right) + \frac{A_{\mathrm{f}}\, f_{\mathrm{y,red}}}{\gamma_{\mathrm{M_o}}}\left(0.5t_{\mathrm{f}} - Z_{\mathrm{pl}} + \frac{Z_{\mathrm{pl}}^2}{t_{\mathrm{f}}}\right) + \frac{A_{\mathrm{r}}\, f_{\mathrm{y,red}}}{\gamma_{\mathrm{M_o}}}\left(t_{\mathrm{f}} + h_{\mathrm{w,T}} - e_{\mathrm{r}} - Z_{\mathrm{pl}}\right) \qquad \textit{Eq 3-50}$$

where:

Z_{pl} is the distance between the plastic neutral axis and the extreme fibre of the steel flange and given by

$$Z_{\mathrm{pl}} = (A_f + A_{w,T} + A_r)/(2b_f)\ for\ A_{\mathrm{r}} \le A_{\mathrm{f}} - A_{\mathrm{w,T}}$$

$A_{\mathrm{w,T}}$ is the cross-sectional area of web of the Tee $= h_{\mathrm{w,T}}\, t_{\mathrm{w,eff}}$

A_{f} is the cross-sectional area of the flange

b_{f} is the breadth of the flange

$h_{\mathrm{w,T}}$ is the depth of the web of the Tee excluding the flange

t_{f} is the thickness of the flange

A_{r} is the cross-sectional area of the horizontal stiffeners

e_{r} is the offset distance of centre of stiffener from tip of web

3.8.6. Elastic bending resistance of Tees

In the event that any element of the cross-section is classified as Class 4, the equivalent Class 3 dimensions will be taken, and the elastic bending resistance of the Tee section will be determined by Eq 3-51.

$$M_{\mathrm{T,el,Rd}} = \frac{A_{\mathrm{w,T}}\, f_{\mathrm{y,red}}\, (0.5h_{\mathrm{w,T}} + t_{\mathrm{f}} - Z_{\mathrm{el}})^2 + A_{\mathrm{f}}\, f_{\mathrm{y,red}}\, (Z_{\mathrm{el}} - 0.5t_{\mathrm{f}})^2 + A_{\mathrm{r}}\, f_{\mathrm{y,red}}\, (h_{\mathrm{w,T}} - e_{\mathrm{r}} + t_{\mathrm{f}} - Z_{\mathrm{el}})^2}{(h_{\mathrm{w,T}} + t_{\mathrm{f}} - Z_{\mathrm{el}})/\Upsilon_{\mathrm{M_o}}} \quad \textit{Eq 3-51}$$

Where Z_{el} is the distance between the elastic neutral axis and the extreme fibre of the steel flange given by Eq 3-52.

$$Z_{\mathrm{el}} = \frac{A_{\mathrm{w,T}}\left(0.5h_{\mathrm{w,T}} + t_{\mathrm{f}}\right) + 0.5t_{\mathrm{f}}\, A_{\mathrm{f}} + A_{\mathrm{r}}(h_{\mathrm{w,T}} - e_{\mathrm{r}} + t_{\mathrm{f}})}{(A_{\mathrm{f}} + A_{\mathrm{w,T}})} \quad \textit{Eq 3-52}$$

To account for the effect of the axial force, the elastic bending resistance is reduced linearly in proportion to the ratio of the applied normal force to the axial resistance of the cross-section as in Eq 3-53.

$$M_{NV,\mathrm{T,Rd}} = M_{T,el,\mathrm{Rd}}\left(1 - N_{\mathrm{m,Ed}}/N_{\mathrm{T,el,Rd}}\right) \quad \textit{Eq 3-53}$$

To account for the shear, the expressions for reducing the yield strength is used.

For long openings, the increased flexibility of the beam introduced by the greater opening length results in a reduction of the local Vierendeel bending resistance due to the composite action, quantified by the flexibility reduction factor K_a, expressed in Eq 3-54.

$$K_{\mathrm{a}} = (1 - \frac{a_{\mathrm{eff}}}{35h_{\mathrm{t}}}) \quad \textit{Eq 3-54}$$

where:

h_{t} is the depth of the top Tee.

K_{a} is taken as 1 for $l_{\mathrm{a}} \leq 5h_{\mathrm{t}}$ for stiffener openings.

3.9. Serviceability limit states

The serviceability limits involved in the design of composite beams encompass both the deflection and vibration checks, however only deflection is considered in this study. For the purposes of deflection calculations, the effective flexural stiffness of the beam must be reduced to account for the loss of stiffness arising from the presence of the web openings, encompassing both the Vierendeel bending deformation of the Tee sections and the flexibility of the web posts. The total deflection is determined by first calculating the deflection of the equivalent solid-webbed composite beam, to which additional deflection components attributable to bending and shear deformations at the opening locations are subsequently superimposed.

For simply supported beams subjected to uniformly distributed loading, the additional deflection coming from bending and Vierendeel bending deformations at the opening locations is expressed as in Eq 3-56 to Eq 3-57.

$$\frac{W_{add}}{W_{\mathrm{b}}} = r_{\mathrm{w1}} + r_{\mathrm{w2}} \ \ for\ x_{\mathrm{o}} \leq 0.5L \qquad \textit{Eq 3-55}$$

$$r_{\mathrm{w1}} = 19.2(1 - \frac{x_{\mathrm{o}}}{L})(\frac{x_{\mathrm{o}}}{L})^2 \frac{a_{\mathrm{eff}}}{L} (\frac{I_{\mathrm{comp}} - I_{\mathrm{comp,eff}}}{I_{\mathrm{comp,eff}}}) \qquad \textit{Eq 3-56}$$

$$r_{\mathrm{w2}} = 1.6(\frac{I_{\mathrm{comp}}}{I_{\mathrm{bT}} + I_{\mathrm{T,comp}}})(1 - \frac{2x_{\mathrm{o}}}{L})(\frac{a_{\mathrm{eff}}}{h})^2(\frac{h}{L})^2 \qquad \textit{Eq 3-57}$$

where:

W_{add} is the additional mid span deflection of the beam due to the openings.

W_{b} is the pure bending deflection of the composite beam calculated using Icomp

I_{comp} is the second moment of area of the equivalent composite beam with a solid web.

$I_{\mathrm{comp,eff}}$ is the second moment of area of the composite beam at the centre of the opening.

I_{bT} is the second moment of area of the top Tee

$I_{\mathrm{T,comp}}$ is the second moment of area of the composite top Tee

a_{eff} is the effective opening length

Furthermore, SCI P355 [10] employs approximate analytical expressions Eq 3-58 and Eq 3-59 derived from empirical formulations for the deflection calculations, which have been demonstrated to yield results in close agreement with more rigorous deflection calculations. This formulation accounts for both the pure bending deflection arising from the reduced stiffness at the opening and the significant shear contribution, the latter being represented by the term $(1 - x/L)$, where x denotes the distance from the nearer support to the centreline of the opening.

For the case of a single web opening.

$$\frac{W_{\mathrm{add}}}{W_{\mathrm{b}}} = K_o \left(\frac{l_{\mathrm{o}}}{l}\right)\left(\frac{h_{\mathrm{o}}}{h}\right)\left(1 - \frac{x}{L}\right)\ for\ x \leq 0.5L \qquad \textit{Eq 3-58}$$

$$\frac{W_{\mathrm{add}}}{W_{\mathrm{b}}} = \mathrm{K_o}\left(\frac{l_{\mathrm{o}}}{L}\right)\left(\frac{h_{\mathrm{o}}}{h}\right)\left(\frac{x}{L}\right)\ for\ x > 0.5L \qquad \textit{Eq 3-59}$$

where the coefficient K_o is taken as:

$K_o = 1$	For longitudinally stiffened openings
$K_o = 1.5$	For unstiffened openings

l_o is the effective length of the opening

W_b is the bending deflection of unperforated composite beam

3.10. Estimating the strength of the CFRP plates

Having established the strength of beams strengthened with steel stiffeners, attention now turns to the alternative approach, which employs fibre-reinforced polymer (FRP) plates as a means of addressing insufficient Vierendeel bending resistance. In contrast to conventional steel strengthening techniques, the FRP member bonded to the bottom Tee is subjected to tension, whereas that bonded to the top Tee experiences compression.

3.10.1. Axial tension

To ensure that the CFRP plate possesses adequate tensile capacity, the tensile capacity is calculated in accordance with Eq 3-61 and the tensile force demand is subsequently verified against the tensile capacity in accordance with Eq 3-60.

$$N_{t,Ed} \leq N_{t,Rd} \qquad \textit{Eq 3-60}$$

$$N_{t,Rd} = \frac{\eta_c}{\Upsilon_m . \Upsilon_{Rd}} A . f_{x,t,k} \qquad \textit{Eq 3-61}$$

where:

$N_{t,Rd}$ is the design value of the tensile resistance of the cross section in the longitudinal (x) direction.

γ_m is a partial factor for the material accounting for the unfavorable deviations of the representative material form its characteristic values.

γ_{Rd} is a partial factor accounting for the uncertainty in the resistance model, and for geometrical deviations, if they are not modelled explicitly.

η_c is a factor accounting for the changes of material properties due to material temperatures in service conditions relative to the material properties at $20°C$, excluding the effects of long-term exposure.

$f_{x,t,k}$ is the characteristic value of the tensile strength in the longitudinal (x) direction of the material.

A is the gross area of the cross section

3.10.2. Axial compression

To make sure that the FRP plate has sufficient compressive force capacity, the compressive capacity is calculated in accordance with Eq 3-63 and the compressive force demand is subsequently verified against the compressive capacity in accordance with Eq 3-62.

$$N_{\mathrm{c,Ed}} \leq N_{\mathrm{c,Rd}} \qquad \textit{Eq 3-62}$$

$$N_{\mathrm{c,Rd}} = \frac{\eta_{\mathrm{c}}}{\Upsilon_{\mathrm{m}}.\Upsilon_{\mathrm{Rd}}} A.f_{\mathrm{x,c,k}} \qquad \textit{Eq 3-63}$$

where:

$N_{\mathrm{c,Rd}}$ is the design value of the compression resistance of the cross section in the longitudinal (x) direction.

$f_{\mathrm{x,c,k}}$ is the characteristic value of the compressive strength in the longitudinal (x) direction of the material.

3.11. Estimating the strength of the CFRP strengthened beam

3.11.1. Debonding load

Following the calculation of the CFRP against the relevant strength limit states, the debonding resistance of the CFRP element is evaluated using Eq 3-64 developed for concrete-to-CFRP interfaces, which has been demonstrated to provide accurate predictions of the end debonding load in steel-to-CFRP applications as per the findings of [53].

$$P_{\mathrm{u}} = b_{\mathrm{p}}\sqrt{2E_{\mathrm{p}}t_{\mathrm{p}}G_{\mathrm{f}}} \qquad \textit{Eq 3-64}$$

where:

b_p is the plate width

t_{p} is the thickness of the CFRP plate

E_{p} is the elastic modulus of the CFRP plate in the longitudinal (X) direction

G_{f} is the interfacial fracture energy

Two configurations for bonding carbon fibre-reinforced polymer (CFRP) to the steel surface are examined in this study. In the first configuration, the opening is located at mid-span, where flexural behaviour governs the failure mode; accordingly, the CFRP plate is attached to the flange of the top and bottom Tee. In the second configuration, the opening is positioned near the support, where the Vierendeel bending mechanism predominates, and the CFRP plate is

therefore bonded to the web on both sides of the top and bottom Tee. The load-carrying capacity is assessed for both configurations, with the CFRP applied either to the web or to the flanges, as depicted in Figure 3-9. To simplify the calculations and exploit symmetry in the flange-attached CFRP configuration, the CFRP was assumed to be bonded to the inside surfaces of both the top and bottom flanges, rather than to the inside surface of the top flange and the outer surface of the bottom flange as represented in the numerical models in Chapter 5.

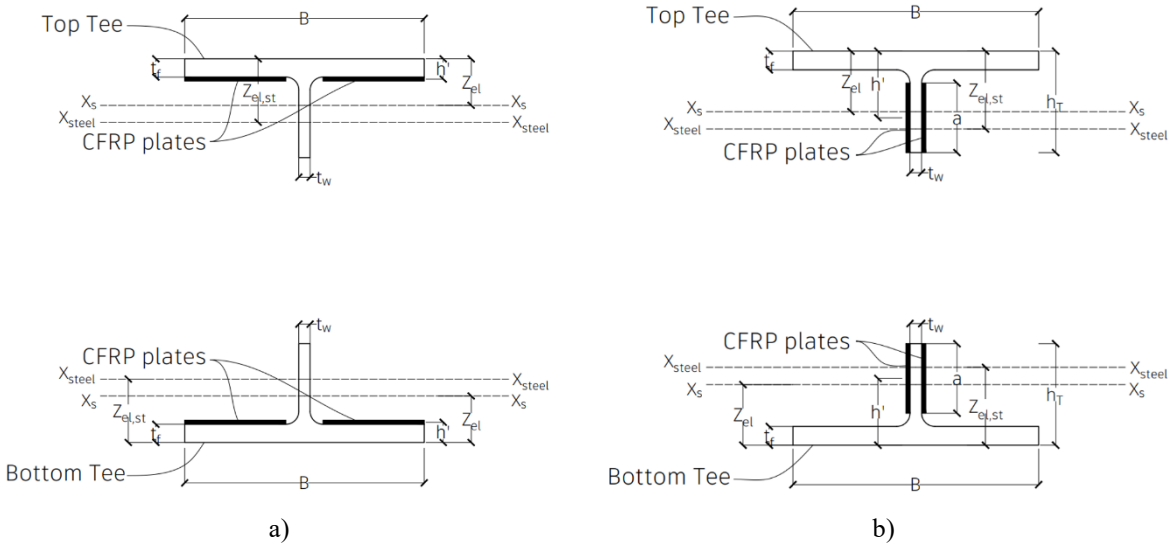


Figure 3-9: Dimensions of the Tee sections at the opening location; a) CFRP attached to the flange; b) CFRP attached to the web

The primary objective of the analytical procedure is to determine the bending moment capacity corresponding to the relevant limit state for the given opening location.

3.11.2. For openings positioned at mid span

To determine the elastic neutral axis of the Tee sections, the first moment of area is calculated with respect to the outer face of the top flange. From the preceding calculations Eq 3-36, the distance from the elastic neutral axis of the top section to the outer face of the top flange, denoted here as $Z_{el,st}$, is calculated. Subsequently, to obtain the new elastic neutral axis Z_{el} following the addition of CFRP to the section, Eq 3-65 is proposed, which accounts for the difference in the modulus of elasticity between the steel and the CFRP material and uses the modulus of elasticity as a weighing factor.

$$Z_{\mathrm{el}} = \frac{A_{\mathrm{T}} Z_{\mathrm{el,st}} E_{\mathrm{st}} + A_{\mathrm{P}}(h') E_{\mathrm{P}}}{(A_{\mathrm{T}}\, E_{\mathrm{st}} + A_{\mathrm{P}}\, E_{\mathrm{P}})} \qquad \textit{Eq 3-65}$$

where:

Z_{el} denotes the distance from the centroid of the Tee section, with the CFRP included, to the extreme fibre of the flange

$.A_{\mathrm{T}}$ is the area of the Tee section

A_{P} is the area of the CFRP plate

E_{st} is the modulus of elasticity of the steel

h' is the distance from the centroid of the CFRP plate to the outer face of the top flange and calculated in Eq 3-66 and Eq 3-67.

For CFRP attached to the flange $h' = t_{\mathrm{f}} + 0.5\, t_{\mathrm{CFRP}}$ *Eq 3-66*

For CFRP attached to the web $h' = h_{\mathrm{T}} - 0.5\, a$ *Eq 3-67*

The axial capacity of the Tee section with the addition of the CFRP plates can be determined using, which incorporates the contributions of both the steel and the CFRP, with the latter considered to carry load only up to the debonding load.

$$N_{\mathrm{bT,Rd,CFRP}} = N_{\mathrm{bT,Rd}} + P_{\mathrm{u}} \qquad \textit{Eq 3-68}$$

where:

$N_{\mathrm{bT,Rd}}$ is the tensile capacity of the bottom Tee section

P_{u} is the load at which debonding of the CFRP plate is expected to occur.

Subsequently, the maximum bending capacity of the section at the centre of the opening is determined as per Eq 3-69.

$$M_{o,\mathrm{Rd}} = N_{\mathrm{bT,Rd,CFRP}} \times h_{\mathrm{eff}} \qquad \textit{Eq 3-69}$$

where:

h_{eff} is the distance between the centroids of the top Tee and bottom Tee Sections which is calculated as in Eq 3-70

$$h_{\mathrm{eff}} = h - 2\, Z_{\mathrm{el}} \qquad \textit{Eq 3-70}$$

Having calculated the moment ($M_{\mathrm{O,Rd}}$), the total applied load on the beam for the case of a uniformly distributed load can be obtained using Eq 3-71, irrespective of the opening shape.

$$P_{\mathrm{Total}} = \frac{8M_{\mathrm{o,Rd}}}{L} \qquad \textit{Eq 3-71}$$

3.11.3. For openings positioned near the support

Two distinct cases are considered in the analysis. The first corresponds to the load at which debonding of the CFRP from the steel surface occurs due to the Vierendeel mechanism formation. The second represents the condition in which the CFRP successfully prevents Vierendeel failure, and ultimate failure occurs instead through the formation of a plastic hinge at midspan of the beam. The lesser of the two loads will be taken as the failure load.

3.11.4. Vierendeel bending failure

The proposed expression for the plastic Vierendeel bending resistance of the CFRP stiffened opening follows the same form as that developed for the steel-stiffened case Eq 3-50,with the steel stiffener term replaced by the debonding load. In calculating the plastic neutral axis using Eq 3-72, the maximum stress is employed as a weighting factor for each contributing term: for the steel component, the yield stress is used, while for the CFRP, the maximum stress is taken as the product of the modulus of elasticity and the strain at failure.

$$M_{\mathrm{T,pl,Rd}} = \frac{A_{\mathrm{w,T}}\, f_{\mathrm{y,red}}}{\Upsilon_{\mathrm{M_o}}}\left(\frac{h_{\mathrm{wt}}}{2} + t_{\mathrm{f}} - Z_{\mathrm{pl}}\right) + \frac{A_{\mathrm{f}}\, f_{\mathrm{y,red}}}{\Upsilon_{\mathrm{M_o}}}\left(0.5t_{\mathrm{f}} - Z_{\mathrm{pl}} + \frac{Z_{\mathrm{pl}}^2}{t_{\mathrm{f}}}\right) + P_{\mathrm{u}}\,(Z_{\mathrm{el}} - h') \qquad \textit{Eq 3-72}$$

where:

P_{u} is the load at which debonding is expected to occur

Z_{el} is the distance from the elastic neutral axis of the steel section with the CFRP plate measured from the outer flange.

Z_{pl} is the plastic neutral axis distance of the steel section with the CFRP plate measured form the outer flange and calculated as in Eq 3-73.

$$Z_{\mathrm{pl}} = \frac{\left(A_{\mathrm{f}} \times f_{\mathrm{y}} + A_{\mathrm{w,T}} \times f_{\mathrm{y,red}} + A_{\mathrm{P}} \times E_{\mathrm{P}} \times \varepsilon_{\mathrm{CFRP}}\right)}{2b_{\mathrm{f}} \times f_{\mathrm{y,red}}} \qquad \textit{Eq 3-73}$$

To determine the shear force at the edge of the opening that leads to the formation of the Vierendeel mechanism, moment equilibrium is established by summing the Vierendeel moments at the four corners of the opening and equating the total to the product of the shear force at the edge and the equivalent length of the opening as in Eq 3-74.

$$2M_{\mathrm{NV,bT,Rd}} + 2M_{\mathrm{NV,tT,Rd}} = V_{\mathrm{Ed}} a_{\mathrm{eq}} \qquad \textit{Eq 3-74}$$

Having determined the shear force at the edge of the opening that induces the formation of the Vierendeel mechanism, the total load required to cause Vierendeel bending can be obtained by establishing equilibrium as seen in Figure 3-10 and calculated per Eq 3-75.

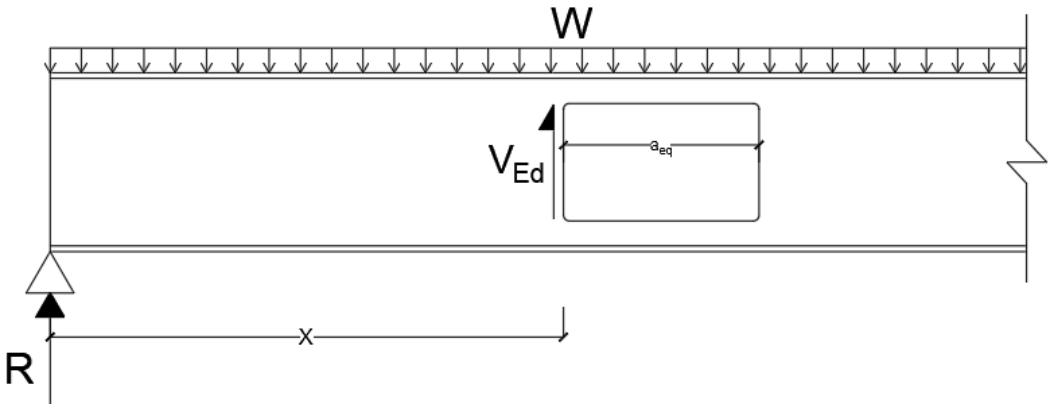


Figure 3-10: Longitudinal section of the beam with the opening

From the applied loading, the shear force at the opening location is expressed as follows:

$$\mathrm{V_{Ed}} = R - WX \qquad \textit{Eq 3-75}$$

where:

W is the value of the uniformly distributed load applied to the beam in kN/m

X is the length of the beam from the support to the nearest edge of the opening

R is the reaction at nearer support and for the case of a uniformly distributed load, the reaction force is given by Eq 3-76.

$$R = 0.5WL \qquad \textit{Eq 3-76}$$

Substituting the value of the reaction into Eq 3-75 yields the shear force as in Eq 3-77 for openings located at quarter the span.

$$\mathrm{V_{Ed}} = \frac{WL}{4} \qquad \textit{Eq 3-77}$$

Thus, the total load required to induce Vierendeel bending at an opening located at the quarter-span of the beam is given by Eq 3-78.

$$P_{\mathrm{Total}} = 2R = 4\,V_{\mathrm{Ed}} \qquad \textit{Eq 3-78}$$

3.11.5. Flexural failure

In the case where the beam fails in flexure at midspan, the cross-section considered is the solid section, which develops the full plastic moment capacity, as illustrated in Figure 3-11.

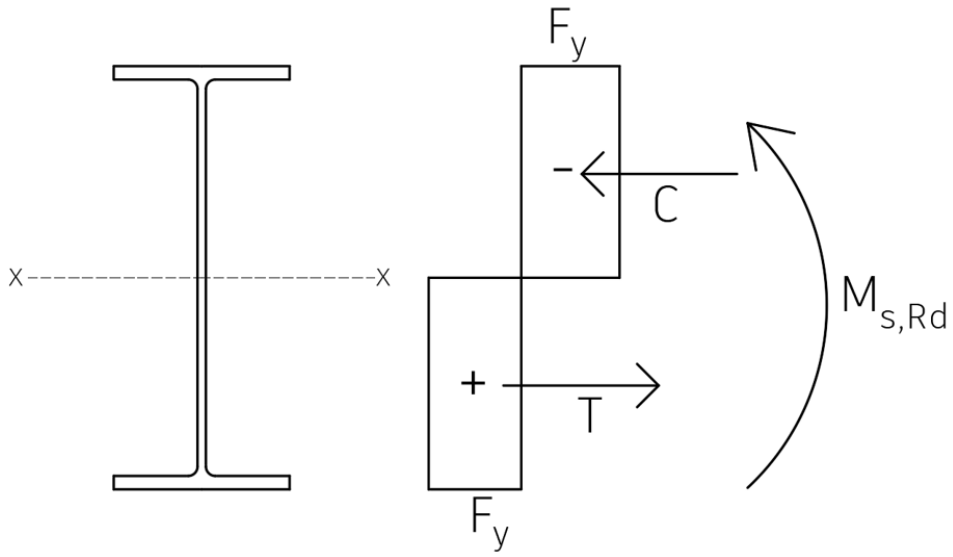


Figure 3-11: Middle cross section with the plastic stress distribution

The plastic moment capacity of the solid section is determined as in

$$M_{\mathrm{s,Rd}} = w \times f_y \qquad \textit{Eq 3-79}$$

where:

w	is the plastic section modulus obtained from the steel tables.
f_y	is the yield strength of the steel

The total load-carrying capacity is obtained by establishing the equilibrium and is expressed by Eq 3-80 for the case of a uniformly distributed load.

$$P_{\mathrm{Total}} = \frac{8M_{s,\mathrm{Rd}}}{L} \qquad \textit{Eq 3-80}$$

4. NUMERICAL MODELLING AND VALIDATION

4.1. Introduction

This chapter presents the finite element modelling framework developed for the numerical investigation of laterally restrained steel beams with large web openings. The analyses are performed using the Abaqus software suite and provide the numerical basis for the parametric study presented in Chapter 5.

The chapter begins with the assessment of the adopted modelling strategy against three experimental studies available in the literature. Two benchmarks concern solid steel beams with different failure mechanisms [39,56], while the third considers a cellular beam with regularly spaced web openings [21]. These comparisons are used to assess the ability of the numerical modelling approach to reproduce the nonlinear response, load-carrying capacity, and relevant instability mechanisms of steel beams.

Subsequently, the numerical model adopted for the parametric investigation is presented. The geometry and material behaviour of the steel beam are defined, followed by the modelling of the CFRP strengthening and the steel–CFRP interface. Both perfect bonding and cohesive-interface formulations are considered to enable the influence of adhesive debonding to be investigated in Chapter 5. The adopted boundary conditions, lateral restraint, loading procedure, finite element discretisation, and mesh sensitivity analysis are also described. The resulting modelling framework is then employed in Chapter 5 to evaluate the influence of opening geometry and location, CFRP configuration, bond behaviour, and adhesive properties on the structural response.

4.2. Finite element modelling and numerical validation

Three experimental benchmarks were reproduced to assess different aspects of the adopted finite element modelling strategy. The finite element analyses presented are performed using the Abaqus software suite. Two of these models involved solid beams, as reported by [39,56], while the third consisted of a cellular beam incorporating web openings [21].

4.2.1. Benchmark 1 – Local buckling

The first model employed for validation is a solid beam, as reported in [56,57] with a cross-section of 127 × 76UB13 and a clear span of 1.1 m as shown in Figure 4-1.

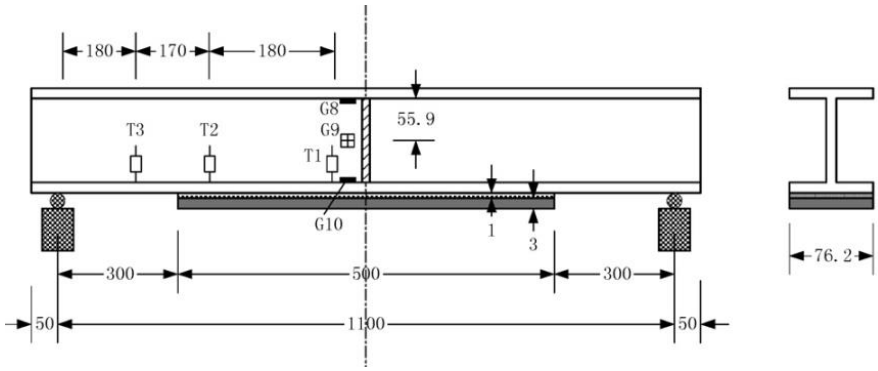


Figure 4-1: Geometry of the beam with the locations for different strain gages [56]

For the steel material, a trilinear elastoplastic model incorporating a yield plateau and linear strain hardening was adopted, as illustrated in Figure 4-2, with a yield stress of 330 MPa and an ultimate strength of 430 MPa.

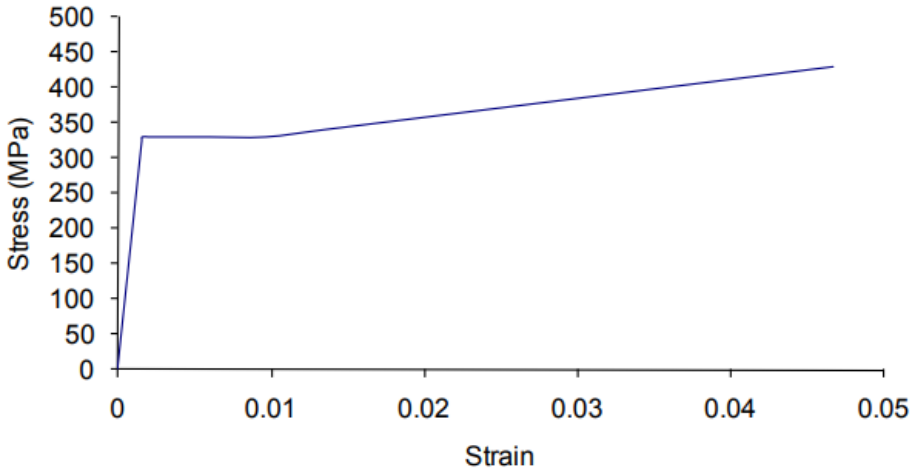


Figure 4-2: Material model for steel [56]

The beam is modelled with simply supported boundary conditions, applied at reference points located at the centroids of the end sections and coupled to the entire cross-section, as shown in Figure 4-3, with vertical displacement restrained at both ends. A three-point loading configuration is adopted, and stiffeners with a thickness of 4 mm are provided at midspan to prevent premature web failure. These stiffeners, modelled as shell extrusions, were connected to the beam using tie constraints. Static Riks analysis is employed to capture both geometric and material nonlinearities, and the model utilizes S4R shell elements with a mesh size of 10 mm.

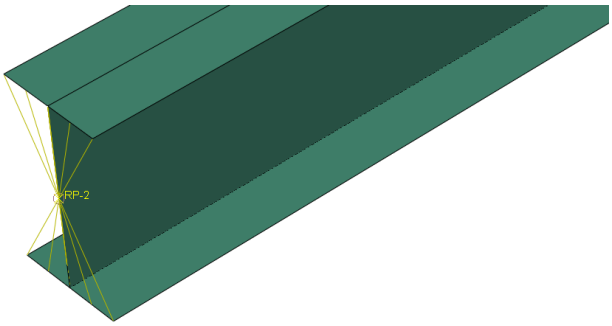


Figure 4-3: Reference point and coupling constraint for support application

Owing to the relatively short span of the beam, lateral torsional buckling does not govern, and initial imperfections were excluded from the analysis; instead, failure is characterized by local buckling of the top flange adjacent to the load application point, consistent with experimental observations, with the corresponding stress distribution presented in Figure 4-4.

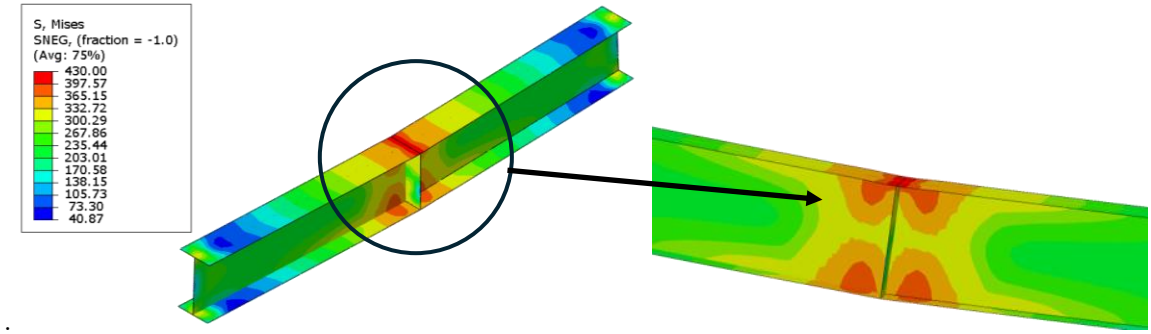


Figure 4-4: Stress distribution of the beam

Figure 4-5 compares the experimental and FE predicted force–displacement responses, revealing good overall agreement in terms of both stiffness and strength. The numerical ultimate load deviates from the experimental value by no more than 2%, confirming the predictive capability of the finite element model.

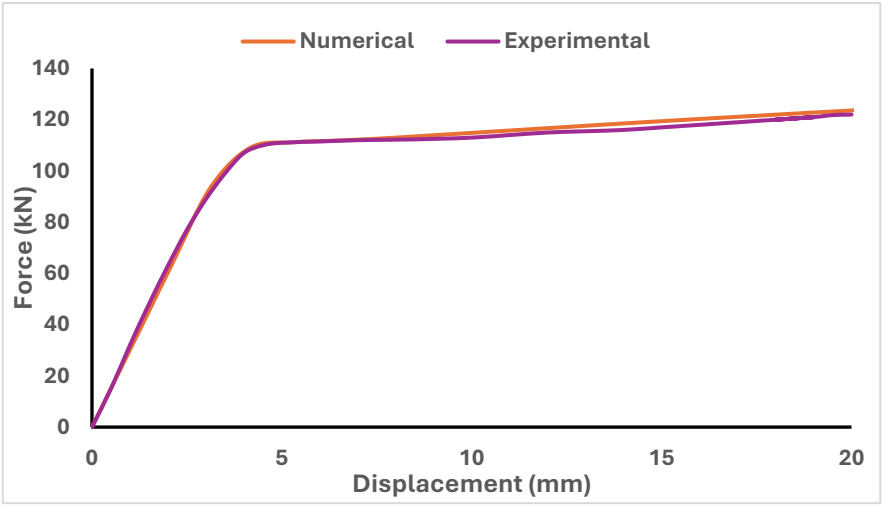


Figure 4-5: Force-displacement response for model 1

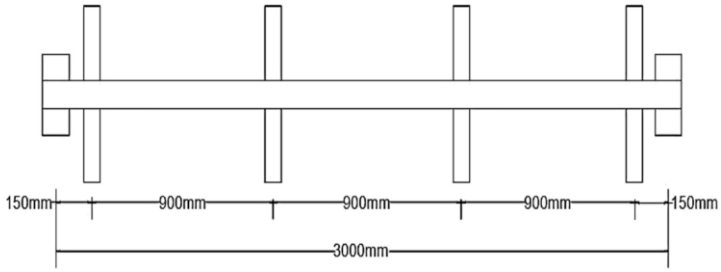
4.2.2. Benchmark 2 – Laterally restrained beams

The second model used for the validation is also a solid beam model from [39]. The beam has 3 m clear span with 305 × 102 × 25 UKBs beam. For the steel material, trilinear elastoplastic model with linear strain hardening idealisation is adopted with the mechanical properties of the steel as given in **Table 4-*1***.

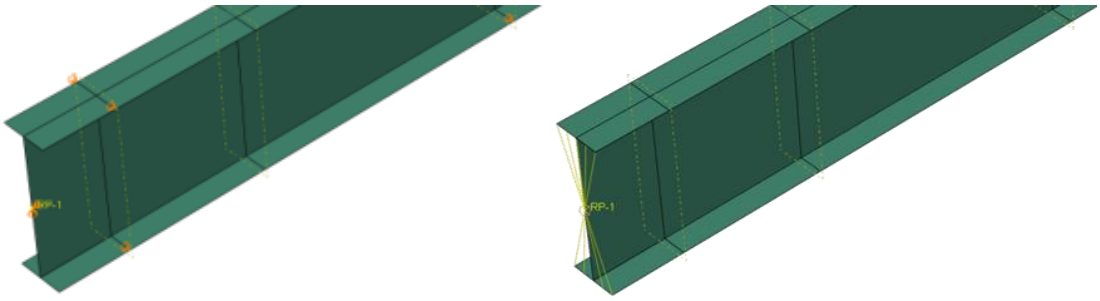
Table 4-1: Material Properties for steel adopted from [39]

	Young's Modulus (GPa)	Yield Stress (MPa)	Ultimate Stress (MPa)
Flange	206	412	566
Web	210	435	569

The beam is modeled with simply supported end conditions, with supports applied at the centroid of each end section through reference points coupled to the entire cross-section. The left support restrains both vertical and longitudinal displacements, whereas the right support prevents only vertical movement. Lateral restraints are applied at four cross-sections, as shown in **Figure 4-*6***.



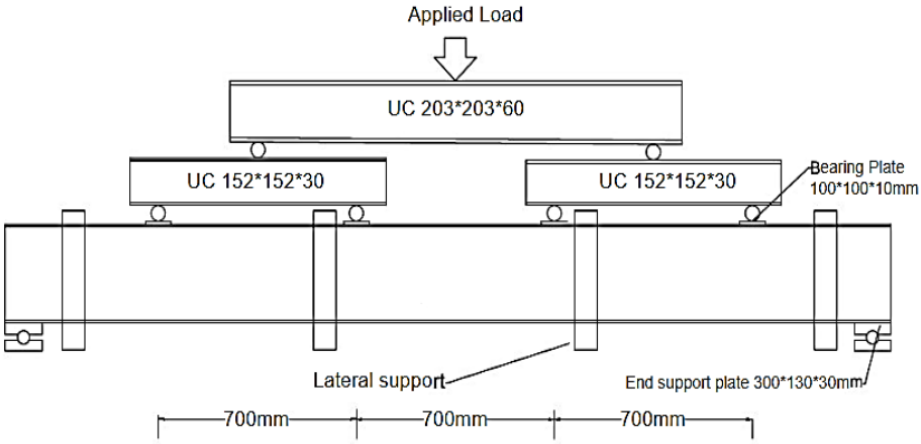
a)



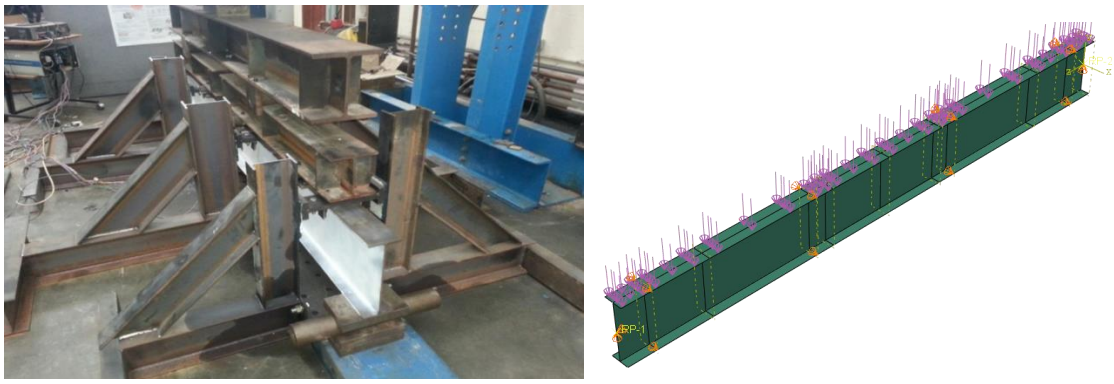
b)

Figure 4-6: Lateral restraint and boundary condition; a) plan view for lateral restraint [39]; b) Reference point with coupling constraint for the support

The load is applied as a pressure on the top surface of the top flange to simulate a uniformly distributed load, as shown in **Figure 4-*7***, and the model employs S4R shell elements with a mesh size of 10 mm.



b)



b)

Figure 4-7: Loading configurations: a) Schematic for loading [39]; b) Tested beam [39] and loading on the model

A linear buckling analysis is conducted to determine the buckling mode shape shown in Figure 4-8 which is subsequently employed as the initial geometric imperfection in the nonlinear analyses. Because the experimental imperfection amplitude was not reported, a sensitivity study was conducted and a magnification factor of 1.25 adopted as the calibration value that best reproduced the measured response.

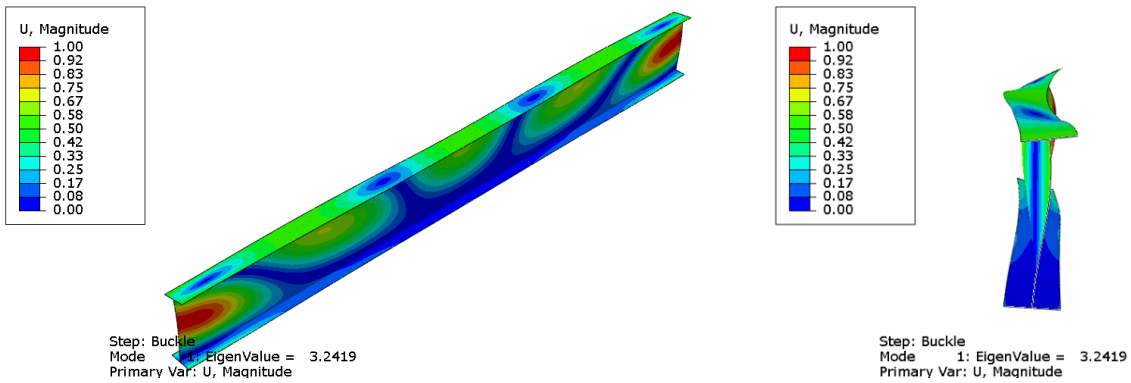


Figure 4-8: First Buckling Mode used as Imperfection

The model is subsequently analysed using the static Riks method, and **Figure 4-*9*** compares the experimental and finite element predicted force–displacement responses. The model exhibits behaviour consistent with the experimental results until reaching a maximum load of 408 kN at a displacement of 27.9 mm, beyond which the beam undergoes excessive lateral buckling in the middle portion compared to the experimental observations. This discrepancy is attributed to the application of lateral restraints at discrete points, whereas in the experimental setup they were distributed over a finite area. With regard to the ultimate load, the deviation between the measured capacity and the numerical prediction is less than 1%. Despite these minor discrepancies, the results confirm the predictive capability of the finite element model.

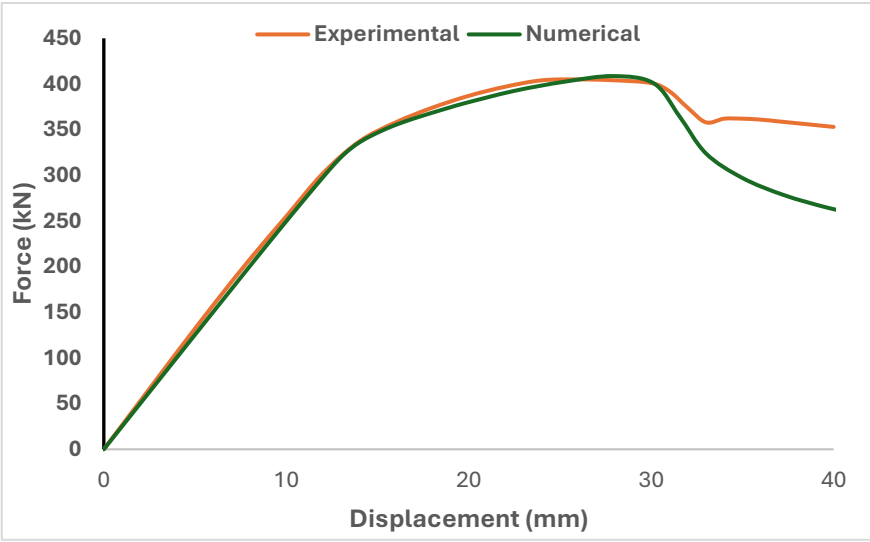
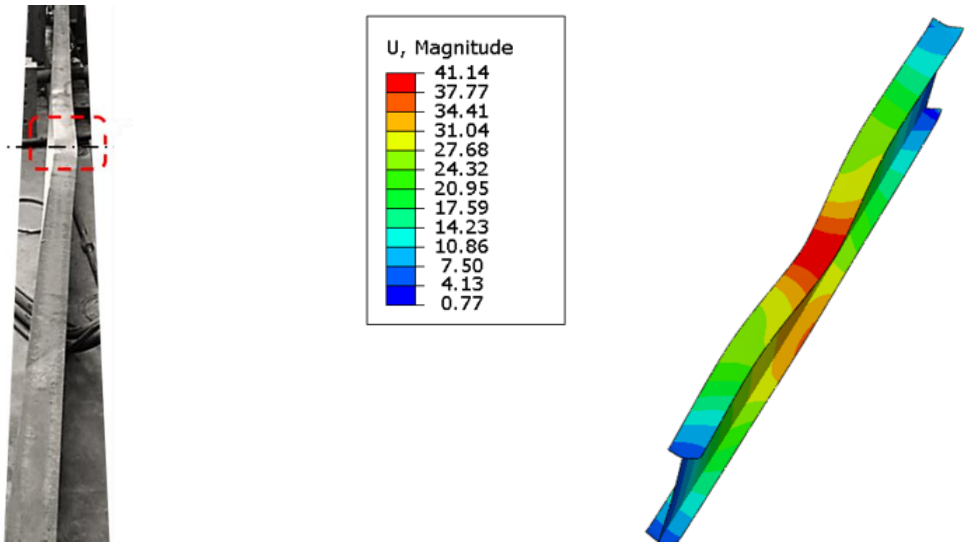


Figure 4-9: Force-displacement response for model 2

The ultimate failure mode was consistent between the numerical and experimental results, characterized by yielding and lateral torsional buckling of the middle portion of the beam, with the numerical model additionally exhibiting some distortion at the end sections, attributable to the simplified boundary conditions adopted in the model (see **Figure 4-*10***)



a) **b)**

Figure 4-10: Failure mode; a) Experiment [39]; b) Numerical model

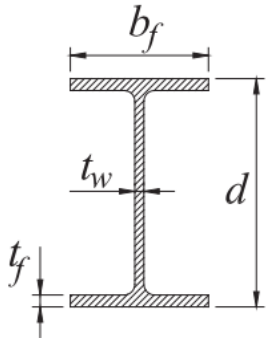
4.2.3. Benchmark 3-Cellular beam

The third model involves the beam with regularly spaced openings, a cellular beam model. **Table 4-*2*** provides a summary of the beam geometry. The model employs C3D10 solid elements with a mesh size of 15 mm. This element is a 10-node quadratic tetrahedron formulation with each element utilising four integration points, selected on account of the geometric complexity introduced by the large web openings. This element type is particularly well-suited to curved boundaries, owing to its midside nodes, and offers the additional advantages of reduced artificial stiffness and enhanced capability in capturing stress concentrations relative to alternative element formulations.

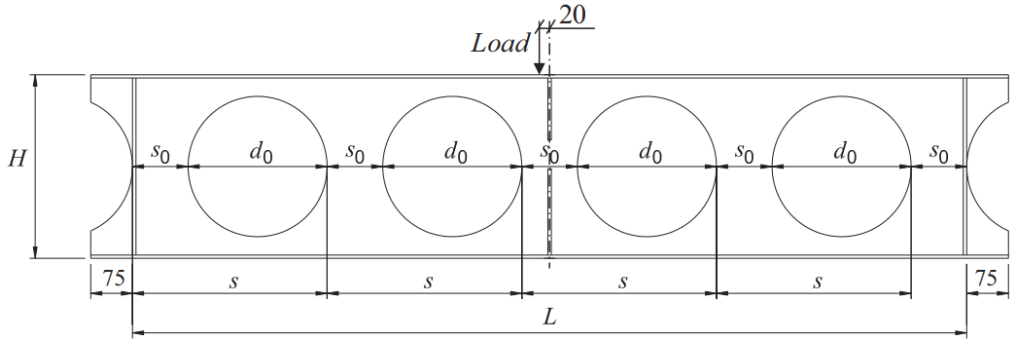
For the steel material, a bilinear elastic-perfectly plastic idealisation is adopted. The mechanical properties assigned to the steel include an elastic modulus of 200 GPa, a Poisson's ratio of 0.3, and a yield strength of 449 MPa.

The beam is modelled with simply supported ends, with vertical and horizontal displacements restrained on the left side and only vertical displacement restrained on the right side. Stiffeners of 5 mm thickness are provided at the supports and midspan to avert premature web failure, and these stiffeners are connected to the beam using tie constraints. The load is offset by 20 mm from the midspan to promote larger web-post buckling on the instrumented side, as adopted in the experimental test, while lateral restraint is applied at the mid-section to suppress lateral torsional buckling and ensure that the desired failure mechanism governs (see **Figure 4-*11***).

Table 4-2: Geometric parameters for the cellular beam adopted from [21]



Dimensions in	t_w	t_f	b_f	d
(mm)	4.7	5.5	104	230



Dimensions in	H	L	d_o	S
(mm)	431	1607	345.3	392.6

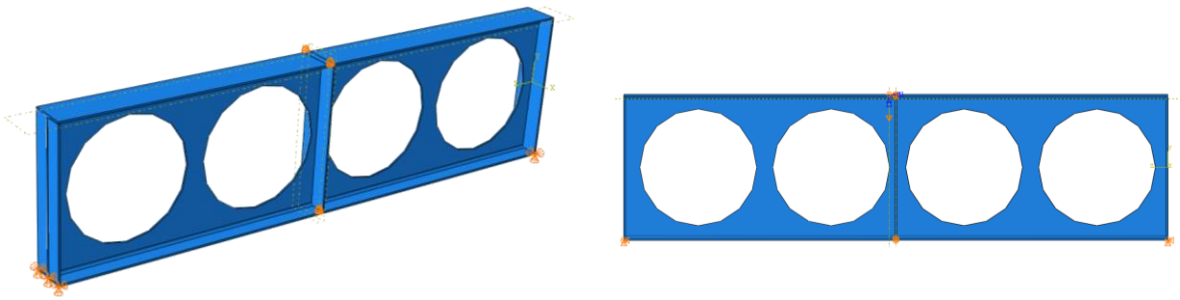


Figure 4-11: Loading, boundary conditions and lateral supports

A linear buckling analysis is first conducted to determine the buckling mode shape, which is subsequently employed as the initial geometric imperfection in the nonlinear analyses. The first buckling mode, depicted in **Figure 4-*12***, is scaled by a factor of 0.2. This scaling approach has been shown to yield satisfactory correlation with experimental observations.

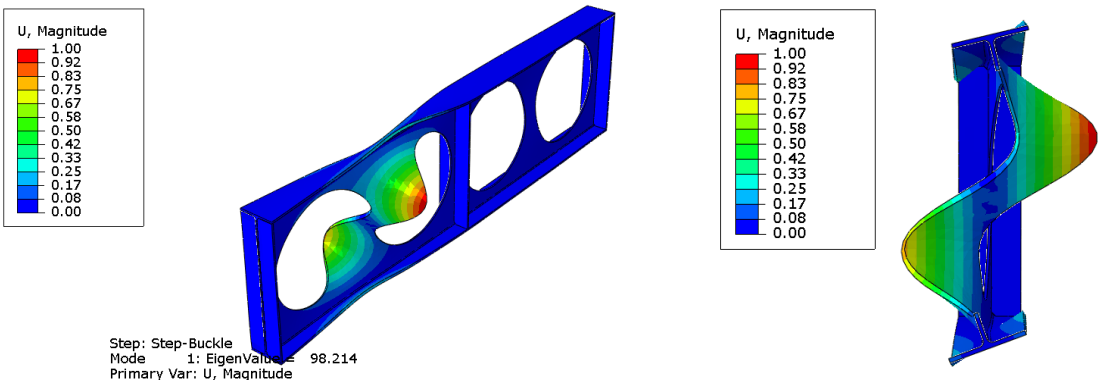


Figure 4-12: Buckling mode

The imperfect model is analysed using the static Riks method, which is ideally suited to capturing the nonlinear material and geometric responses while enabling the tracking of instabilities. **Figure 4-*13*** compares the experimental and FE predicted force-displacement responses, revealing good overall agreement. The deviation between the numerical ultimate load and the measured capacity is less than 4 %, confirming the predictive capability of the finite element model.

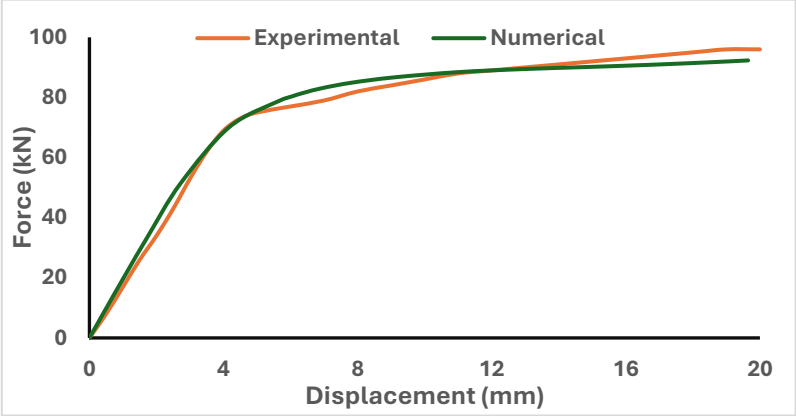
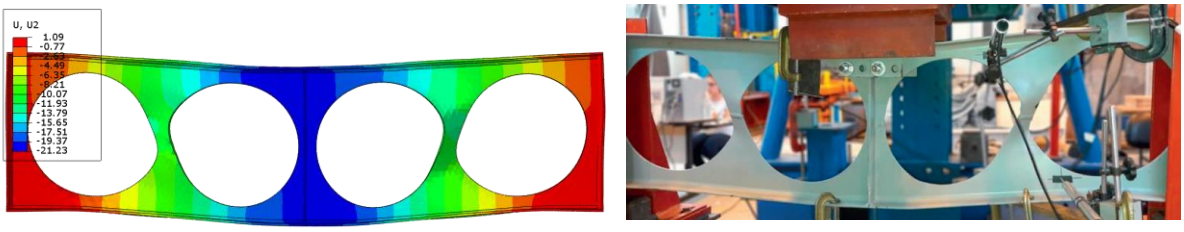


Figure 4-13: Force-displacement response for model 3

A further comparison of the deformed shapes is presented in **Figure 4-*14***, which shows the experimental and numerical deformed configurations, demonstrating agreement in the failure mode characterized by web-post buckling.



a) b)

Figure 4-14: Deformed beam; a) Model vertical displacement; b) Deformed shape from experiment [21]

4.2.4. Summary of Validation

Table 4-*3* summarizes the initial stiffness, ultimate load-carrying capacity, corresponding displacement, and associated failure mode derived from both the numerical and experimental models across all three benchmark cases. It is evident that, for all three benchmarks, the parameters governing structural performance, namely, initial stiffness, ultimate load, and displacement at failure, demonstrate good agreement, with maximum deviations observed for model 3 not exceeding 4% in load-carrying capacity and a maximum deviation in initial stiffness of 10% across all three models. Furthermore, all numerical models exhibited failure modes closely consistent with the experimental observations across the range of failure mechanisms considered.

Table 4-3: Comparison of the capacity for different benchmarks

	Experimental				Numerical			
	Initial stiffness (kN/mm)	Peak force (kN)	Displacement at peak (mm)	Failure mode	Initial stiffness (kN/mm)	Peak force (kN)	Displacement at peak (mm)	Failure mode
Model 1	31.5	122.5	20	Top flange local buckling	30.188	124.28	20.87	Top flange local buckling
Model 2	25.5	405	26	Yielding and L.T.B	24.93	408.63	27.93	Yielding and L.T.B
Model 3	17.2	96	20	Web Post buckling	18.91	92.33	19.64	Web Post buckling

4.3. Numerical model adopted for the parametric study

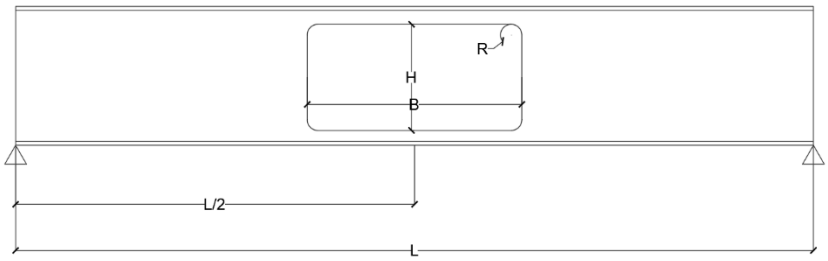
4.3.1. Geometry and steel material

The developed model for the parametric analysis has a 10 m length 457×191×74 UKB beam section. For the sake of computational efficiency, only half of the beam's cross section is modelled using symmetry about the longitudinal vertical plane through the web centerline, as shown in **Figure 4-*15***, with the geometric parameters of the opening being defined as in **Figure 4-*16***.



a) b)

Figure 4-15: Beam model; a) 3D view; b) Cross section view



Dimensions in	H	B	R
(mm)	300	500	15

Figure 4-16: Geometric Parameters of the opening

For the steel material, a bilinear elastic-perfectly plastic idealisation is adopted. The mechanical properties assigned to the steel include an elastic modulus of 200 GPa, a Poisson's ratio of 0.3, and a yield strength of 355 MPa.

4.3.2. CFRP material and strengthening configurations

The CFRP material was modelled as a lamina, a choice dictated by the small thickness of the plate, which measures 3.175 mm in accordance with [23]. Two sets of material properties were assigned: the elastic properties, to define the initial stiffness as per **Table 4-*4***, and the failure stresses as given in **Table 4-*5***, to enable the tracking of any failure that may develop within the CFRP during loading. For simplicity, CFRP failure was assessed based on whether the induced stress levels reached the tensile or compressive failure thresholds.

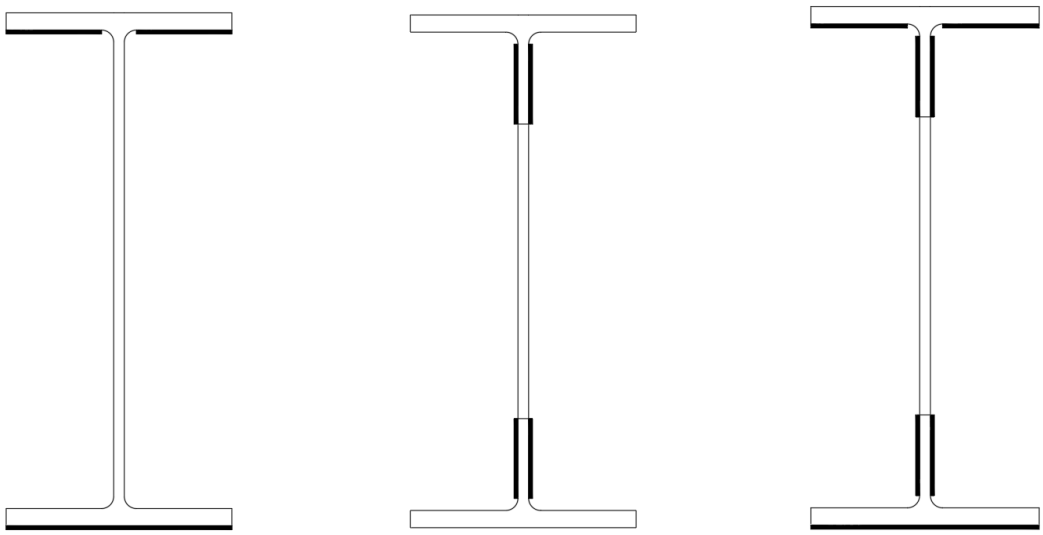
Table 4-4: Engineering properties of the CFRP [23]

E1 (GPa)	E2 (GPa)	υ12	G12 (MPa)	G13 (MPa)	G23 (MPa)
200	12	0.28	5000	5000	4400

The CFRP configuration considered for the analysis include the following CFRP attached to the flanges alone or to the web alone or to the flanges and webs as shown in **Figure 4-*17***.

Table 4-5: Stresses at failure [23]

X_t (MPa)	X_c (MPa)	Y_t (MPa)	Y_c (MPa)	S_{12} (MPa)
2970	1800	60	200	90



a) b) c)

Figure 4-17: Different CFRP configurations: a) To flanges; b) To web; c) To flanges and web

4.3.3. Steel-CFRP interface

The adhesive materials employed to bond the CFRP to the steel surface, comprising both linear and nonlinear types, were represented using a cohesive interface, defined through the interaction property module. The traction–separation response of the interface is governed by three sets of parameters. The first is elastic behaviour, characterized by normal and shear stiffnesses represented by Eq 4-1 [56].

$$\begin{Bmatrix} t_n \\ t_s \\ t_t \end{Bmatrix} = \begin{bmatrix} k_{nn} & 0 & 0 \\ 0 & k_{ss} & 0 \\ 0 & 0 & k_{tt} \end{bmatrix} \begin{Bmatrix} \delta_n \\ \delta_s \\ \delta_t \end{Bmatrix} \qquad \textit{Eq 4-1}$$

where:

k_{nn} is the elastic stiffness of the normal direction

k_{ss}, k_{tt} are the elastic stiffness of the two shear directions

t_{n} is the interfacial normal stress at the interface between the CFRP and the steel

t_{s} are the interfacial shear stress along the beam axis at the interface between the CFRP and the steel

t_{t} is the interfacial shear stress at the interface between the CFRP and the steel perpendicular to the beam axis

The elastic stiffness in the normal direction is obtained from the slope of the bond separation curve derived from double cantilever beam (DCB) tests, or alternatively from the tensile stress–strain curve of the adhesive, and in this case is calculated using Eq 4-**2**. The shear stiffnesses, k_{ss} and k_{tt}, are assumed to be equal and are taken as the initial slope of the bond–slip model [56].

$$\mathrm{k_{nn}} = \frac{\mathrm{E_a}}{\mathrm{T_a}} \qquad \textit{Eq 4-2}$$

where:

E_a is the slope of the tensile stress strain curve of the adhesive

T_a is the thickness of the adhesive layer

The second is the damage initiation criterion, which, under mode II loading, is satisfied when the shear stress reaches the peak bond shear stress. For simplicity, this was adopted as the maximum nominal stress criterion, as expressed in Eq 4-3 [56].

$$\mathrm{Max}\left\{\frac{\langle t_\mathrm{n}\rangle}{t_n o}, \frac{t_\mathrm{s}}{t_\mathrm{s}}, \frac{t_\mathrm{t}}{t_\mathrm{t} o}\right\} = 1 \qquad \textit{Eq 4-3}$$

where:

$t_n o$ is the tensile strength of the adhesive

t_s, t_t^o are the bond shear strengths

$< >$ represent Macaulay bracket which is used to signifies that compressive stresses do not initiate damage

This formulation assumes no interaction between the different traction components, an assumption deemed appropriate for the present study. After damage initiation a scalar damage variable D is introduced to track damage evolution, which is equal to zero at the initiation of the damage and is equal to one at the complete failure. The interfacial behaviour is represented by Eq 4-4. Complete failure of the interface is when D is equal 1 based on the fracture energy with the linear criterion is adopted for its simplicity and expressed as in Eq 4-5 [56].

$$\begin{Bmatrix} t_n \\ t_s \\ t_t \end{Bmatrix} = \begin{bmatrix} (1-D^*)k_{nn} & 0 & 0 \\ 0 & (1-D)k_{ss} & 0 \\ 0 & 0 & (1-D)k_{tt} \end{bmatrix} \begin{Bmatrix} \delta_n \\ \delta_s \\ \delta_t \end{Bmatrix} \qquad \textit{Eq 4-4}$$

where:

D is the scalar damage variable

(*) means that if t_n is compressive, D^* is equal to zero

$$\frac{G_n^*}{G_I} + \frac{G_\mathrm{s}}{G_{II}} + \frac{G_\mathrm{t}}{G_{II}} = 1 \qquad \textit{Eq 4-5}$$

where:

G_n , G_s , G_t are the works done by the traction and its conjugate displacement in the normal and the two shear directions, respectively.

G_I , G_{II} are the interfacial fracture energy required to cause failure when for pure mode I loading and pure mode II loading respectively.

To define the effective displacement δ_m at damage evolution stage Eq 4-6 is used [56].

$$\delta_m = \sqrt{\langle \delta_n \rangle^2 + {\delta_s}^2 + {\delta_t}^2} \qquad \textit{Eq 4-6}$$

The damage at complete failure δ_m^f can be found using for a certain mode mix ratio of the energies. The damage variable D is defined Eq 4-7 for the case of linear softening of the adhesive as shown inFigure 4-18.

$$D = \frac{\delta_m^f (\delta_m^{max} - \delta_m^0)}{\delta_m^{max} (\delta_m^f - \delta_m^0)} \qquad \textit{Eq 4-7}$$

Where:

δ_m^0 is the effective displacement at the initiation of damage

δ_m^{max} is the maximum value of the effective displacement attained in the loading process

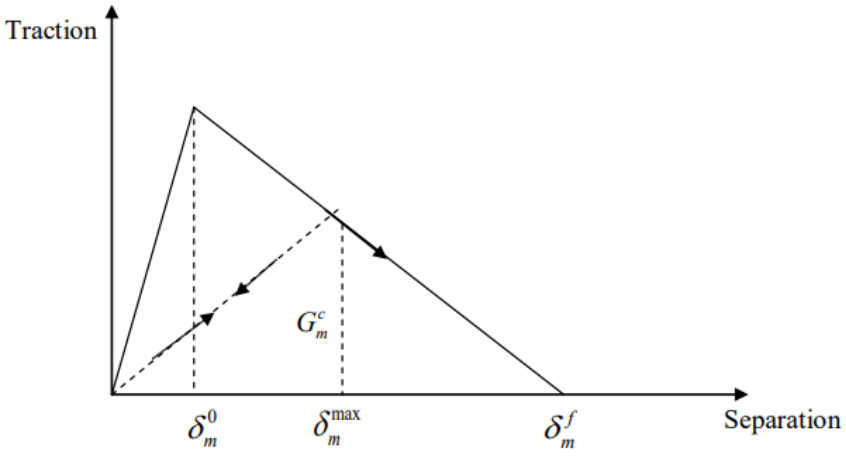


Figure 4-18: Linear damage evolution model [56]

The adhesive properties employed in the analysis are summarized in Table 4-6, as reported in [53].

Table 4-6: Properties of the adhesives used [53]

Linear adhesive			Nonlinear adhesive		
Elastic Stiffnesses					
K_{nn} (MPa/mm)	K_{ss1} (MPa/mm)	K_{ss2} (MPa/mm)	K_{nn} (MPa/mm)	K_{ss1} (MPa/mm)	K_{ss2} (MPa/mm)
11250	4327	4327	1750	673	673
Stresses for damage initiation criterion					
σ (MPa)	τ_1 (MPa)	τ_2 (MPa)	σ (MPa)	τ_1 (MPa)	τ_2 (MPa)
22.34	18	18	14.73	17.9	17.9
Fracture energy (N/mm)					
1.31			12.78		

4.3.4. Loading and boundary conditions

The beam is modelled with simply supported boundary conditions. Each support is represented over an area of 25 mm at the end of the beam, with a reference point positioned at the centre of this area. The reference point is kinematically coupled to the support area, and the boundary conditions are applied at this point, as illustrated in Figure 4-19. To simulate realistic conditions, the left support is restrained against vertical and out-of-plane displacements, while the right support is fully restrained against translations in all three directions. No transverse stiffeners are required, as the section is classified as Class 2 and therefore possesses sufficient thickness to resist local web instability, with the loading applied uniformly to the top flange. The top flange is restrained against out-of-plane movement, reflecting the lateral restraint provided by the roof metal deck, while it remains free to displace in the vertical direction.

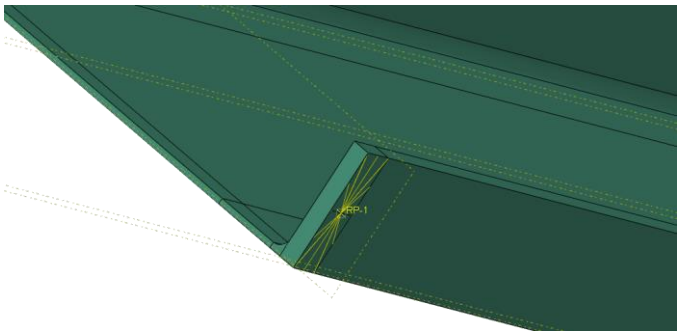


Figure 4-19: Reference point coupled to the support area

4.3.5. Loading and solution procedure

The load is applied under displacement control to facilitate the tracking of the post-peak response of the load–displacement behaviour, with static Riks step used to facilitate the tracking of nonlinear instability and post-peak response. To apply the displacement to the top flange, a reference point was defined at the midspan of the beam, located at the center of the top flange, as illustrated in **Figure 4-*20***, and the entire top flange was coupled to this point. To represent realistic loading conditions and to distribute the load without constraining the nodes to identical motion, an essential consideration, particularly in the presence of the Vierendeel mechanism the distributing continuum coupling option is selected.

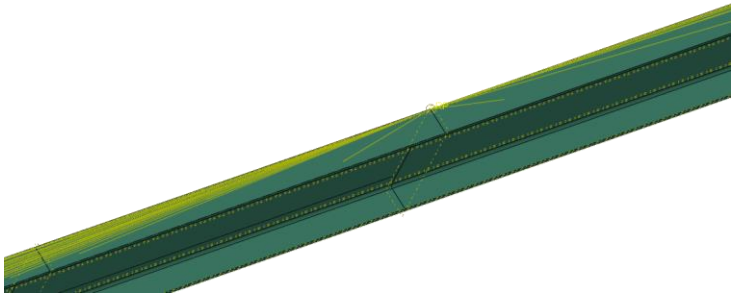
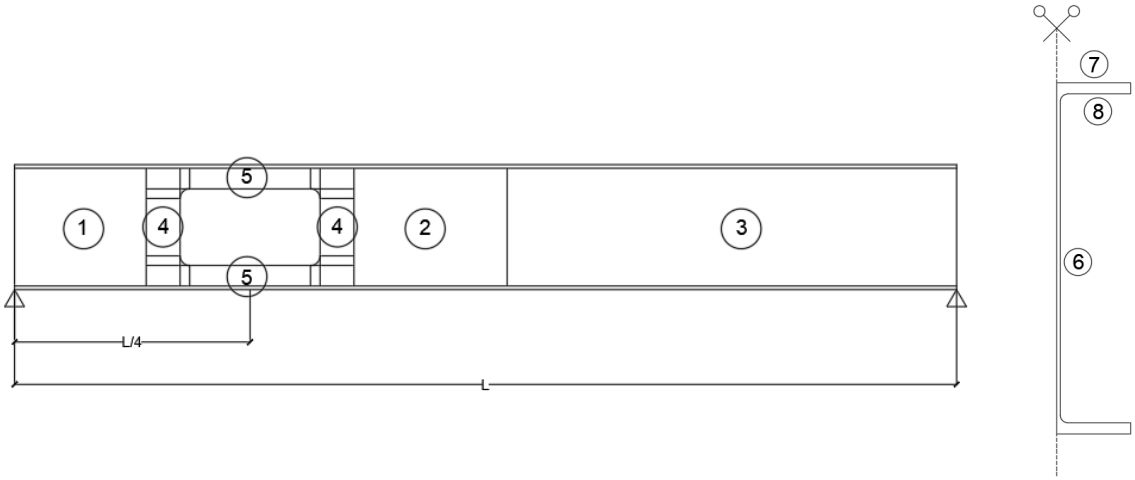


Figure 4-20: Reference point coupled to the top flange for load application

4.3.6. Element type and mesh sensitivity

Having defined the loading and support conditions, the model employs C3D8R solid elements for the beam and S4R shell elements for the CFRP plate. This C3D8R element is an eight-node hexahedral formulation with linear shape functions and reduced integration, wherein each node possesses three translational degrees of freedom and no rotational degrees of freedom, utilising a single integration point at the centre of the element. It was selected on account of its computational efficiency, particularly for large-scale nonlinear models. To determine the appropriate mesh size for the beam, a mesh sensitivity analysis was carried out. The beam is discretised into five regions along the span and three regions across the width (see **Figure 4-*21***).



a) b)

Figure 4-21: Beam divisions in sensitivity analysis a) Longitudinal Section; b) Cross section

Table 4-*7* illustrates the various regions of the beam and the corresponding number of elements assigned to each.

Table 4-7: Different schemes used for mesh sensitivity analysis

Region	Scheme 1	Scheme 2	Scheme 3	Scheme 4	Scheme 5	Scheme 6	Scheme 7
1	70	70	100	100	120	120	120
2	100	100	100	100	120	120	120
3	140	140	200	290	330	330	330
4	15	20	20	20	20	20	30
5	32	50	50	50	50	50	50
6	15	15	15	15	15	30	30
7	7	7	7	7	7	7	12
8	6	6	6	6	6	6	10

It is evident from the mesh sensitivity analysis that negligible differences exist between the various discretisation schemes in terms of the stiffness, ultimate capacity and the post-peak response as shown in **Figure 4-*22***. This can be attributed to the relatively large span of the beam, which renders fine meshes computationally inefficient without yielding appreciable improvements in accuracy. Accordingly, the second scheme is adopted, both for computational convenience and because it corresponds to a global mesh size of approximately 15 mm, which is consistent with the mesh density employed by Al Taee [23].

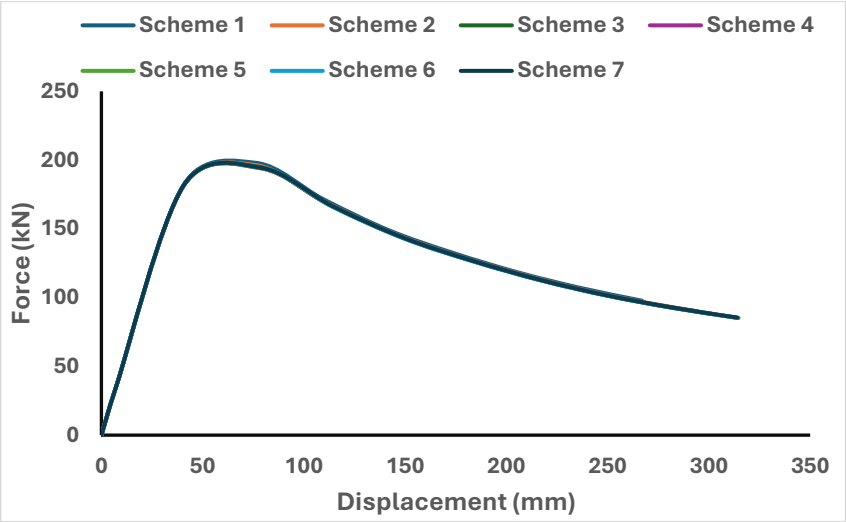


Figure 4-22: Force-displacement response for the models used for sensitivity analysis

5. PARAMETRIC STUDY

5.1. Introduction

This chapter presents the parametric numerical investigation conducted using the finite element modelling framework described in Chapter 4. The study aims to assess the influence of the main geometric and strengthening parameters on the structural response of laterally restrained steel beams with large web openings, with particular emphasis on load-carrying capacity, stiffness, failure mechanisms, and the effectiveness of CFRP strengthening.

The investigation is conducted progressively. First, the influence of the opening geometry, depth, and location is examined for unstrengthened beams in order to establish the corresponding reduction in structural capacity and identify the governing failure mechanisms. Rectangular and circular openings are considered at quarter span and at midspan, allowing the effects of regions with different combinations of shear force and bending moment to be compared. The resulting unstrengthened configurations provide the reference cases for the subsequent strengthening analyses.

The effectiveness of different CFRP strengthening configurations is then investigated by considering reinforcement applied to the web, the flanges, or both. In an initial stage, perfect bonding between the CFRP and the steel substrate is assumed, providing an upper-bound assessment of the potential strengthening effect. Selected configurations are subsequently analysed using the cohesive-interface formulation described in Chapter 4 to evaluate the influence of progressive interface damage and debonding. Conventional steel stiffeners are also considered for selected cases as a reference strengthening solution.

The influence of the adhesive behaviour is subsequently examined by comparing the two adhesive models considered in this study for representative CFRP-strengthened configurations. Finally, the numerical capacities are compared with the predictions obtained from the analytical approach developed in Chapter 3, allowing its accuracy and limitations to be assessed for the selected configurations. The main findings from the complete parametric investigation are synthesised at the end of the chapter.

The complete parametric investigation is summarised in **Table 5-*1***, which identifies the combinations of opening geometry, depth and location, strengthening configuration, bond

assumption, and adhesive model considered in the numerical analyses. The matrix also distinguishes the reference unstrengthened beams from the CFRP- and steel-stiffened configurations used in the subsequent comparisons.

Table 5-1: Parametric study matrix

<table>
<tr><td colspan="7"><u>Opening location:</u> Quarter span</td></tr>
<tr><td colspan="4">Circular</td><td colspan="3">Rectangular</td></tr>
<tr><td>0.5h</td><td>0.65h</td><td>0.75h</td><td>0.8h</td><td>0.5h</td><td>0.65h</td><td>0.75h</td></tr>
<tr><td colspan="3" rowspan="4">No need for strengthening</td><td>Perfect bonding</td><td rowspan="4">No need for strengthening</td><td colspan="2">Perfect bonding</td></tr>
<tr><td>Flange / Web / Flange + Web</td><td colspan="2">Flange / Web / Flange + Web</td></tr>
<tr><td>Cohesive interface</td><td colspan="2">Cohesive interface</td></tr>
<tr><td>Web</td><td colspan="2">Flange / Web</td></tr>
<tr><td colspan="7"><u>Opening location:</u> Mid Span</td></tr>
<tr><td colspan="4">Circular</td><td colspan="3">Rectangular</td></tr>
<tr><td>0.5h</td><td>0.65h</td><td>0.75h</td><td>0.8h</td><td>0.5h</td><td>0.65h</td><td>0.75h</td></tr>
<tr><td rowspan="2">Not considered</td><td>Perfect bonding</td><td rowspan="2">Not considered</td><td>Perfect bonding</td><td rowspan="2">Not considered</td><td colspan="2">Perfect bonding</td></tr>
<tr><td>Flange/ Web / Flange + Web</td><td>Flange/ Web / Flange + Web</td><td colspan="2">Flange/ Web / Flange + Web</td></tr>
<tr><td>Not considered</td><td>Cohesive interface</td><td>Not considered</td><td>Cohesive interface</td><td>Not considered</td><td colspan="2">Cohesive interface</td></tr>
<tr><td></td><td>Web / flange</td><td></td><td>Web / flange</td><td></td><td>Web / flange</td><td>Not considered</td></tr>
</table>

5.2. Influence of opening geometry and location

5.2.1. Quarter-span openings

5.2.1.1. Rectangular openings

Generally, beams with varying opening sizes exhibit the same stiffness as reported by [3,4,39], as illustrated in **Figure 5-*1***. Notably, the beam featuring an opening depth of 50% of the section height demonstrates behaviour largely similar to that of the solid beam, exhibiting no observable reduction in either strength or stiffness. This finding aligns with the observations reported in [3], despite the fact that the aforementioned study concerned composite steel–concrete beams, whereas the present investigation pertains to steel beams alone. Although stress concentrations appear at the corners of the opening, failure does not occur due to Vierendeel bending; instead, the greater depth of the Tee section allows the formation of a plastic hinge at mid-span to prevail. This suggests that, at this location, an opening of such size is not critical, consistent with the findings reported in [3]. **Figure 5-*2*** presents the stress distribution and displacement at the instant of plastic hinge formation for both the solid beam and the beam with an opening depth of 0.5h.

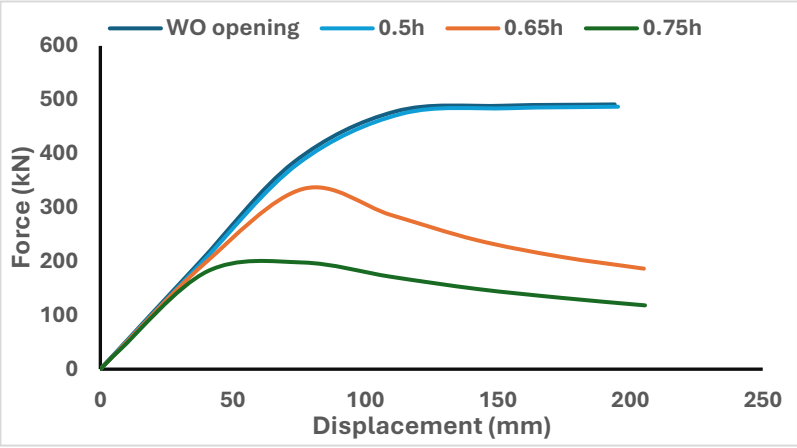


Figure 5-1: Force-displacement response for various rectangular opening sizes at quarter span

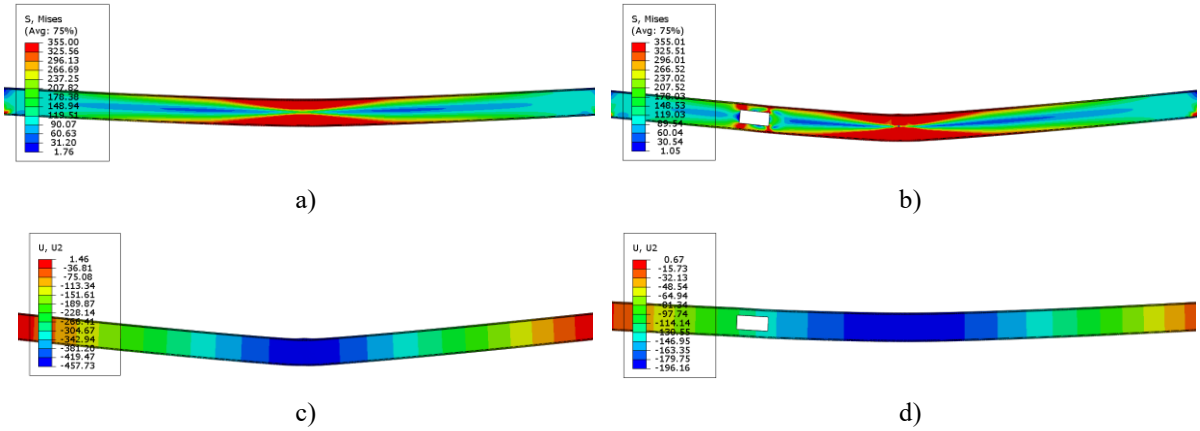


Figure 5-2: Stress distribution and displacement for beam with 0.5h rectangular opening: a) Solid beam-stress distribution; b) Stress distribution; c) Solid beam-displacement; d) Displacement

Conversely, the specimens with larger opening depths of 0.65h and 0.75h both failed through the formation of a Vierendeel mechanism, characterised by the development of four plastic hinges at the corners of the opening. This behaviour is consistent with the findings reported in [4,39], with the notable distinction that the opening sizes considered in the present study are larger. Notably, both beams reached their maximum load at a similar displacement of approximately 77 mm. The ultimate strength of the beam with a 0.65h opening decreased from 491 kN for the solid beam to 335 kN, corresponding to a 32% reduction in capacity. A more pronounced decline was observed for the beam with a 0.75h opening, where the load-carrying capacity dropped from 491 kN to 198 kN, representing a 60% reduction. This finding is in agreement with the results reported in [3,39]. This progressive loss of strength with increasing opening size can be primarily attributed to the diminishing depth of the Tee sections, which compromises their ability to transfer shear forces and resist Vierendeel bending which agrees with the findings of [3]. **Figure 5-*3*** presents the stress distribution and displacement for the opening size of 0.65h, precisely where the plastic hinges develop.

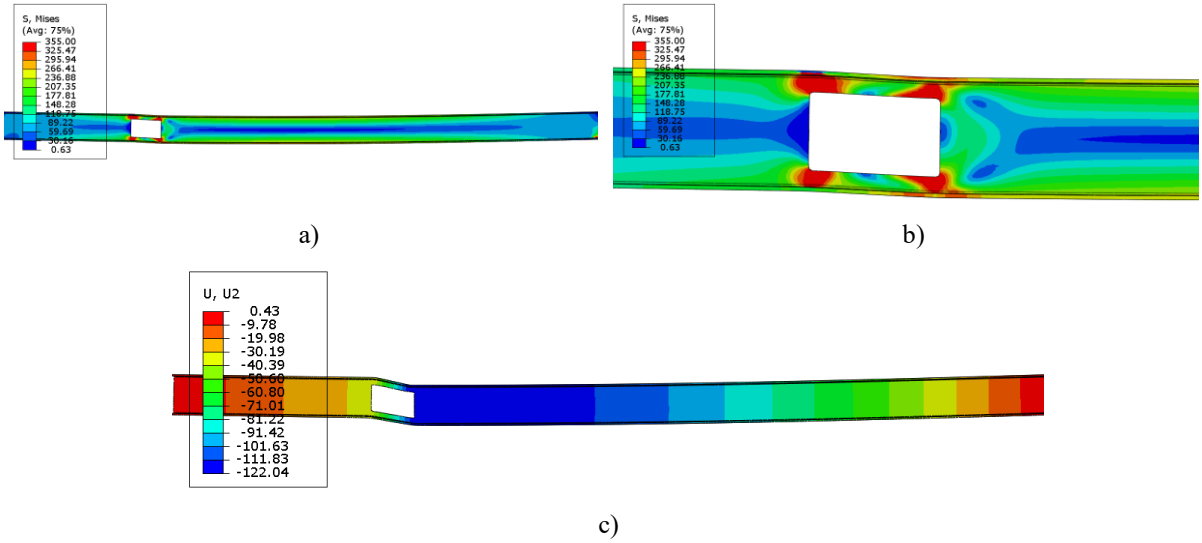


Figure 5-3: Stress distribution and displacement for beam with 0.65h rectangular opening: a) Stress distribution; b) Stress distribution around the opening; c) Displacement

Furthermore, with continued loading, the beam undergoes excessive deflection as a consequence of the opening's collapse, as illustrated in **Figure 5-*4***a. It is particularly noteworthy that the top and bottom flanges of the Tee sections on the high-moment side specifically, the right-hand side of the opening, experienced buckling. This local instability is attributed to the compressive stresses induced by the local Vierendeel bending, as depicted schematically in **Figure 5-*4***b.

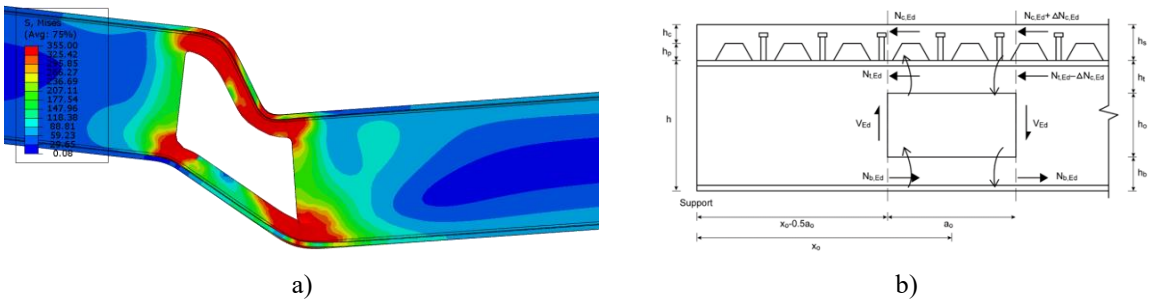


Figure 5-4: Explanation of plastic hinge formation for 075h. opening a) Opening collapse from model; b) Forces and moments around the opening [12]

5.2.1.2. Circular openings

The structural response of beams incorporating circular openings at quarter span region diverges notably from that observed in beams with rectangular openings agreeing with what is reported in [4]. This distinction arises primarily from two factors. First, the length of circular openings is considerably shorter than that of rectangular openings, and opening length is an important parameter influencing Vierendeel action. Second, circular openings eliminate the severe sharp-corners stress concentrations characteristic of rectangular openings [3]. These geometric advantages are clearly manifested in the force–displacement responses presented in

Figure 5-*5*, wherein all three opening sizes 0.5h, 0.65h, and 0.75h demonstrate behaviour virtually identical to that of the reference solid beam, with both strength and stiffness remaining unchanged which agrees with the observations reported in [5]. As a result, the governing failure mode transitions from one dictated by Vierendeel bending to a flexural mechanism, characterised by the formation of a plastic hinge at mid-span, as depicted in Figure 5-6.

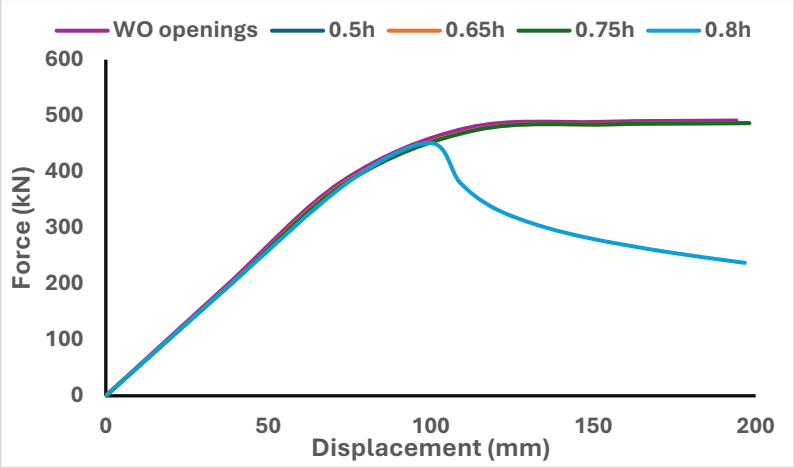
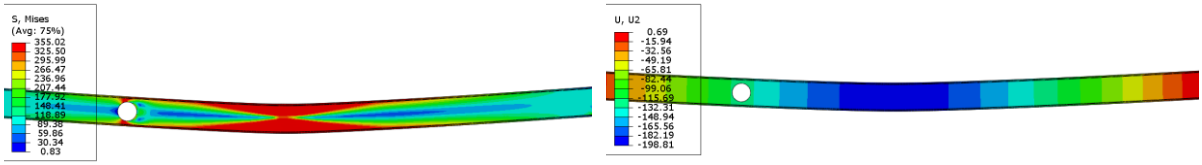


Figure 5-5: Force-displacement response for quarter span circular opening



a) b)

Figure 5-6: Stress distribution and displacement for beam with 0.65h circular opening; a) Stress distribution; b) Displacement

For the beam with a 0.8h opening, the stiffness remains consistent with that of the other models; however, the ultimate strength is reduced by approximately 8%, declining from 492 kN for the reference beam to 450 kN. This reduction is attributed to the formation of the Vierendeel mechanism. At this opening size, the depth is sufficiently large that the Tee sections formed above and below the opening become markedly slender, while the increased opening length further promotes the development of Vierendeel bending, as illustrated in **Figure 5-*7***. This behaviour aligns with the observations previously reported for rectangular openings situated at the same location. Consistently, local buckling of the top and bottom flanges is observed in the high-moment region, driven by the compressive stresses arising from the local Vierendeel bending. Notably, this response suggests the existence of a threshold opening size for circular openings at which the behavioural transition occurs.

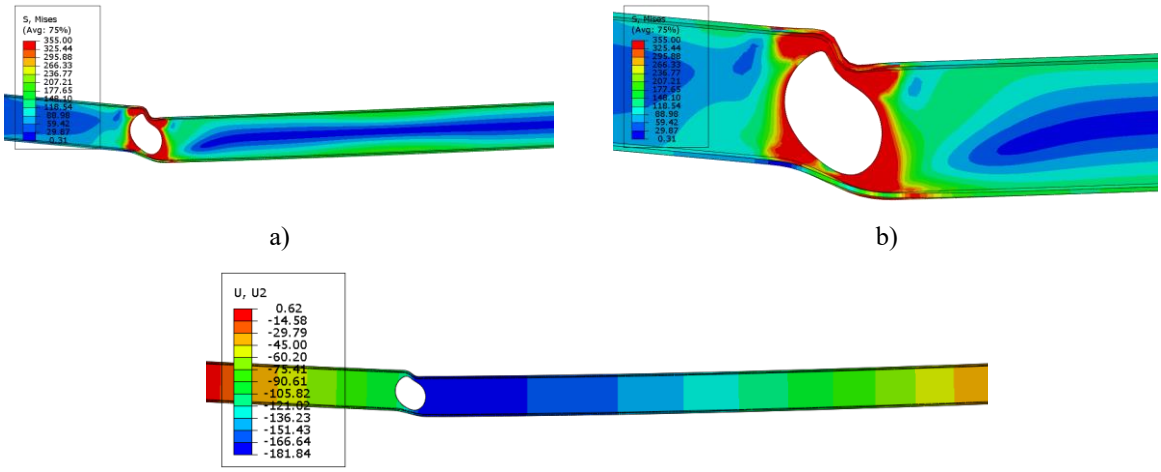


Figure 5-7: Stress distribution and displacement for beam with 0.8h circular opening: a) Stress distribution; b) Stress distribution around the opening; c) Displacement

5.2.2. Mid-span openings

5.2.2.1. Rectangular openings

In case of web openings positioned at mid-span, the dominant failure mode is flexural, characterised by the formation of a plastic hinge at the centre of the beam, which ultimately leads to a collapse mechanism [3]. The force–displacement response of the beams is presented in Figure 5-8. Once again, all specimens exhibited the same stiffness, indicating that the presence of an opening primarily diminishes the strength of the beam without significantly affecting its stiffness consistent with the findings of [1,3,16,39].

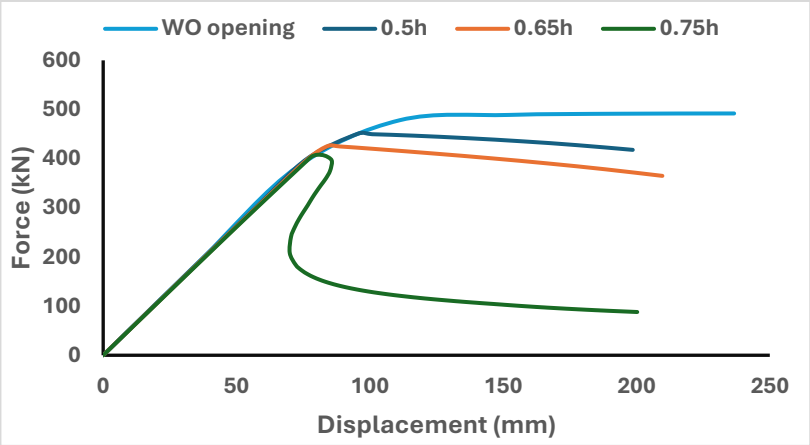


Figure 5-8: Force-displacement response for various rectangular opening sizes at mid span

Moreover, it is noteworthy that both the 0.5h and 0.65h opening sizes exhibit a similar post-peak behaviour, characterised by a gradual reduction in stress after attaining the maximum load which agrees with the findings of [16], albeit at different capacity levels. The reduction in load-

carrying capacity for the beam with a 0.5h opening is approximately 8.5%, decreasing from 492 kN for the reference beam to 450 kN. In contrast, the beam with a 0.65h opening experiences a more substantial reduction of approximately 13.5%, with the capacity declining from 492 kN to 425 kN, despite the opening depth increasing by only 15%.

To further elucidate the behaviour of the beams with 0.5h and 0.65h openings, reference is made to **Figure 5-*9***. Owing to the length of the opening and the boundary conditions defined in the numerical model, where the left support restrains only vertical movement while the right support restrains both vertical and longitudinal displacements, the beam deflects downwards under loading, causing the left side to be drawn inwards, thereby translating longitudinally. This behaviour proceeds in a conventional manner until a critical point is reached where stress concentrations develop in both the top and bottom Tee sections on the left side. Near the left end of the opening in the transition from the solid beam to the perforated section, the beam exhibits greater rigidity at this location due to the relatively larger depth of the Tee sections compared to the 0.75h case. Consequently, the hinge location shifts, and this region effectively functions as a plastic hinge, undergoing substantial deformation.

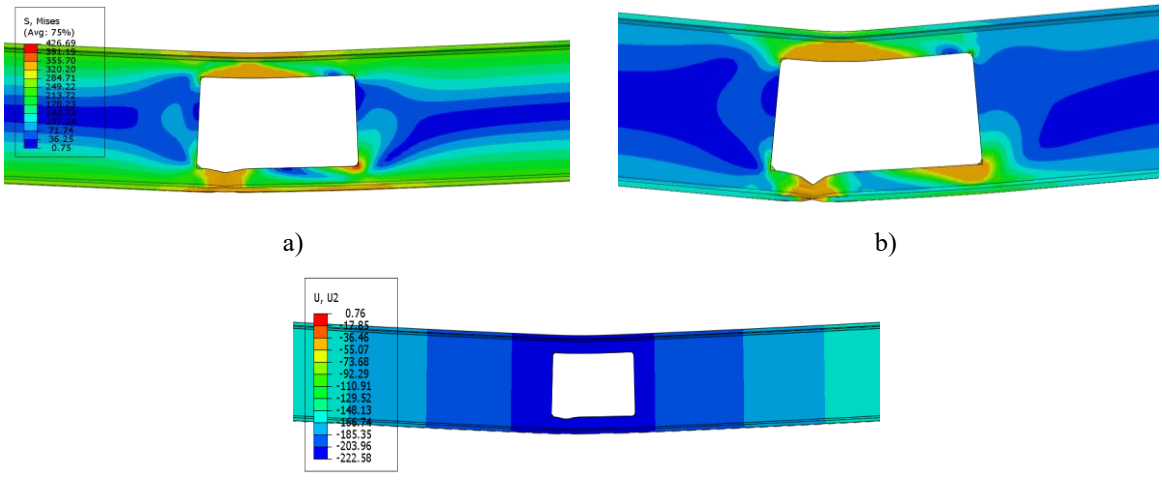


Figure 5-9: Stress distribution and displacement for beam with 0.65h rectangular: a) Stress distribution; b) Stress distribution around the opening; c) Displacement

Regarding the beam with a 0.75h opening, the strength reduces to approximately 410 kN, corresponding to a 17% reduction from the reference capacity, and the beam exhibits the distinct behaviour of snap-back buckling unlike the other opening sizes. The shift in structural behaviour observed between the smaller opening sizes and the 0.75h case can be attributed to the increased depth of the opening. This greater opening depth introduces flexibility at the end sections of both the top and bottom Tees on either side, thereby permitting the beam to rotate

symmetrically about both supports. Consequently, two plastic hinges form at the corners of the top Tee, causing it to behave as an independent beam, which is consistent with the behaviour reported in [7,16]. Under these conditions, an arching mechanism develops to transfer the load, as the top Tee is predominantly subjected to compression. Ultimately, failure occurs through the formation of a plastic hinge at mid-span of the top Tee (see **Figure 5-*10***), localising the deformations within this region rather than distributing them across the entire beam consistent with the findings of [7].

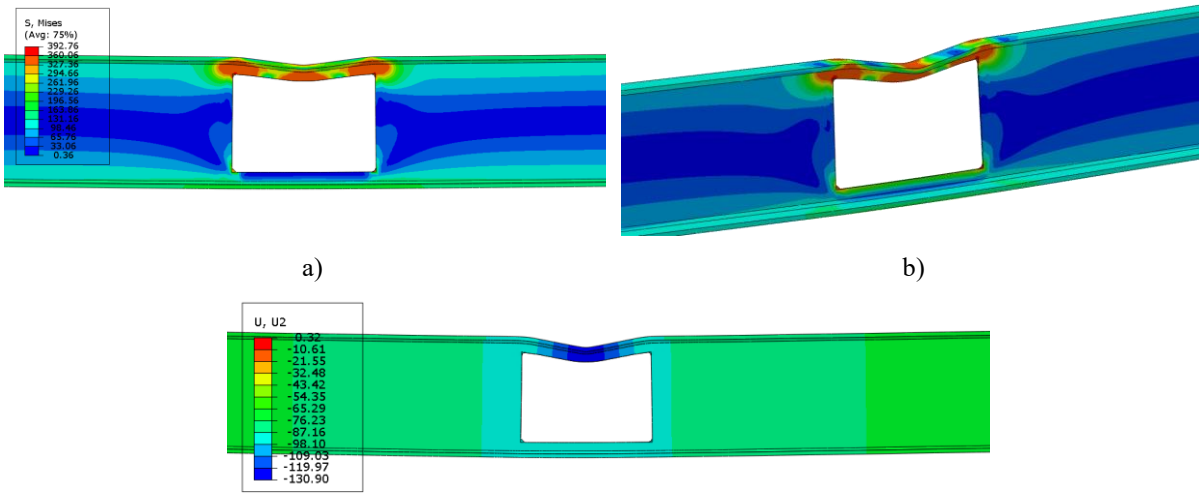


Figure 5-10: Stress distribution and displacement for beam with 0.75h rectangular opening: a) Stress distribution; b) Stress distribution around the opening; c) Displacement

It is worth noting that Figure 5-11 illustrates the trend in strength reduction, which appears to be nearly linear; a similar observation has been reported in [3].

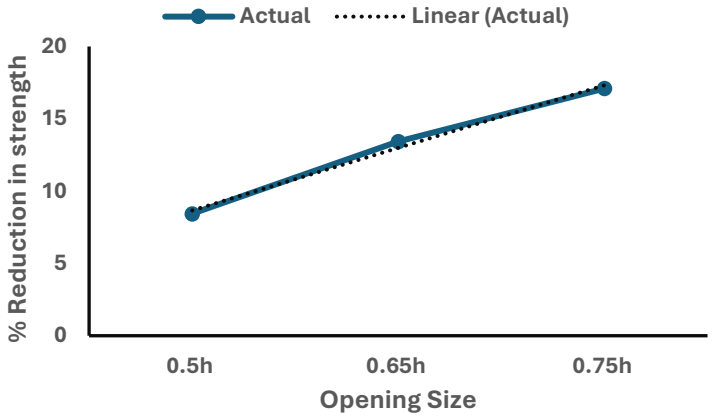


Figure 5-11: Trend in strength reduction with opening size

5.2.2.2. Circular openings

In contrast to the near-support configuration, where three opening sizes exhibited no discernible reduction in capacity, the introduction of openings at mid-span resulted in a measurable loss of strength agreeing with the findings of [1] as seen in **Figure 5-*12*** for the force–displacement curves.

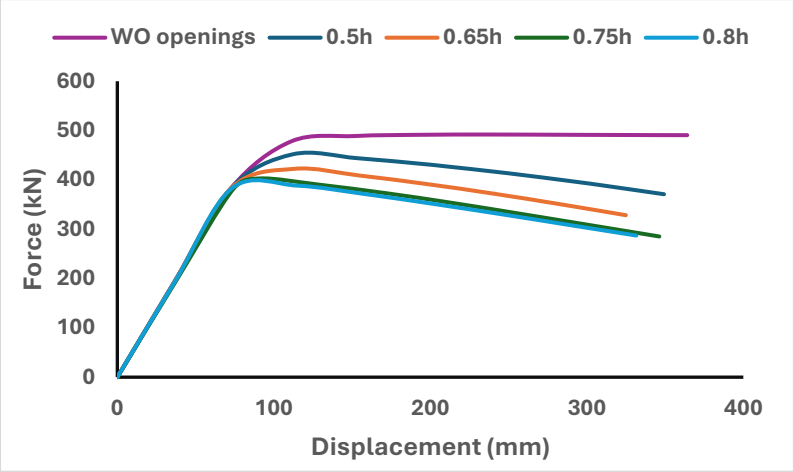
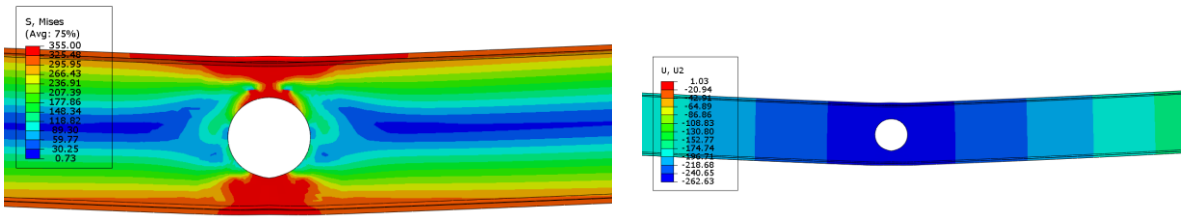


Figure 5-12: Force-displacement response for various circular opening sizes at mid span

The overall structural response remains consistent across various openings: stress accumulates progressively until the flanges at the mid-span section begin to yield, after which the yielding propagates through the cross-section then the top flange will buckle which agrees with the observations in [1], as illustrated in Figure 5-13.



a) b)

Figure 5-13: Stress distribution and displacement for beam with 0.5h circular opening: a) Beam stress distribution; b) Beam displacement

In this configuration, the trend of the strength reduction is presented in Figure 5-14 indicating a strength reduction that closely approximates a linear decline across the different opening depths agreeing with what is reported in [3].

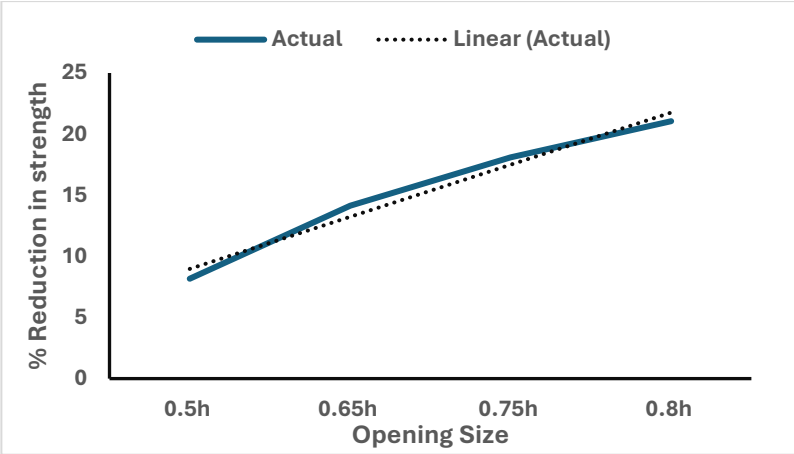


Figure 5-14: Trend in strength reduction with opening size

5.3. Influence of strengthening configuration – perfect bond

5.3.1. Quarter-span opening

5.3.1.1. Rectangular opening

As demonstrated previously, the 0.5h opening exhibited no reduction in strength, in contrast to the 0.65h and 0.75h openings, which experienced a notable decline in capacity. Therefore, the subsequent strengthening investigation focuses exclusively on the latter two opening sizes.

5.3.1.1.1. CFRP flange strengthening

The first configuration examined involves the attachment of CFRP plates exclusively to the flanges. In this scheme, the CFRP is bonded to the underside of the top flange and to the outer face of the bottom flange of the beam with a 0.65h opening. The resulting force–displacement response, presented in **Figure 5-*15***, reveals that the nonlinear portion of the curve exhibits a gradually decreasing stiffness up to the peak load, at which the Vierendeel mechanism develops, and the load-carrying capacity progressively diminishes afterwards. The ultimate strength is enhanced by 28%, rising from 335 kN for the unstrengthened beam with the opening to 430 kN.

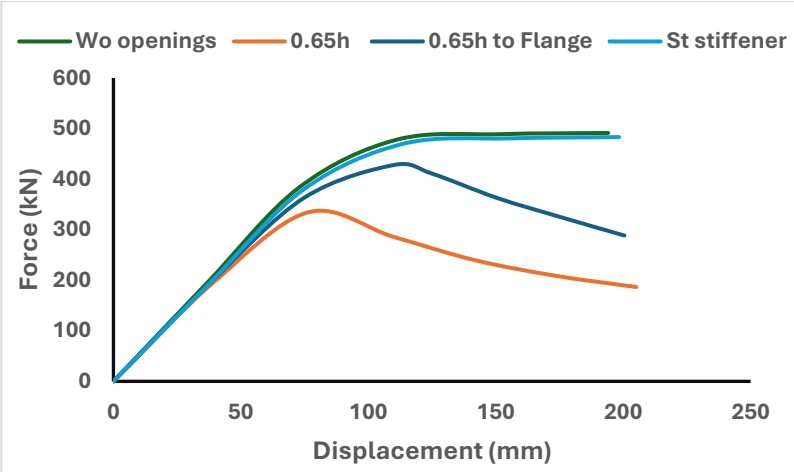
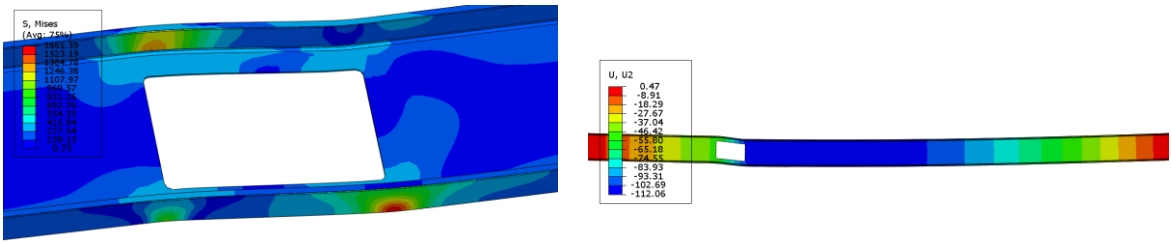


Figure 5-15: Force-displacement response for rectangular opening quarter span with strengthening schemes for 0.65h

However, the failure mode remains unchanged, with the Vierendeel mechanism prevailing, as illustrated in **Figure 5-*16*.** Despite this improvement, the strengthened beam does not fully recover the capacity of the solid reference beam; a strength reduction of 12% relative to the beam without an opening persists. It is important to highlight that the CFRP experiences high stress concentrations at two specific locations: the inner side of the top left corner of the opening, corresponding to the plate attached to the top flange, and the inner right side of the plate bonded to the bottom flange. This stress distribution arises because these flat regions of the plates are subjected to higher tensile forces compared to the other areas corresponding to the remaining opening corners, where the beam undergoes local buckling induced by the compressive component of the Vierendeel bending moment, thereby relieving a portion of the stresses.



a) b)

Figure 5-16: Stress distribution and displacements; a) Beam stress distribution with CFRP to the flange; b) Displacement

In addition, a steel stiffener measuring 800 mm in length, 80 mm in width, and 10 mm in thickness was investigated. According to the results obtained from the Excel spreadsheet calculations, this stiffener was deemed sufficient to resist Vierendeel bending. The force–displacement curve demonstrates that the strength is effectively recovered, with a negligible

reduction of only 1.5% compared to the solid beam without an opening. Furthermore, the failure mode shifts from the Vierendeel mechanism to a flexural failure at mid-span in accordance with the findings of [7], accompanied by slight buckling of the stiffener above the opening on the low-moment side (LMS), as shown in **Figure 5-*17*.**

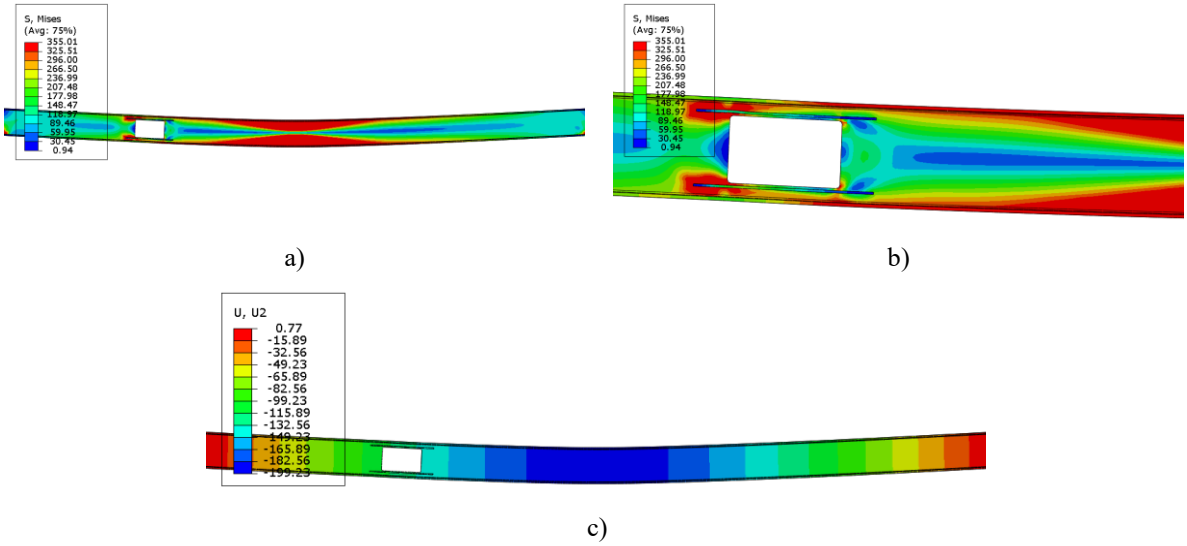


Figure 5-17: Stress distribution and displacement for beam with 0.65h rectangular opening ; a) Beam with steel stiffener stress distribution; b) Stresses around the opening; c) Displacement

Turning to the beam with a 0.75h opening, the application of CFRP to the flanges exhibits a similar trend in strength reduction to that observed for the 0.65h opening, as depicted in **Figure 5-*18***.

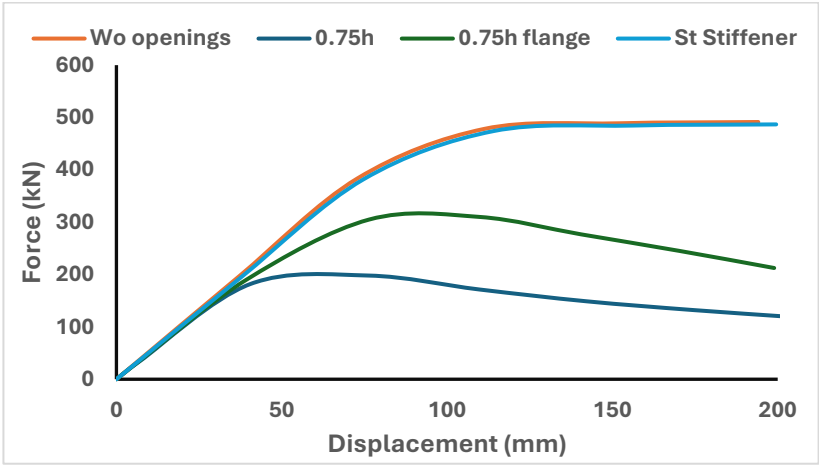
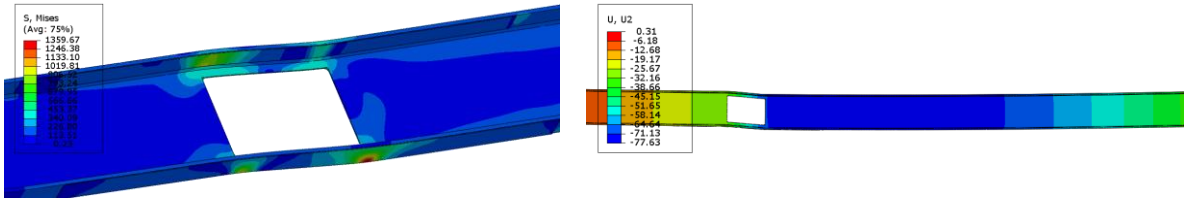


Figure 5-18: Force-displacement response for rectangular opening quarter span with strengthening schemes for 0.75h

However, the reduction is more pronounced for this opening size owing to the increased opening depth and the consequent decrease in the depth of the Tee sections above and below the opening consistent with the findings of [3]. In this case, the application of CFRP to the flanges yields a substantial strength enhancement of 56% relative to the unstrengthened beam

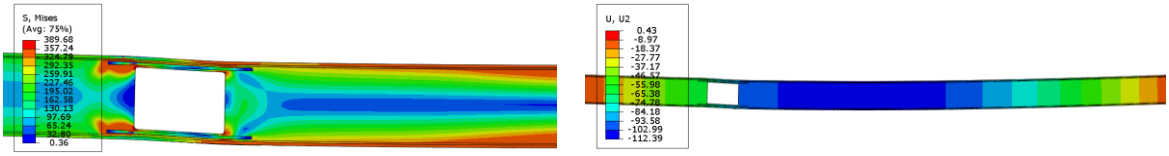
with the opening, with the capacity increasing from 200 kN to 310 kN. Nevertheless, the ultimate strength remains 36% lower than that of the solid reference beam, declining from 490 kN to 310 kN. Despite this improvement, failure continues to be governed by the Vierendeel mechanism, as illustrated in **Figure 5-*19***.



a) b)

Figure 5-19: Stress distribution and displacement for beam with 0.75h rectangular opening; a) Beam stress distribution with CFRP to the flange; b) Displacement

Shifting the focus to the steel stiffener, the analytical calculations performed using the Excel spreadsheet indicate that a 15 mm thick steel stiffener is sufficient to reinforce the opening against Vierendeel bending. However, the numerical analysis reveals that this stiffener effectively resists Vierendeel bending only up to a displacement of 112 mm, at which point plastic hinges form at the corners on the left side of the opening, and the stress concentration extends beyond the left end of the steel stiffener. Consequently, the steel stiffener can be considered adequate within the serviceability limits, that is, within the allowable deflection criteria. Beyond these limits, the Vierendeel bending mechanism governs the failure, as illustrated in Figure 5-20**.**



a) b)

Figure 5-20: Stress distribution and Displacement for beam with 0.75h rectangular opening; a) Beam stress distribution with steel stiffener with 150 mm anchorage length; b) Displacement

Figure 5-*21* demonstrates that increasing the anchorage length that is, extending the steel stiffener beyond the opening from 150 mm to 250 mm serves to encompass the region of stress concentration extending beyond the left side of the opening. This modification shifts the failure mode from Vierendeel bending to a flexural failure at mid-span as shown in **Figure 5-*22***. Accordingly, the revised stiffener, with dimensions of 1000 mm in length, 80 mm in width, and 15 mm in thickness, enabled the beam to fully recover the capacity of the original solid beam.

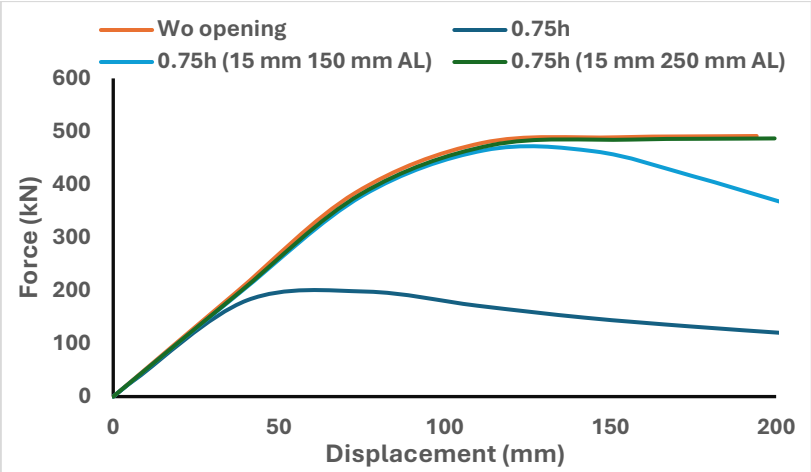
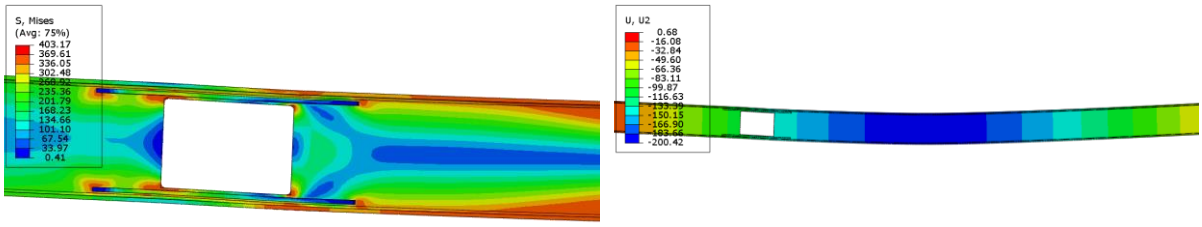


Figure 5-21: Force-displacement response for rectangular opening quarter span with different anchorage length for steel stiffeners



a) b)

Figure 5-22: Stress distribution and displacement; a) Beam stress distribution with steel stiffener of 250 mm anchorage length; b) Displacement

5.3.1.1.2. CFRP web strengthening

The second configuration, involving the attachment of CFRP exclusively to the web, has demonstrated greater potential than the flange-only scheme. This is attributed to the fact that the shear area is increased by thickening the webs of the top and bottom Tee sections, which facilitates more effective shear transfer from the left side to the right side of the opening and, concurrently, enhances the Vierendeel bending resistance of the Tees. For the 0.65h opening, the strengthened beam nearly recovered the full capacity of the solid reference beam, exhibiting a marginal strength reduction of approximately 2% relative to the solid beam as shown in **Figure 5-*23***. This corresponds to a 45% enhancement in capacity, from 335 kN for the unstrengthened beam with the opening to 483 kN for the strengthened specimen. Notably, the failure mode reverted to that of the solid beam as illustrated in Figure 5-24, agreeing with the observations in [4].

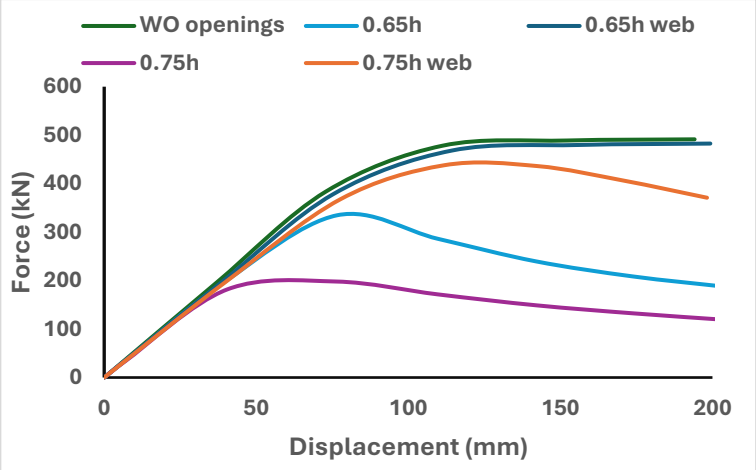


Figure 5-23: Force-displacement response for rectangular opening quarter span with web strengthening schemes

Conversely, for the 0.75h opening, the application of CFRP to the web enhanced the capacity by 123%, increasing from 200 kN to 440 kN. However, the strength was not fully recovered; a reduction of approximately 10% relative to the solid beam persisted, as failure continued to be governed by the Vierendeel mechanism, with the CFRP serving only to delay its onset. Subsequently, the CFRP became highly stressed and ultimately failed at the corners of the opening, where the stress concentration was most severe as shown in **Figure 5-*24***.

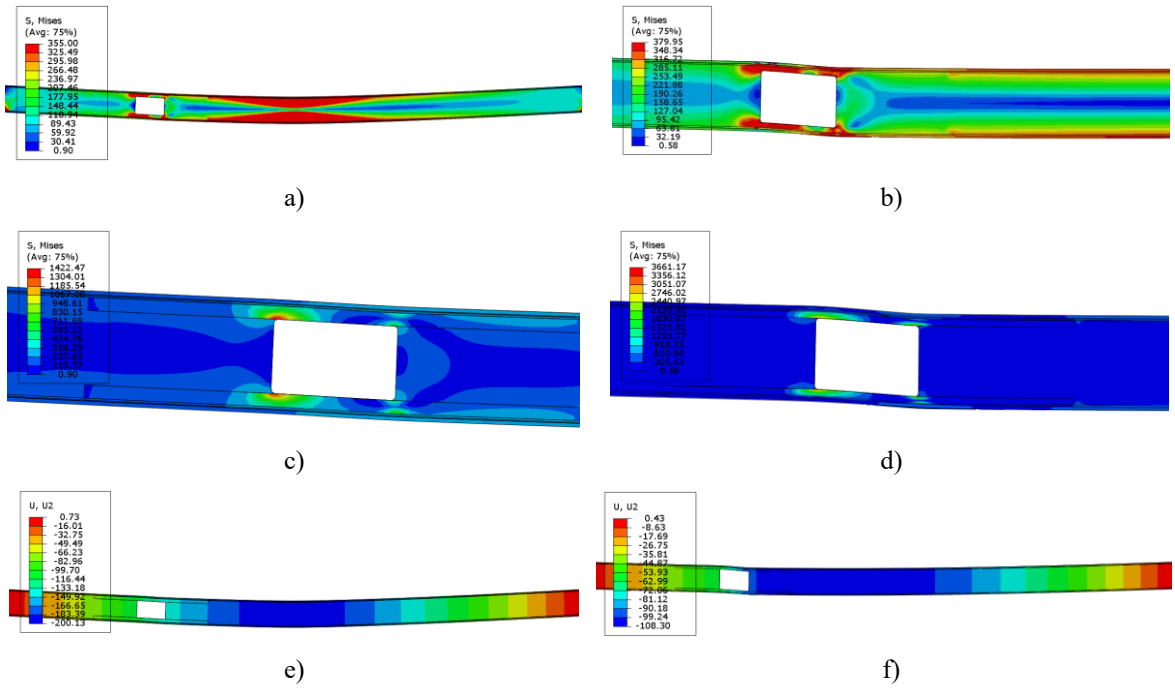


Figure 5-24: Stress distribution and displacement: a) Beam with 0.65h opening-stress distribution; b) Beam with 0.75h opening-stress distribution; c) CFRP stress distribution for 0.65h opening; d) CFRP stress distribution for 0.75h opening; e) Displacement for beam with 0.65h opening; f) Displacement for beam with 0.75h opening

5.3.1.1.3. CFRP web and flange strengthening

From the foregoing discussion, it is evident that the application of CFRP to both the flanges and the web results in the full recovery of strength for both opening sizes consistent with the findings of [1], as illustrated in **Figure 5-*25***.

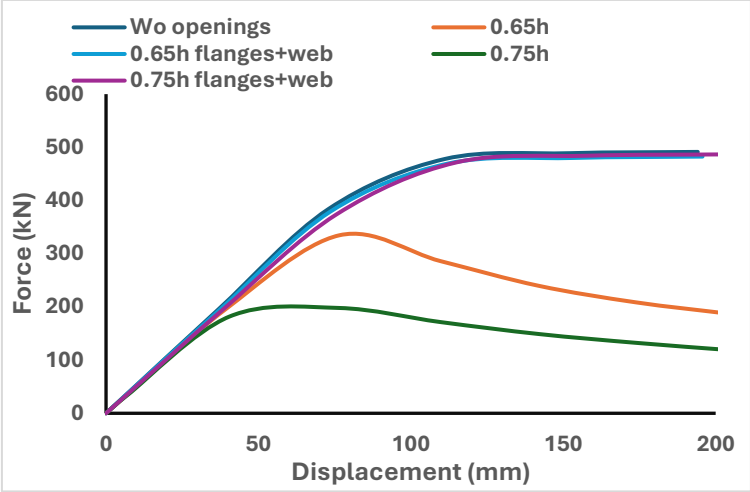


Figure 5-25: Force-displacement response for rectangular opening quarter span with flanges and web strengthening schemes

Importantly, although the beam with the 0.75h opening exhibited a slight Vierendeel bending action, this did not impede its ability to achieve full flexural capacity. In each case, the failure mode reverted to that of the solid beam, as shown in **Figure 5-*26***. Moreover, the CFRP experiences considerably lower stress levels under this configuration for both the 0.65h and 0.75h opening sizes, although the latter exhibits comparatively higher stresses.

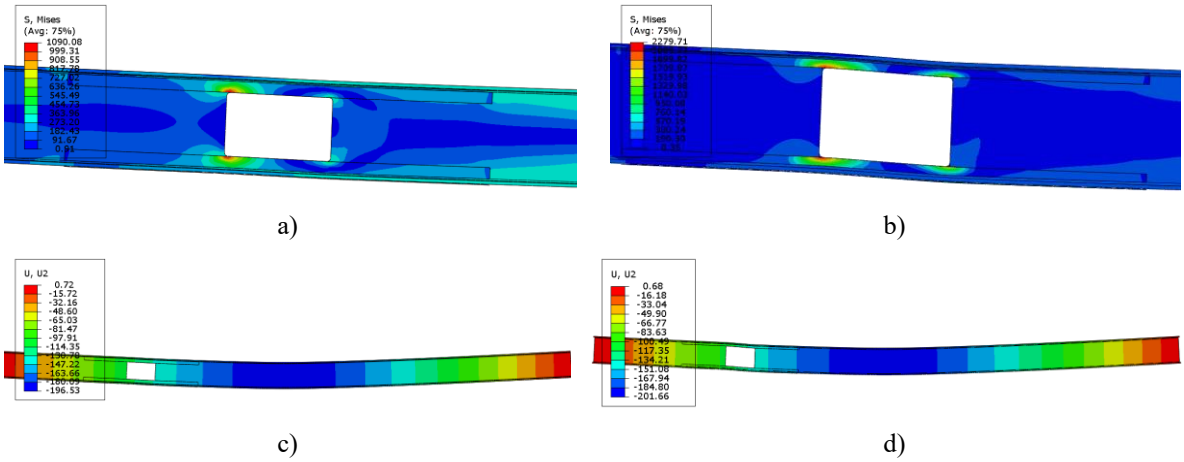


Figure 5-26: Stress distribution and displacement: a) Beam with 0.65h opening-stress distribution; b) Beam with 0.75h opening-stress distribution; c) Displacement for beam with 0.65h opening; d) Displacement for beam with 0.75h opening

5.3.1.2. Circular opening

It is evident from the force–displacement curves presented in Figure 5-27 that all strengthening strategies employed in this case whether involving CFRP or steel stiffeners proved effective. The stress distributions, illustrated in **Figure 5-*28***, reveal that the level of stress sustained by the CFRP varies across the different configurations. Nevertheless, all schemes successfully suppressed the development of the local Vierendeel mechanism, resulting in a failure mode governed by flexural yielding as in [1,4].

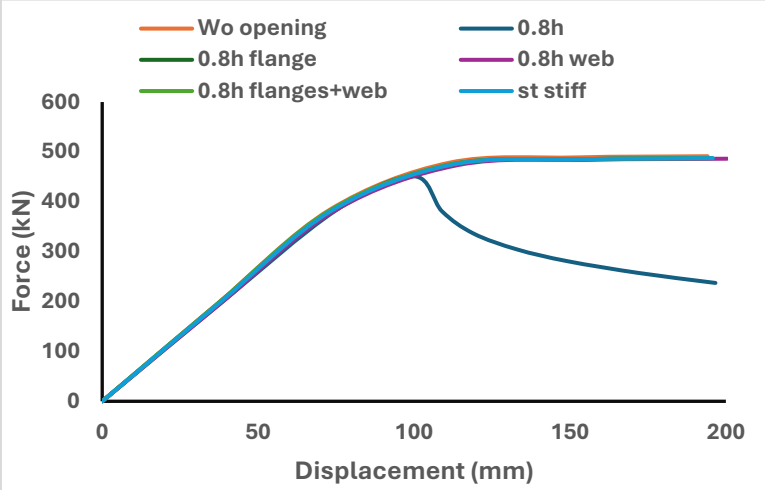


Figure 5-27: Force-displacement response for circular opening quarter span strengthening schemes for 0.8h

The reason why the various CFRP configurations do not increase the capacity beyond that of the solid beam when the opening is located near the support is that, once the strengthening system restores the local capacity at the opening region, the overall behaviour becomes governed by the mid-span section, which retains its original dimensions and therefore limits the ultimate strength to that of the reference solid beam agreeing with the findings of [4].

The highest CFRP stresses are observed when the plates are attached exclusively to the web. This is attributed to the limited CFRP area available above and below the opening compared to the other configurations. As expected, these elevated stresses occur on the left side of the opening, owing to the substantial shear transfer from the left to the right side. Furthermore, this configuration increases the effective thickness of the web within the Tee sections above and below the opening, which reduces the stresses in the steel Tee below the yield limit and thereby prevents the formation of the Vierendeel bending mechanism.

In contrast, attaching CFRP to the flanges alone induces comparatively lower stresses in the composite material. This is because the increased flange thickness provides a greater cross-

sectional area to resist the local Vierendeel bending generated by shear transfer, rather than relying on an enlarged shear area as in the web-only configuration. The combined configuration, in which CFRP is applied to both the flanges and the web, yields intermediate stress levels in the CFRP, falling between those recorded for the web-only and flange-only cases.

The use of steel stiffeners has similarly proven effective in averting the formation of the Vierendeel mechanism. However, minor buckling of the steel stiffener was observed above the opening, which led to a reduction in capacity at larger displacement levels.

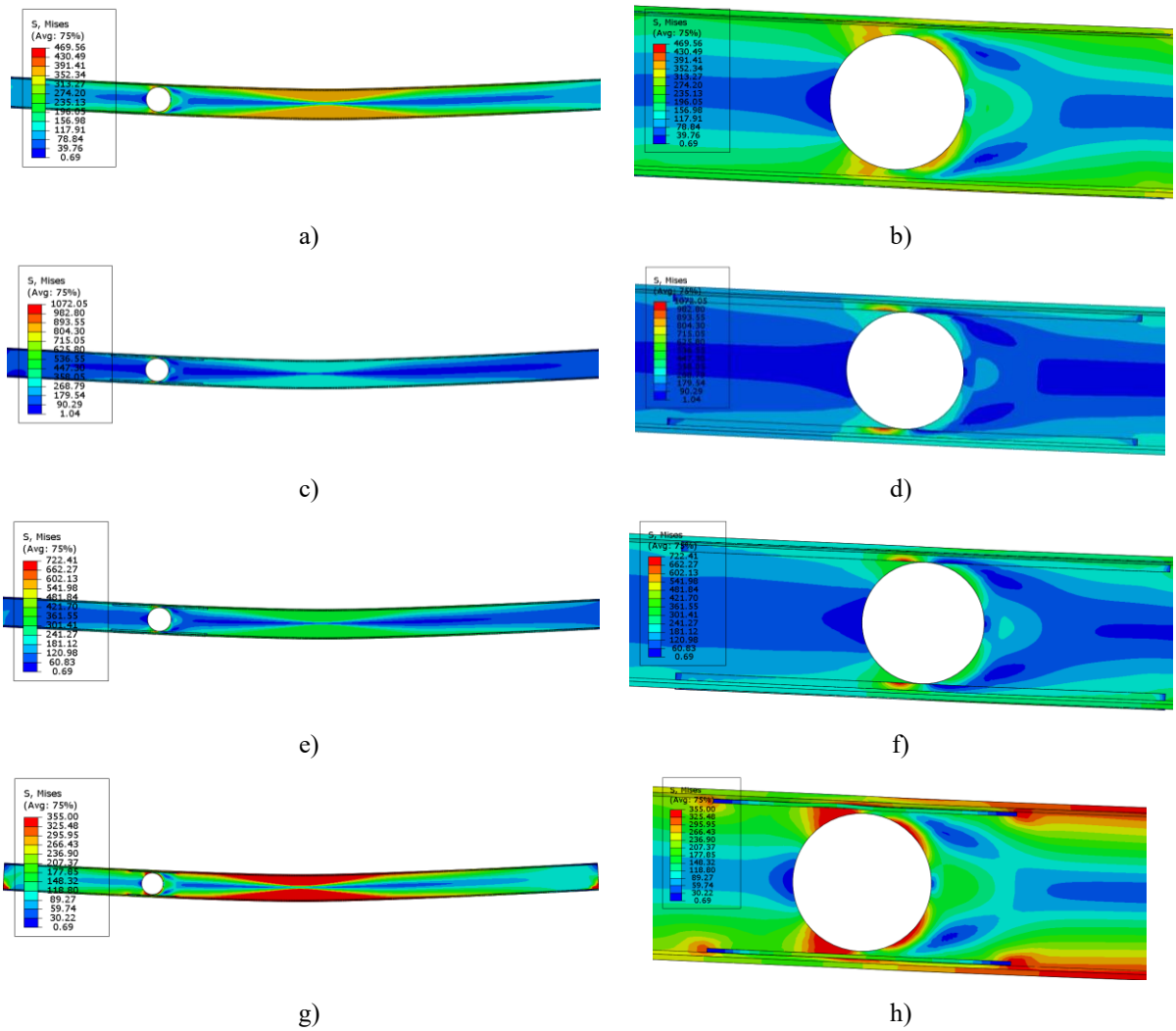


Figure 5-28: Stress distribution for beam with 0.8h circular opening with various strengthening schemes; a) Beam; b) CFRP to the flange; c) Beam; d) CFRP to the web; e) Beam; f) To flanges and web; g) Beam; h) Steel stiffener

5.3.2. Mid-span opening

5.3.2.1. Rectangular opening

In the case of openings positioned at mid-span, as previously discussed, the strength of the beam is reduced owing to the diminished cross-sectional area at the location of maximum bending moment. As illustrated in **Figure 5-*29***, the application of CFRP, whether to the flanges alone, the web alone, or both the flanges and web, for the 0.65h opening, successfully recovered the lost strength with variations observed in the inelastic stiffness phase; the flange-strengthened configuration exhibited greater stiffness than the web-strengthened case.

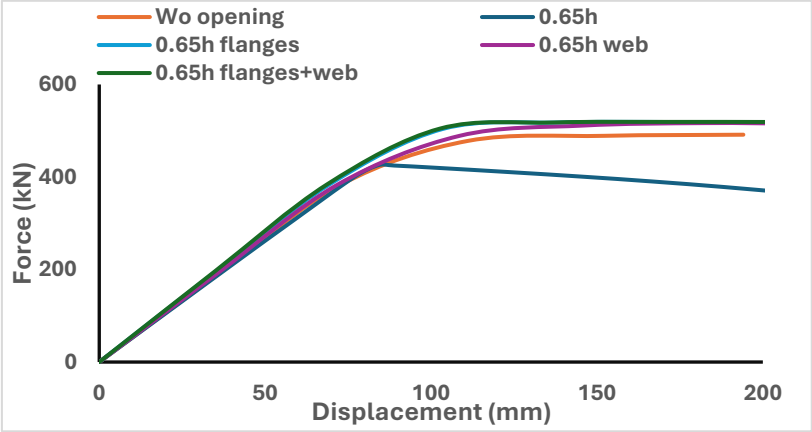
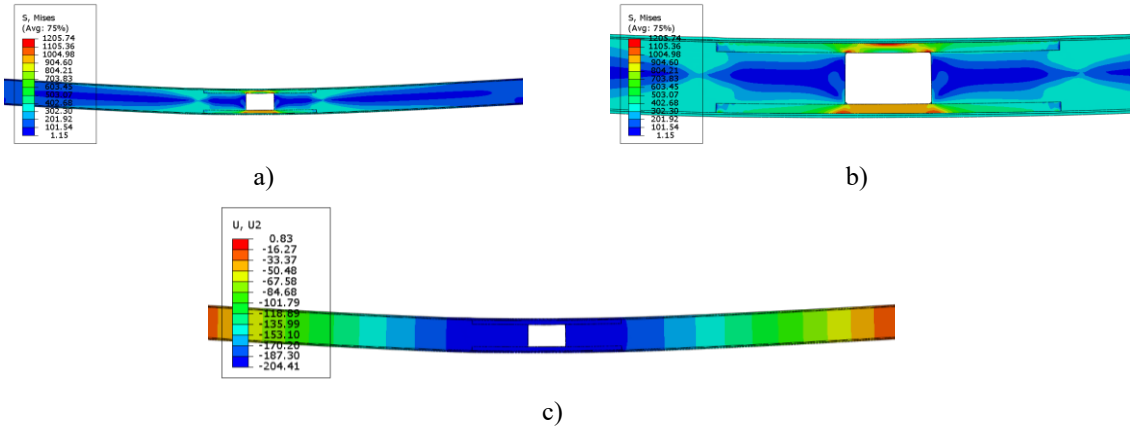


Figure 5-29: Force-displacement response for rectangular opening with different strengthening scheme for 0.65h

As shown in **Figure 5-*30***, the failure mode shifted to the formation of plastic hinges to the left of the opening, at the termination point of the CFRP plates, accompanied by buckling of the top flange agreeing with the findings of [7,16,39]. It is noteworthy that the strengthened beams attained a strength exceeding that of the solid web reference beam. This enhancement is attributed to the increased cross-sectional area at mid-span due to the attachment of the CFRP, which provides greater resistance to the bending moment consistent with the of [4,7,16,39].



a) b)

c)

Figure 5-30: Stress distribution and displacement for 0.65h rectangular opening with CFRP to web; a) Beam stress distribution; b) Stresses around the opening; c) Displacement

As for the beam with the 0.75h opening, the situation is different. The application of CFRP to the flanges alone successfully recovered the lost strength and enhanced the capacity. A similar outcome was observed for the combined configuration, in which CFRP was attached to both the flanges and the web. Notably, as shown in **Figure 5-*31***, no discernible difference exists between the flange-only and the flange-and-web configurations. This is primarily attributed to the fact that the bending moment is almost entirely resisted by the flanges, with only a minor contribution from the web.

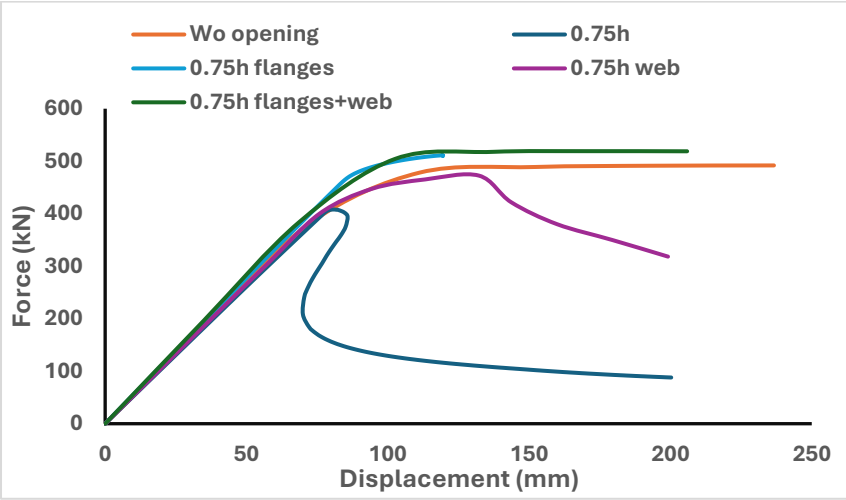


Figure 5-31: Force-displacement response for rectangular opening with different strengthening scheme for 0.75h

However, while attaching CFRP exclusively to the web did enhance the beam's strength, the failure mode remained unchanged from that of the unstrengthened beam, governed by the formation of a mechanism in the top Tee as can be seen in **Figure 5-*32***.

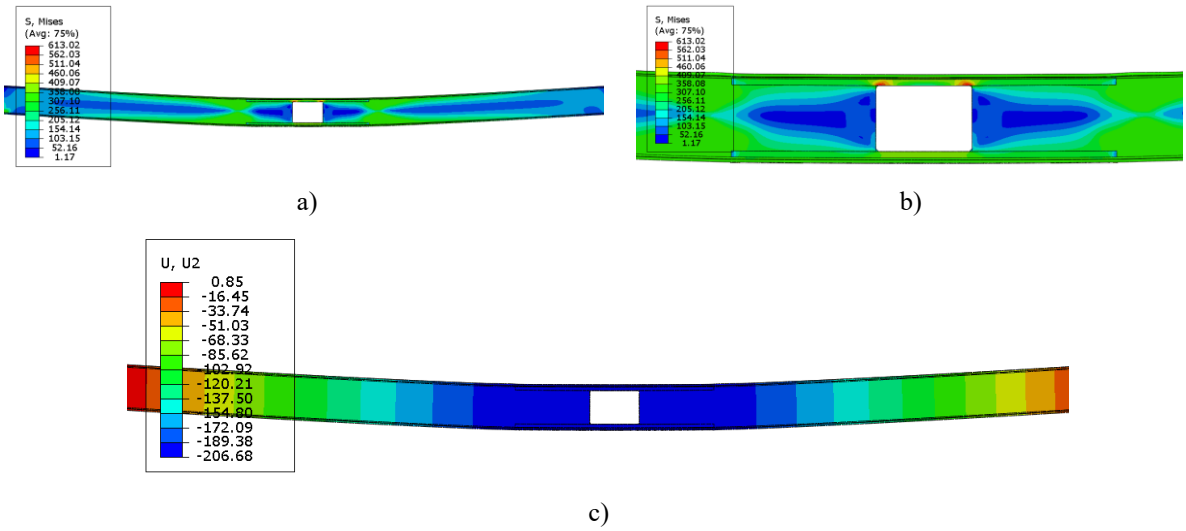
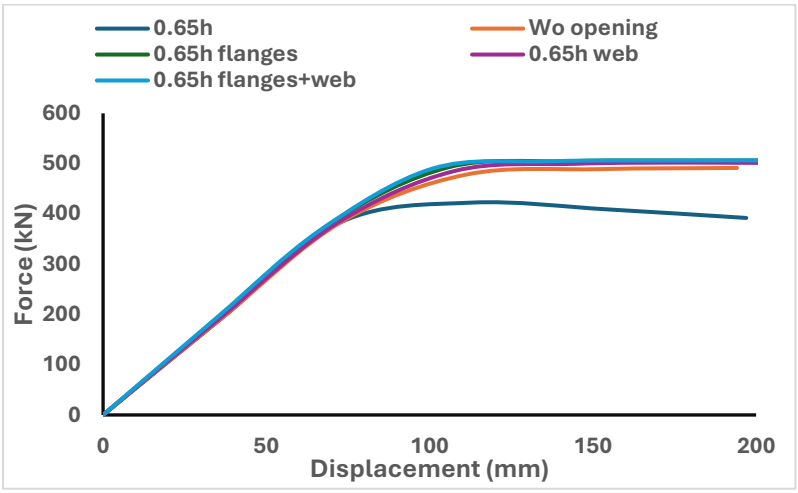


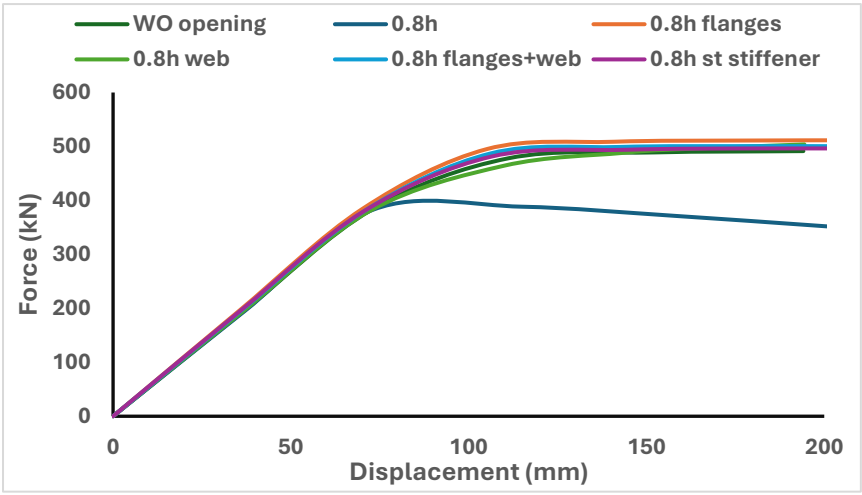
Figure 5-32: Stress distribution and displacement for beam with 0.75h rectangular opening with CFRP to web; a) Beam stress distribution; b) Stresses around the opening; c) Displacement

5.3.2.2. Circular opening

With regards to circular openings, all three strengthening configurations were able to recover the lost strength irrespective of the opening size, as shown in **Figure 5-*33***. For brevity, the discussion herein focuses on the beam with the largest opening size of 0.8h, which serves as a representative severe case for investigating the effects of strengthening, as it possesses the greatest opening depth and consequently the smallest top and bottom tee sections, agreeing with the observations of [1].



a)



b)

Figure 5-33: Force-displacement response for circular opening with different strengthening scheme for a) 0.65h; b) 0.8h

It is evident that the application of CFRP to the flanges alone, the web alone, or both the flanges and web not only recovers the original capacity but also enhances the load-carrying capacity. This enhancement is attributed to the increased thickness of the structural elements whether the flanges or the web at the mid-span section, which is the region subjected to the highest bending

moment and where the plastic hinge ultimately forms. The configuration involving CFRP attached exclusively to the web proved effective in this case, in contrast to the rectangular opening scenario where the greater length of the top Tee provides sufficient room for the snap-back failure mechanism previously observed. In the case of circular openings, the Tee length is considerably shorter, and the absence of sharp corners reduces severe corner stress concentrations and hence the top Tee mechanism agreeing with [4]. Notably, the ultimate failure was characterised by the development of a plastic hinge on the left side, as shown in **Figure 5-*34*** and **Figure 5-*35***.

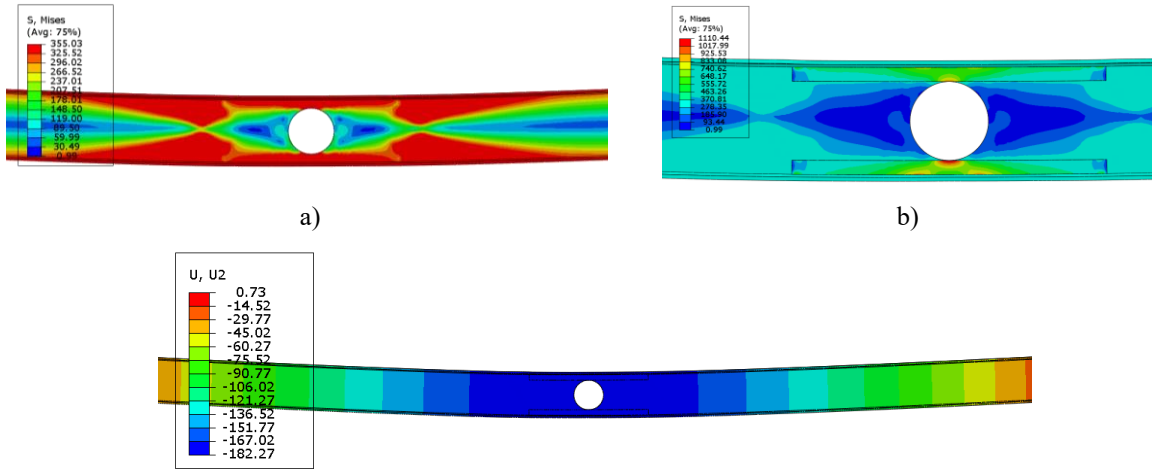


Figure 5-34: Stress distribution and displacement; a) Beam stress distribution; b) CFRP stress distribution; c) Displacement (0.65h)

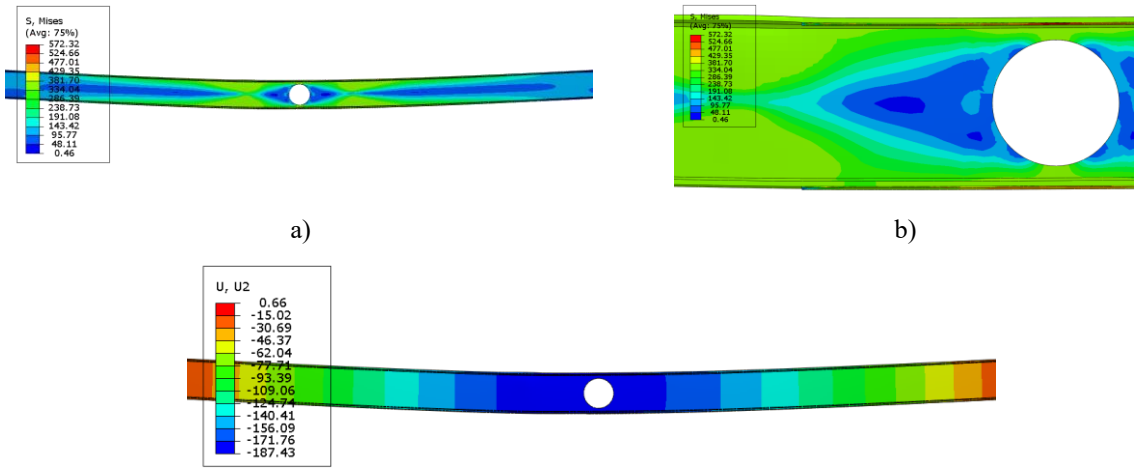


Figure 5-35: Stress distribution and displacement; a) Beam stress distribution; b) CFRP stress distribution; c) Displacement (0.8h)

5.4. Influence of interface debonding

Based on the perfect-bond analyses presented in Section 5.3, selected CFRP configurations were subsequently analysed using the cohesive-interface model in order to quantify the influence of interface damage and debonding. The configurations were selected to include the most effective strengthening arrangement for each opening location, together with representative alternative arrangements where required for comparison.

To monitor the damage initiation and progression within the cohesive interface, two parameters were employed. The first, CSMAXSCRT, indicates the point at which the local interfacial stresses first exceed the corresponding strength, thereby marking the onset of damage. The second, CSDMG, serves as a local scalar damage variable that tracks the extent of debonding; a value of unity signifies complete local loss of cohesive stiffness (debonding), at which point the interface has lost all strength and stiffness. Damage concentrates in two primary regions associated with high stress concentrations such as areas where discontinuity of the material exists or where there are cracks or defects [45].

5.4.1. Quarter-span opening

5.4.1.1. Rectangular opening

Having examined the various CFRP configurations under the assumption of perfect bonding, the investigation now proceeds to the more realistic case of debonding. Debonding refers to the progressive loss of cohesion between the CFRP layer and the steel surface, leading to the deterioration of the composite action between the two materials as a result of the gradual degradation of the adhesive's stiffness and strength. The reason the failure in this case is predominantly governed by the adhesive, rather than the CFRP or the steel surface, is that in FRP-to-metallic bonded connections the adhesive typically constitutes the weakest link. This stands in contrast to FRP-to-concrete applications, where failure is generally dictated by the concrete substrate [9,32,53,45].

The adhesive employed in this section is a nonlinear adhesive, selected for its ability to provide enhanced ductility and higher fracture energy, thereby promoting a more ductile structural response and a gradual decline in load-carrying capacity [53].

Two configurations are investigated in this section: the attachment of CFRP to the flanges alone and to the web alone. As established in the preceding section, the web-only configuration at this location yields the highest strength recovery. Nevertheless, the flange-only configuration is also examined herein to facilitate a direct comparison with the perfect bonding case.

5.4.1.1.1. CFRP web strengthening

It is evident from Figure 5-36 that the response of the strengthened beam with CFRP attached to the web and incorporating a debonding interface is nearly identical to that of its perfectly bonded counterpart, because complete local debonding did not occur before the governing structural failure. Furthermore, the behaviour of the web-strengthened beam under both bonding conditions closely approximates that of the solid beam, consistent with the observations reported in [4,32] and [16], despite the latter employing angles rather than plates, with a deviation of only 2%. The load-carrying capacity under both bonding conditions was enhanced by 44%, increasing from 335 kN for the unstrengthened beam to 483 kN. While the elastic stiffness of the strengthened beam under both bonding conditions remained identical to that of the solid beam, the inelastic stiffness was consistent between the two bonding conditions, albeit differing marginally from the solid beam.

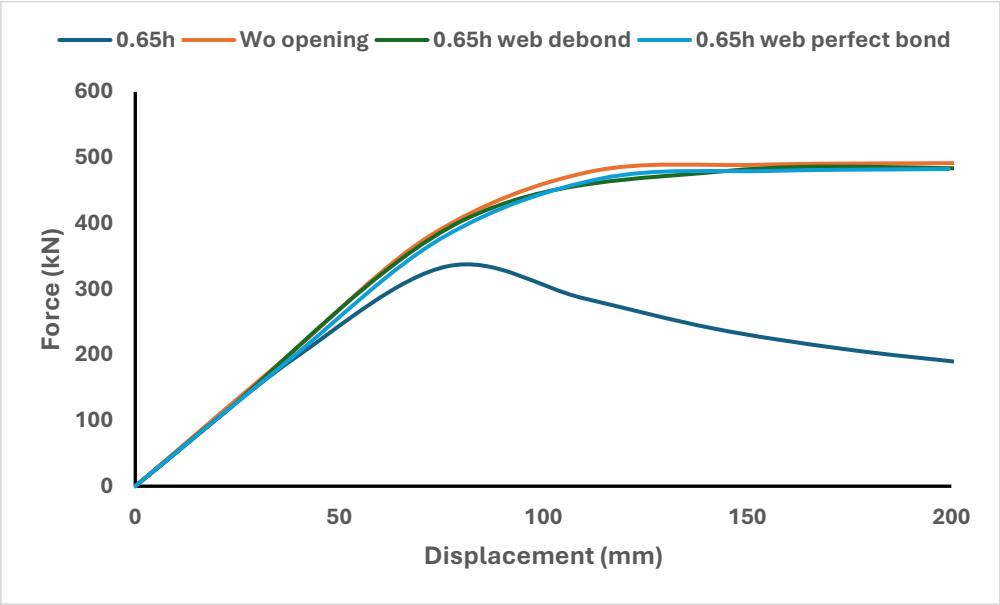


Figure 5-36: Force-displacement response for rectangular opening with different web bonding conditions for 0.65h opening

When the CFRP is bonded to the web, damage initiates at the right end of the plate on the webs of both the top and bottom tee sections adjacent to the opening, as well as at the left corner of

the opening, consistent with the observations reported in [7] and similarly noted for GFRP in [53], where high shear forces and stress concentrations prevail. At these critical corners, plastic hinges develop and bond degradation commences at a displacement of approximately 80 mm, corresponding to a load of 405 kN, beyond which the inelastic stiffness diminished substantially as local CSDMG value reached 0.75 at the critical location as shown in **Figure 5-*37***. Thereafter, damage continued to propagate. By a displacement of 216 mm, local CSDMG value approximately reached 0.92 at the left corners, as damage accumulated preferentially at these locations due to the concentration of high shear stresses, surpassing that observed at the CFRP ends. Nevertheless, a residual, albeit weakened, bond persisted and remained stable until ultimate failure, as illustrated in **Figure 5-*38***.

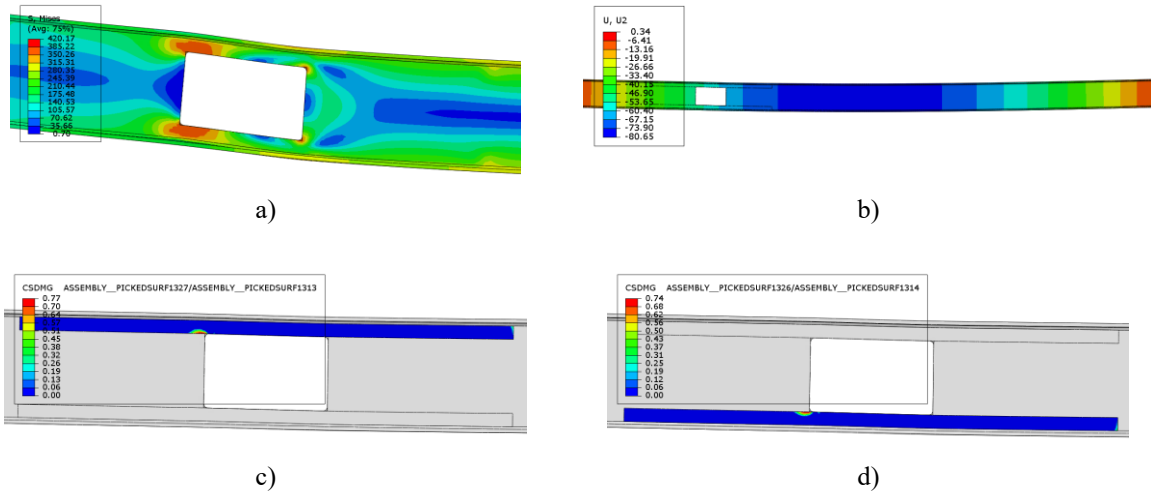


Figure 5-37: Stress distribution and displacement; a) Plastic hinges formed at the LMS; b) Displacement at damage initiation; c) Damage initiation top stem; d) Damage initiation bottom stem

The beam ultimately failed by flexural yielding at midspan, consistent with the findings of [7] and in partial agreement with [39], where discrete lateral restraint resulted in a combined failure mode involving lateral torsional buckling and yielding of the middle section, accompanied by relatively high stress levels in the CFRP plates. Consequently, the CFRP strengthening under both bonding conditions successfully shifted the global failure mode to flexure, despite the presence of limited Vierendeel action at the opening. This restrained Vierendeel mechanism is attributed to the formation of plastic hinges on the left side of the opening know as Low Moment Side (LMS), while the right side remained intact. Although the stiffness of the cohesive interface degraded locally by 0.92 and damage initiated over extensive portions of the bond area, complete loss of cohesion did not occur, as illustrated in **Figure 5-*38***.

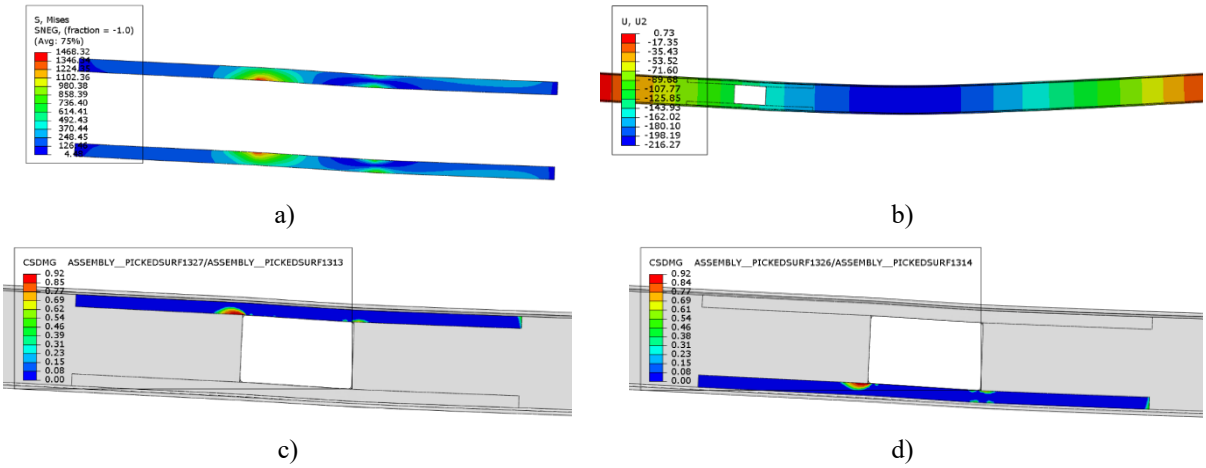


Figure 5-38: Stress distribution and displacement; a) CFRP stress distribution; b) Displacement; c) Damage evolution top stem; d) Damage evolution bottom stem

5.4.1.1.2. CFRP flange strengthening

Conversely, the CFRP attached to the flanges under both bonding conditions did not fully restore the strength of the solid beam (See **Figure 5-*39***). For the cohesive interface condition, the capacity was enhanced by 22%, increasing from 335 kN to 408 kN, corresponding to a 17% reduction relative to the solid reference beam. In contrast, under perfect bonding conditions, the strength improved by 28%, rising from 335 kN for the unstrengthened perforated beam to 430 kN, representing a reduction of approximately 12% relative to the solid beam. The maximum load was attained at a displacement of 92 mm for the case of the cohesive interface, in contrast to the perfectly bonded case, where it was reached at 110 mm. The elastic stiffness remained unchanged for both bonding conditions compared to the solid beam; however, at a displacement of approximately 50 mm, damage initiated and the stiffness decreased slightly for both conditions relative to the solid beam, with the debonding case exhibiting a more pronounced reduction than the perfectly bonded case.

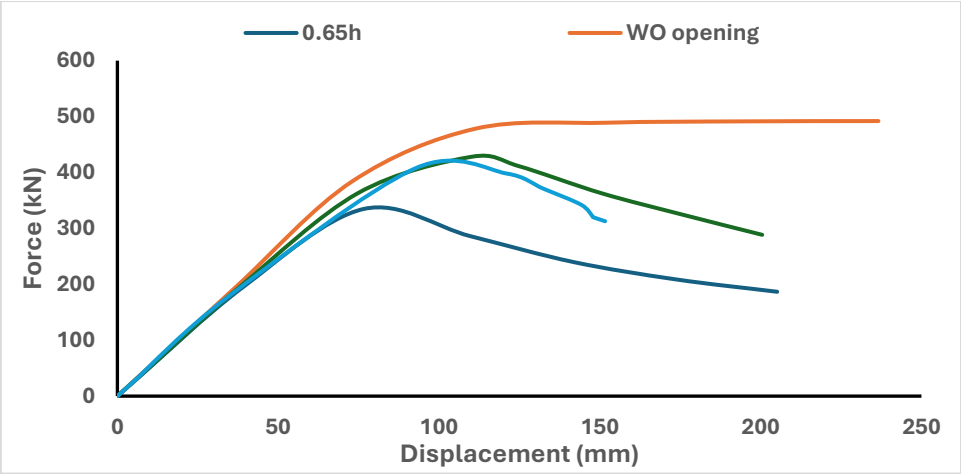


Figure 5-39: Force-displacement response for different bonding conditions for CFRP flange strengthening

For the cohesive interface condition, damage initiated at a displacement of 92 mm at the edges of the CFRP plates and at locations corresponding to the opening corners at the LMS, where stresses induced by the Vierendeel bending moment are most severe. Plastic hinges formed completely at the left corners (LMS), whereas at the right corners, hinge development remained incomplete, consistent with the behaviour observed in the web-attached CFRP case. At this stage, local CSDMG reached 0.6 for the top flange CFRP and 0.82 for the bottom plate, as shown in **Figure 5-*40***.

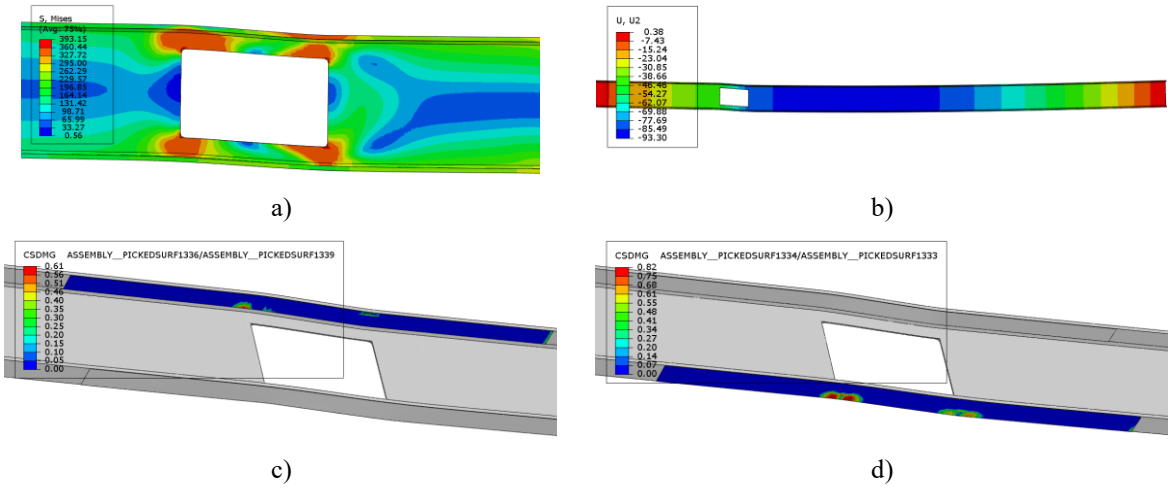


Figure 5-40: Stress distribution and displacement for beam with 0.65h rectangular opening; a) Stress distribution around the opening; b) Displacement at damage initiation; c) Damage initiation top flange; d) Damage initiation bottom flange

Damage initiates from the internal corners rather than the external edge at the interface on the low-moment side (LMS) of the opening and at the bottom corner of the high-moment side (HMS), attributable to high out-of-plane stresses induced by flange buckling under Vierendeel bending. Conversely, damage at the top corner of the HMS originates from the external edge, driven by extensive yielding resulting from the tensile component of Vierendeel bending at that location. This behavior is further validated by the stress distribution within the CFRP plates, where regions of elevated stress correspond directly to these interfacial locations (see **Figure 5-*41***).

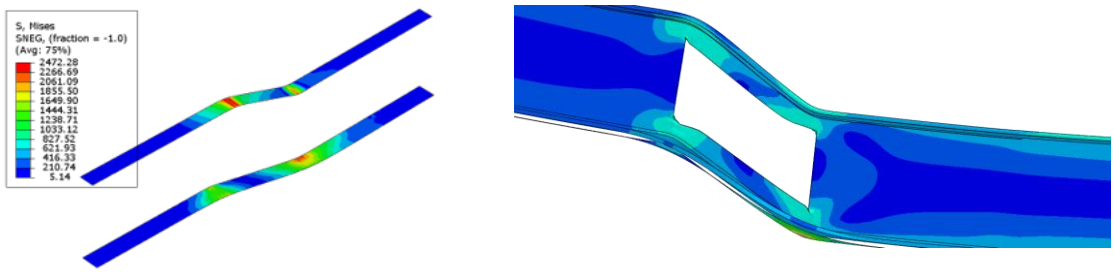


Figure 5-41: CFRP stress distribution

Beyond this point, the bond continued to deteriorate, accompanied by a pronounced increase in deflection resulting from the full development of the Vierendeel mechanism, while the CFRP had not yet fully detached owing to the nonlinear nature of the adhesive. Complete debonding ultimately occurred at a displacement of 176 mm for the CFRP attached to the top flange in the region corresponding to the opening, as illustrated in **Figure 5-*42***. Under both bonding conditions, the CFRP was unable to prevent the Vierendeel bending mechanism but merely delayed its onset.

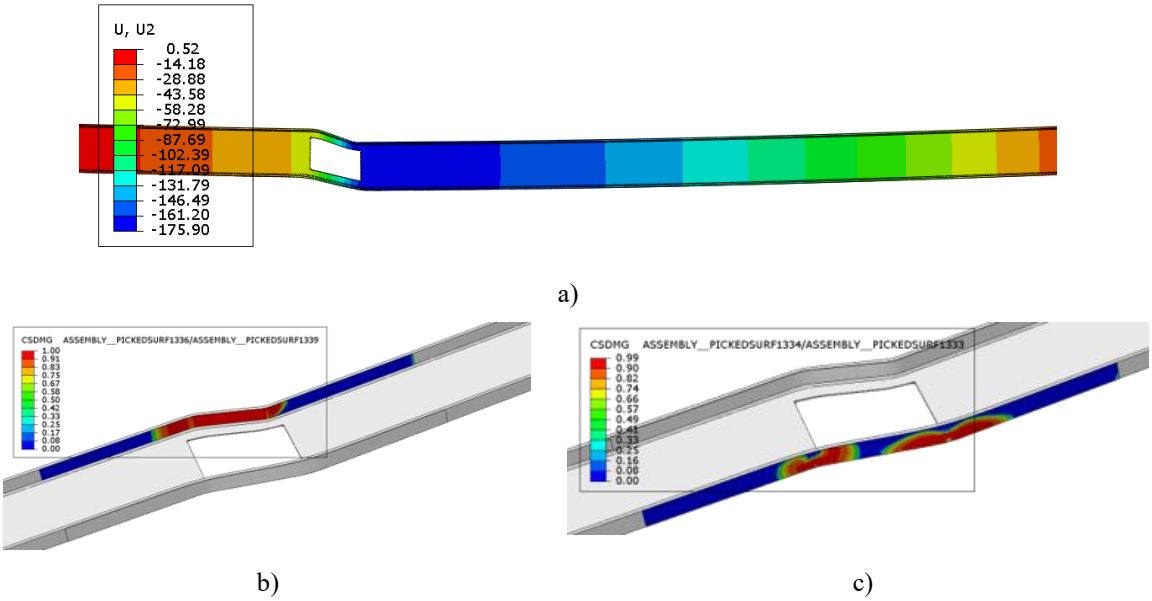


Figure 5-42: Displacement and damage evolution for beam with 0.65h rectangular opening; a) Displacement at debonding; b) Damage top flange; c) Damage bottom flange

5.4.1.2. Circular opening

For the circular opening, only the configuration involving CFRP attached to the web is examined in the interest of efficiency. As shown in **Figure 5-*43***, the application of CFRP to the web under both bonding conditions successfully restored the strength to that of the solid reference beam, consistent with the observations reported in [4,32]. The stiffness was likewise recovered in both the elastic and inelastic stages, matching that of the solid beam. Under the cohesive interface condition, the capacity was enhanced by 7%, increasing from 450 kN to 482 kN, corresponding to a reduction of only 1.82% relative to the solid beam. In the perfectly bonded case, the capacity increased by 7.86%, rising from 450 kN to 487 kN, with a reduction of merely 1%. The maximum load was attained at a displacement of 235 mm for the debonding case and 244 mm for the perfectly bonded case.

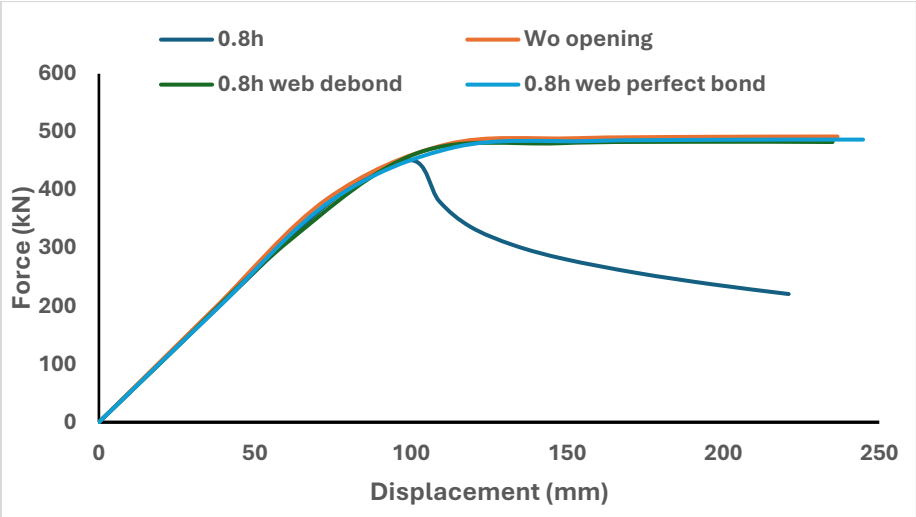


Figure 5-43: Force-displacement response for circular opening with different bonding conditions for 0.8h opening

It is important to note that at a displacement of 61 mm, two plastic hinges formed in the steel beam on the LMS, accompanied by a very small Vierendeel displacement, as shown **Figure 5-*44***a,b. Concurrently, damage initiated at the ends of the CFRP plate and at the top and bottom regions of the CFRP adjacent to the highly stressed area corresponding to the plastic hinge location. However, the damage criterion was satisfied only over a very limited portion at the right edge, with local CSDMG value of 0.12 , as illustrated in **Figure 5-*44***c,d.

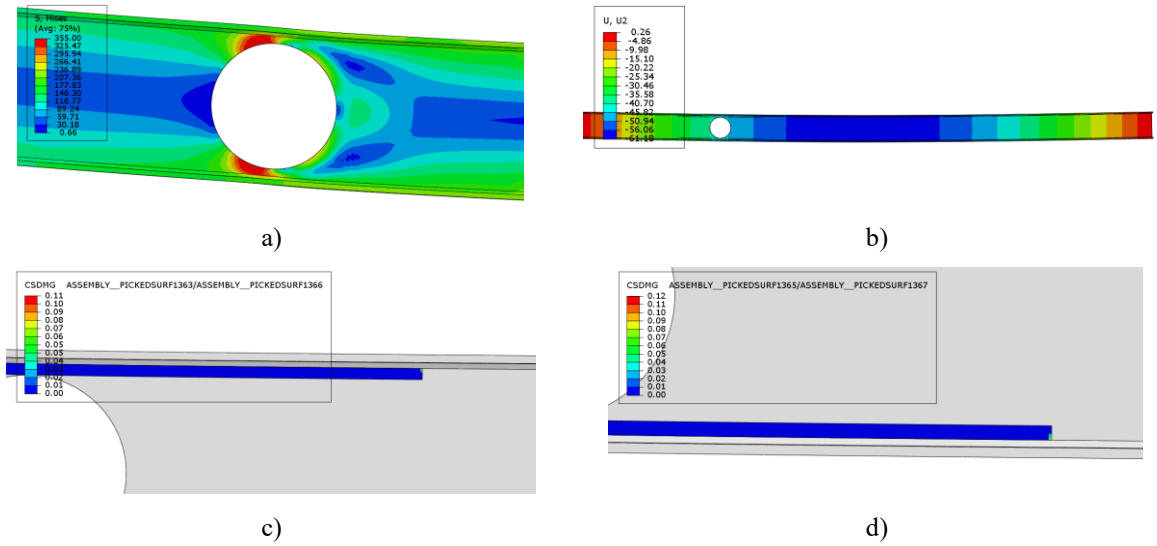


Figure 5-44: Stress distribution and displacement for beam with 0.8h circular opening; a) Stress distribution around the opening; b) Displacement at damage initiation; c) Damage initiation top stem; d) Damage initiation bottom stem

Upon further loading, the beam ultimately failed in flexure at a deflection of 195 mm. At this stage, the interface had accumulated substantial damage, with local bond degradation CSDMG value near the opening edges at the plastic hinge location reaching 0.75; however, complete debonding did not occur, as illustrated in **Figure 5-*45***.

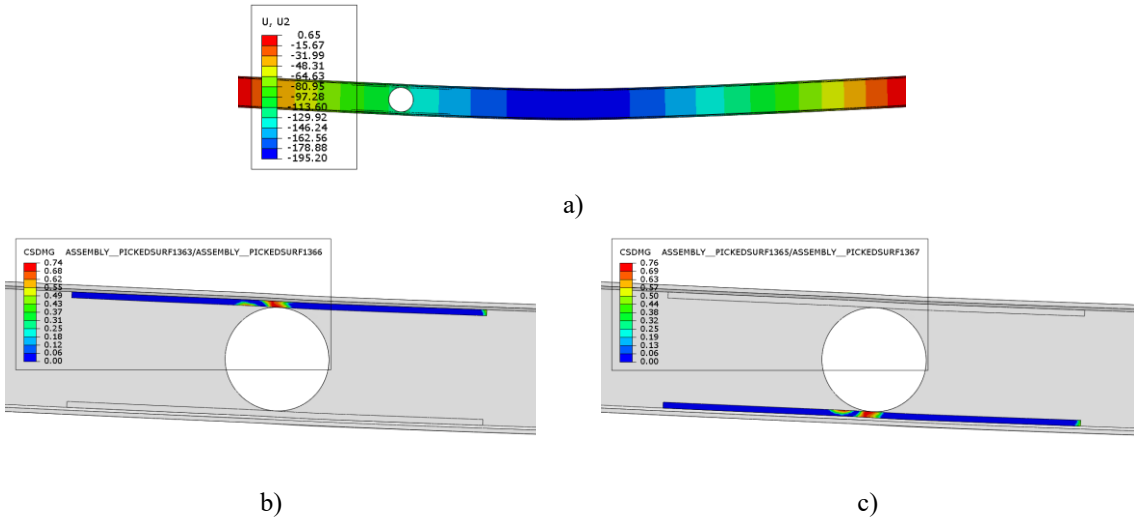


Figure 5-45: Displacement and damage evolution for beam with 0.8h circular opening; a) Displacement b) Damage top stem; c) Damage bottom stem

Both bonding conditions successfully prevented the Vierendeel bending mechanism and shifted the failure mode to that of the solid beam, characterized by the formation of a plastic hinge at midspan with the stress level in the CFRP approximately 1000 MPa, as shown in **Figure 5-*46***.

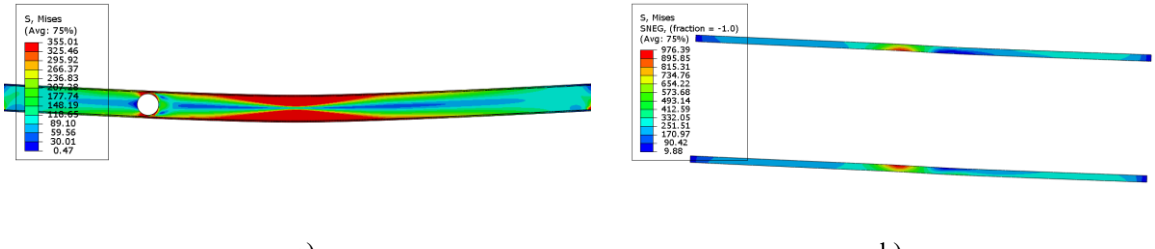


Figure 5-46: Stress distribution for beam with 0.8h circular opening; a) Steel beam; b) CFRP plates

5.4.2. Mid-span opening

5.4.2.1. Rectangular opening

For this case, the CFRP under both bonding conditions successfully restored the strength and stiffness of the solid beam, as illustrated in **Figure 5-*47***. or the cohesive interface condition, the strength was fully restored to that of the solid beam and further enhanced by 4.2%, increasing from 490 kN to 512 kN, representing a 20.4% improvement relative to the perforated beam. Under the perfectly bonded condition, the capacity exhibited a marginal increase of 5% relative to the solid beam, rising from 490 kN to 516 kN. This enhancement is attributed to the attachment of CFRP to the web, which increases the effective cross-sectional area at midspan, particularly because the CFRP is positioned away from the neutral axis and in proximity to the flanges, where stresses are more pronounced. Notably, the beam with the cohesive interface

condition exhibited an abrupt loss of stiffness in the inelastic range, attributable to rapid yielding of the mid-section induced by interface damage, in contrast to the gradual stiffness degradation observed in the perfectly bonded case, which is ascribed to the integrity of the interface.

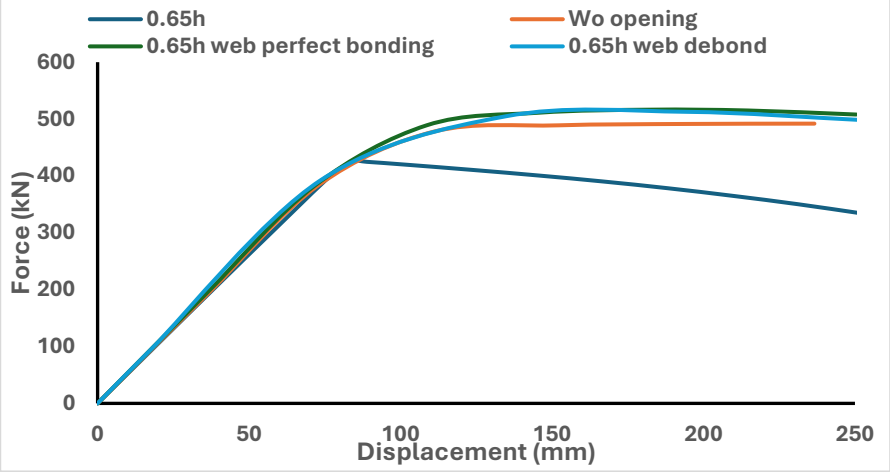
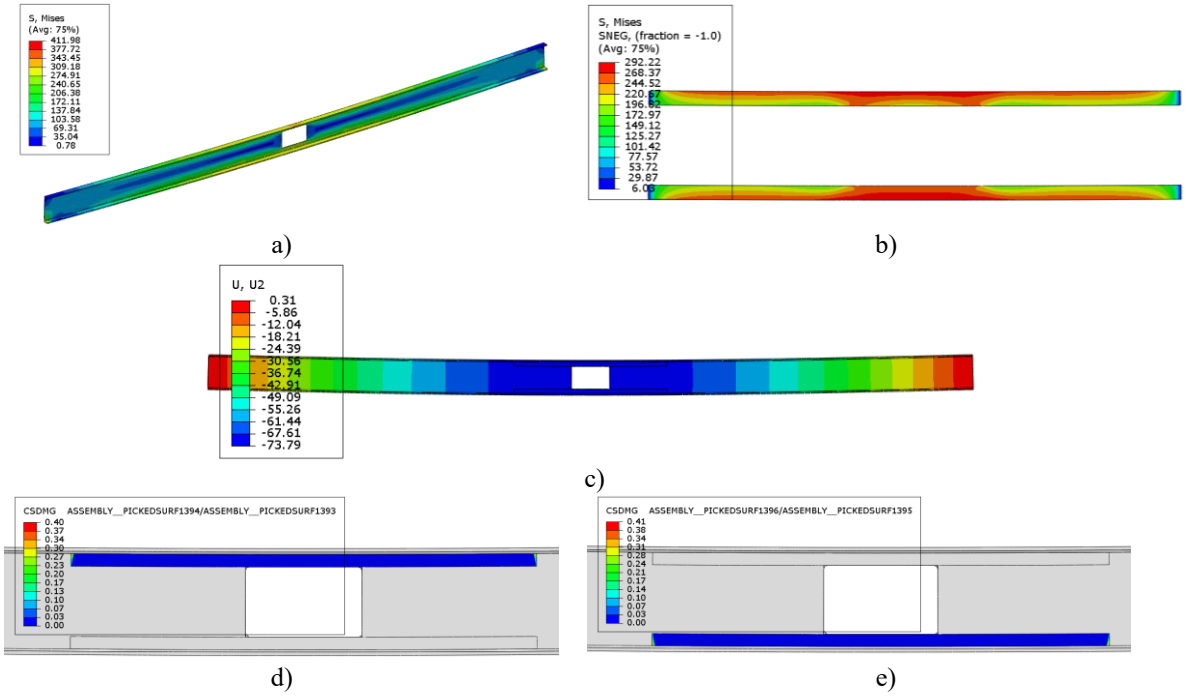


Figure 5-47: Force-displacement response for rectangular opening with different bonding conditions for 0.65h opening

For the interface debonding condition, at a displacement of 73 mm, both the top and bottom flanges had yielded, and the strength limit of the cohesive interface was reached over a very limited area at the ends of the CFRP plates, with only local CSDMG value of 0.4 interface degradation at that stage. At this point, the CFRP experienced relatively low stress levels, and damage subsequently initiated at the corners of the opening, as shown in **Figure 5-*48***.



a) b)

c)

d) e)

Figure 5-48: Stress distribution and displacement for beam with 0.65h rectangular opening; a) Beam stress distribution; b) CFRP stress distribution; c) Displacement at damage initiation; d) Damage initiation top stem; e) Damage initiation bottom stem

Upon further loading, yielding propagated through the steel sections beyond the CFRP-strengthened region, and the top flange adjacent to the CFRP underwent slight buckling, leading to a reduction in beam strength under both bonding conditions, with the cohesive interface exhibiting a more pronounced reduction than the perfectly bonded case.

Concurrently, damage continued to accumulate within the interface until, at a displacement of 261 mm, the CFRP plate debonded on the left side, and a plastic hinge became fully developed at that location, as shown in **Figure 5-*49***. Following debonding, the beam capacity decreased more substantially than in the perfectly bonded condition. The final failure was consequently governed by the formation of this shifted hinge, consistent with the corresponding perfectly bonded case and in agreement with the observations of [7], with the CFRP experiencing higher stresses in the top Tee owing to the high compressive forces acting in that region.

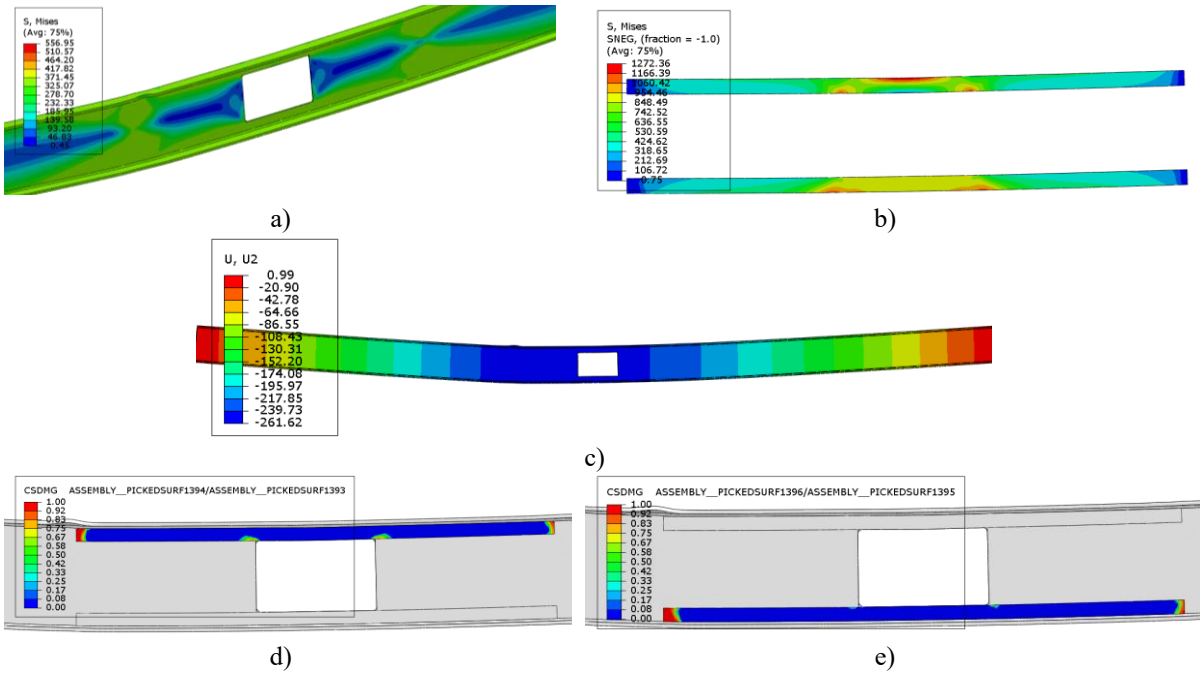


Figure 5-49: Stress distribution and displacement; a) Beam stress distribution; b) CFRP stress distribution; c) Displacement at debonding; d) Damage evolution to top stem; e) Damage evolution to bottom stem

For the CFRP attached to the flanges under both bonding conditions, the beam exhibited full recovery of stiffness and strength as shown in **Figure 5-*50***, with a more pronounced loss of stiffness in the inelastic range observed for the cohesive interface condition compared to the perfectly bonded case, consistent with the findings reported in [4,7,16,39]. The gradual stiffness degradation in the perfectly bonded case is attributed to the greater structural contribution of the CFRP. The strength of the beam exceeded that of the solid reference beam under both conditions, with enhancements of 5.5% and 4.6% for the perfectly bonded and debonding cases, respectively, increasing from 490 kN to 518 kN and 514 kN.

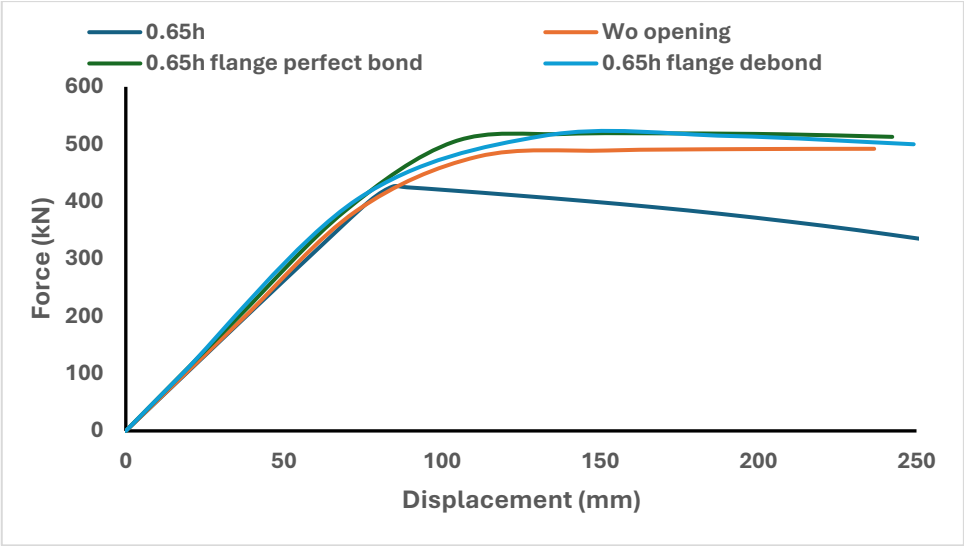


Figure 5-50: Force-displacement response for different bonding conditions for 0.65h rectangular openings

Damage initiated at the interface at a displacement of 74 mm, occurring at the ends of both the top and bottom flange CFRP plates. At this stage, approximately local CSDMG value of 0.5 had been reached at these extremities, driven by the high stresses arising from the stress concentration, as illustrated in **Figure 5-*51***.

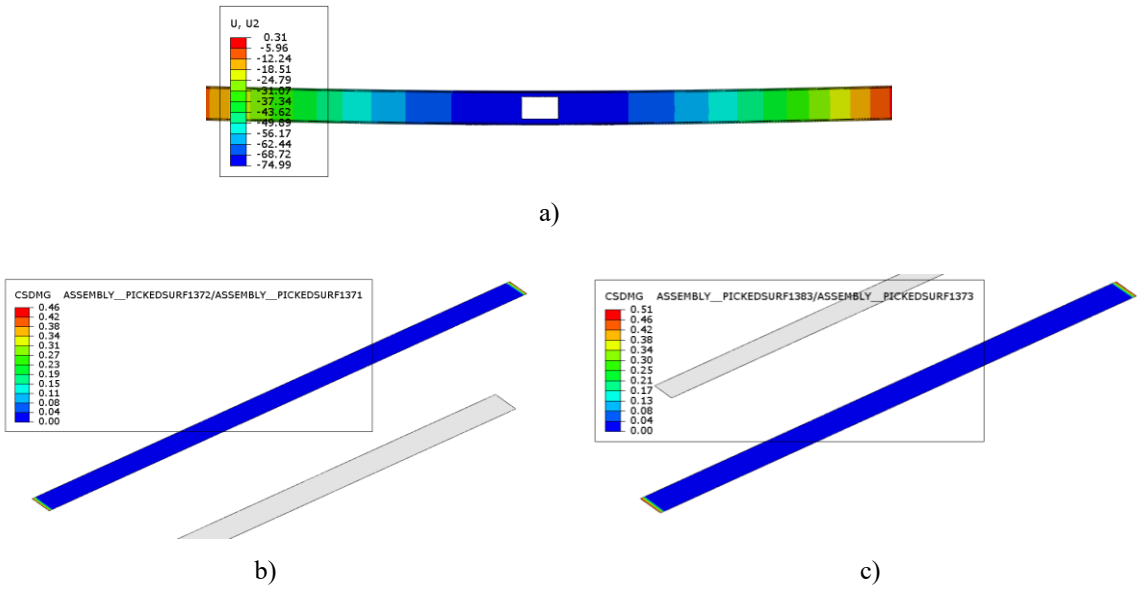


Figure 5-51: Displacement and damage initiation for beam with 0.65h rectangular opening; a) Displacement at damage initiation; b) Damage initiation top flange; c) Damage initiation bottom flange

Upon further loading, yielding of the steel beam propagated while the interface continued to accumulate damage and lose stiffness, resulting in increased deflection. This process induced buckling of the top flange adjacent to the CFRP plate on both sides, consistent with the observations reported in [7]. At a displacement of 194 mm, the ends of the CFRP plate attached to the bottom flange underwent debonding at the edges, with a more extensive debonded area

observed on the left side. Consequently, stresses redistributed to the steel section, a plastic hinge formed at this location, and buckling of the top flange is amplified, mirroring the behaviour observed in the perfectly bonded condition. The CFRP stresses at the ends reached 650 MPa, as shown in Figure 5-52, notably lower than the corresponding stresses of approximately 1200 MPa recorded for the perfectly bonded case.

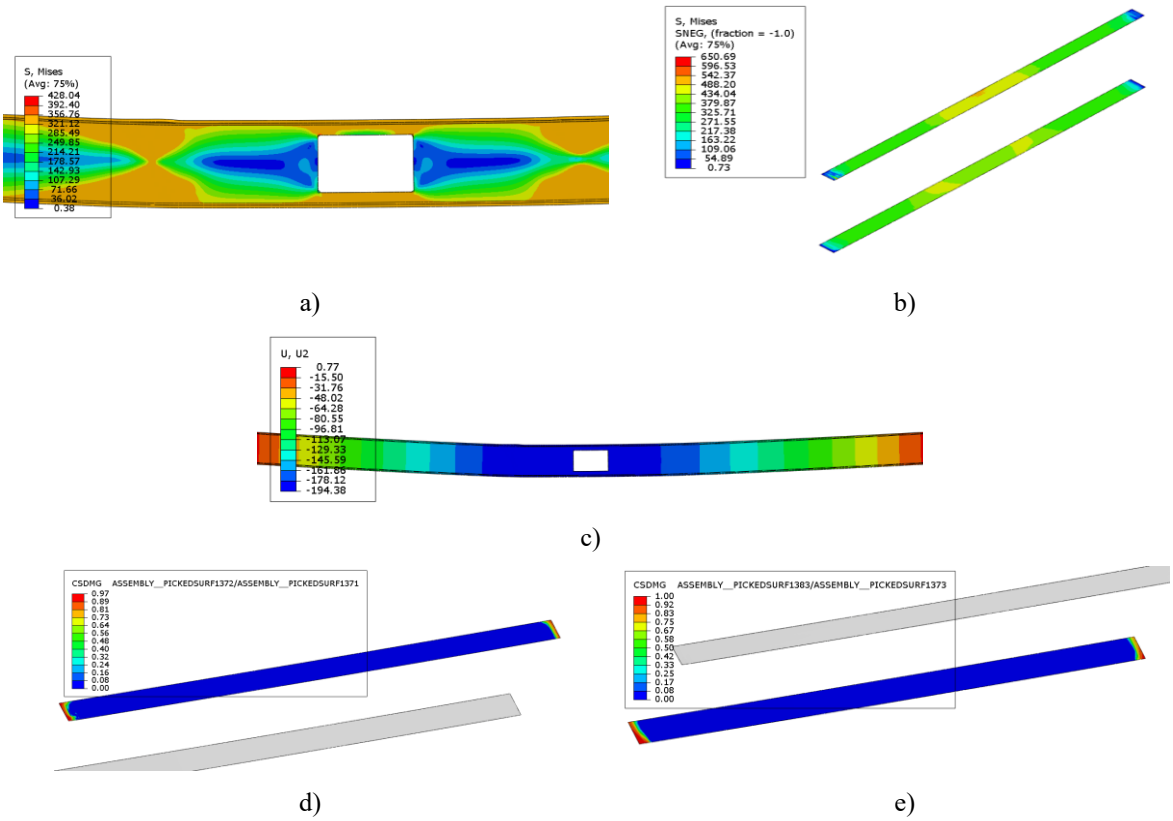


Figure 5-52: Stress distribution and displacement for beam with 0.65h rectangular opening; a) Beam stress distribution; b) CFRP stress distribution; c) Displacement at debonding; d) Damage evolution top flange; e) Damage evolution bottom flange

5.4.2.2. Circular opening

It is evident from Figure 5-53 that the response of the strengthened beam with CFRP attached to the web and incorporating a cohesive interface is nearly identical to that of the solid beam model. The elastic stiffness under both bonding conditions matches that of the solid beam, while the inelastic stiffness is identical for the two bonding conditions and differs only marginally from the solid beam. The decline in stiffness in the inelastic region occurs at a displacement of approximately 75 mm, attributable to plastification of the midspan section and buckling of the top flange, consistent with the observations reported in [4]. Despite the propagation of plasticity through the beam, the load continues to increase owing to the contribution of the CFRP, as the interface has not yet failed. At a displacement of 145 mm and a load of 488 kN, the cohesive interface case exhibits a lesser increase in strength similar to that of the solid beam, in contrast

to the perfectly bonded condition, where the load continues to rise, achieving a 3% enhancement relative to the solid beam, with the capacity rising from 490 kN to 506 kN.

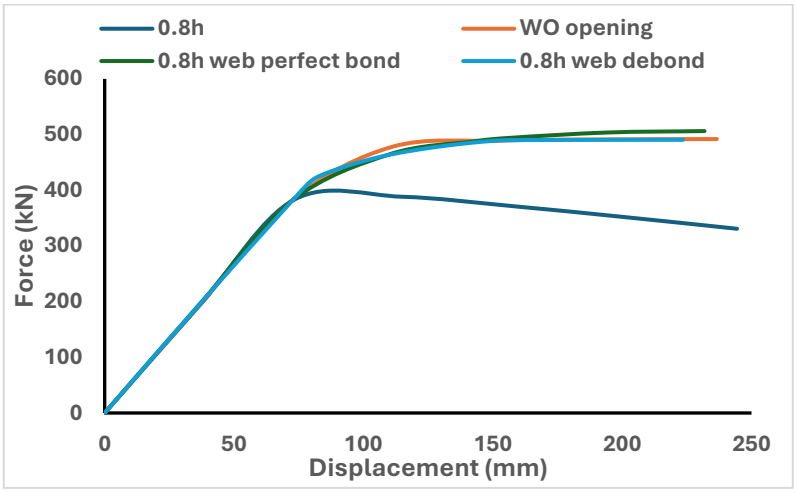


Figure 5-53: Force-displacement response for 0.8h circular opening with different bonding condition

Interface damage initiated at a deflection of 50 mm, at which point the CFRP stresses remained relatively low at 300 MPa, as shown in **Figure 5-*54***. At a deflection of approximately 100 mm, a further reduction in stiffness occurred, attributable to the extensive damage accumulated within the interface of the CFRP bonded to the top tee stem.

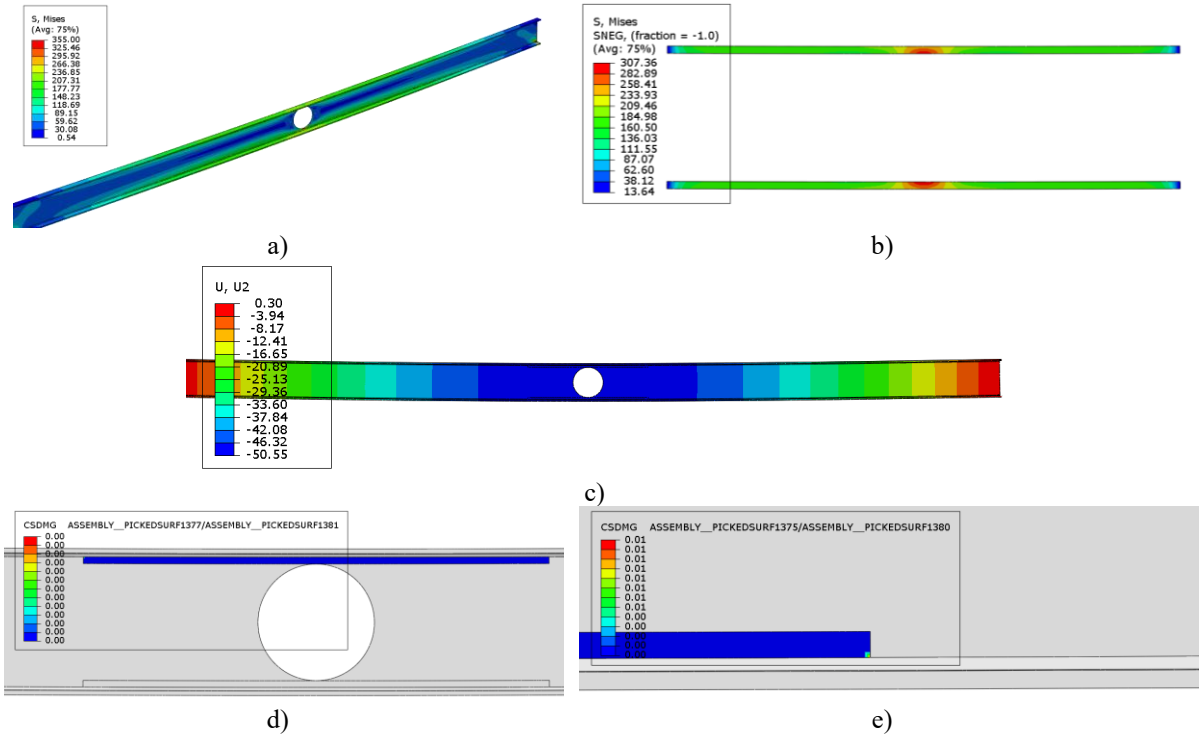


Figure 5-54: Stress distribution and displacement for beam with 0.8h circular opening; a) Beam stress distribution; b) CFRP stress distribution; c) Displacement at damage initiation; d) Damage initiation top stem; e) Damage initiation bottom stem

At a displacement of approximately 120 mm, the CFRP attached to the top tee stem, which is subjected to compression, fails without any evidence of debonding. Beyond this point, the beam sustains a only marginal increase in load as forces are redistributed to the steel section and the bottom CFRP plate. This redistribution intensifies the stresses in the bottom CFRP, ultimately leading to complete local debonding at a displacement of 176 mm, with the debonded region extending more extensively at the opening location, where stresses are most severe, as illustrated in Figure 5-55.

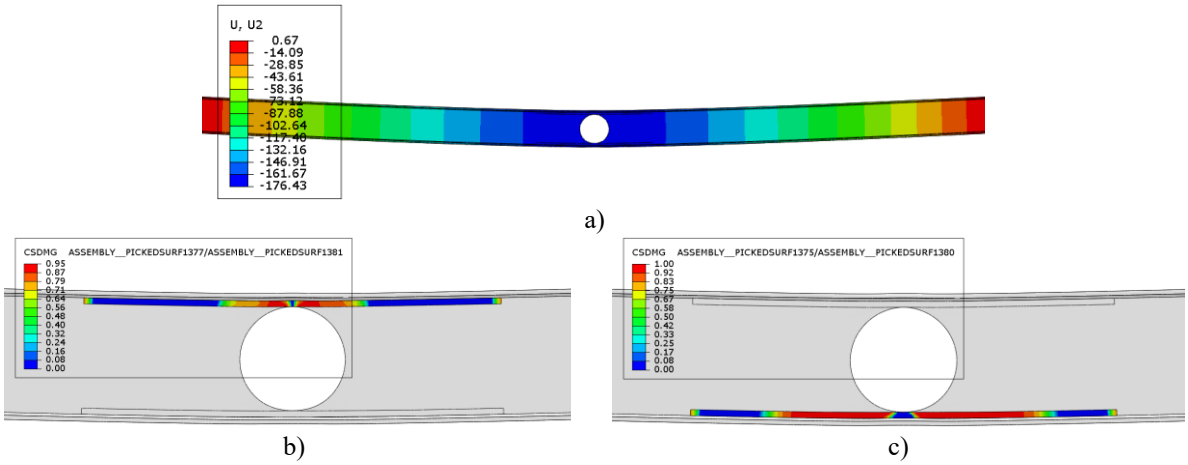


Figure 5-55: Displacement and damage evolution for beam with 0.8h circular opening; a) Beam displacement; b)Damage evolution top stem; c) Damage evolution bottom stem

The failure mode in this case is not governed by a shifted plastic hinge, as the section at the end of the CFRP has not fully plastified. Rather, failure is initiated by the compressive failure of the top CFRP plate, owing to the lower compressive strength of CFRP relative to its tensile capacity, followed by local debonding of the bottom CFRP plate under high stresses, as illustrated in **Figure 5-*55***. In contrast, under the perfectly bonded condition, the top CFRP plate fails first, after which the bottom CFRP plate fails in tension (see **Figure 5-*56***).

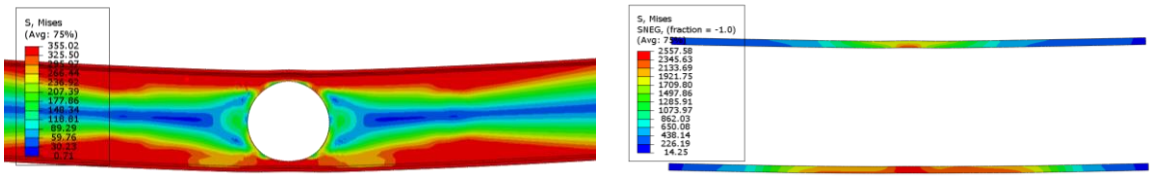


Figure 5-56: Stress distribution; a) Steel Beam; b) CFRP plates

When the CFRP is attached to the flanges, the beam exhibits a response similar to that observed for the rectangular opening with the same strengthening configuration. The perfectly bonded and cohesive interface conditions display comparable behaviour in terms of stiffness and strength up to a displacement of 150 mm, beyond which the debonding case begins to experience a reduction in capacity, whereas the perfectly bonded case maintains its load-

carrying capacity. The strength enhancement relative to the solid beam is 4% for the perfectly bonded condition, increasing from 490 kN to 511 kN, while the debonding condition achieves a 2.5% enhancement, rising from 490 kN to 504 kN. The inelastic stiffness exceeds that of the solid beam, accompanied by a more gradual loss of stiffness, because the attachment of CFRP to the flanges is considerably more effective than web attachment, as it increases the second moment of inertia of the section to a greater extent. Despite the differing final failure modes, the beam achieves nearly the same strength as observed in the case of CFRP attached to the web (see Figure 5-57).

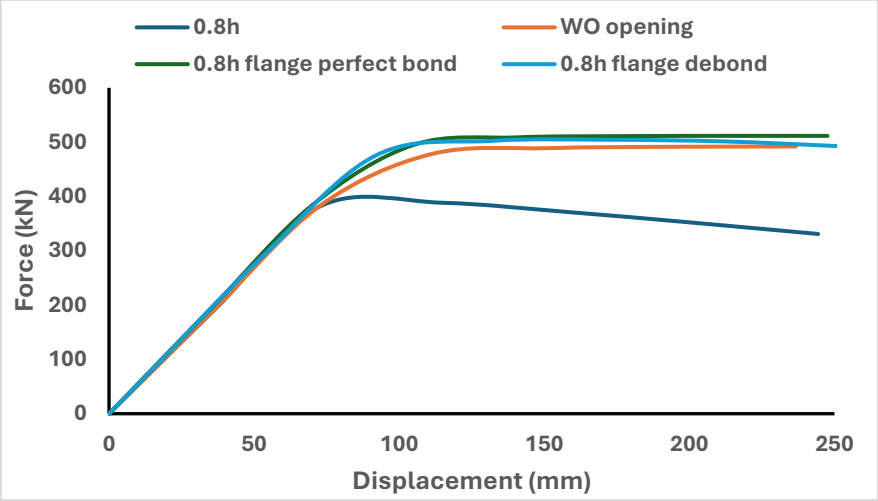
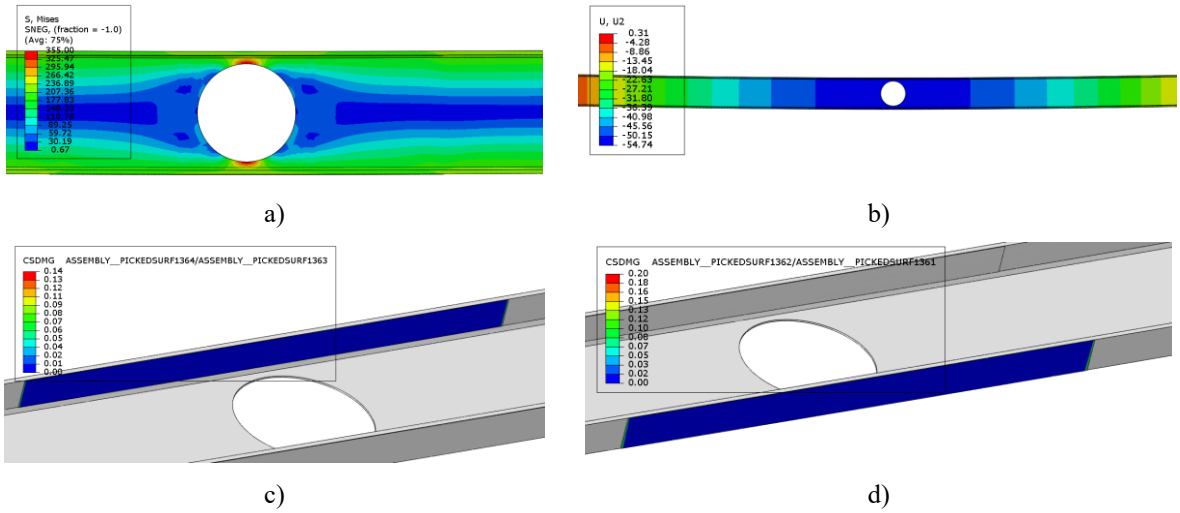


Figure 5-57: Force-displacement response for 0.8h circular opening with different bonding conditions

For the cohesive interface condition, the interface experiences first damage at a displacement of 54 mm at the ends of the CFRP plates where local CSDMG of 0.22 interface damage has accumulated as shown in Figure 5-58. At this point yielding commences at the mid-span section, where the bending stresses are highest.



a) b)

c) d)

Figure 5-58: Stress distribution and displacement for beam with 0.8h circular opening; a) Beam stress distribution; b) Displacement; c) Damage top flange; d) Damage bottom flange

As the load increases, stresses in the midspan section intensify, yielding propagates, and the CFRP stresses correspondingly rise. Owing to the enhanced flexural strength of the midspan section resulting from the contribution of the CFRP plates, stress concentrations develop at both ends of the top CFRP plate, with plasticity concentrating in this region and inducing slight buckling of the top flange adjacent to the plate ends, consistent with the observations reported in [39,16,4]. The combined effects of yielding and localized buckling in this region contribute to a softening response, which persists until the beam attains its peak capacity at a displacement of 172 mm and a load of 504 kN. Thereafter, the response enters a plateau phase with only a marginal reduction in load-carrying capacity, as similarly noted in [32,39], during which plastic flow continues. Complete local debonding of the CFRP ends occurs at a displacement of 219 mm, with the left end of the CFRP plate being more severely affected, coinciding with progressively increasing top flange buckling at this location, while the stress level in the CFRP remains below 800 MPa, as shown in **Figure 5-*59***.

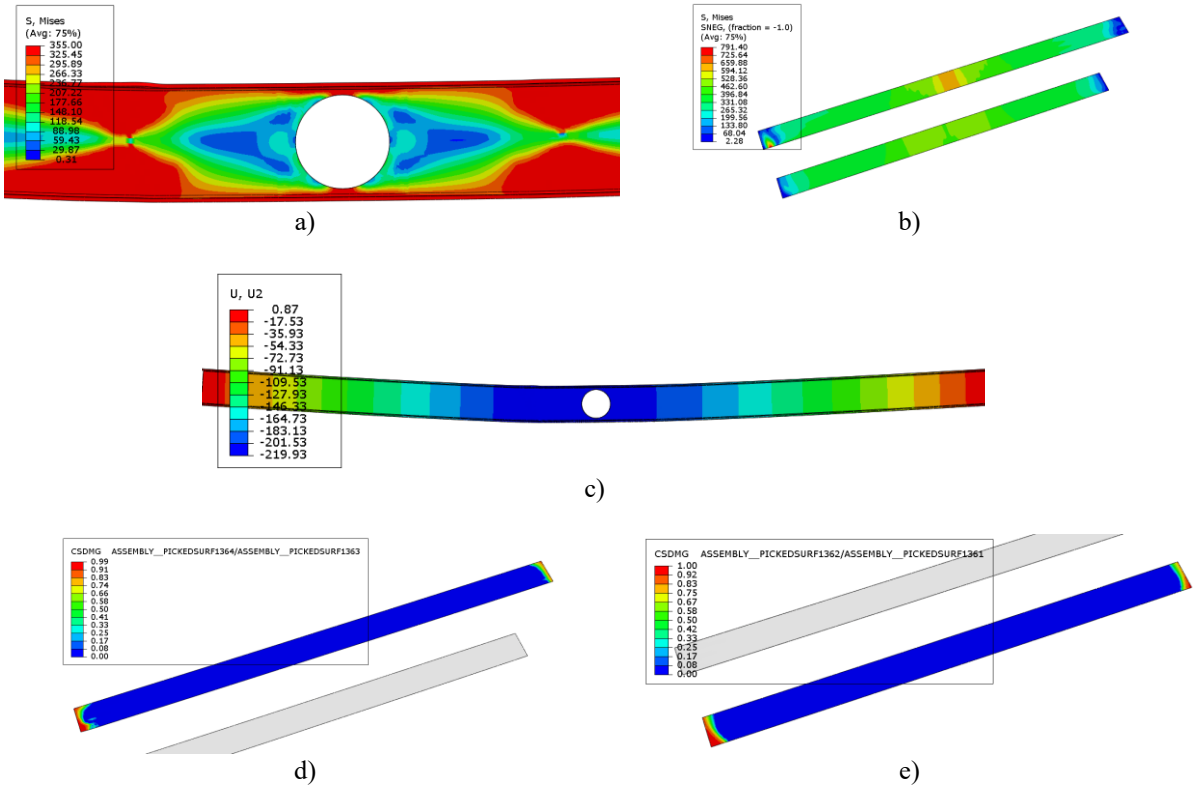


Figure 5-59: Stress distribution and displacement for beam with 0.8h circular opening; a) Beam stress distribution; b) CFRP stress distribution; c) Displacement at debonding; d) Damage top flange; e) Damage bottom flange

5.5. Influence of adhesive behaviour

The influence of adhesive behaviour is investigated for the representative case of a rectangular opening with a depth of 0.65h, located at quarter span. Two adhesive models are considered, corresponding to the linear and nonlinear constitutive responses introduced in chapter 4. As illustrated in **Figure 5-*60***, the two models exhibit distinctly different traction–separation behaviour. The linear adhesive is characterised by a higher initial stiffness, whereas the nonlinear adhesive is more compliant and exhibits a substantially higher fracture energy, allowing greater deformation and energy dissipation before complete interface failure [9]. The comparison is performed for two CFRP strengthening configurations, with the CFRP bonded either to the web or to the flanges and focuses on the resulting global load–displacement response, the initiation and progression of interface damage, and the governing failure mechanism.

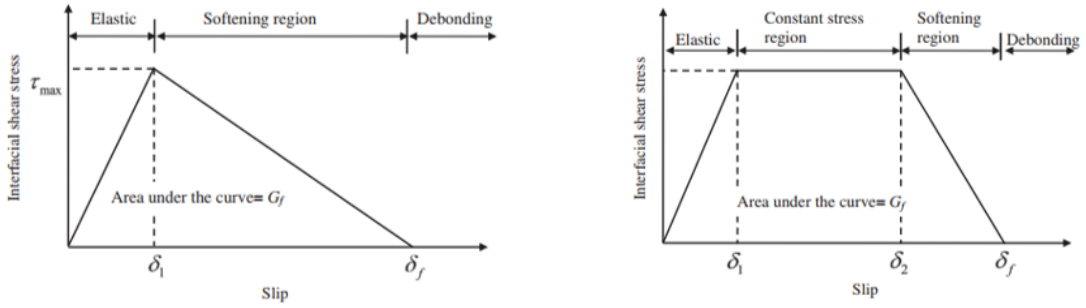


Figure 5-60: Constitutive model for adhesive; a) Linear; b) Nonlinear [9]

5.5.1. CFRP web strengthening

For the case of CFRP bonded to the web using a linear adhesive, the elastic stiffness of the beam is identical to that observed in the nonlinear adhesive model. However, at a displacement of 37 mm, the stiffness begins to deviate from that of the perforated steel beam as a result of the interface damage at lower load levels, whereas the nonlinear adhesive maintains its stiffness throughout this phase, as shown in **Figure 5-*61***. At a displacement of approximately 75 mm, the beam with the nonlinear adhesive experiences a reduction in stiffness, whereas the linear adhesive retains nearly constant inelastic stiffness until sudden failure occurs at its maximum load of 448 kN, corresponding to a displacement of 91 mm. This capacity is below that of the solid beam, indicating that the linear adhesive configuration does not fully recover the strength of the solid beam, despite restoring its stiffness, with a reduction in capacity of 9.5% relative

to the solid beam. In contrast, the beam with the nonlinear adhesive, owing to the greater deformation capacity of the adhesive, continues to sustain increasing load until it attains a maximum load of 483 kN at a displacement of 215 mm, representing a reduction of only 1.8% relative to the solid beam.

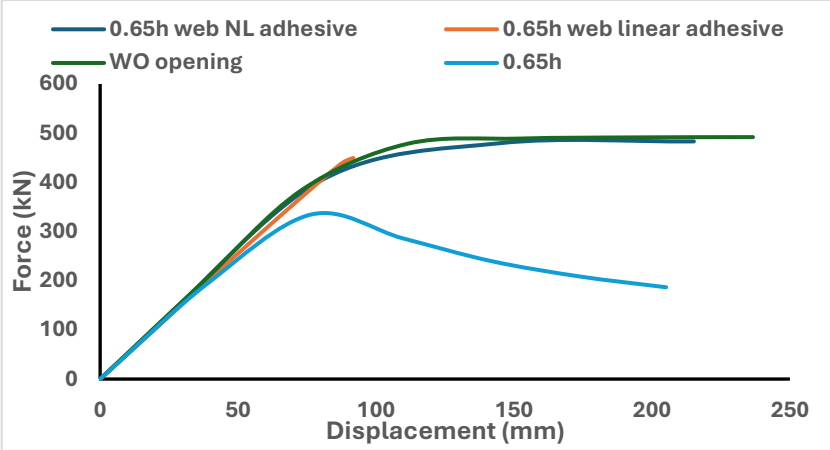


Figure 5-61: Force-displacement response for 0.65h rectangular opening with linear and nonlinear adhesive

The first signs of interface degradation in the linear adhesive case appeared at a displacement of 37 mm, initiating at the right ends of the CFRP, where material discontinuity induces high bending stresses, with the CFRP plates at stress levels less than 400 MPa, as shown in **Figure 5-*62***. Damage subsequently accumulated in these regions and extended to the corners on the LMS, where plastic hinges began to develop, leading to high interfacial shear stresses. In contrast, for the nonlinear adhesive, damage initiated at a displacement of approximately 80 mm, occurring simultaneously at the right end of the CFRP and at the left corners of the opening.

Upon further loading, two plastic hinges develop at the corners on the left side of the opening, inducing small relative displacements between the left and right sides of the opening. This leads to complete local debonding of the CFRP at the LMS at a load of 377 kN and a deflection of 74 mm, as illustrated in **Figure 5-*63***.

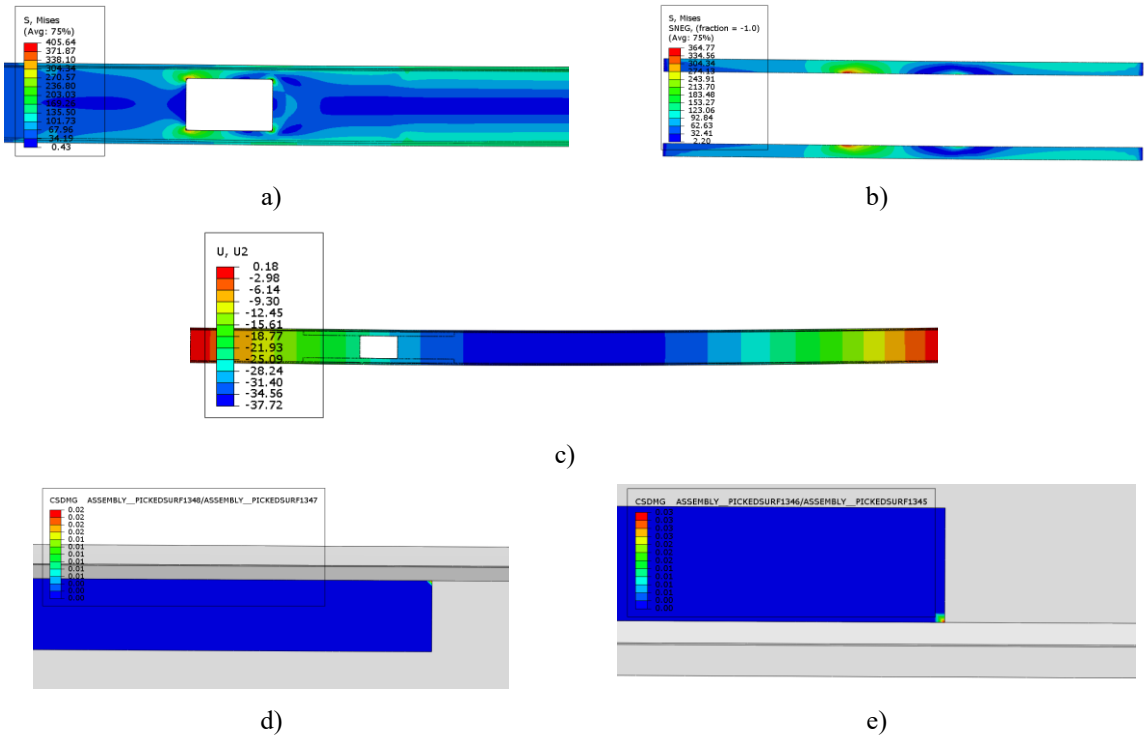


Figure 5-62: Stress distribution and displacement for beam with linear adhesive; a) Beam stress distribution; b) CFRP stress distribution; c) Displacement at damage initiation; d) Damage top stem; e) Damage bottom stem

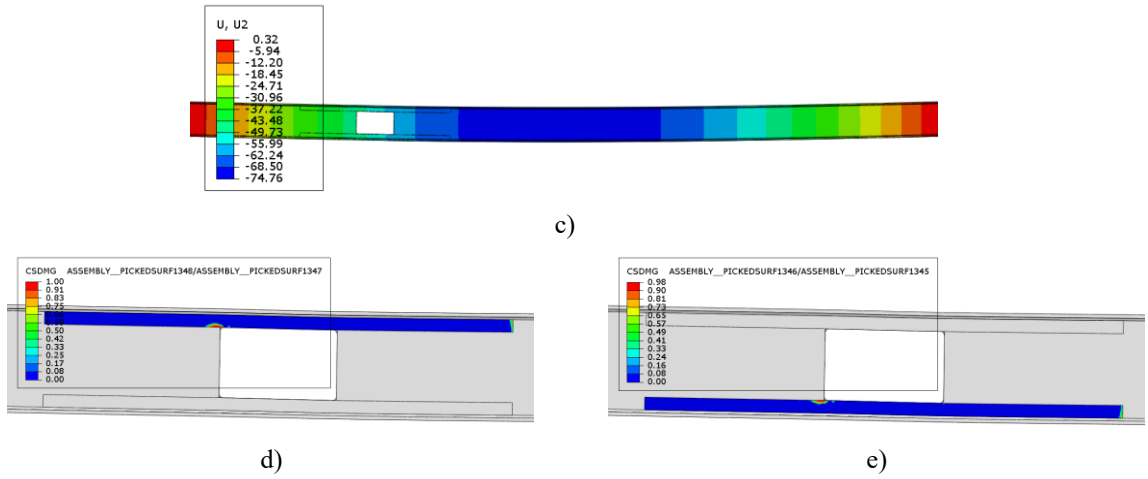
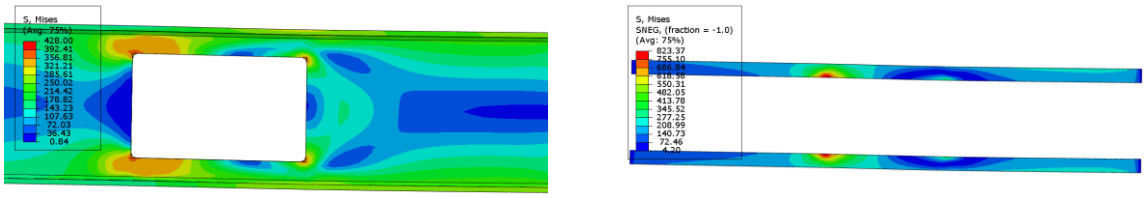


Figure 5-63: Stress distribution and displacement for beam with linear adhesive; a) Beam stress distribution; b) CFRP stress distribution; c) Displacement at debonding; d) Damage top stem; e) Damage bottom stem

This behaviour contrasts markedly with that of the nonlinear adhesive, where local debonding did not occur owing to the high deformation capacity of the adhesive, with a maximum CSDMG value of 0.92 recorded at a displacement of 216 mm. It is important to note that the beam with the linear adhesive experienced CFRP debonding at a load lower than its maximum capacity of 448 kN, with the top CFRP plate debonding slightly before the bottom plate. The beam continued to sustain load even after debonding because the failure mode had already shifted from Vierendeel bending to flexural failure at midspan, as evidenced by the absence of plastic hinge formation on the right side at the final displacement recorded. Although the global failure

mode was essentially identical for both adhesive types. In the case of the linear adhesive, the sequence involved slight Vierendeel movement, followed by local debonding, and subsequently flexural failure, whereas the nonlinear adhesive is characterized by slight Vierendeel movement followed by global flexural failure. The nonlinear adhesive led to the CFRP reaching stresses as high as 1400 MPa, whereas the linear adhesive achieved only 820 MPa (see Figure 5-64).



a) b)

Figure 5-64: Stress distribution a) around opening corners; b) CFRP plate

5.5.2. CFRP flange strengthening

For the case of CFRP bonded to the flange using a linear adhesive, the elastic stiffness of the beam is identical to that observed in both the nonlinear adhesive model and the solid beam model, as well as the perforated beam model, during the early loading stages (see **Figure 5-*65***). This similarity arises because the contribution of the CFRP remains low at this stage at stress levels below 200 MPa for the linear adhesive.

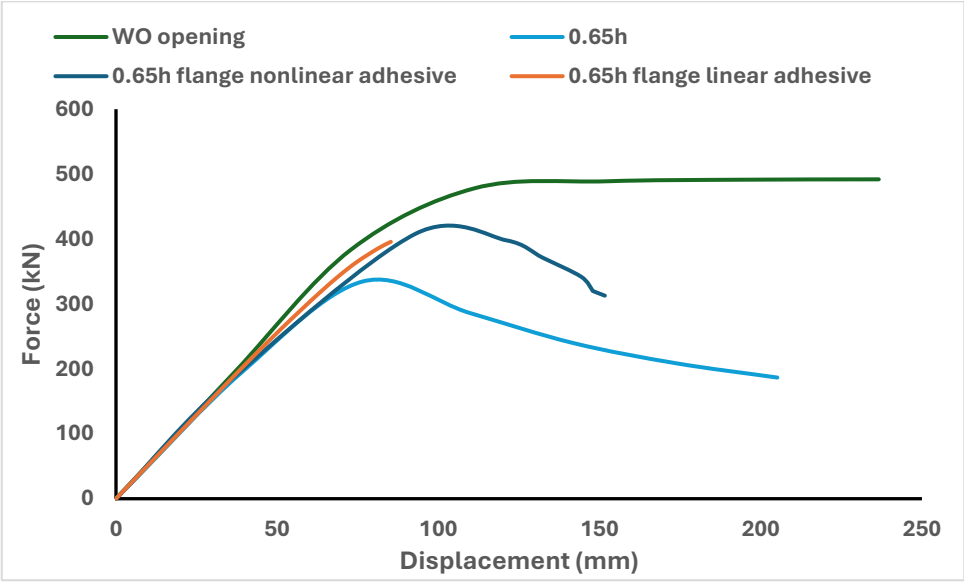


Figure 5-65: Stress distribution vs displacement for 0.65h rectangular opening with different adhesives

At a displacement of 40 mm, stiffness begins to deviate from that of the perforated steel beam as interface damage progressively increases for the linear adhesive, which exhibits higher stiffness than the nonlinear adhesive owing to its greater rigidity. The beam with the nonlinear

adhesive maintains an inelastic stiffness similar to that of the perforated beam, attributable to the limited contribution of the CFRP when attached to the flange. In contrast, the linear adhesive experiences a loss of inelastic stiffness at a displacement of 65 mm, resulting from damage propagation along the LMS toward the CFRP plate bonded to the bottom flange. The nonlinear adhesive retains its stiffness until reaching a maximum load of 407 kN at a displacement of 92 mm, which is comparable to the linear adhesive case, where a maximum load of 395 kN is attained at a displacement of 85 mm, as shown in Figure 5-54. In both cases, the beam fails to restore the capacity of the solid beam.

Local interface damage initiates at a displacement of 34 mm in the linear adhesive case, commencing at the right end of the CFRP plate bonded to the bottom flange, as illustrated in Figure 5-66. This differs from the nonlinear adhesive case, where damage encompasses not only the right ends but also the areas of the CFRP plate corresponding to the opening corners.

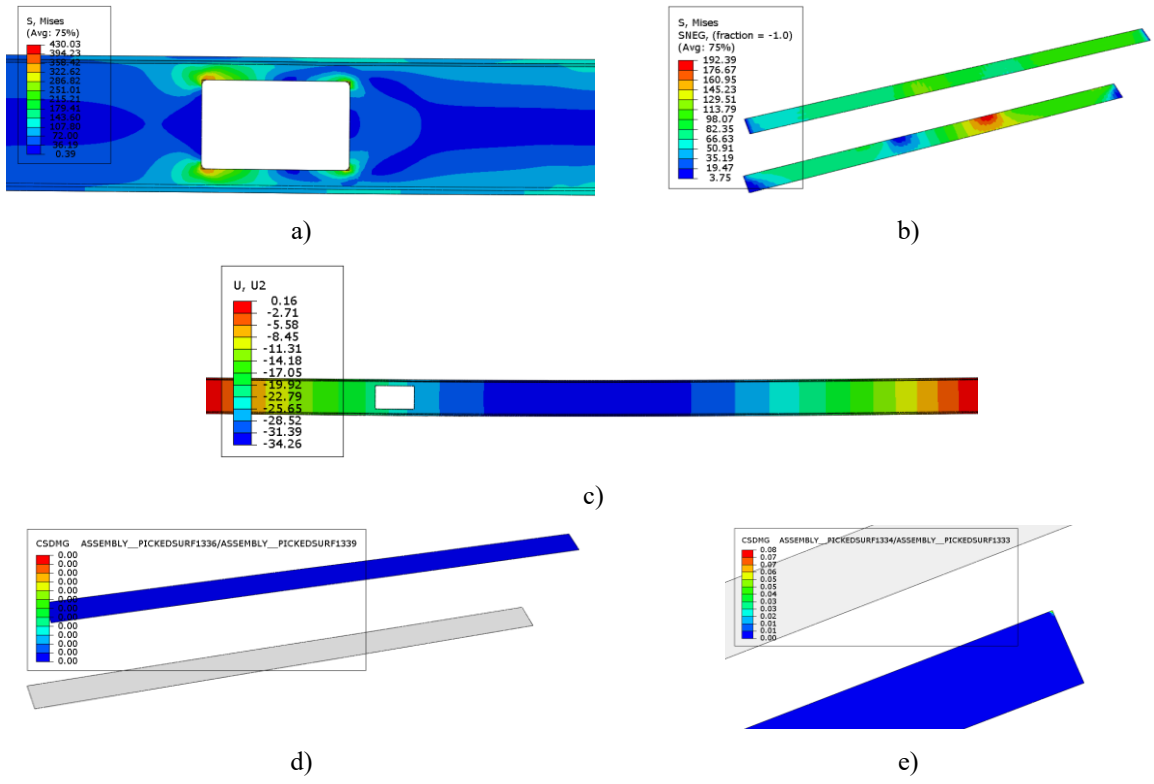


Figure 5-66: Stress distribution and displacement; a) Beam stress distribution; b) CFRP stress distribution; c) Displacement at damage initiation; d) Damage initiation top flange; e) Damage initiation bottom flange

As loading progresses, plastic hinges form once again at the corners of the opening, with those on the LMS being more developed owing to the higher shear forces in that region. At a displacement of 81 mm, debonding occurs in the CFRP bonded to the bottom flange, specifically along the inner side of the CFRP corresponding to the bottom corner on the LMS, as shown in **Figure 5-*67***. This behaviour differs from the nonlinear adhesive case, where

debonding initiated in the same region but occurred first in the CFRP attached to the top flange, followed by the bottom flange, and was distributed over a larger area owing to the higher strain tolerance of the nonlinear adhesive.

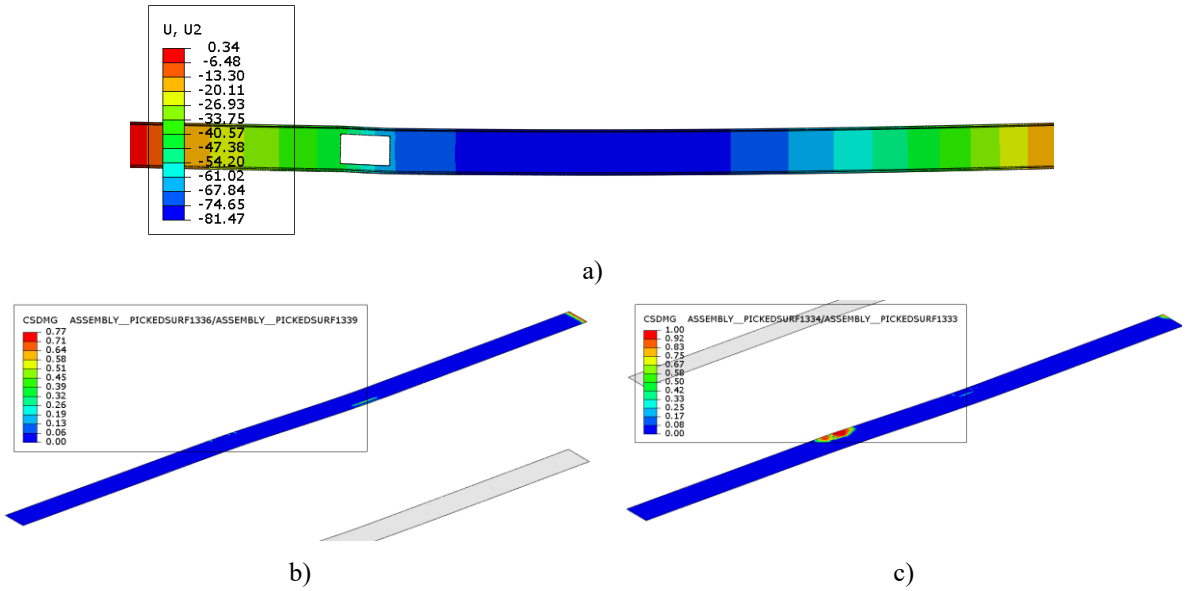


Figure 5-67: Displacement and damage initiation; a) Displacement at damage initiation; b) Top flange damage initiation; c) Bottom flange damage initiation

Regardless of the adhesive type, failure remained governed by the formation of the Vierendeel mechanism, as illustrated in Figure **Figure 5-*68***a. However, debonding occurred at a higher displacement for the nonlinear adhesive compared to the linear adhesive, as reflected in the CFRP stress levels at debonding, which reached 2400 MPa for the nonlinear adhesive and approximately 900 MPa for the linear adhesive, as shown in **Figure 5-*68***b. Consequently, the use of the nonlinear adhesive not only resulted in a higher load-carrying capacity but also enabled more efficient utilization of the CFRP material than the linear adhesive.

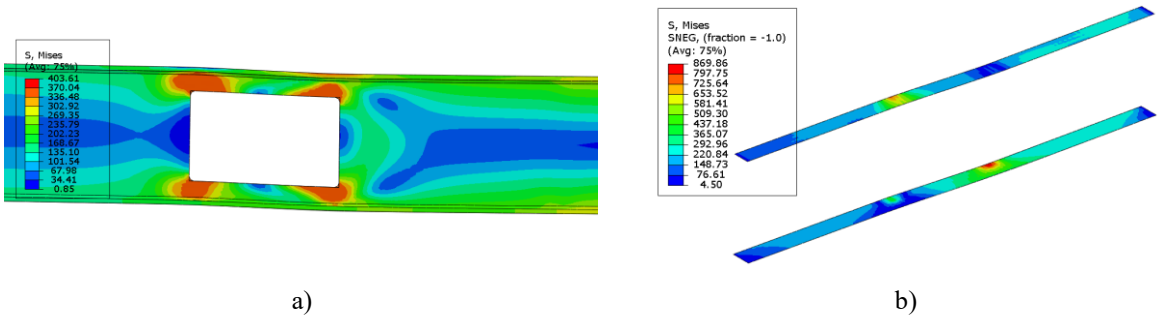


Figure 5-68: Stress distribution; a) Around the corners of the opening; b) CFRP plates

5.6. Assessment of the analytical approach

The analytical approach developed in Chapter 3 was employed to assess the load-carrying capacity of steel beams with web openings for the different failure mechanisms considered in this study. The analytical formulation accounts for three relevant limit states: Vierendeel bending failure at the opening; flexural failure of the solid beam in CFRP-strengthened quarter-span configurations for which strengthening of the opening region shifts the governing failure mode to the unperforated section; and flexural failure of the perforated section for beams with openings located at midspan. To assess the predictive accuracy of the proposed analytical approach, its results are compared with those obtained from the numerical analyses for selected configurations with an opening depth of 0.65h for rectangular openings and 0.8h for circular openings including different CFRP strengthening arrangements. The resulting analytical and numerical load-carrying capacities are presented in **Table 5-*2***, together with the corresponding deviations.

Table 5-2: Comparison between the analytical predictions and the corresponding numerical model

Opening location	Opening shape	CFRP configuration	Analytical capacity (kN)	Numerical capacity (kN)	Deviation (%)	Governing analytical limit state	Numerical failure mode
Quarter-span	Rectangular	Flange	407.88	407.67	0.05	Vierendeel mechanism + Debonding	Vierendeel mechanism + Debonding
Quarter-span	Rectangular	Web	469.44	483.20	2.93	Flexural failure	Flexural failure
Quarter-span	Circular	Web	469.44	482.86	2.86	Flexural failure	Flexural failure
Mid-span	Rectangular	Flange	521.60	514.53	1.35	Flexural failure + End debonding	Shifted hinge + End debonding
Mid-span	Rectangular	Web	478.40	512.72	7.17	Flexural failure + End debonding	Shifted hinge + End debonding
Mid-span	Circular	Flange	505.60	504.32	0.25	Flexural failure + End debonding	Flexural failure + End debonding
Mid-span	Circular	Web	469.44	490.63	4.51	Flexural failure + End debonding	Flexural failure + CFRP failure + intermediate debonding

The analytical approach predicts the load-carrying capacity with generally good agreement with the numerical results for the selected configurations. For cases involving CFRP bonded to the

flanges, the deviation remains below 1.5%, regardless of whether the opening is located at quarter-span or mid-span. The analytical predictions for these configurations are slightly higher than the corresponding numerical capacities, although the differences are small. In contrast, for configurations with CFRP bonded to the web, the analytical approach consistently underestimates the numerical capacity, with deviations ranging from approximately 2.9% to 7.2%. Overall, the comparison indicates that the proposed analytical approach is able to reproduce the numerical load-carrying capacities with reasonable accuracy, while showing a conservative tendency for the web-strengthened configurations.

The comparatively larger deviations observed for the web-strengthened configurations may be associated with the simplified treatment of CFRP debonding adopted in the analytical approach. The debonding expression implemented in Chapter 3 corresponds to an end-debonding mechanism, whereas the numerical analyses showed that, for CFRP bonded to the web, interface damage can develop predominantly at intermediate locations, particularly in the vicinity of the opening corners. Consequently, the analytical formulation does not reproduce the same damage mechanism observed in the finite element models. This difference in the representation of the steel–CFRP interface is therefore considered a likely contributor to the conservative analytical predictions obtained for the web-strengthened cases and represents a limitation of the proposed simplified approach.

It should be noted that the present assessment is limited to the selected configurations, including an opening depth of 0.65h for rectangular openings and 0.8h for circular openings, as well as the cross-section seometry, loading conditions, and lateral-restraint assumptions adopted in this study. The comparison therefore demonstrates the applicability of the analytical approach within the investigated range but does not establish its accuracy for other beam geometries, opening sizes, strengthening arrangements, or loading conditions. Further assessment would be required before extending the proposed approach beyond the configurations considered herein.

5.7. Summary

The results of the unstrengthened beams demonstrate that the influence of a web opening on the load-carrying capacity depends strongly on its geometry, depth, and location, as summarised in **Table 5-*3*.** For rectangular openings located at quarter span, an opening depth of 0.50h resulted in virtually no reduction in strength, whereas increasing the opening depth to 0.65h and 0.75h produced progressively more significant reductions in capacity as the

Vierendeel mechanism became governing. In contrast, circular openings located at quarter span had little influence on the beam capacity for opening depths up to 0.75h, with an appreciable reduction occurring only for the 0.80h opening. For openings positioned at midspan, the load-carrying capacities obtained for circular and rectangular openings of equivalent depth were generally comparable and decreased progressively as the opening depth increased. These results show that the effect of opening location cannot be considered independently of opening geometry: large rectangular openings are particularly detrimental at quarter span due to Vierendeel action, whereas for circular openings the midspan location is generally more critical up to a depth of 0.8h. In general, the initial elastic stiffness of the beam was only slightly affected by the presence of the openings within the range investigated.

Table 5-3: Load-carrying capacity of unstrengthened beams with different opening shapes, sizes and locations

Opening shape	Opening location	Opening depth	Load-carrying capacity (kN)	Governing failure mode
Rectangular	Quarter-span	0.50h	487.91	Flexural failure
Rectangular	Quarter-span	0.65h	334.64	Vierendeel mechanism
Rectangular	Quarter-span	0.75h	198.04	Vierendeel mechanism
Rectangular	Mid-span	0.50h	450.43	Flexural failure
Rectangular	Mid-span	0.65h	425.83	Flexural failure
Rectangular	Mid-span	0.75h	407.85	Top Tee flexural failure
Circular	Quarter-span	0.50h	487.15	Flexural failure
Circular	Quarter-span	0.65h	487.18	Flexural failure
Circular	Quarter-span	0.75h	486.89	Flexural failure
Circular	Quarter-span	0.80h	451.18	Vierendeel mechanism
Circular	Mid-span	0.50h	451.75	Flexural failure
Circular	Mid-span	0.65h	422.40	Flexural failure
Circular	Mid-span	0.75h	402.87	Flexural failure
Circular	Mid-span	0.80h	388.36	Flexural failure

Under the perfect-bond assumption, the effectiveness of the CFRP strengthening configuration was found to depend on the governing failure mechanism. For quarter-span openings in which the response was governed by Vierendeel action, CFRP bonded to the web was the most effective configuration among those investigated for recovering the capacity lost due to the opening. For the 0.65h rectangular opening, web strengthening increased the capacity from approximately 335 kN to 483 kN, almost restoring the capacity of the solid reference beam and shifting the governing failure mode towards that of the unperforated section. For the more severe 0.75h opening, the same configuration increased the capacity from approximately 200

kN to 440 kN, although the original capacity was not completely recovered and Vierendeel failure remained governing. For circular quarter-span openings, the CFRP and steel-stiffener configurations investigated were generally capable of suppressing the local Vierendeel mechanism, after which the capacity became limited by flexural yielding of the unstrengthened midspan section. Conversely, for openings located at midspan, where the response is governed primarily by flexure, CFRP bonded to the flanges was the most effective configuration for capacity recovery because it directly increases the flexural resistance of the perforated section.

The perfect-bond analyses provide an upper-bound estimate of the strengthening effect and were therefore complemented by models in which the steel–CFRP interface behaviour and progressive debonding were explicitly considered. The comparison between the perfect-bond and cohesive-interface results for the 0.65h configurations is summarised in **Table 5-*4*.** For the quarter-span rectangular opening, the reduction in capacity due to interface damage was approximately 4.8% for flange strengthening but only 0.1% for web strengthening, while a reduction of approximately 2.7% was obtained for the web-strengthened circular opening. For the midspan configurations, the reductions ranged from approximately 0.7% to 3.1%, depending on the opening shape and CFRP location. These results indicate that, for the nonlinear adhesive considered, substantial local interface damage may develop without necessarily controlling the global failure load. In several configurations, the CFRP remained sufficiently engaged to recover most or all the capacity lost due to the opening and, in some cases, to shift the governing failure mechanism. The influence of debonding is nevertheless configuration-dependent and becomes more significant when interface degradation prevents the CFRP from being fully mobilised before structural failure.

Table 5-4: Comparison of load-carrying capacity for perfect-bond and cohesive-interface models

Location	Opening shape	CFRP configuration	Perfect bond (kN)	Cohesive interface (kN)	Reduction (%)
Quarter-span	Rectangular	Flange	428.11	407.66	4.78
Quarter-span	Rectangular	Web	483.74	483.20	0.11
Quarter-span	Circular	Web	488.04	474.98	2.68
Mid-span	Rectangular	Flange	518.80	514.53	0.82
Mid-span	Rectangular	Web	516.49	512.72	0.73
Mid-span	Circular	Flange	511.52	504.32	1.41
Mid-span	Circular	Web	506.28	490.63	3.10

The influence of adhesive behaviour was investigated for the representative case of a 0.65h rectangular opening located at quarter span, considering CFRP bonded either to the web or to

the flanges. The results showed that the adhesive model can significantly affect the extent to which the CFRP strengthening is mobilised. Compared with the nonlinear adhesive, the linear adhesive reduced the ultimate capacity from 407.66 kN to 395.75 kN for flange strengthening and from 483.20 kN to 449.45 kN for web strengthening, corresponding to reductions of approximately 2.9% and 7.0%, respectively (see Table 5-5). The linear adhesive was associated with earlier debonding and lower CFRP stress utilisation, whereas the nonlinear adhesive, owing primarily to its substantially higher fracture energy and greater deformation capacity, allowed progressive interface damage to develop over a larger deformation range before complete local debonding. Consequently, for the configurations investigated, the nonlinear adhesive enabled a greater proportion of the potential CFRP strengthening effect to be mobilised.

The analytical approach developed in Chapter 3 was assessed against the numerical results for selected configurations with a rectangular opening depth of 0.65h and circular opening depth of 0.8h, as presented in Table 5-2 in Section 5.6. Overall, good agreement was obtained between the analytical and numerical load-carrying capacities. For configurations with CFRP bonded to the flanges, the deviations remained below 1.5%, whereas the web-strengthened configurations were conservatively underestimated by approximately 2.9% to 7.2%. The comparatively larger deviations obtained for web strengthening are considered to be associated, at least in part, with the simplified debonding formulation adopted in the analytical approach, which represents end debonding, whereas the numerical models showed that interface damage may develop at intermediate locations around the opening. The comparison therefore indicates that the simplified analytical approach provides encouraging predictions within the range investigated, while also identifying the representation of debonding as an important limitation of its present formulation.

Table 5-5: Influence of adhesive behaviour on the load-carrying capacity of the CFRP-strengthened beam

CFRP configuration	Nonlinear adhesive (kN)	Linear adhesive (kN)	Reduction (%)
Flange strengthening	407.66	395.75	2.92
Web strengthening	483.20	449.45	6.98

Overall, the parametric study demonstrates that the effectiveness of CFRP strengthening is governed by the interaction between the opening characteristics, the structural demand at the opening location, the strengthening configuration, and the behaviour of the bonded interface. The most effective CFRP arrangement is therefore not unique: web strengthening is particularly

effective for the investigated quarter-span configurations in which Vierendeel action governs, whereas flange strengthening is more effective for midspan openings governed by flexure. The comparison with conventional steel stiffeners further indicates that CFRP can provide an effective alternative strengthening solution for the selected configurations, although its performance depends on the capacity of the adhesive interface to transfer stresses and sufficiently mobilise the CFRP. The results also demonstrate the importance of accounting for debonding when evaluating CFRP-strengthened steel beams, since the perfect-bond assumption represents an upper-bound response and may conceal premature interface-controlled failure. Within the scope of the configurations investigated, the numerical study therefore confirms the potential of appropriately positioned CFRP plates to recover a substantial proportion of the capacity lost due to large web openings and, where sufficient strengthening is achieved, to alter the governing structural failure mechanism.

THIS PAGE WAS INTENTIONALLY LEFT BLANK

6. CONCLUSIONS AND FUTURE WORK

6.1. Summary of research

The research presented in this thesis was motivated by the increasing application of carbon fibre-reinforced polymer (CFRP) plates for the strengthening of steel beams. While a substantial body of research has been devoted to the strengthening of solid beams, particularly through the application of CFRP to the tension side, comparatively little attention has been directed towards the use of CFRP plates to strengthen beams incorporating large web openings. This study addresses this gap by systematically investigating a range of parameters that influence the structural behaviour of steel beams with web openings and, in turn, assessing the extent of enhancement achievable through the addition of CFRP strengthening plates.

The investigation encompasses two distinct opening locations along the beam span: at quarter-span and at mid-span. The opening depth was varied up to the maximum permissible size specified by Eurocode, and both circular and rectangular opening geometries were examined. Building upon previous research, a primary CFRP configuration was adopted, with selected variations introduced to evaluate their relative effectiveness. The perfect bonding condition was first examined and regarded as an upper-bound limit, after which a cohesive-interface formulation allowing progressive interface damage and debonding was considered. Two adhesive types, nonlinear and linear, were investigated to capture the influence of the adhesive constitutive behaviour on the overall response. In addition, steel stiffeners were employed in a few models, serving as a benchmark for comparison, particularly in cases governed by the Vierendeel bending mechanism.

The methodology adopted in this study combined numerical and analytical approaches. A finite element modelling framework was developed in Abaqus and assessed against three experimental steel-beam benchmarks reported in the literature, covering different structural responses and failure mechanisms. This framework was subsequently used to perform the parametric investigation of the unstrengthened and strengthened beams, including the simulation of CFRP strengthening and progressive damage at the steel–CFRP interface through a cohesive-interface formulation. In parallel, a simplified analytical approach was developed to estimate the load-carrying capacity of beams with web openings, considering the relevant governing failure mechanisms and the contribution of the CFRP strengthening. The analytical

predictions were subsequently assessed against the numerical results obtained for selected configurations, allowing the accuracy and main limitations of the proposed approach to be evaluated.

6.2. Key conclusions

The influence of web openings on the structural response was found to depend on the combined effects of opening geometry, depth, and location, rather than on any of these parameters individually. Increasing the opening depth generally resulted in a reduction in load-carrying capacity, although the magnitude of this reduction depended strongly on the opening shape and the governing failure mechanism. For rectangular openings located at quarter span, larger openings produced significant reductions in capacity due to the development of a Vierendeel mechanism, whereas circular openings at the same location had a comparatively limited influence for opening depths up to 0.75h. At midspan, where the response was predominantly governed by flexure, the capacity decreased progressively with increasing opening depth, while the influence of opening shape was comparatively small. Overall, the presence of the openings had only a limited influence on the initial global stiffness of the beams within the range investigated.

The effectiveness of the CFRP strengthening configuration was closely related to the governing structural mechanism. For the investigated quarter-span configurations in which Vierendeel action governed, CFRP bonded to the web was the most effective arrangement among those considered, as it improved the local resistance of the Tee sections around the opening and reduced the severity of the Vierendeel mechanism. When sufficient strengthening was provided, the governing failure mode shifted from the opening region to flexural failure of the unperforated section. Conversely, for openings located at midspan, CFRP bonded to the flanges was the most effective configuration, since the response was predominantly flexural and the flange reinforcement directly increased the resistance of the perforated section. These results demonstrate that the most effective CFRP arrangement depends on the structural demand and failure mechanism at the opening location and should therefore be selected accordingly.

The analyses considering the steel–CFRP interface demonstrated the importance of accounting for interface damage and debonding when assessing the effectiveness of CFRP strengthening. The perfect-bond assumption provides an upper-bound estimate of the strengthening response, while the introduction of a cohesive interface generally resulted in some reduction in load-

carrying capacity, the magnitude of which depended on the strengthening configuration and opening location. Nevertheless, substantial local interface damage did not necessarily result in a significant reduction in global capacity when another structural failure mechanism became governing before complete debonding occurred. The comparison between the two adhesive models further showed that, for the configurations investigated, the adhesive with substantially higher fracture energy and deformation capacity allowed a greater degree of progressive interface damage before complete local debonding, thereby enabling greater mobilisation of the CFRP strengthening.

The comparison with conventional steel stiffeners showed that the selected CFRP strengthening arrangements were capable of providing comparable, and in some cases greater, recovery of the capacity lost due to the web opening. The results therefore support the potential use of externally bonded CFRP as an alternative strengthening technique for steel beams with large web openings, particularly where the governing failure mechanism and the CFRP configuration are appropriately matched. However, the relative performance of CFRP and steel stiffeners in the present study was assessed primarily in terms of structural response and load-carrying capacity; consequently, the results should not be interpreted as demonstrating a general superiority of CFRP over conventional steel strengthening. Practical aspects such as material quantity, cost, installation, durability, and long-term performance were outside the scope of the numerical comparison.

Finally, the simplified analytical approach developed in this study provided generally good estimates of the numerical load-carrying capacities for the selected configurations considered in the assessment. Particularly close agreement was obtained for the flange-strengthened cases, whereas the web-strengthened configurations were conservatively underestimated to a somewhat greater extent. The larger deviations observed for web strengthening are considered to be associated, at least in part, with the simplified representation of debonding in the analytical formulation, which is based on an end-debonding mechanism, whereas the numerical models showed that interface damage may develop at intermediate locations around the opening. The analytical approach therefore provides encouraging capacity estimates within the investigated range, while the treatment of debonding remains an important limitation when extending its applicability to other configurations.

6.3. Limitations and future work

The present study provides insights into the strengthening of steel beams with web openings using CFRP plates, several limitations are identified, each of which presents opportunities for future research:

- **Experimental validation of the CFRP-strengthened system**: The experimental benchmarks used in the numerical assessment focused on the structural response of steel beams and did not provide direct validation of the complete CFRP-strengthened system or of the adopted steel–CFRP cohesive-interface formulation. Future work should therefore include experimental testing of representative CFRP-strengthened beams with large web openings, with particular attention to interface damage initiation and propagation, debonding mechanisms, CFRP stress development, and the resulting structural failure modes.
- **Beam and opening parameter space:** The numerical investigation was restricted to a single beam span, cross-section and steel grade, together with selected rectangular and circular opening geometries and two opening locations. The influence of other span-to-depth ratios and, consequently, different combinations of shear force and bending moment at the opening should be investigated. Future studies should also consider additional opening shapes and lengths, different opening locations, multiple or regularly spaced openings, and other steel sections and material grades in order to establish the extent to which the trends identified in the present study can be generalised. This would also allow the applicability of the proposed strengthening strategies to a broader range of structural configurations to be assessed.
- **Boundary, loading and lateral-restraint conditions:** The present study considered simply supported beams subjected to the adopted loading arrangement, with the top flange continuously restrained against lateral displacement. This idealisation suppresses global lateral–torsional buckling and represents a perfectly effective restraint condition. Further work should investigate alternative loading and support conditions, including concentrated loads and continuous beams, together with more realistic representations of the lateral restraint, such as discrete restraint locations and finite restraint stiffness. Explicit modelling of the interaction with a steel deck or composite slab could also be considered where relevant, allowing the influence of the actual restraint system on both global and local behaviour to be assessed.

- **CFRP and adhesive parameters and interface modelling:** The investigation considered a limited set of CFRP and adhesive properties. The CFRP thickness and material properties were fixed, while the interface analyses were based on the selected adhesive models and an adopted adhesive thickness. Future parametric studies should investigate the influence of CFRP thickness, stiffness, fibre orientation, plate width, plate length and anchorage length, as well as adhesive thickness, cohesive stiffness, nominal strength and fracture energy. The sensitivity of the predictions to the adopted traction–separation law and mixed-mode damage formulation should also be assessed, particularly because the effectiveness of the strengthening was shown to depend strongly on the ability of the interface to mobilise the CFRP before significant debonding occurs.
- **Analytical approach and debonding formulation:** The simplified analytical approach was assessed against a limited range of numerical configurations and showed generally good agreement within the investigated domain. However, the adopted debonding formulation represents an end-debonding mechanism, whereas the numerical models showed that interface damage may also develop at intermediate locations around the opening, particularly for web strengthening. Future development should therefore include analytical formulations capable of representing different debonding mechanisms and should investigate the influence of available and effective bond length, CFRP dimensions and opening geometry. The approach should also be assessed over a wider range of beam geometries, opening configurations and loading conditions before its applicability is extended beyond the cases considered in this study.
- **Local instability, imperfections and load introduction:** Transverse stiffeners were omitted from the primary numerical models because the applied loading was uniform and the section was classified as Class 2; consequently, the influence of localized effects at the supports and load-introduction regions was not investigated. Future work should therefore assess web bearing, web crippling and other local instability mechanisms and determine when transverse stiffening is required. In addition, the influence of initial geometric imperfections and residual stresses should be investigated, particularly for configurations in which local buckling contributes to the observed response. Sensitivity analyses considering different imperfection shapes and amplitudes would help establish their effect on the predicted capacity and post-peak behaviour.

- **Long-term and environmental behaviour:** The present investigation was restricted to monotonic structural response and did not consider the long-term durability of the bonded CFRP system. Future studies should examine the influence of temperature, moisture and environmental ageing, cyclic and fatigue loading, and time-dependent behaviour of the adhesive. These effects are particularly relevant for the long-term performance of the steel–adhesive–CFRP interface and should be considered before extending the conclusions of the present study to practical strengthening applications. The exclusion of environmental and long-term effects is already consistent with the scope established earlier in the thesis.

REFERENCES

[1]. P. K. Silwal, A. Parvin, and M. Alhusban, "Numerical investigation on strengthening of steel beams for corrosion damage or web openings using carbon fiber reinforced polymer sheets," *Buildings*, vol. 14, Art. no. 1069, 2024, doi: 10.3390/buildings14041069

[2]. K. F. Chung, T. C. H. Liu, and A. C. H. Ko, "Investigation on Vierendeel mechanism in steel beams with circular web openings," *Journal of Constructional Steel Research*, vol. 57, pp. 467–490, 2001.

[3]. T. M. Cameira Neto, "Analysis and design of composite beams with web openings," thesis, Instituto Superior Técnico, 2014

[4]. S. A. A. Mustafa, E. Fathy, and M. S. Rezk, "Analysis of FRP strengthening web-opening in a steel I-beam under static loading," *European Journal of Advances in Engineering and Technology*, vol. 5, no. 10, pp. 824–836, 2018.

[5]. T. C. H. Liu and K. F. Chung, "Steel beams with large web openings of various shapes and sizes: Finite element investigation," *Journal of Constructional Steel Research*, vol. 59, pp. 1159–1176, 2003

[6]. Institute for Steel Development & Growth (INSDAG), *Steel Beams with Web Openings*, Teaching Material on Structural Steel Design, ch. 28, ver. II.

[7]. M. Altaee, L. S. Cunningham, and M. Gillie, "Practical application of CFRP strengthening to steel floor beams with web openings: A numerical investigation," *Journal of Constructional Steel Research*, vol. 155, pp. 395–408, 2019.

[8]. X. Lü, W. Liao, B. Li, Y. Ding, C. Lü, Y. Sun, S. Mu, and Z. Zhou, "Strengthening effect of stiffener configuration on steel-concrete composite beams with web openings," *Engineering Failure Analysis*, vol. 184, Art. no. 110291, 2026

[9]. J. G. Teng, T. Yu, and D. Fernando, "Strengthening of steel structures with fiber-reinforced polymer composites," *Journal of Constructional Steel Research*, vol. 78, pp. 131–143, 2012.

[10]. D. Lawson and G. Rackham, *SCI P355: Design of Composite Beams with Large Web Openings*. Ascot, U.K.: Steel Construction Institute (SCI), 2011.

[11]. European Committee for Standardization (CEN), *EN 1993-1-13: Eurocode 3—Design of Steel Structures—Part 1-13: Rules for Beams with Large Web Openings*. Brussels, Belgium: CEN, 2006

[12]. European Committee for Standardization (CEN), *EN 1994-1-1: Eurocode 4—Design of Composite Steel and Concrete Structures—Part 1-1: General Rules and Rules for Buildings, Annex N: Composite Beams with Web Openings*. Brussels, Belgium: CEN, 2004.

[13]. S. A. A. Hosseinzadeh and M. Tehranizadeh, "Introduction of stiffened large rectangular openings in steel plate shear walls," *Journal of Constructional Steel Research*, vol. 77, pp. 180–192, 2012, doi: 10.1016/j.jcsr.2012.05.010.

[14]. R. M. Lawson, J. Lim, S. J. Hicks, and W. I. Simms, "Design of composite asymmetric cellular beams and beams with large web openings," *Journal of Constructional Steel Research*, vol. 62, pp. 614–629, 2006.

[15]. M. Pratap and G. R. Vesmawala, "The state-of-the-art review on development of replaceable fuse components in resilient moment resisting frame," *Structures*, vol. 56, Art. no. 104888, 2023, doi: 10.1016/j.istruc.2023.104888

[16]. M. Benzerara, H. Guedaoura, S. M. Anas, M. Yolchiyev, and B. Daminova, "Advanced strengthening of steel structures: Investigating GFRP reinforcement for floor beams with trapezoidal web openings," *E3S Web of Conferences*, vol. 497, Art. no. 02013, 2024

[17]. A. S. de Carvalho, A. Rossi, and C. H. Martins, "Assessment of lateral–torsional buckling in steel I-beams with sinusoidal web openings," *Thin-Walled Structures*, vol. 175, Art. no. 109242, Jun. 2022, doi: 10.1016/j.tws.2022.109242

[18]. D. Kerdal and D. A. Nethercot, "Failure modes for castellated beams," *Journal of Constructional Steel Research*, vol. 4, pp. 295–315, 1984

[19]. M. F. Ezzat, M. A. Elsabaawy, and B. A. Eltaly, "Structural performance of strengthened steel girders with web openings under shear forces," *Engineering Research Journal, Faculty of Engineering, Menoufia University*, vol. 44, no. 2, pp. 175–188, Apr. 2021.

[20]. P. Panedpojaman, T. Thepchatri, and S. Limkatanyu, "Novel design equations for shear strength of local web-post buckling in cellular beams," *Thin-Walled Structures*, vol. 76, pp. 92–104, 2014.

[21]. L. F. Grilo, R. H. Fakury, A. L. R. de Castro e Silva, and G. de S. Veríssimo, "Design procedure for the web-post buckling of steel cellular beams," *Journal of Constructional Steel Research*, vol. 148, pp. 525–541, 2018

[22]. K. D. Tsavdaridis and C. D'Mello, "Web buckling study of the behaviour and strength of perforated steel beams with different novel web opening shapes," *Journal of Constructional Steel Research*, vol. 67, pp. 1605–1620, 2011

[23]. M. Al Taee, L. Cunningham, and M. Gillie, "CFRP strengthening of steel beams with web openings," in *Proceedings of Structural Faults & Repair 2016: 16th International Conference*, M. C. Forde, Ed., Edinburgh, U.K., May 17–19, 2016, Art. no. 1754.

[24]. A. B. Hussein, "Web crippling behavior of cold-formed steel built-up I-sections with stiffened and unstiffened perforated webs," *Results in Engineering*, vol. 28, Art. no. 107565, 2025, doi: 10.1016/j.rineng.2025.107565.

[25]. Z. Xu, G. Tong, L. Zhang, B. Liu, Y. Huang, and T. Ren, "Behaviour and design of steel beams with unstiffened and stiffened rectangular web openings," Thin-Walled Structures, vol. 216, Art. no. 113713, 2025

[26]. S. D. Jadhav and P. D. Kumbhar, "Non-linear behavior of castellated beams consisting hexagonal and diamond openings using CFRP stiffeners," *Asian Journal of Civil Engineering*, vol. 25, no. 6, pp. 4713–4724, 2024, doi: 10.1007/s42107-024-01075-z

[27]. H. W. Al-Thabhawee and A. Mohammed, "Experimental study for strengthening octagonal castellated steel beams using circular and octagonal ring stiffeners," *IOP Conference Series: Materials Science and Engineering*, vol. 584, no. 1, Art. no. 012063,2019

[28]. P. D. Kumbhar and A. M. Jamadar, "Comparative study on load carrying capacities of castellated beams provided with mild steel and CFRP stiffeners," *Materials Today:* Proceedings, https://doi.org/10.1016/j.matpr.2023.03.391

[29]. C. G. Salmon, J. E. Johnson, and F. A. Malhas, *Steel Structures: Design and Behavior*, 5th ed. Upper Saddle River, NJ, USA: Prentice Hall, 2009

[30]. A. Cyril Thomas and K. Baskar, "Behaviour of thin-walled castellated beams strengthened using CFRP," *Structures*, vol. 30, pp. 338–351, 2021

[31]. X.-L. Zhao and L. Zhang, "State-of-the-art review on FRP strengthened steel structures," *Engineering Structures*, vol. 29, pp. 1808–1823, 2007

[32]. P. Colombi and C. Poggi, "An experimental, analytical and numerical study of the static behavior of steel beams reinforced by pultruded CFRP strips," *Composites Part B: Engineering*, vol. 37, no. 1, pp. 64–73, 2006, doi: 10.1016/j.compositesb.2005.03.002

[33]. Borrie D, Al-Saadi S, Zhao XL, Raman RKS, Bai Y. Bonded CFRP/Steel Systems, Remedies of Bond Degradation and Behaviour of CFRP Repaired Steel: An Overview.

Polymers (Basel). 2021 May 10;13(9):1533. doi: 10.3390/polym13091533. PMID: 34068770; PMCID: PMC8126256.

[34]. A. Bilotta, "FRP++ 5: Inspection, Diagnosis, Repairing and Strengthening of existing Structures, Lesson 5 – Strengthening of Existing Structures with FRP (I)," European Master in Advanced Structural Analysis and Design using Composite Materials – FRP++, [Lecture notes].

[35]. I. Valente, "FRP++ 4: Design of Structures with FRP Materials, Lesson 05 – Profiles " European Master in Advanced Structural Analysis and Design using Composite Materials – FRP++, [Lecture notes].

[36]. C. H. Chetan, S. Kattimani, and S. M. Murigendrappa, "Prediction of cohesive zone length and accurate numerical simulation of delamination under mixed-mode loading," Applied Composite Materials, vol. 28, no. 6, pp. 1861–1898, 2021, doi: 10.1007/s10443-021-09939-2.

[37]. A. Turon, "FRP++ 2: Mechanics of Composite Materials, Lecture 9: Failure and damage mechanisms (intralaminar)," European Master in Advanced Structural Analysis and Design using Composite Materials – FRP++, [Lecture notes].

[38]. E. C. Karam, R. A. Hawileh, T. El Maaddawy, and J. A. Abdalla, "Experimental investigations of repair of pre-damaged steel-concrete composite beams using CFRP laminates and mechanical anchors," *Thin-Walled Structures*, vol. 112, pp. 107–117, Mar. 2017.

[39]. M. Al Taee, L. Cunningham, and M. Gillie, "Experimental investigation of CFRP-strengthened steel beams with web openings," *Journal of Constructional Steel Research*, vol. 138, pp. 750–760, 2017

[40]. H. Guedaoura, Y. Hadidane, and M. Altaee, "Numerical investigation on strengthening steel beams with web openings using GFRP," *Frattura ed Integrità Strutturale*, no. 62, pp. 26–53, 2022.

[41]. S. G. Morkhade, K. R. Jagtap, P. S. Ghorpade, D. D. Ahiwale, and H. M. Najm, "Buckling performance evaluation of steel cellular beams strengthened with flange cover plate," *Asian Journal of Civil Engineering*, vol. 23, no. 8, pp. 1277–1290, Jul. 2022, doi: 10.1007/s42107-022-00483-3

[42]. K. Pawar and P. Kumbhar, "Performance analysis of castellated steel I-beam using FRP stiffeners," *International Journal for Research in Applied Science & Engineering Technology (IJRASET)*, vol. 10, no. 2, Feb. 2022

[43]. A. Cyril Thomas and K. Baskar, “Strengthening of thin-webbed castellated beam using CFRP,” *International Journal for Computational Methods in Engineering Science and Mechanics*, vol. 19, no. 6, pp. 396–404, 2018.

[44]. K. Tanady and B. Suryoatmono, “Numerical study of behavior of castellated beam under cyclic loading,” *Civil Engineering and Architecture*, vol. 12, no. 1, pp. 185–202, 2024, doi: 10.13189/cea.2024.120116

[45]. A. M. Okeil, Y. Bingol, and M. R. Ferdous, “Novel technique for inhibiting buckling of thin-walled steel structures using pultruded glass FRP sections,” *Journal of Composites for Construction*, vol. 13, no.6, pp. 547–557, 2009, doi: 10.1061/(ASCE)CC.1943-5614.0000042

[46]. M. A. Kadhim, W. S. AbdulSahib, and A. A. Ali, “CFRP strengthening of steel plate girders with web openings subjected to shear and bending,” *IOP Conference Series: Materials Science and Engineering*, vol. 737, no. 1, Art. no. 012013, 2020, doi: 10.1088/1757-899X/737/1/012013

[47]. M. Hamood, W. AbdulSahib, and A. Abdullah, “The effectiveness of CFRP strengthening of steel beams with web openings,” *MATEC Web of Conferences*, vol. 162, Art. no. 04012, 2018

[48]. N. Yossef, “Strengthening thin-web panel with and without opening using CFRP laminate,” *Structural Faults & Repair*, Edinburgh, UK, 2012.

[49]. M. Hamood, W. Abdulsahib, and A. Abdullah, “Effect of CFRP layer orientation on the behavior of shear-strengthened steel plate girders,” *Engineering and Technology Journal*, vol. 36, no. 7A, pp. 709–714, Jul. 2018, doi: 10.30684/etj.36.7a.

[50]. Y. Du, Y. Shao, C. Wu, M. Su, M. Zhang, and Y. Cao, “Behavior of steel plate shear walls reinforced with stiffened FRP plates,” *Thin-Walled Structures*, vol. 204, Art. no. 112236, 2024

[51]. M. A. Tabrizi and A. Rahai, “Perforated steel shear walls with FRP reinforcement of opening edges,” *Australian Journal of Basic and Applied Sciences*, vol. 5, no. 10, pp. 672–684, 2011.

[52]. European Committee for Standardization (CEN), *EN 1993-1-1: Eurocode 3—Design of Steel Structures—Part 1-1: General Rules and Rules for Buildings*. Brussels, Belgium: CEN, 2005

[53]. T. Yu, D. Fernando, J. G. Teng, and X. L. Zhao, “Experimental study on CFRP-to-steel bonded interfaces,” *Composites Part B: Engineering*, vol. 43, pp. 2279–2289, 2012.

[54]. European Committee for Standardization (CEN), *EN 1992-1-1: Eurocode 2—Design of Concrete Structures—Part 1-1: General Rules and Rules for Buildings*. Brussels, Belgium: CEN, 2004

[55]. European Committee for Standardization (CEN), *EN 1990:2002—Eurocode: Basis of Structural Design*. Brussels, Belgium: CEN, 2002

[56]. N. D. Fernando, "Bond behaviour and debonding failures in CFRP-strengthened steel members," Ph.D. dissertation, Dept. Civil and Structural Engineering, The Hong Kong Polytechnic University, Hong Kong, Aug. 2010

[57]. J. Deng and M. M. K. Lee, "Behaviour under static loading of metallic beams reinforced with a bonded CFRP plate," *Composite Structures*, vol. 78, no. 2, pp. 232–242, 2007, doi: 10.1016/j.compstruct.2005.09.004